

AKADEMIA GÓRNICZO-HUTNICZA IM. STANISŁAWA STASZICA W KRAKOWIE

FIELD OF SCIENCE ENGINEERING AND TECHNOLOGY
SCIENTIFIC DISCIPLINE MATERIALS ENGINEERING

DOCTORAL DISSERTATION

Electromagnetic and gas stirring as a new approach to purifying the steelmaking process in metallurgical industry - investigations based on the advanced, multiphase numerical models

Author: MSc Eng. Monika Zielińska

First supervisor: Prof. Łukasz Madej
Auxiliary supervisor: PhD DSc Eng. Łukasz Malinowski

Completed at: AGH University of Krakow, Faculty of Metals Engineering and Industrial Computer Science, Department of Applied Computer Science and Modeling

Krakow, 2025

Acknowledgement

I would like to thank my supervisors, Professor Lukasz Madej and Doctor Hongliang Yang for their support and guidance during the last few years. Their motivation, discussions, supervision, and time were invaluable in finishing this thesis. I am grateful for their help in organizing my daily activities to cope with my regular work and PhD preparation. Many thanks to Hongliang Yang for his support in participating in the international conferences; thanks to that, I was able to develop myself in public presentations.

I would like to thank my supervisor from ABB company, Doctor Lukasz Malinowski. His help and understanding were invaluable. He always believes in my work and supports my decisions, which motivates me to further hard work to achieve scientific and business goals.

I am grateful to Adam Sitko for inspiring me and motivating to start working with metallurgy engineering; without that, the idea of a PhD would not have been possible. Thank you for irreplaceable support at the beginning of my work.

I would also like to thank the whole ABB Metallurgy R&D Team and ABB Simulation Specialist Team for great and valuable discussions and support during the whole PhD preparation. I could not prepare the whole work without your help and motivation.

Special thanks to Lidong Teng for invaluable help, knowledge sharing, discussions related to metallurgy, and patience in explaining details of the metallurgy processes. Thanks to his scientific curiosity, the models used within this work are continuously being developed to reflect the real conditions accurately. Moreover, his help during the preparation of scientific papers and water modelling measurements was irreplaceable.

I would also like to thank my husband, Marcin, for his support, motivation for harder work, understanding and help in daily activities so I could focus more on the PhD related topics. Without him, this thesis could never have been realized.

The work is dedicated to my inspiration, Marcin.

Table of Contents

Acknowledgement....2
1. Introduction....5
2. Steelmaking technology....7
2.1.1 Electric arc furnace (EAF)....10
2.1.2 Ladle furnace (LF)....12
2.1.3 Tundish and continuous casting (CC) process....12
2.2 Stirring technologies....15
2.3 Improvements in EMS-based manufacturing chain....20
3. Numerical simulation methods in the metallurgy industry....22
3.1 General numerical approaches....22
3.2 Computational Fluid Dynamic (CFD)....24
3.3 Multiphase approach....29
3.3.1 Volume of Fluid (VOF)....29
3.3.2 Discrete Phase Model (DPM)....31
3.3.3 Population Balance Model (PBM)....33
4. Aim of the work....35
5. Development of the advanced CFD model for EMS stirring....37
5.1 Development of the simulation workflow....37
5.2 Model validation....41
5.2.1 Experimental setup....41
5.2.2 Steady-state approach....43
5.2.3 Transient approach....46
5.3 Development and implementation of the inclusion model....51
5.4 Development of the indicator for specific stirring energy....56
6. Development of the robust CFD simulation of the electric arc furnace (EAF)....58
6.1 Motivation for CFD simulations in EAF....58
6.2 Description of the EMS EAF simulation....59
6.2.1 Geometry of the model....59
6.2.2 Boundary and initial conditions....60
6.2.3 Material properties....64
6.2.4 Mesh sensitivity study....65
6.3 Temperature homogenization....67
6.4 Dead zones evaluation for BGS – multiphase simulation....70
6.5 Heating....74
6.6 Scrap charging....78
6.7 Validation of the CFD results with EAF industrial data....80
6.8 Development of the new stirrer (Donut-shaped stirrer)....81
7. Development of the robust CFD simulation of the ladle furnace (LF)....86
7.1 Motivation for CFD simulations in LF....86
7.2 Description of the model....87
7.2.1 Geometry....87
7.2.2 Boundary and initial conditions....88
7.2.3 Material properties....89
7.2.4 Mesh sensitivity study....90
7.3 Single-phase and multiphase simulations....93
7.4 Comparison between horizontal, vertical and gas stirring for multiphase simulations....95
7.5 Comparison between mixing times....100

7.6 Inclusions modelling for horizontal EMS 105
7.7 Comparison of CFD results with water model results 107
8. Development of the robust CFD simulations of tundish 121
8.1 Motivation for CFD simulations in tundish 121
8.2 Description of the model 121
8.2.1 Geometry 121
8.2.2 Boundary and initial conditions 124
8.2.3 Material properties 125
8.2.4 Mesh sensitivity study 125
8.3 Comparison between cases without EMS, with baffle wall and with EMS 128
8.3.1 Mixing 128
8.3.2 RTD curves and dead zone calculations 131
8.3.3 Clogging of outlets 140
8.3.4 Inclusions modelling 143
8.4 Comparison of CFD results with water model results 145
8.5 Transfer to industrial application and comparison between the numerical simulations and real test results 148
9. Comparison of stirring speed and stirring energy in investigated metallurgical vessels 154
10. Conclusions 157
11. References 163

1. Introduction

The steelmaking industry is one of the most important industries in the world, as the majority of modern buildings and vehicles include vast amounts of steel in their construction. Steel is also the cornerstone of the renewable energy industry, serving as a construction material for wind turbines, solar and geothermal plants or electric cars[1]. Presently, it is impossible to reduce the need for steel, as most of the time, other materials cannot replace it due to its unique properties and technological aspects. The demand for steel has increased three times over the last 50 years, reaching the level of 95% of the entire metal production[1]. Moreover, it is expected that steel demand will increase in the near future due to the developing industries, economies and the direct relations with GDP growth[2].

However, despite their importance, steelmaking processes are extremely intensive in terms of carbon dioxide emission, reaching up to 10% of the total world's emission[3–5]. A similar situation is in the case of greenhouse gas emissions, with 7% of the worldwide share. Moreover, CO_2 as a greenhouse gas has a residence time of up to 200 years, where 20-60% of CO_2 can remain in the atmosphere over 1000 years[6]. Due to the fact that from 1950, the concentration of carbon dioxide in the atmosphere increased significantly, the global focus is on the reduction of CO_2 emission. Therefore, very demanding environmental regulations have been set, forcing the steelmaking industry to undergo a major change in its local and global operations. The Paris Agreement sets a target for industries characterized by high emissions and energy consumption to reduce CO_2 emissions by 58-93% before 2050 in comparison to the levels from 2010[7]. These kinds of regulations require a lot of effort from the European industry to fulfil the requirements and improve the technologies to achieve the targets[8,9]. As a result, nowadays, the steelmaking industry is in the transition phase, with the goal to significantly reduce CO_2 emissions and eventually obtain neutrality for climate[3,7,10,11].

Unfortunately, steel and iron production requires a vast amount of energy, which is mainly from coal. Coal is ideal for obtaining the required chemical reactions inside the dedicated blast furnaces and producing steel from iron ore. The blast furnaces provide 72% of steel from iron ore but are responsible for 93% of CO_2 emissions in the steelmaking industry. Therefore, it is evident that the blast furnace technology is a high-energy consumption process with high carbon dioxide emissions. Therefore, the blast furnace technologies must be improved or replaced by new, more environmentally sustainable technologies[12,1315].

One solution to this issue is electric steelmaking, which is a technology based on melting steel scrap. This technology is based on electricity and is now responsible for 28% of steel production worldwide, with CO_2 emission at the level of approximately 7%[14]. The steel production with electric arc furnaces (EAF) saves 30% of energy compared to blast furnaces. The iron ore and carbon consumptions are reduced by around 1.5 and 0.65 tons in comparison to the blast furnace route[15]. Moreover, the EAF enables great flexibility in the production of different grades of steel and addressing different market needs, such as increased production efficiency. However, large EAF units in the range of 150 – 350 [tons] have to be used to replace

blast furnace technology. In this case, additional operations, such as stirring, are required to ensure the high efficiency of the production process and the quality of the steel. Without any stirring in the EAF, the efficiency of the process would be very low compared to the basic oxygen furnace[16,17]. Additional mixing is possible through the use of neutral gas injection or additional electromagnetic stirring (EMS) technologies[18]. In the case of the EAF, additional devices like ladle furnace (LF) and tundish are also required to improve the quality of the steel. In these processes, the role of stirring technologies also remains critical.

Nevertheless, the additional improvement of the technology is available from a wider point of view, focusing not only on a single stage but on the whole steel route during the production process. That is the area of engineering where new solutions and continuous development are desired.

This motivated the current research work, which focused on increasing production efficiency and improving steel quality by developing effective stirring solutions for the melt throughout the entire bath. Due to the limitations of the direct experimental investigation under industrial conditions, the research focuses on the use of computer-aided design techniques.

2. Steelmaking technology

Steel is a material that is very important nowadays, and its demand is still increasing in modern life, due to new technologies in civil engineering, transportation, or science. Based on the data from the whole world, the crude steel production (directly after the solidification of liquid), which is sold or used for further processes, in 2023 reached 1 892 [Mt] and is relatively stable from 2000 (Figure 1)[19].

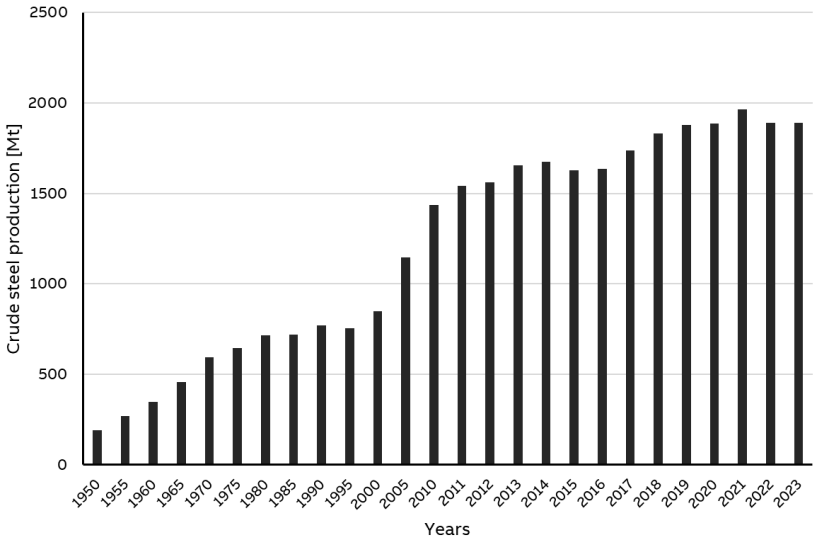


Figure 1. World steel production in years.

By dividing the steel production into geographical distribution, in 2023, the highest crude steel production was in China (53.9%), while in the European Union, 6.7% of the whole world's steel production took place (Figure 2)[19].

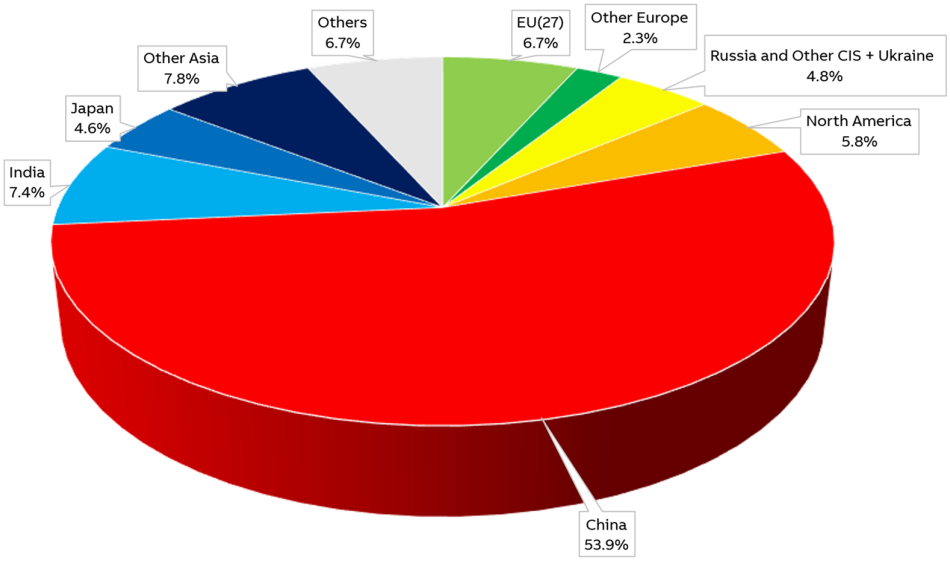


Figure 2. World crude steel production, geographical distribution, 2023.

The steel industry requires advanced technologies to improve processes and increase the efficiency of production while reducing the pollution, so the understanding of these technologies is very important.

There are several technologies related to steel production that, in general, can be divided into primary and secondary metallurgy, as presented in Figure 3. For the electric arc furnace (EAF), the process can be realized by the melting of the scrap or direct reduced iron (DRI), which is an alternative production process and will not be covered in detail by this work.

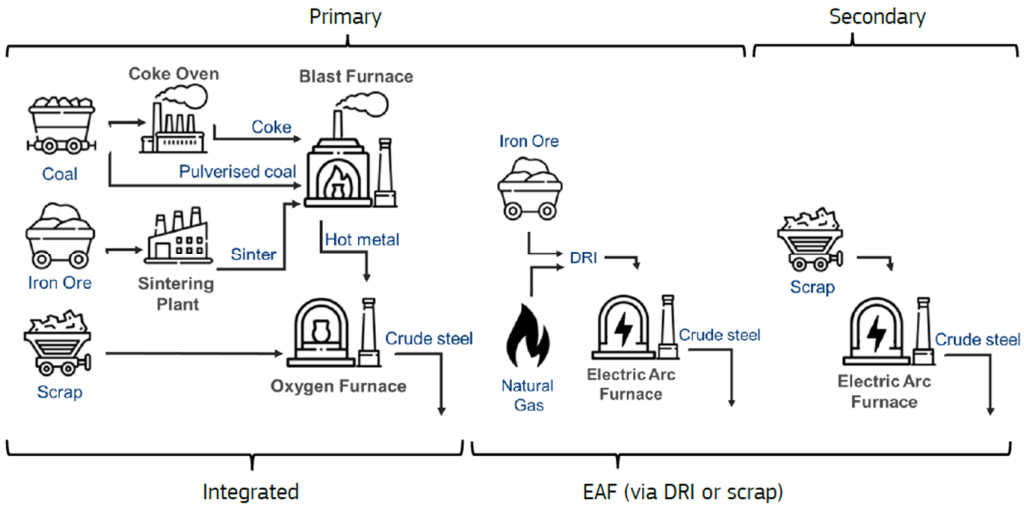


Figure 3. Different production paths for steel[20].

Primary steelmaking is focused on the utilization of iron ore, which is treated as a raw material in iron and steel production. This process route includes the melting and additional cleaning and alloying technologies. The majority of the production is realized in a blast furnace (BF) and a basic oxygen furnace (BOF).

To start the production of the steel in the blast furnace, additional initial steps must be included, like the preparation of the coke by a coke oven made from coking coal, where the coal is heated up to the needed temperatures without the presence of air and also the agglomeration of the iron ore, which is sinter in the dedicated sinter plants. In these plants, the iron ore is crushed, then the additional process of the homogenization and mixing with special additions like coke breeze, limestone, slag-forming agents and additional fluxes in high temperatures are executed. After that, the prepared sinter product is used in the blast furnace. The next step includes feeding to the blast furnace earlier prepared coke, sinter, iron ore and the proper amount of limestone. Thanks to the division of the blast furnace processes into separate zones with respect to the physical and chemical properties of the feeding and temperature, there is a possibility to distinguish different stages. The feeding, which is provided into the blast furnace is heated up and dried by the hot gases injected by the special nozzles in the bottom part of the furnace. Due to the fact that the oxygen is present, the chemical reactions are executed, which causes the transformation of the molten metal and slag into the bottom part

of the furnace, below the level of nozzles. Then, the molten metal and slag start to separate and move down to the bottom level of the furnace, where the final chemical structure and temperature are obtained. The process in the blast furnace is continuous, and the tapping is executed 6-10 times per 24 hours. The next step is executed in the BOF, where the pure oxygen is blown by the special lances above the bath, which causes the chemical reaction of molten steel mixed with the scrap steel to convert the pig iron into crude steel. After that process, additional refining is required to reduce impurities, such as non-metallic inclusions. Moreover, additional alloy additions of other metals can be introduced to the bath to achieve the required chemical structure before casting. Before the casting, molten steel temperature must decrease and is transferred to the mold to start the continuous casting process to create slabs, billets or blooms[21,22].

In the case of primary steelmaking, the other processes for steel production are also available. One example is a production process based on DRI. This process utilizes pelletized iron ore. Moreover, additional reduction of gases like natural gas or reduction of agents in the solid state, like coal, are used. The goal is to remove the oxygen from the iron in the solid state as oxides. The most popular in DRI-based production is natural gas, which is used to obtain the mixture of carbon oxide and hydrogen, where the oxygen content is removed to reduce iron ore. In this case, considering hydrogen produced from renewable electricity instead of natural gas, the process can be environmentally neutral thanks to reduced carbon content.

Secondary metallurgy is based on the melting of scrap to recycle the material, reduce the demand for coke, and significantly reduce carbon dioxide emissions by using an EAF. The technology is under fast development, where a high focus is put on the high efficiency of the production to replace highly effective blast furnaces and meet the requirements of high quality of the produced steel.

The EAF utilizes additional high-current electrodes to generate an electric arc, which is responsible for melting the scrap into the liquid phase. The benefits of this process include thermal control and the ability to incorporate various alloy additions. Due to the availability of recycled materials, the amount of available scrap is high, and this technology can be used to satisfy the demand of the European market in the near future[23]. Unfortunately, the available scrap is very often poor from trace element content point of view, which limits the steel applications in different areas of usage[24]. Moreover, the EAF process requires additional steps in the liquid steel route to continuous casting, as the melting, purifying, and alloying processes differ from those in the BF and BOF and cannot be directly realized in the EAF. Therefore, after the EAF, the steel goes further into the ladle furnace to control the steel's purity and obtain homogenous structure of the steel. Then, the molten steel is transferred into the tundish, where the final structure is stabilized just before the continuous casting machine. The process scheme is presented in Figure 4.

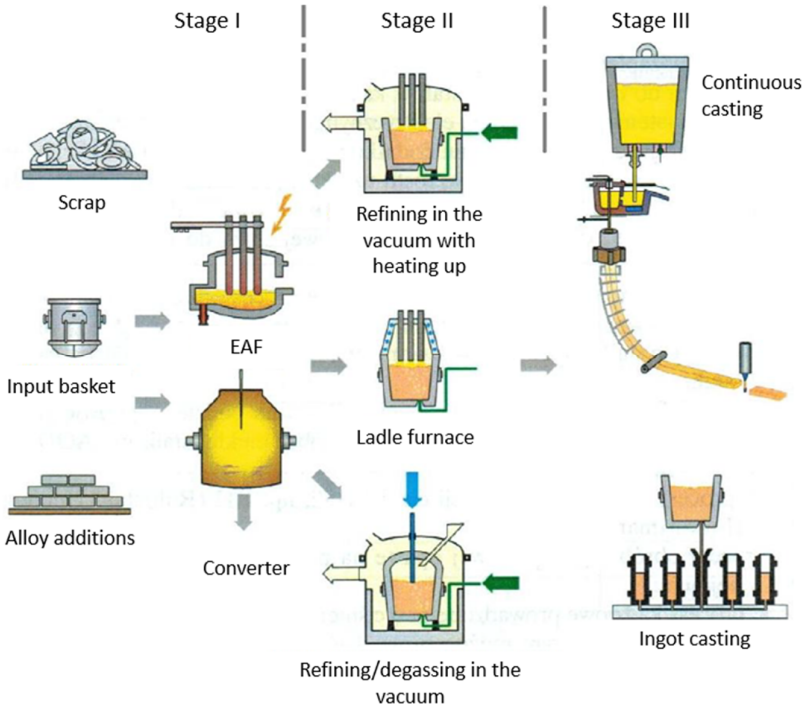


Figure 4. The modern steelmaking process[25,26].

As the main focus of the work is electric and secondary steelmaking, this concept will be described in more detail.

2.1.1 Electric arc furnace (EAF)

The first electric furnace was used in the XIX century to produce different steel grades. Nowadays, this type of furnace is used in the industry for large-scale production and is responsible for approximately 25% of the world's steel production[27].

The electric furnace has a lot of advantages, like:

- heat generation in the metal inside or in its nearest neighborhood,
- easy modifications of the furnace's atmosphere and the possibility of working together with oxidized or reduced slag.

There are several different types of electric furnaces like:

- resistive furnace, where the heat is generated by the current flow via the metal bath or dedicated heaters to heat up the metal by the convection or radiation phenomena,
- arc furnace, where the heat is produced by the electric arc generated by the dedicated electrodes. The temperature generated by the arc is up to 3000 – 5000 [°C],
- induction furnace, where the heat is generated by the current flow due to electromagnetic induction.

The typical construction of the EAF is presented in Figure 5. It should also be mentioned that the capacity of EAF is different, from 10 to 300 tons, which directly influences the overall

dimensions of the furnace. For example, the diameter of the shell of a 10-ton furnace is around 2.5 [m], whereas the diameter of the shell of a 300-ton furnace is up to 9 [m].

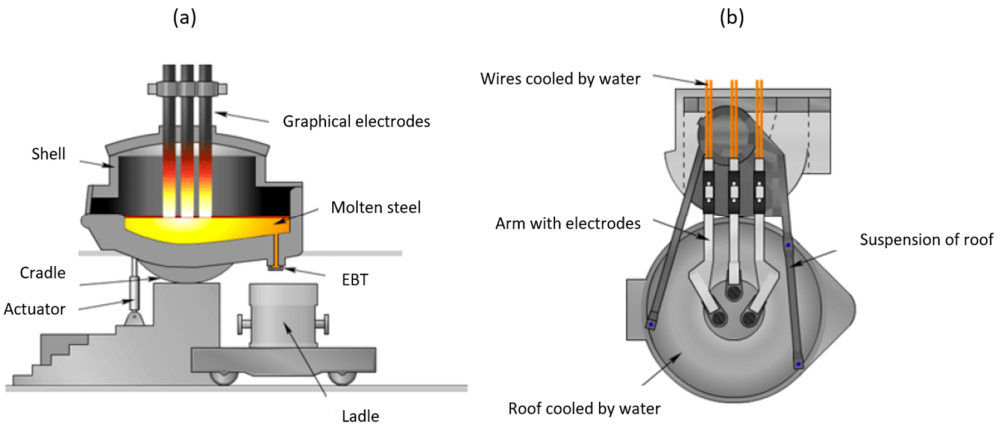


Figure 5. Electric arc furnace, (a) middle cross-section, (b) view from top[28].

The shell of the furnace includes the refractory inside and is cooled down by the water cooling system. The furnace includes a roof with openings to allow the electrodes to be inserted inside. The water system also cools down this roof. The electrodes are made from graphite and are movable in the vertical position. The number of electrodes depends on the type of furnace: DC (Direct Current) or AC (Alternating Current). The additional opening to exhaust the gases from the process is included in the roof. The scrap is put into the furnace from the top or through the special batch door. The tapping process is realized by the rotation of the furnace in the vertical position in the eccentric bottom tap (EBT) direction, while the special window on the opposite side is used to remove the slag.

The majority of the furnaces are powered by the AC current and three graphite electrodes, which are introduced into the furnace by the opening in the roof. In the case of the DC furnace, it is a pair of electrodes, where the first one is located in the shell, and the second one in the roof. During the working process, the DC arc furnace is quieter, but the process is more expensive. Moreover, the refractory must be made from dedicated, more expensive materials to secure the process.

In general, during the process, the first portion of the scrap is put into the furnace when the roof is opened, and electrodes rise up to the maximum top position. Then, the roof is closed, and the electrodes are inserted into the furnace to start the melting process. This initial heating is realized with low power to minimize the reduction of the refractory. The additional heat is provided by the oxygen lances, which are located on the walls and windows to melt the scrap in areas where lower temperatures are expected. When the electrodes are inserted into the furnace in maximum position, the power increases to melt the entire scrap portion. Then, the next portion of the scrap is provided, and the process is repeated to obtain the maximum tapping

capacity. The oxygen lances continue to operate until the required carbon content is achieved. Thanks to the chemical reactions, the bath temperature increases and CO_2 is produced.

The refining processes are often executed by injecting the inert gas into the molten steel from the bottom of the shell via the special, porous plugs. The process enhances mixing within the furnace, which accelerates chemical reactions and promotes temperature homogeneity. During that process, the slag is automatically removed by the slag window, but it can also be removed manually by the rise of the electrodes and rotation of the furnace in the vertical position in the direction of the slag window to the special slag ladle. The mixing can also be achieved by other methods, such as electromagnetic stirring (EMS).

After the process of melting and temperature homogenization, the molten steel is tapped into the ladle by the eccentric bottom tap (EBT). After tapping, around 20% of the molten steel, with some portion of the slag, still remains in the furnace, which increases the effectiveness of the melting of the new scrap load.

The new type of EAF uses around 360 [kWh] and 3 [kg] of graphite electrodes to melt 1 [ton] of the scrap. The process is very efficient and short; it takes around 1 [h][28].

2.1.2 Ladle furnace (LF)

The ladle furnace (LF) is one of the parts that can be used in post-furnace steel processing. The build of that furnace is similar to the EAF and includes the ladle put into the movable trolley and roof with electrodes used only to heat up the steel, so the power needed for LF is much smaller than for EAF. The furnace has an automatic system that includes the alloy additions at the proper time for the refining process. The LF is responsible for:

- maintaining a proper atmosphere above the steel bath,
- temperature and composition adjustment
- effective mixing to reduce the amount of non-metallic inclusions and provide high-quality steel with a homogenized structure. The mixing can be achieved by argon being blown from the bottom plugs or by electromagnetic stirring (EMS) systems.

The LF can be treated as a buffer between the EAF and the continuous casting process and keeps the constant temperature inside. Moreover, due to the chemical reactions, the desulfurization of the steel ensures a reduction of the sulfur content by over 80%, but on the other hand, the reduction of carbon, nitrogen and hydrogen is impossible[28].

2.1.3 Tundish and continuous casting (CC) process

Currently, approximately 90% of steel production is achieved through the continuous casting process. The technology enables the reduction of the requirements related to further forming processes like rolling[28].

The process is based on controlled flow via the casting machine to obtain the proper shape of the material after crystallization, without additional issues on the surface of the billet, bloom, or slab. The steel from the ladle is poured into the tundish, and then, thanks to the system of

outlets, the melt is delivered to different production lines (up to a maximum of 8 separate production lines). The process is carried out in an inert gas atmosphere or within a specialized pipe system to prevent direct oxygen exposure. The process scheme is presented in Figure 6.

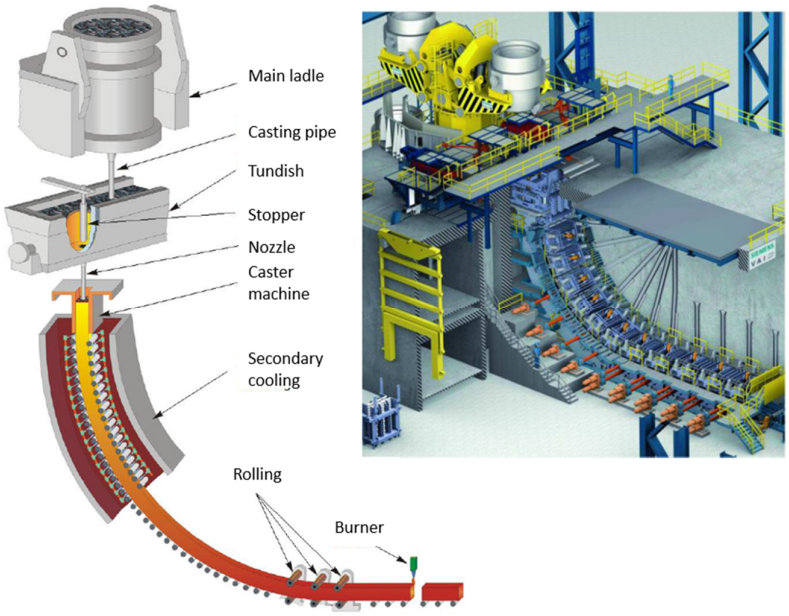


Figure 6. Scheme of the continuous casting process[28].

Inside the caster, the steel starts to solidify from the sides, which are cooled. At this stage, the core of the billet or slab is still fluent. The additional lubricating powders are added to prevent adhesion between the steel and mold. Moreover, the mold is often made from copper and oscillates to avoid adhesion to the surface. The cooling of the billet/slab is realized by the water system or water sprays. At the end of the process, after complete solidification, the steel is cut into sections by the special fuel-oxygen burner.

To fulfil the high requirements for the quality of the steel, the following conditions must be ensured:

- the chemical composition of the steel must be in a narrow, specified range,
- the melt must be delivered to the continuous caster at the right time to ensure the continuity of the process and prevent changes in chemical properties,
- the melt must be provided in the continuous caster machine in a narrow temperature range to ensure correct chemical properties and no issues with further solidification. The temperature should be constant throughout the whole casting process.

The tundish, positioned at the start of the CC process, plays a crucial role in helping to meet these requirements. Due to that fact, many authors focus on the improvements in this technological step[29–37].

The tundish is mainly responsible for the distribution of the steel to different strands of the continuous caster, as presented in Figure 7. Moreover, inside the tundish, the final non-metallic

inclusions removal process is executed, and this device is responsible for stable conditions and continuous process during the ladle changes. To achieve the goals, additional dams, weirs, or baffle walls are often used (Figure 7) to modify the melt flow and increase the steel residence time, which helps in the inclusion removal process. Often, the shape of the tundish is taken into consideration by the authors to optimize the melt flow and temperature for each strand based on mathematical and physical modelling[38].

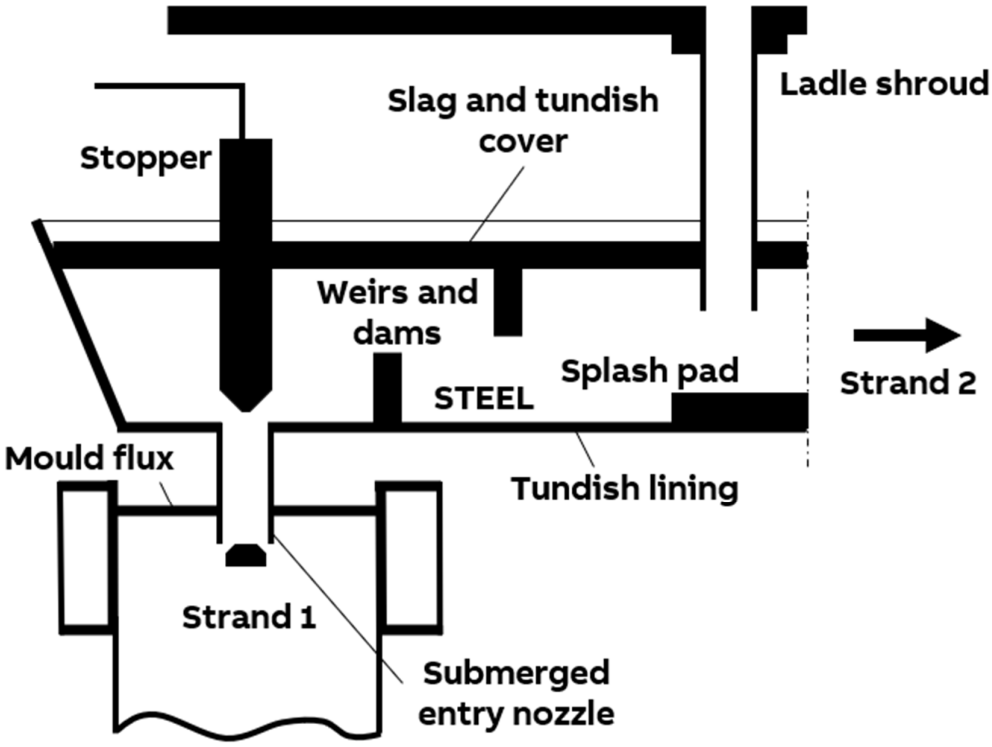


Figure 7. Tundish design for two strands[39].

The main factors that limit the continuity of the process are the issues related to the nozzles and stoppers, and improvements in this area are also intensively studied[37,40–43]. Moreover, the refractory of the tundish plays an important role in being neutral in the case of chemical reactions to stabilize the structure of the steel directly before casting[37,44,45].

Nowadays, to ensure the high quality of steel, the deoxidation process in the ladle is also under scientific investigation[46–48]. Often, calcium is added to reduce the inclusions and increase the quality of the steel. Moreover, the requirements for high-quality steel include low nitrogen and sulfur content. Therefore, the steel must be treated appropriately; for example, the exposition to the atmosphere must be controlled to avoid picking up nitrogen. On the other hand, slag is also an issue that can influence the steel structure and must be eliminated. It is important to use a dedicated system, which can prevent the flow of slag from the ladle to the tundish. This system monitors the steel level and blocks the flow as soon as the slag appears.

The methods mentioned above are capable of maintaining the steel structure within the narrow range required for further casting.

The flow is also controlled inside the tundish, which features a system of solid rods, known as stoppers, that regulate the flow rate via each strand. During the casting, all devices responsible for the flow between the tundish and cater must be tight to ensure no influence of the atmosphere on the steel.

Unfortunately, due to the chemical reactions inside the tundish, the outlets or nozzles can be clogged. To avoid this kind of situation, an inert gas, often argon, is injected into the nozzle through the porous plugs located at the bottom of the stoppers. In this case, the immersion depth, diameter and configuration of the outlets have an additional influence on the quality of the final product.

As presented, due to the variety of factors influencing the behavior of steel in the tundish, research in this area is very important. In particular, many authors are focused on flow optimization and control to provide high-quality steel[32,36,45,49–58].

Finally, it should be emphasized that the required level of stirring throughout all the above-mentioned stages of steel production is critical from the point of view of steel quality.

2.2 Stirring technologies

As mentioned, stirring the molten steel is an important process to increase the efficiency of the chemical reactions and obtain the steel's homogenous temperature and chemical composition. In the case of the ladle furnace and tundish, stirring is also important from a cleanliness perspective, as it improves the non-metallic inclusion removal process. The low stirring efficiency in EAF causes the rate of decarburization to be much lower than in oxygen converter[16,17]. To achieve a high decarburization rate, a high stirring intensity with the occurrence of high turbulence is necessary to form an emulsion between the molten steel and the slag layer.

The mixing in EAF comes from several sources:

- natural convection, due to the temperature gradients and buoyancy forces – the phenomena occurs due to the steel density difference related to the difference in the temperature. The flow caused by the natural convection is across the entire volume of the molten steel, but the velocity is quite low,
- injection of the oxygen from dedicated lances mounted on the sides of the furnace – oxygen is used to obtain the proper conditions and simultaneous refining and melting processes inside the furnace. The intensity of the mixing close to the lance end is quite high, but the phenomena have a very local character and do not increase the velocity inside the whole furnace,
- CO generation during decarburization of the molten steel – a very intense process that occurs in the whole bath, and is caused by chemical reactions with the formation of CO bubbles. Unfortunately, the process is short and dependent on the

carbon content in the steel, which causes the efficiency to decrease with time and is almost impossible to control,

- electromagnetic stirring generated around the electrodes – AC or DC current causes the additional electromagnetic field. Moreover, the phenomenon has a very local character with a high risk of occurrence of dead zones.

Mixing generated from the above-mentioned processes is still insufficient to provide the homogenization of the temperature and prevent uncontrolled temperature gradients. The temperature gradients without additional stirring can reach up to 50-100 [°C][59,60]. To assess the efficiency of the mixing, velocity measurements are often used in the literature. The velocity ranges are presented in Table 1.

Table 1. Average and maximum velocities for several stirring sources.

Source of motion in the liquid steel	Average velocity ranges [m/s]	Maximum velocity ranges [m/s]
Natural convection[61–63]	0.0001-0.0004	0.001-0.002
Oxygen injection[64–67]	0.015-0.02	0.1-0.5
Electromagnetic forces for AC and DC EAF[68–73]	0.01-0.02 (AC), 0.03-0.04 (DC)	0.03-0.04 (AC), 0.1-1.5 (DC)
CO bubbles in decarbonization process[64,74]	0.036	Lack of data

The measurements confirm that these stirring sources are characterized by the low velocities inside the bath. The most intensive is the CO mixing, but due to the fact that the process is difficult to control and measure, it has not been investigated in detail[74].

Therefore, additional forced mixing is used to improve the stirring phenomenon. The most popular in the case of the EAF and LF are bottom gas stirring (BGS)[13,18,75,76] and electromagnetic stirring (EMS)[77–84].

The BGS method has been widely investigated as a means to improve mixing conditions, primarily in the LF, but it is also utilized in EAF applications to enhance heat and mass transfer, melting phenomena, velocity and temperature distribution, and slag eye formation. The dedicated porous plugs are used in conjunction with inert gas injection to facilitate gas stirring. Often, to stir the molten steel, argon is injected into the bath through porous plugs at the bottom of the furnace. The mixing phenomena in the EAF are significantly different from those in the LF due to the fact that the height of the molten steel inside the LF is much greater than in the EAF. Moreover, in the EAF, the height of the melt increases with the melting of scrap. Research about gas stirring in the EAF confirms that the BGS improves the mixing inside the furnace[13,18,76]. The first implementation of the BGS method was in the 1980s, but since 1990, it has lacked interest for 20 years due to problems with the blocking of porous plugs and issues with maintenance. It was reported in[85,86] that in the late 1980s, the installation for the natural gas injection was used in two steel plants located in Mexico, but due to the difficulties with

porous plugs, mainly very short lifetime and difficulties with replacement of the plugs, the use of this technology was cancelled. Similar issues were reported in[18] for Japanese plants in 1990. In this case, the new removable bottom section system was designed to solve the issue of plug maintenance. Then, starting in 2010, this technology was again researched to address the steel production issues. The new technology, based on new types of extremely resistant materials, an updated design, and a production process, has caused the solution to return to daily use in the metallurgy industry[87,88].

Nowadays, from a metallurgical perspective, the BGS method can be realized through direct purging and porous purging. In detail, porous purging can be realized by indirect and hybrid method, so finally, three different types of BGS plugs can be distinguished: direct and indirect[75] as well as the combination of the two, as presented in Figure 8.

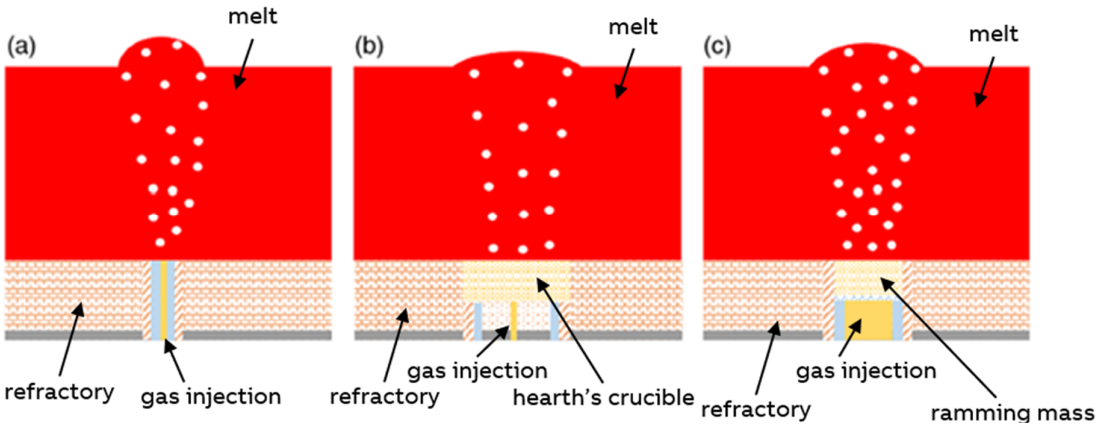


Figure 8. Three different types of plugs: (a) direct, (b) indirect, (c) combination of both methods[18].

The direct system is characterized by the contact of the purging holes, which inject an inert gas into the molten steel. The stirring efficiency is higher with lower gas consumption. The character of the gas column, named a plume, is very narrow, which influences the formation of the slag eye. The solution also has some disadvantages, like a short lifetime, around 700 heats[89], and needs additional maintenance due to the direct contact with the molten steel at high temperatures. Moreover, the stirring conditions must be continuously controlled because the bath in the EAF is quite shallow, and the flow rate via the porous plugs is very limited. This is directly related to the residence time of the bubbles inside the molten steel, which also influences the chemical reactions within the steel[90].

The second type, indirect, is characterized by a plug immersed in the material of the refractory, which should be carefully selected to avoid the leakage of molten steel through the porous material and to ensure high efficiency of the gas flow. The main disadvantage of that solution is that it has less control over the mixing process and high gas consumption. Based on the research in[91], the indirect system has a much longer lifetime, up to 3000 heats.

Unfortunately, the indirect system has additional limitations, such as clogging and dispersed inert gas.

Due to these limitations, a hybrid system was proposed to leverage the advantages of both solutions. The system includes a porous plug below the cylinder, made from a material with a ramming mass that has similar or higher permeability than refractory. The conducted research on these systems confirms that decarburization is more effective, oxygen consumption is lower, and iron oxide levels are decreased. Moreover, the equilibrium between the molten steel and slag is better in hybrid mode[75].

The intensity of the gas stirring inside the EAF is adjusted to ensure optimal conditions during the process. Three main stages can be distinguished: melting, flat bath operations and tapping[92]. During the melting process, the gas flow is moderate; after that, it increases for the flat bath operations. The final tapping stage does not require high stirring, and the gas flow rate is reduced. Typically, the gas flow rate ranges from 10 to 100 [Nl/min]. The BGS utilize different inert gases like Ar, natural gas, N_2, CO and CO_2, and sometimes air[93].

The second forced stirring approach based on the EMS is an older system than BGS. The EMS system was invented in the 1930s by Dr. Ludwig Dreyfus, an employee of ASEA. The proposed solution was patented in Sweden in 1937, and this date is considered as the starting point for EMS technologies in the steelmaking industry[94], with the first industrial application in 1947[95].

The EMS system includes the special coils located at the bottom of the furnace (in the case of EAF) or along the sidewalls for other applications. The intensity of mixing can be fully controlled by adjusting the current flow via the windings of the stirrer. Moreover, the stirring direction could be easily reversed. The bottom shell of the furnace must be made from austenitic stainless steel plate, which is a non-magnetic material. The EMS system is based on a low-frequency current, which passes through a special winding system to generate a magnetic field. The field penetrates from the bottom and generates forces acting on the molten steel, eventually leading to its motion. Due to the limited volume of the furnace, the flow of the molten steel reaches the furnace walls, reflects, and comes back along the side walls. At the same time, the flow distribution affects the generated magnetic field, and this change should be considered in the mathematical considerations of the model description. In general, the electromagnetic stirrer covers the whole bottom diameter of the furnace, meaning that the electromagnetic stirring occurs in the whole bath. Moreover, the forces generated by EMS act in both horizontal and vertical directions, ensuring excellent stirring efficiency.

The EMS system can be easily designed and applied for all of the stages of the molten steel route up to continuous casting processes. Since 1947, several thousands of EMS solutions have been installed in various applications, like EAF, ladle furnace (LF), and continuous casting. Moreover, the system was applied to steel and aluminum melting and remelting[95].

From an early stage of that technology, the researchers reported a lot of benefits like better deoxidation and higher rates of desulphurization[18,81]. The EMS seems to increase the stirring

velocity 10 times in comparison to natural convection[96] and increases the heat transfer from the arc to the molten steel, which decreases the time of melting[97]. Moreover, the sulfur content can be reduced from 200 to 160 ppm by using the EMS stirring. Temperature homogenization achieved through EMS has been reported to decrease the temperature difference from over 102 to 26 [°C], which is an impressive achievement. As a result, the thermal stratification was reduced[60,98]. As an additional advantage, the EMS system is a much safer solution because the stirrer is not exposed to the melt temperature, and its maintenance is much easier than that of BGS. Such a solution is safe and not expensive[99].

The benefits of EMS in the case of EAF include[81]:

- stabilization of the arc and increase in efficiency of the heat and mass exchange inside the EAF,
- speedup of the scrap melting processes,
- homogenization of temperature and velocity in the melt bath, which prevents slag superheating during the arc generation,
- increased decarburization rate,
- reduced tapping temperature with reduced oxygen in tapping processes, which lead to a reduction in the consumption of ferroalloys,
- increased effectiveness and productivity of the operation,
- increased safety of the operation.

The EMS technology was also applied to the ladle furnace, with the first industrial installation by SKF and ASEA companies in the 1960s. The technology enabled the resolution of the issue with bearing steel quality after the EAF process. The proposed technology ASEA-SKF focused on EMS combined with argon gas, vacuum treatment, and heating by electric arc, which started a new trend in the production of high-quality steels. Between the '60s and '80s, around 70 furnaces with EMS systems were installed worldwide. The ASEA-SKF technology was later replaced by more modern solutions, but the EMS stirring technology is still a very important process for enhancing the quality of steel[94]. Nowadays, around 140 devices are installed in LF systems around the world.

The EMS solutions have also found their application in continuous casting processes in the 1970s. The technology improved the solid structure and the surface quality. The first industrial installation was in the 1980s, when the electromagnetic field was used to improve the quality of the slab. This technology was based on the DC current, which enabled the reduction of the flow speed and decreased the oscillation of the melt flow inside the slab[95]. This technology, called electromagnetic breaking (EMBR), is still successfully used in casting the thin slab to stabilize the meniscus oscillations, reduce the additional powder utilization, and increase the quality of the steel.

In the early 2000s, ABB proposed a new type of high-efficiency stirrer[95]. The solution was patented as ArcSave® solution and was used for EAF applications. The proposed technology

reduces energy consumption while maintaining an excellent mixing efficiency. The developments and improvements in this technology are constantly increasing to address the challenges of the modern steelmaking industry.

2.3 Improvements in EMS-based manufacturing chain

Nowadays, the major challenge ahead of the stirring processes is to increase production efficiency while maintaining the high quality of the steel. As a provider of stirring technologies, the ABB company focuses on the continuous improvement of EMS devices. The available reports from these investigations[100–103] are focused on the 90-ton AC EAF equipped with the EMS. They denote a lot of advantages of the developed solutions, like great temperature homogeneity, with a temperature difference of less than 5[°C], better power output from the electrodes, or a higher rate of melting due to the better heat exchange and prevention of the superheating. Moreover, it was proven that the EMS stirring increases the lifetime of the electrode system and reduces the power consumption of the process. The process of decarburization was also intensified while decreasing the oxygen content. Improvements in the area of stainless steel production were also reported[18,77–82,104]. The additional investigations based on the Consteel EAF included the different stirring directions and its effectiveness. Lab-scale water modelling was often used to support investigations in this area[105].

It was pointed out in [106] that the water modelling helps to understand the EMS stirring concept, which can also be easily compared to the BGS method. The important criterion is proper similarity between the models. If the similarity of stirring energy or velocity is considered, the water pumps can generate the proper flow corresponding to the EMS stirring conditions. Based on that, investigations regarding the efficiency of the mixing, such as measurements of the mixing time, can be realized[107]. Under industrial conditions, the mixing time can be measured by the use of a Cu tracer to assess the stirring efficiency[108].

The improvements in EMS stirring technology focus not only on the EAF but also on the other stages of steel production. The technology is under continuous development to obtain the best control and improvement of the processes. One of the examples of new solutions is complete control of the slab casting thanks to the FC Mold approach proposed by ABB[95]. The main goal of that system is to stabilize the fluctuations of the meniscus and control the velocity distribution. The system features multiple DC fields positioned in the upper and lower parts of the slab to enhance casting speed while maintaining the high quality of the surface. Nowadays, the third generation of this approach is available, combining the AC and DC fields[95]. The mentioned solution is the most advanced commercially available system for controlling slab casting. The ABB continues the investigations and develops additional solutions like OptiMold Monitor to control the temperature of the steel inside the mold during the casting process[95]. Combining that technology with FC Mold ensures full control of the process in real-time, which is a game changer in the metal industry for steel quality control.

The improvements of available technologies also focus on the LF and tundish applications. The current activities on that topic are directly related to the research undertaken within this thesis.

Finally, it should also be noted that due to the large industrial-scale character of such research, direct experimental investigations and measurements are very limited. That is why advanced numerical modelling techniques are crucial to support this type of investigation.

3. Numerical simulation methods in the metallurgy industry

3.1 General numerical approaches

Numerical simulations play a crucial role in the metallurgical industry, as they enable the modelling of subsequent processes and respective phenomena with limited reliance on laboratory or industrial experiments. Therefore, they reduce the time and costs of research and development of new technologies. Nowadays, numerical approaches are undergoing rapid development due to the increased capabilities of computational power and the availability of commercial software. At the same time, the increase in these capabilities leads to the development of design methods and process optimization techniques. As a result, numerical simulations are often used in the early stages of the technology design as a standard tool to understand the processes and phenomena in different fields of engineering, also in metallurgy[109].

Numerical approaches can be successfully used in the steel-making industry to, e.g., develop the furnace geometry or design the flow control devices for particular industrial applications[32,50,96,110]. Moreover, the numerical simulations enable to observe and understand phenomena, which are difficult to measure during the experimental tests, like molten steel flow distribution[52,54,110–112], behavior of the non-metallic inclusions[32,53,113,114] and sedimentation or solidification[115–119]. Dedicated solutions enable the inclusion of the nucleation and growth or motion of the crystals in solidification processes based on the volume-average and multiphase simulations[120].

The stirring processes described in Chapter 2.2 are essential in the metallurgical industry, and their development often requires numerical simulations due to the difficulties associated with observing and measuring of melt motion[121]. However, the selection of the numerical simulation model depends on the concept of the investigated stirring method. For example, the EMS stirring requires the magnetohydrodynamic (MHD) approach[122]. Moreover, the multiphase approach to the simulation is often required to cover the electro-slag remelting or copper refining electrolysis[122,123]. It is also worth pointing out that thanks to computer-aided engineering and advanced numerical simulation techniques, designing solutions for particular industrial applications focused on increasing of the purity and quality of steel while reducing carbon dioxide emissions and maintaining the efficiency of the metallurgical processes is possible[122]. However, reaching the current state of development has required years of fundamental research conducted by scientists from various disciplines.

The significant development of the numerical methods was initiated by Newton and Leibnitz. Then, in the 18th and 19th centuries, many mathematicians focused on developing numerical approaches to simplify and speed up the calculation procedures in different fields of science. The most important mathematicians, from the point of view of this thesis, Euler (1707 – 1783) and Lagrange (1736 – 1813)[124], carried out their research in this period.

At that time, the newly available basic laws of physics, developed mainly by Newton, motivated other scientists to work on the mathematical description of various phenomena both

in solid and fluid mechanics. Most of the developed models are still used to design new engineering solutions. With time, mathematical models in additional fields of physics, such as electricity, magnetism or heat transfer, were developed and implemented in numerical methods that are currently used in everyday engineering work[125].

It is challenging to establish a unified set of criteria for categorizing numerical methods. The most basic division classifies problems as linear or nonlinear ones[126]. The linear problems are focused on the solution of the linear equations presented by the matrix-vector notation. These kinds of problems can be solved by direct or iterative methods. Theoretically, the direct methods can lead to obtain the exact solution, but practically, the solution is presented with an error related to the rounding of the values during computation. Iterative methods are based on the approximation with increasing accuracy in each iteration[127,128]. The nonlinear problems, due to the complexity of the solution, are often replaced by the sequence of the linear solutions. Of course, for such problems, the solution is based on the approximation with linear functions. This issue is typical for optimization problems and is related to topics where the prediction of the solution is difficult, like business applications[129,130].

In natural science and engineering applications, the most popular methods are based on the solution of differential or integral equations. These methods include well-known finite element or finite difference methods[131–134]. However, this class of approaches enables the obtaining of only approximate solutions.

As pointed out, numerical algorithms are widely used in different fields of physics and civil engineering. In the case of the metallurgical industry, numerical research plays a continuously increasing role in replicating real tests or measurements. Numerical models can support the prediction of the behavior of different devices under operational conditions or the analysis of the impact of particular new solutions on the entire manufacturing chain. However, numerical algorithms must be properly selected to fulfil all the requirements of a particular application and lead to the correct solution.

At the early stages of the steel production chain, the observation and control of the molten steel behavior are essential from the process point of view. In that case, the numerical techniques, based on fluid mechanics, seem to be adequate. Moreover, additional phenomena, including heat transfer analysis, multiphase flows, electromagnetism or chemical reactions, should also be captured by the selected numerical technique.

All of the mentioned aspects suggest that Computational Fluid Dynamics (CFD) should fulfil all requirements and should be able to cover all the topics related to the steelmaking industry[32,50,52–54,61,62,96,111–113].

In general, CFD is one of the available methods that can accurately capture complex physics behind phenomena controlling the behavior of fluids. As the name suggests, the approach primarily enables the simulation of fluid flow and other phenomena related to the liquid phase. Moreover, the CFD method's capabilities involve conjugate heat transfer modelling, multiphase flow modelling, combustion simulations, and all other phenomena related to fluid interactions.

With the development of the numerical simulations and continuous increase in complexity of the computed models and phenomena, the intensive development of the CFD numerical algorithms was also realized to enable fast, parallel computing of a large number of linear equations. With time, many new solutions and methods were introduced and tested. A majority of them are based on parallel programming and computing systems, which also require high computational power, like supercomputers and clusters, to ensure high efficiency of the computations and the possibility to accurately solve complex phenomena[135].

3.2 Computational Fluid Dynamic (CFD)

The CFD tackles the solution of discretized governing equations, like the Navier-Stokes equations, specified for mass, momentum and energy conservation as follows[136]:
continuity equation:

$$\frac{\partial \rho}{\partial t} + \rho \frac{\partial U_i}{\partial x_i} = 0, \frac{\mathrm{D}\rho}{\mathrm{Dt}} + \rho \frac{\partial \mathrm{U_i}}{\partial \mathrm{x_i}} = 0 \tag{1}$$

momentum equation:

$$\underbrace{\rho \frac{\partial U_j}{\partial t}}_{\text{Local change with time}} + \underbrace{\rho U_i \frac{\partial U_j}{\partial x_i}}_{\text{Momentum convection}} = \underbrace{-\frac{\partial P}{\partial x_j}}_{\text{Surface force}} \underbrace{-\frac{\partial \tau_{ij}}{\partial x_i}}_{\text{Diffusion}} + \underbrace{\rho g_j}_{\text{Mass force}}, \tag{2}$$

where:

$$\tau_{ij} = -\mu \left(\frac{\partial U_j}{\partial x_i} + \frac{\partial U_i}{\partial x_j} \right) + \frac{2}{3} \delta_{ij} \mu \frac{\partial U_k}{\partial x_k},$$

energy equation:

$$\underbrace{\rho c_\mu \frac{\partial T}{\partial t}}_{\text{Local energy change with time}} + \underbrace{\rho c_\mu U_i \frac{\partial T}{\partial x_i}}_{\text{Convective term}} = \underbrace{-P \frac{\partial U_i}{\partial x_i}}_{\text{Pressure work}} + \underbrace{\lambda \frac{\partial^2 T}{\partial x_i^2}}_{\text{Heat flux (diffusion)}} \underbrace{-\tau_{ij} \frac{\partial U_j}{\partial x_i}}_{\text{Irreversible transfer of mechanical energy into heat}}, \tag{3}$$

where: U – velocity [m/s], ρ – density [kg/m^3], P – pressure [Pa], τ – shear stress [Pa], g – force per unit mass [m/s^2], μ – molecular viscosity [kg/(m s)], c – specific heat [J/(kg K)], T – temperature [K], λ – thermal conductivity [W/(m K)].

In the 18th century, two mentioned earlier mathematicians presented different approaches to the observation of fluid behavior:

a) Euler proposed that the observation of the fluid behavior should be from a stationary point, located away from fluid in motion,
b) Lagrange proposed that the fluid flow observations should be executed from the perspective of this movable fluid as a point which travels together with the fluid.

Nowadays, CFD techniques can be distinguished by the Eulerian and Lagrangian methods, which are dependent on the location of the observation point. To conclude, the Eulerian

approach requires the stationary computational mesh, which enables observation of the behavior of the fluid flow from a distance. On the other hand, the Lagrangian approach does not require a mesh but is based on the freely movable particles, which are able to travel with the fluid motion, and the observations of fluid flow are made from this particle perspective. As a result, the CFD methods can be divided into mesh-based and meshless techniques, as illustrated in Figure 9.

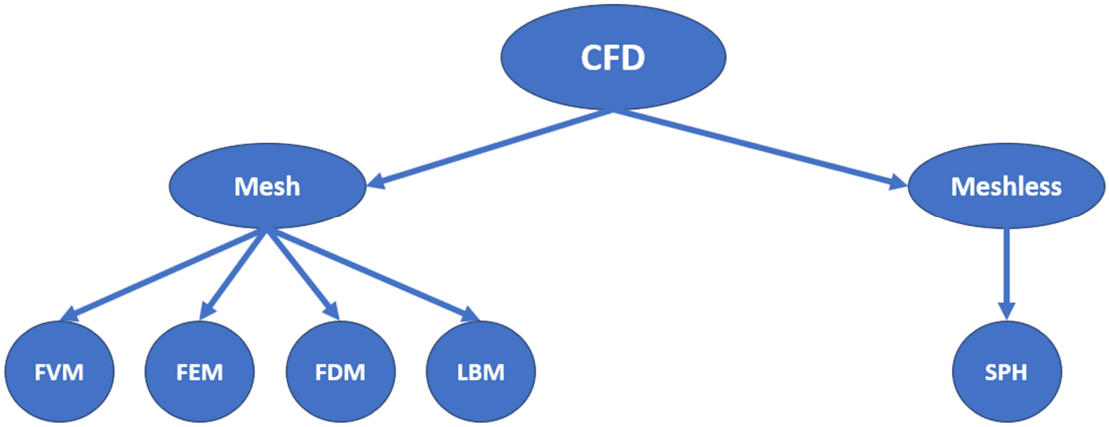


Figure 9. The general division of the CFD methods.

It should be highlighted that Figure 9 presents only some examples of the most commonly used methods in this area. The typical approaches for discretization purposes include finite volume, finite element, finite difference, lattice-Boltzmann, or smoothed particle hydrodynamic methods.

Historically, the oldest and most famous numerical algorithm used in the case of fluid mechanics is the finite difference method (FDM) based on the Eulerian method, where the derivative of the function is approximated by the finite differences[137–139]. To execute this method, the computational domain has to be discretized by computational nodes. Unfortunately, the method is adequate for quite simple cases, like one-dimensional problems[139]. The main disadvantage of this method is its limited capability to capture phenomena related to both solid and fluid physics. Moreover, it is challenging to prepare the computational mesh for complex three-dimensional geometries due to limitations related to the uniform grid size field. In such problems, the method is unstable, and the solution is not accurate because of the difficulties with proper assignment and description of the boundary conditions. All of the mentioned aspects caused that the FDM is now rarely used in engineering applications[135].

On the other hand, the finite volume method (FVM) is a common approach for modelling fluid behavior in practical engineering applications[140–142]. The method is based on an Eulerian approach to model the fluid flow inside the computational domain, which is discretized by the finite volume or control volume elements. The mentioned fact suggests that the FVM is a typical

mesh-based approach, where the balance equations must be fulfilled to obtain the convergence of the solution. The typical example involving both volumetric and surface balancing equations is the combustion process, where the heat generated during the process must be continuously calculated during simulation. The set of the balance equations includes the mass, momentum and energy balance[142]. The FVM utilizes the cell-centered structured or unstructured computational mesh, where the application of the boundary conditions and their interpretation is quite easy. Moreover, the FVM method enables solving the turbulences at different levels of complexity, from very simplified, averaged models based on mathematical assumptions to the direct solving of the Navier-Stokes governing equations, which enable accurate capturing of the turbulent regime of the flow. The additional advantage of the FVM is that it can be applied to both single-phase and multiphase modelling. For the homogeneous approach, the additional phases are considered by a supplementary set of balance equations to track the mass and the volume fraction of each particular phase[143]. A good example of this concept is the Euler-based volume of fluid (VOF) method, which enables to model the non-mixing phases with tracking of a free surface between them[144,145]. On the other hand, the continuous phase (Euler method) is often coupled with the additional, discrete phase (Lagrangian method) as for the discrete phase model (DPM). In the case of the Lagrangian approach, each component of the considered mixture has assigned a set of balance equations that can model the non-homogeneous cases[146]. As mentioned, the FVM is successfully used in engineering problems, but the disadvantage of this method is the high computational power required to solve complex problems[135].

The finite element method (FEM) is another approach for solving fluid problems[147–149]. The FEM approach requires the discretization of the computational domain by the finite elements, where the piecewise polynomial functions are used to approximate the solution. In the case of fluid mechanics, the weak formulation of the FEM requires the additional Galerkin method of stabilization[150–154]. The main advantages of the method are the popularity of the solution and its generality, but the accurate solution requires a higher order of the discretization scheme or high density of the computational mesh, which significantly increases the computation time. Moreover, due to the specific applications of the usage, the FEM is rather often used in the case of solid mechanics and in the applications for coupling solid and fluid interactions, so the popularity of pure CFD in FEM software is not popular.

An alternative to the aforementioned CFD approaches is the lattice-Boltzmann method (LBM). In that method, each dimension in the space corresponds to the different variables. From a classical mechanics perspective, this space includes the momentum or velocity, position and time[155]. The objective of the method is to determine the probability that the particular particle will be at a specific position in space, with a specific velocity and at a specific time. Moreover, the computational mesh does not accurately represent the computational domain, but rather has a rather binary character. The binary approach to discretization allows for the use of quite complex geometries without additional preparation and simplification, which leads to shorter solution times. Unfortunately, the quality of results strongly depends on the resolution

of the lattice. An increase in the number of nodes strongly increases the computational effort and complexity of computation needed to obtain a stable, converged solution[156,157]. In general, the LBM technique, although not based on the Navier-Stokes equations, enables to model similar phenomena as standard FVM, including one-phase or multiphase systems, turbulences, etc. The applicability of that method is the same as that of FVM, but the LBM enables the modelling of complex geometries without the need of any additional preprocessing operations. The method found its application in different fields of science like medicine or chemical engineering[158–160], energetics[161] or material science[162,163]. Moreover, the method can be used standalone or coupled with other methods, like the discrete element method (DEM)[160,164]. The main disadvantage of the LBM is the high computational power needed for complex geometries.

The mentioned DEM analyses the motion of solid systems in the Lagrangian reference frame[165]. The approach utilizes the standard Newtonian dynamics. The particles can be modelled as simple shape bodies and can be coupled with other methods like FVM and LBM to understand the principles of the multiphase system from the Euler-Lagrange perspective. Moreover, the particles used in that method can be deformable or non-deformable, which influences the types of contacts between the particles and then forces and moments between them. The computational domain is defined based on the location of the particles and does not have a given dimension; however, an additional limitation corresponding to the maximum coordinates of the domain can be defined to reduce the computational space. The DEM method is often used to understand the behavior of the granular material during, e.g., filling or emptying of different tanks etc. What is important is that the method lies between classical solid mechanics and typical granular mechanics and enables simulations of cracks development in the solid structures, delamination or other phenomena with the formation or disruption of the materials' internal cohesion. Due to that, the method is not a typical CFD approach but can be easily coupled with the standard CFD method to be able to observe the interactions between the fluid and solid structures[166–169] or to create the model of porous media[170]. DEM can be used standalone, but only to model the materials with semi-liquid consistency[171–173].

The second major class of methods from Figure 9 are meshless solutions. The most well-known method in this case is the smoothed particle hydrodynamics (SPH). SPH is based on the Lagrangian method and is used to understand the behavior of solids and fluids with the assumption that the set of particles corresponds to the continuity of the domain[174–176]. Each particle can be treated as an individual body with its own properties like density, mass, velocity, etc. The SPH technique utilizes the governing equations of fluid dynamics and enables the discretization of the mass balance equation. The characteristic feature of the SPH method is a special definition of the boundary conditions as additional artificial forces, ghost particles outside the walls with opposite velocity direction or additional fluid particles with motion set to zero. The SPH technique is often used to model the materials under large deformation conditions[177–179], but, the standard fluid mechanics can also be solved by this method.

The general procedure of conducting the numerical simulations with all the above-presented methods is very similar and includes the following steps:

1. *Preparation of the geometry of the investigated problem domain for calculations (preprocessing).*

The geometry of the investigated problem domain is typically developed using CAD software, which enables the accurate representation of investigated shapes in a 3D model. Such a model can be additionally divided into regions of interest, where the specified variables can be observed during the calculation procedure. Very often, the CAD model must be simplified to be able to discretize the model with high quality.

2. *Preparation of the discretization of the model (preprocessing).*

The discretization of the model must fulfil the main quality requirements to ensure good convergence and high quality of the obtained results. In case of turbulent flows, the mesh must contain the additional inflation layer, which includes the additional layers of the mesh close to the walls to provide proper distribution of the velocity profile[136,180]. To avoid an excessive number of mesh elements, the inflation layer cannot be modelled directly, but the wall functions are applied. In this case, the thickness of the first inflation layer is described by the y+ parameter. Its value is important during the solution process because of the correctness of the assumptions of the equation describing the velocity profile near the walls in laminar, buffer and turbulent sublayer, which are located close to the walls[136]. In the CFD model development, a thorough mesh sensitivity study should be performed to avoid the unphysical influence of the discretization scheme, discretization method and mesh element size on the simulation results.

3. *Setup of the solution*

The CFD concept enables solving the governing equations in both steady-state and transient modes. The proper settings include the selection of the physical problem, the definition of the material properties, describing and assigning the additional source terms to the cell zones of the models (if required) and the definition of the boundary conditions, which directly influence the simulation results. The settings of the solver are also important to ensure that the numerical technique is properly selected. It is worth mentioning that proper replication of different phenomena requires different solver settings, and the selection must be carried out with the utmost care.

4. *Solution*

The solution of the governing equations is based on an iterative process to obtain the convergence of the results. During the calculation process, the values of residuals should be tracked to ensure that the convergence of the solution was obtained. Moreover, the mass and energy balance (it depends on the simulation case and physics behind the particular phenomenon) must be fulfilled to ensure the correctness of the numerical solution.

5. *Postprocessing of the results*

Postprocessing includes the preparation of visualization and analysis of the obtained data to assess the correctness of the results.

The same steps must be performed when the metallurgical phenomena are under investigation. However, it should also be mentioned that most of the numerical simulations in the metallurgical industry require the use of a multiphase approach. The multiphase flows can be involved in the case of the free surface behavior tracking and identifying its influence on the velocity flow distribution[144,145]. Moreover, the slag behavior can be investigated thanks to the concept of an additional phase[144,145]. With the consideration of the additional phases, the stirring effects, such as those observed in bottom gas stirring, can also be modeled[13,145]. Moreover, the multiphase modelling enables the non-metallic inclusion investigation[113] reflecting the sedimentation processes[181,182]. Finally, the additional phase can be treated as a tracer to observe the fluid flow in the computational domain[31]. This flow visualization method enables an understanding of the mixing phenomena and its effectiveness, which is crucial in metallurgy[144] and green steel technologies[13,183].

3.3 Multiphase approach

As pointed out, multiphase CFD simulations are often used in metallurgical industry investigations[31]. Most of the research in this area is based on the FVM, which is the most commonly used approach for fluid flow modelling in metallurgical applications and is available in commercial software. As it was mentioned, the FVM is an Eulerian approach with a mesh composed of finite volume elements. In the case of multiphase flows, the particular methods are also distinguished into the Euler and Lagrangian approaches[31,184,185]. The description of the different methods for multiphase modelling is limited to the techniques used within this work.

3.3.1 Volume of Fluid (VOF)

The volume of fluid model is the Euler-Euler approach used to model the interface between different fluids in the form of the free surface between them. In this approach, the phases are immiscible and continuous. The model solves the momentum equations as a single set, and each fluid phase is tracked by the additional parameter known as the volume fraction (α) of each phase. The volume of fluid approach is used to calculate the motion of bubbles or droplets in the liquid, with the availability of tracking interactions between phases. The main assumption is that the bubbles/droplets should be relatively large. The model enables the prediction of the breakup phenomena and is applicable for both steady-state and transient simulations of the interface tracking[31,136,184].

Interface tracking is realized by the modifications of the continuity equation to include the volume fraction of each phase. If the qth phase is assumed, the continuity equation is as follows:

$$\frac{1}{\rho_q}\left[\frac{\partial}{\partial t}\left(\alpha_q \rho_q\right) + \nabla \cdot \left(\alpha_q \rho_q \overrightarrow{v_q}\right) = S_{\alpha_q} + \sum_{p=1}^{n}\left(\dot{m}_{pq} - \dot{m}_{qp}\right)\right], \tag{4}$$

where: $\dot{m}_{qp}$ – mass transfer from phase q to phase p, $\dot{m}_{pq}$ – mass transfer from phase p to phase q, S_{α_q} – user-defined mass source term for each phase (default value is zero).

The volume fraction parameter is not solved for the primary phase, but it is assumed as a constraint:

$$\sum_{q=1}^{n} \alpha_q = 1. \tag{5}$$

The model incorporates various methods for interpolating the interface between two phases. The general approach requires that the diffusion and convection flux via the faces of the control volume must be in balance with the source term presented in that control volume[136,186–188]. The exemplary interpolation methods used in the commercial software Ansys Fluent are presented in Figure 10.

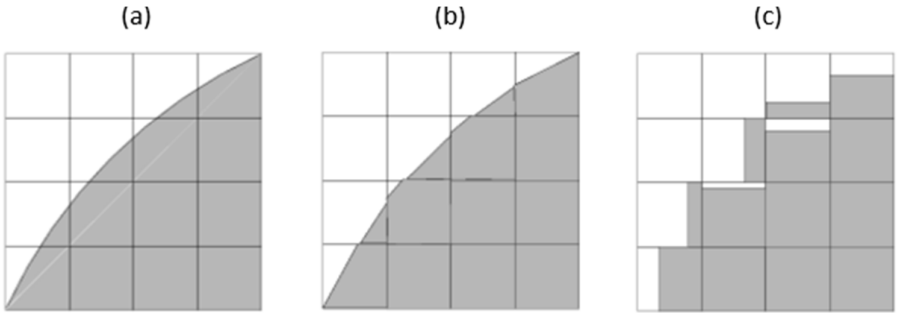


Figure 10. Methods of interpolation of the interface between the two phases: (a) the actual interface shape, (b) the geometric reconstruction method and (c) the donor-acceptor method[136].

In general, the VOF model is often used in the metallurgy industry to replicate the interaction between different phases[144,185]. The exemplary results obtained from other authors[144], like open-eye area prediction and free surface behavior are presented in Figure 11 and Figure 12, respectively.

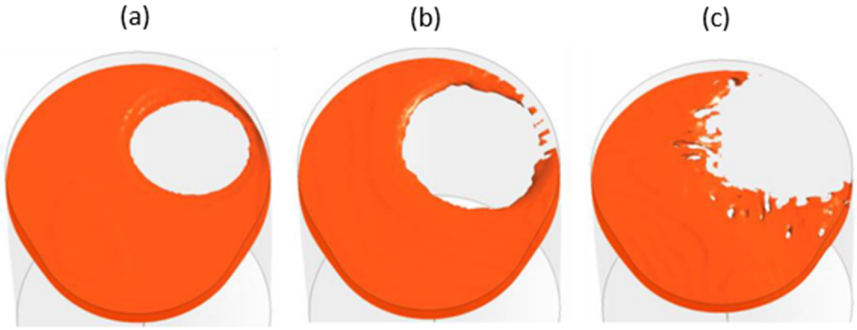


Figure 11. Exemplary open-eye area from VOF simulation (a) Q = 100 [NL/min], (b) Q = 300 [NL/min] and (c) Q = 500 [NL/min][144], where: Q – argon flow rate in normal conditions [Nl/min].

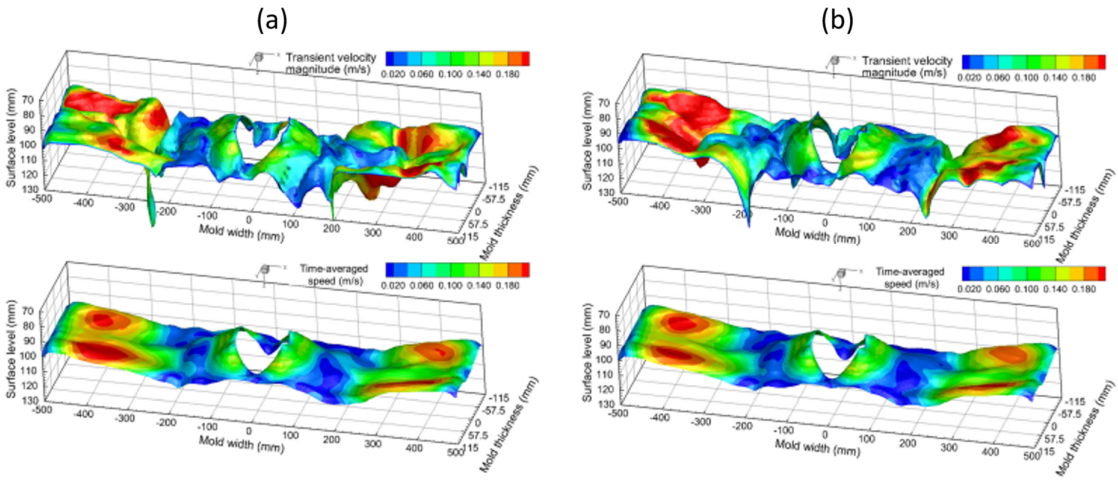


Figure 12. Transient and time-averaged shape of the meniscus: (a) t = 38 [s], (b) t = 40 [s][185].

3.3.2 Discrete Phase Model (DPM)

The discrete phase model (DPM) is a Lagrangian framework for the discrete modelling of the phase in the general Eulerian-Lagrangian approach, enabling coupling between the continuous and discrete phases. It also captures the interaction of the discrete phase with the continuous phase from the Eulerian approach. The fluid in the Eulerian approach is treated as a continuous phase based on the solution of the Navier-Stokes equations, where the discrete phase from the Lagrangian approach is dispersed. The DPM model is executed by tracking dispersed particles, which can be understood as droplets or bubbles in the flow field. The mass, momentum and energy can be exchanged between the continuous and discrete phases[31,136,184].

The interactions between particles can be neglected to simplify the approach, but the second phase volume fraction should be relatively low. The second phase can be quite heavy in comparison with the fluid phase. The particles are calculated separately for every single particle, which is tracked throughout the solution.

The trajectory of the particles is predicted by the calculation of its force balance in the Lagrangian frame of reference. The assumption includes that the inertia of each particle is equal to the force which is acting on that particle and is described by the following equation:

$$m_p \frac{\overrightarrow{du_p}}{dt} = m_p \frac{\vec{u} - \overrightarrow{u_p}}{\tau_r} + m_p \frac{\vec{g}(\rho_p - \rho)}{\rho_p} + \vec{F}, \tag{6}$$

where: m_p – mass of the particle, $\vec{u}$ – velocity of the continuous phase, $\overrightarrow{u_p}$ – velocity of the particle, ρ – density of the continuous phase, ρ_p – density of the particle, $\vec{F}$ – the additional force, $m_p \frac{\vec{u}-\overrightarrow{u_p}}{\tau_r}$ – the drag force, τ_r – relaxation time of particle/droplet[136]. The relaxation time is presented as follows:

$$\tau_r = \frac{\rho_p d_p^2}{18\mu} \frac{24}{C_d Re}, \tag{7}$$

where: μ – molecular viscosity of the continuous phase, d_p – diameter of the particle, Re – relative Reynolds number:

$$Re \equiv \frac{\rho d_p \left|\overrightarrow{u_p} - \vec{u}\right|}{\mu}. \tag{8}$$

The rotation of the particles is part of their motion and influences the particle's trajectory in the continuous phase during its motion. The impact of this dependence is related to the moment of inertia. The calculation of the rotation of every single particle is included by an ordinary differential equation (ODE), which is solved for the angular momentum of the particle:

$$I_p \frac{d\overrightarrow{\omega_p}}{dt} = \frac{\rho_f}{2}\left(\frac{d_p}{2}\right)^5 C_\omega \left|\overrightarrow{\Omega}\right| \cdot \vec{\Omega} = \vec{T}, \tag{9}$$

where: I_p – moment of inertia, $\overrightarrow{\omega_p}$ – angular velocity of a particle, ρ_f – density of fluid, d_p – diameter of the particle, C_ω – rotational drag coefficient, $\vec{T}$ – torque, which is applied to the continuous, fluid domain, $\vec{\Omega}$ – relative angular velocity between the particle and fluid:

$$\vec{\Omega} = \frac{1}{2}\nabla \times \overrightarrow{u_f} - \overrightarrow{\omega_p}. \tag{10}$$

In the case of the particle with a sphere shape, the inertia momentum is calculated by the equation:

$$I_p = \frac{\pi}{60}\rho_p d_p^5. \tag{11}$$

The DPM model has been successfully applied to the simulation of liquid fuel combustion[189], spray dryers[190], etc. However, in cases with high volume fractions, such as mixtures of different liquids, where the second phase cannot be neglected, the model does not provide accurate results[136].

In general, the DPM is often used to track the fluid flow in different vessels. In this case, it is assumed that the particles are without mass and are treated only as tracers[191,192]. In the metallurgical applications, the DPM particles are used to model the argon gas injected into the molten steel via porous plugs in the case of the electric arc furnace and ladle furnace with gas stirring (Figure 13 and Figure 14)[13,145] or sometimes to model the non-metallic inclusions behavior[193].

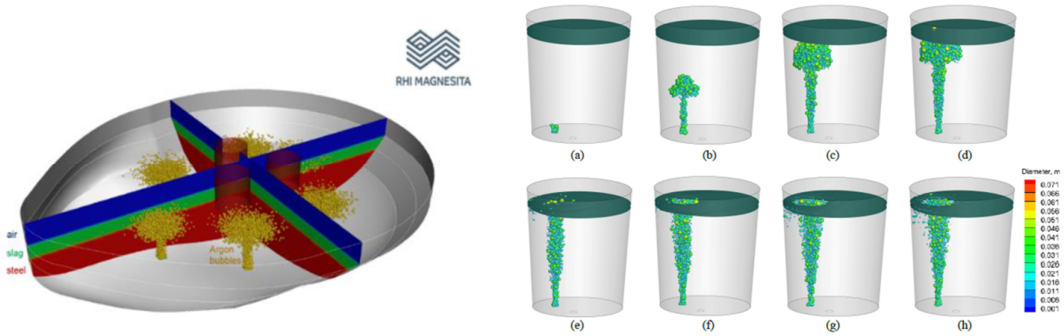


Figure 13. Coupling between the Eulerian and Lagrangian in DPM approach for EAF (left) and LF (right) for (a) 0.5[s], (b) 2.5[s], (c) 5[s], (d) 5.5[s], (e) 6[s], (f) 9[s], (g) 35[s], (h) 45[s] of the process, while gas stirring is realised[13,145].

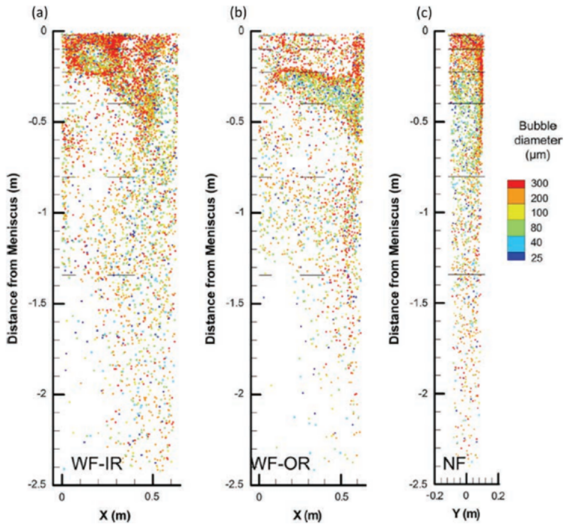


Figure 14. Bubbles captured in the solidified shell in the DPM simulation for (a) inner radius, (b) outer radius and (c) narrow face[31].

The particle modelling in the multiphase approach is also used to track non-metallic inclusions[35,113,193–207]. However, for these kinds of simulations, the population balance model (PBM) appears to be a more suitable solution.

3.3.3 Population Balance Model (PBM)

The population balance model (PBM) is a special approach to multiphase modelling used mainly in industrial applications which require the size distribution of a secondary phase[208–210]. This distribution can be related to transport or chemical reactions in the case of the multiphase flow. The method enables the modelling of nucleation, dispersion, growth, aggregation, dissolution or breakage of the particles. The balance equation must be considered for momentum, energy and mass to calculate size distribution in this approach. The model is often

used in the literature for simulation of the crystallization[211], reactions between the gas and liquid phase[212], sprays[213–215], bubble columns[216,217], etc.

The PBM is based on the population balance equation (PBE), where the equation of the transport calculated for number density function *n* is as follows:

$$\frac{\partial}{\partial t}[n(V,t)] + \nabla \cdot [\vec{u}n(V,t)] + \underbrace{\nabla_V \cdot [G_v n(V,t)]}_{\text{Growth term}} = \frac{1}{2}\int_0^V a(V-V',V')n(V-V',t)\,n(V',t)dV' - \underbrace{\int_0^\infty a(V,V')n(V,t)n(V',t)dV'}_{\text{Death due to aggregation}} + \underbrace{\int_{\Omega_V} pg(V')\beta(V|V')n(V',t)dV'}_{\text{Birth due to breakage}} - \underbrace{g(V)n(V,t)}_{\text{Death due to breakage}}, \quad \text{Birth due to aggregation} \tag{12}$$

where the boundary conditions are described as:

$$n(V,t=0) = n_V; n(V=0,t)G_V = \dot{n_0}, \tag{13}$$

where: $\dot{n_0}$– nucleation rate in particles.

The presented literature review enabled the selection of the set of techniques, which will be used in the further sections of the dissertation.

However, more importantly, the literature review, in general, enabled the formulation of the research hypothesis and the definition of specific objectives that will be addressed during the work.

4. Aim of the work

As presented, the required fast transformation of the steel industry from high carbon dioxide emission to low carbon footprint production requires the development of new manufacturing technologies and modern computational methods to effectively and accurately predict the processes and phenomena inside the molten steel[13,183].

The literature review clearly highlighted the capabilities and limitations of current steelmaking technologies, as well as the available computational tools for computer-aided technology design. The primary identified technological challenge is attributed to the efficiency of the steel stirring process, which directly affects the final product quality. Therefore, the following hypothesis of the dissertation was formulated:

The development of a multi-physics computational fluid dynamics model, which captures all major phenomena controlling the electromagnetic-supported steelmaking operations, is possible and allows a reliable computer-aided technology design of different types of metallurgical vessels.

To confirm the formulated hypothesis, a set of objectives was specified as follows:

- development of a multi-physics computational fluid dynamics model that captures critical phenomena and processes, including electromagnetic stirring, gas stirring, heat transfer, inclusion removal, etc. Within this objective, several tasks will be realized:
    - formulation of the approach to interpolation of the electromagnetic forces into the CFD model,
    - development of the CFD model of three metallurgical vessels (EAF, LF and tundish) to cover main phenomena and processes stages,
    - validation of the numerical CFD model with experimental measurements,
    - development and validation of a new method to evaluate the effectiveness of the stirring.
- investigation of the flow characteristics in EAF, LF and tundish using CFD under the influence of electromagnetic stirring and gas stirring for selected vessels to provide insights and guidelines for the further development and application of this technology,
- development of new electromagnetic stirring methods for EAF, LF and tundish to improve the metallurgical performance, such as stirring efficiency, mixing time and steel cleanliness.

As presented, the last goal is devoted to the development of new electromagnetic stirring devices that could be used directly by the industry in mass steelmaking production.

The work is organized into five main chapters presenting fundamental and applied research on the topic, followed by the conclusion chapter. First, in Chapter 5, the model of electromagnetic stirring, its coupling scheme, and its assumptions are presented. This chapter

also focuses on the confirmation of the correctness of the developed CFD approach based on the validation and comparison between the simulation and real test measurements for a case study model with mercury. Since the research focuses on stirring technologies and improving the cleaning of steel, a numerical approach to simulate non-metallic inclusions is also presented in this chapter. Finally, a new indicator to evaluate the stirring energy is formulated. These developed and validated computational tools for EMS stirring are further used to study the melt behavior in the EAF, LF and tundish in Chapters 6, 7 and 8, respectively. These chapters present a description of the steps required to adapt the developed CFD model to simulate a particular vessel. A developed set of numerical models was also validated against industrial measurements or water model test results to confirm their accuracy. Eventually, a series of case studies examining different stirring methods and process parameters was conducted. As a result, in each case, the new EMS stirrer setup was designed for industrial use. Finally, in Chapter 9, all the investigations are summarized with particular emphasis on stirring energy measurements in various vessels under different stirring parameters. The obtained results are also compared with available literature data, thereby extending the understanding of the capabilities and limitations of the proposed technological solutions. Chapter 10 is finally devoted to the conclusions and discussion on possible further directions of this research.

5. Development of the advanced CFD model for EMS stirring

As mentioned, the main concept of the investigated steel-making technology assumes that mixing inside the melt is realized by the electromagnetic stirrer, which generates the electromagnetic Lorentz forces acting on the motion of the liquid steel inside the vessel. From a numerical point of view, the full coupling between the electromagnetic and CFD parts represents the best-case scenario; however, due to the high computational effort, it is very time-consuming and ultimately unacceptable to the industry. At the same time, the motion of the melt influences the distribution of the electromagnetic field, by up to 30%, and therefore, to accelerate the simulation process, its direct consideration can be neglected and replaced by the compensation of the force by the theoretical assumptions[218,219]. The presented approach is focused on the time-average solution, which should not affect the final result from a macro scale perspective, so is considered satisfactory for industrial applications. As a result, a one-way coupling solution with a compensation term was developed in the current research.

5.1 Development of the simulation workflow

The first step of the model development was focused on capturing electromagnetic forces generated by the EMS. In this case, the main core is based on the Lorentz force calculations:

$$F = \sigma(\boldsymbol{E} + \boldsymbol{U} \times \boldsymbol{B}) \times \boldsymbol{B}, \tag{14}$$

where: σ – electrical conductivity [S/m], $\boldsymbol{E}$ – electric field [V/m], $\boldsymbol{U}$ – velocity [m/s] and $\boldsymbol{B}$ – magnetic field [T].

During the utilization of the EMS, the electromagnetic and electric fields are harmonic in time and can be expressed as:

$$\boldsymbol{E}(t) = \boldsymbol{E}_0(t) - \nabla\emptyset(t), \tag{15}$$

where: $\boldsymbol{E}_0(t)$ – harmonic electric field induced by the harmonic magnetic flux in the case of the stationary melt, $\emptyset(t)$ – electrostatic potential induced by magnetic flux density and molten steel flow.

The above-presented assumptions result in the stirring force density formula:

$$F = \sigma(\boldsymbol{E_0} - \nabla\emptyset + \boldsymbol{U} \times \boldsymbol{B}) \times \boldsymbol{B}, \tag{16}$$

which can be further decomposed to include the parts independent and dependent on velocity:

$$F = \sigma(\boldsymbol{E_0} \times \boldsymbol{B}) - \sigma\nabla\emptyset \times \boldsymbol{B} + \sigma(\boldsymbol{U} \times \boldsymbol{B}) \times \boldsymbol{B}. \tag{17}$$

The major part of the total force density does not depend on the velocity (first part of equation (17)). However, to increase the accuracy of the model, the second part of the equation (17), which depends on the velocity, should also be included. It has been proved that the influence of the motion of the melt on the magnetic field is around 30%[219] and that coupling between the electromagnetic and CFD solver should be included.

To simplify the approach and reduce the calculation time, the assumption of the time-average harmonic force is taken into account:

$$\langle\vec{f}\rangle = \langle\overrightarrow{f_0}\rangle + \langle\overrightarrow{f_{damp}}\rangle + \langle\overrightarrow{f_\varphi}\rangle, \tag{18}$$

$$\langle\overrightarrow{f_0}\rangle = \frac{1}{2} Re\{\vec{\boldsymbol{J}} \times \overrightarrow{\boldsymbol{B}_0^*}\}, \tag{19}$$

$$\langle\overrightarrow{f_{damp}}\rangle = \frac{\sigma}{2} Re\{\{\vec{v} \times \overrightarrow{\boldsymbol{B}_0}\} \times \overrightarrow{\boldsymbol{B}_0^*}\}, \tag{20}$$

$$\langle\overrightarrow{f_\varphi}\rangle = \frac{\sigma}{2} Re\{\vec{\nabla}\boldsymbol{\varphi} \times \overrightarrow{\boldsymbol{B}_0^*}\}, \tag{21}$$

where: $\langle\overrightarrow{f_0}\rangle$ – time-averaged harmonic force for melt, which is stationary, $\langle\overrightarrow{f_{damp}}\rangle$ – force damped because of the occurrence of the velocity $\vec{v}$, $\langle\overrightarrow{f_\varphi}\rangle$ – potential force, which is caused by the eddy currents and magnetic field density occurrence in the moving molten steel, $\vec{\boldsymbol{J}}$ – current density [A/m^2], $\boldsymbol{\varphi}$ – electric potential [kg m^2/(s^3 A)]. The harmonic dynamics for the electromagnetic fields are punctuated as bold entities, the complex conjugate is highlighted by the asterisk *, and the fields for stationary melt are depicted by the subscript 0.

Finally, the above assumptions lead to the simplified equation:

$$\langle\vec{f}\rangle = \langle\overrightarrow{f_0}\rangle \left(1 - \frac{\langle\overrightarrow{f_0}\rangle \cdot \vec{v}}{|\langle\overrightarrow{f_0}\rangle| v_{travelling\ wave}}\right), \tag{22}$$

where: $v_{travelling\ wave}$ – travelling speed of electromagnetic waves along the stirrer described as:

$$v_{travelling\ wave} = 2\tau f, \tag{23}$$

where: τ – pole pitch [m], f – frequency [Hz] (both are stirrer's parameters).

The presented reasoning confirms that the factor responsible for the compensation of the forces can be simplified, leading to the following formulation:

$$\langle\vec{f}\rangle = \langle\overrightarrow{f_0}\rangle \left(1 - \frac{v}{2\tau f}\right). \tag{24}$$

This term is valid along the direction of the travelling wave.

After all the simplifications, the compensated stirring force ($\overrightarrow{F_c}$) distribution, which includes the dependency on the velocity distribution in the melt, can be presented by the following equation:

$$\overrightarrow{F_c} = \vec{F} \left(1 - \frac{\vec{F} \bullet \vec{v}}{2\tau f \bullet |\vec{F}|}\right). \tag{25}$$

In the presented work, the FEM method is selected to tackle electromagnetic forces investigation as it is the most popular method used in the industry during daily operations. In this case, the preparation of the simulation model requires the structured FE mesh. The main advantage of this solution is the possibility of direct export of the results in the form of each coordinate value set of the discretized model[220]. The availability of the software and the possibility of preparing the user-defined scripts dedicated to EMS solutions led to the selection of Dassault Systems software, Opera.

The coupling is realized between two separate solvers: the electromagnetic solver from Opera, which calculates the distribution of the stirring forces for stationary melt and then the CFD solver of Ansys Fluent software. The graphical interpretation of the coupling concept between the electromagnetic and CFD simulation for tundish geometry is presented in Figure 15.

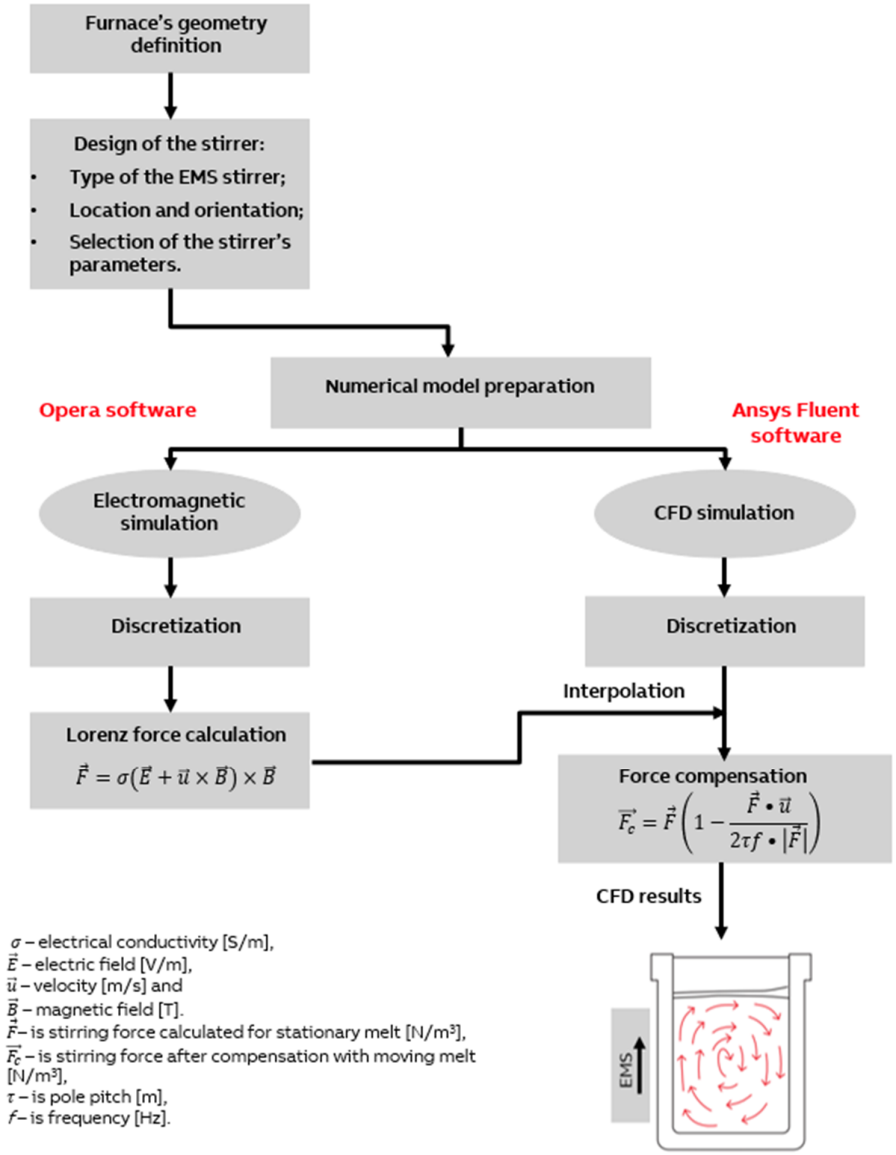


Figure 15. Graphical interpretation of the forces mapping from electromagnetic to CFD solver.

As shown in Figure 15, the concept of the model assumes that the electromagnetic and CFD simulations are run sequentially, where the electromagnetic Opera solver is used for electromagnetic simulation, while the CFD Ansys Fluent solver is executed for CFD simulation.

The electromagnetic simulation required the discretization of the computational domain of the melt, where the Lorentz force distribution is calculated. The developed approach is based on dedicated user-defined scripts, where the main data regarding the furnace, stirrer and process can be provided. The outcome of the simulation includes the distribution of the force density in each direction, which is saved to a special format file with the extension “table” and then modified to prepare the interpolation file to the Ansys Fluent software. The results obtained from electromagnetic simulation are calculated for a stationary melt, and then the additional dependence on velocity will be included in the next step, utilizing the concept of force compensation, thanks to the development of additional modifications in user-defined scripts described below.

The corresponding CFD model for melt flow simulation was also developed. The discretization of the model was prepared to include the RANS (Reynolds Averaged Navier-Stokes) approach incorporating wall functions for turbulence modelling. This simplified approach was employed to reduce computational time, which is crucial for industrial applications. The developed CFD model includes a proper definition of the boundary conditions, such as the correct selection of walls and the top surface, where the zero shear stress reflects the numerical behavior of the free surface in the case of the one-phase model or the pressure outlet in the case of the extended geometry for multiphase simulation. The solver setup includes the more advanced and accurate coupled scheme with PRESTO!/Body Force Weighted interpolation of the Pressure and Second Order Upwind interpolation of the Momentum. The remaining parameters are controlled during the calculations to achieve acceptable convergence of the results. The correctness of the defined boundary conditions and setup was confirmed through numerous numerical tests performed on simplified vessel geometries.

As mentioned above, the coupling between the Opera and Ansys Fluent is an important part of the model and is realized by the interpolation of the force distribution for stationary melt in each direction. The computational mesh is not consistent in this case, so the interpolation was based on zero-order interpolation to transfer data directly between computational meshes according to the coordinates of the data points. The approach required the preparation of the interpolation file in a format that is readable for Ansys Fluent. Moreover, the interpolation of the force distribution was not possible in a direct way. In this case, the data must be stored in a separate variable, UDS (User Defined Scalar) or UDM (User Defined Memory). In the developed approach, the UDMs were selected to assign the force distribution in each direction and then to use these values for further calculation. The dedicated UDFs (User Defined Function(s)) and Ansys DEFINE_ON_DEMAND macro were used to realize and control the process. The force distribution was then used for further calculations of the force compensation according to (25) to include the dependence on the velocity. Finally, the compensated force was used as a source term in (2) to act on the melt inside the furnace. Such a solution is updated with each iteration/time step depending on the simulation type but does not include a full two-

way coupling between the solvers. The implemented UDFs enable the update of forces using the DEFINE_PROFILE and DEFINE_ADJUST macros available in Ansys.

As presented, the CFD model was defined, and the calculation process can be executed to achieve the convergence of the solution. This convergence is monitored based on the residuals and additional monitors specified according to the computational case. The most important parameters measured during the calculation are volume-averaged and maximum velocity, integral and maximum turbulence dissipation rate, which is needed for stirring energy calculations, and y+ parameter to assess the correctness of the selection of the wall function for a particular case. Based on the solution, the graphical interpretation of the results as contours of the velocity or stirring energy can be presented and used for further analysis and comparison.

It has to be emphasized that the presented approach can now be freely modified depending on the type of simulation and the type of process considered, but the developed model assumptions remain unchanged and are treated as a core for further investigations. The validation of this model is given in the next section to confirm the correctness of the approach.

5.2 Model validation

As mentioned in Chapter 2, real experiments in the metallurgy industry are difficult to carry out due to the very high temperature of the processes in the range of 1400-1800 [℃], high density of the molten steel and turbulent flow in the applications of the electromagnetic stirrer. The measurement equipment is very expensive, and procedures are difficult due to the safety of the personnel. Therefore, the validation of the developed CFD approach was based on a comparison of the simulation results with measurements from an internal ASEA (now ABB) experiment carried out in cooperation with Cambridge University, equipped with a laboratory stand filled with mercury replicating the flow inside the ladle furnace subjected to the additional electromagnetic stirring[221]. The experiment was conducted in the early 80s and has been used by the ABB as a benchmark case for scientific investigations since then.

The mercury was used to avoid heating the metal to high temperatures. Such a setup allows for direct observation of the flow, which is a unique and useful feature. However, using mercury is extremely dangerous. The first approaches to this test were unsuccessful and were stopped early due to the high mercury concentration in a doctoral student's blood, which was dangerous for his health. The test was successfully realized after introducing sufficient safety measures, and the results are often used for validation purposes.

5.2.1 Experimental setup

During the research, a 150-ton ladle furnace equipped with a linear stirrer system featuring a vertical direction of stirring was selected as a case study. The test model of the furnace was set up in the lab in a scale of 1:10. The same test setup is taken in the current research and replicated in the form of a numerical setup to validate the capabilities of the model developed in Chapter 5.1. The dimensions of the model are presented in Figure 16.

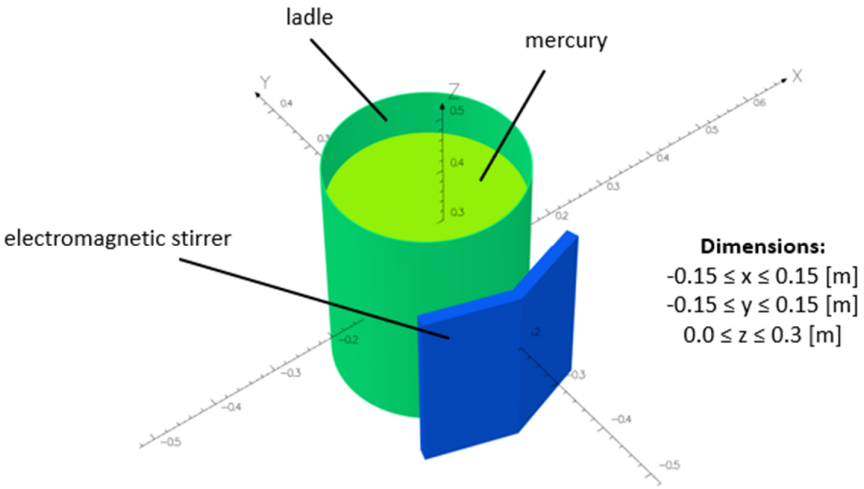


Figure 16. Dimensions of the ladle furnace used in Cambridge's experiment.

During the model preparation stages, particular attention was paid to the mercury domain, where fluid motion is investigated. The ladle and electromagnetic stirrer geometry are not explicitly included in the CFD model and are used here only for the visualization of the experimental setup.

The CFD approach is realized by the Reynolds-Averaged Navier-Stokes (RANS) model. The flow regime is assumed to be turbulent due to the presence of electromagnetic stirring, and the fluid is considered incompressible and viscous. The mercury properties at ambient temperature are gathered in Table 2.

Table 2. Mercury properties at ambient temperature.

Mercury properties	
Density [kg/m^3]	13 545
Viscosity [kg/(m s)]	0.00154413

To compare the numerical results with experimental results, a set of additional planes and points was defined according to[221]. The visualization of the velocity field is presented on the top plane, which is located 20 [mm] below the free surface of the mercury; the middle plane, which is located in the middle of the height of the mercury domain; and the bottom plane, which is located 10 [mm] above the bottom of the cavity. Moreover, one additional vertical plane, which is positioned longitudinally to the stirrer, is defined. In addition to that, two points where the quantitative data are measured are defined as point A along the stirrer and point B in the center of the melt and 20 [mm] below the free surface. The illustration of defined planes and points is presented in Figure 17.

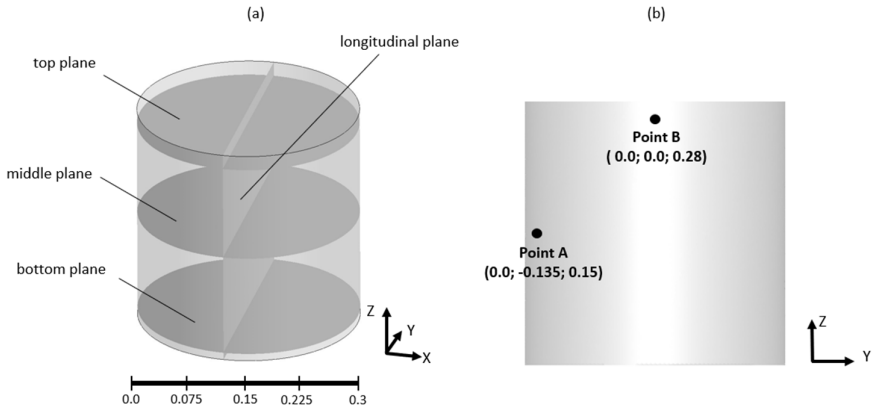


Figure 17. Definition of the planes and points to compare the results between the numerical approach and real experiment.

The steady-state type of simulation was used during the initial trials to model validation.

5.2.2 Steady-state approach

The computational domain includes a one-phase fluid domain, where the mercury is assigned. The gravitational acceleration and energy equation are not taken into consideration. The boundary conditions of the model were prepared according to the experimental setup and included the no-slip wall type on the vessel walls, as well as a separate wall at the top with a specified shear equal to zero as a numerical free surface condition. The summary of the boundary conditions used in the model is presented in Figure 18.

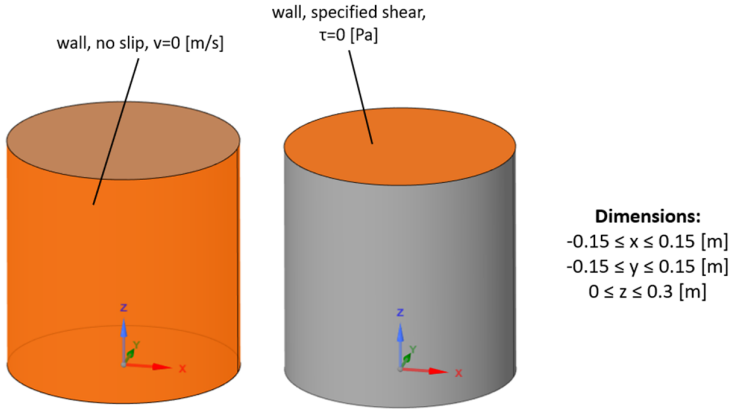


Figure 18. The boundary conditions used in the steady state, one-phase CFD simulation.

The results of the numerical approach should not depend on the discretization and volume element's size. Therefore, the mesh sensitivity study was done prior to the main simulation. The three different polyhedral meshes with different element sizes were prepared in Ansys Fluent Meshing software. The comparison of the meshes' quality is presented in Figure 19 and Table 3.

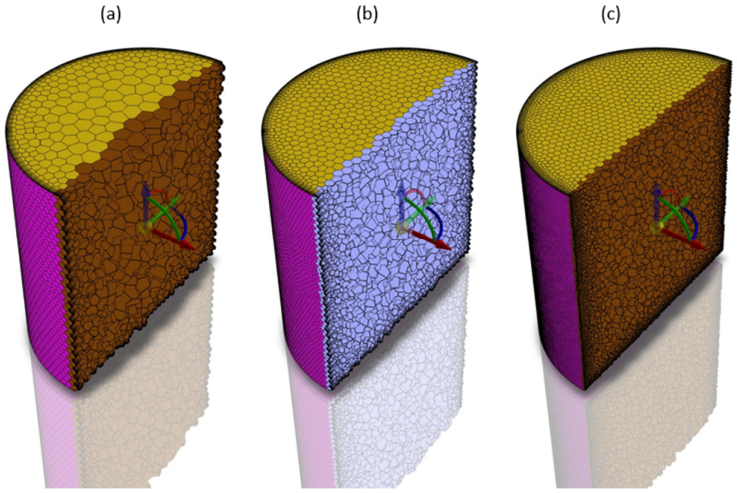


Figure 19. Meshes for mesh sensitivity study (a) coarse, (b) medium and (c) fine.

Table 3. Mesh parameters.

Mesh	Coarse	Medium	Fine
Number of elements	72 752	182 843	747 104
Min. Orthogonal quality	0.628	0.587	0.471
Max. Skewness	0.372	0.413	0.529

The influence of the size was evaluated based on the measurements in selected points from Figure 17b. The maximum speed and maximum turbulent kinetic energy were measured during the study. The comparison in graphical form is presented in Figure 20. Moreover, to confirm that the solution is fully converged, the residuals and other quantities like maximum or average velocity in the fluid domain or velocity in the selected points were measured. The exemplary dependence between the velocity vs iteration during the whole simulation process is presented in Figure 21.

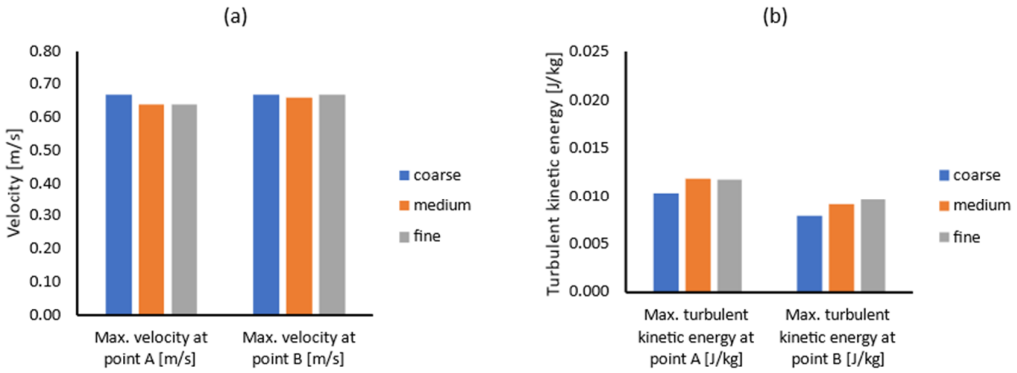


Figure 20. Comparison between maximum velocity (a) and maximum turbulent kinetic energy (b) in selected points for different meshes – steady state, one-phase simulation.

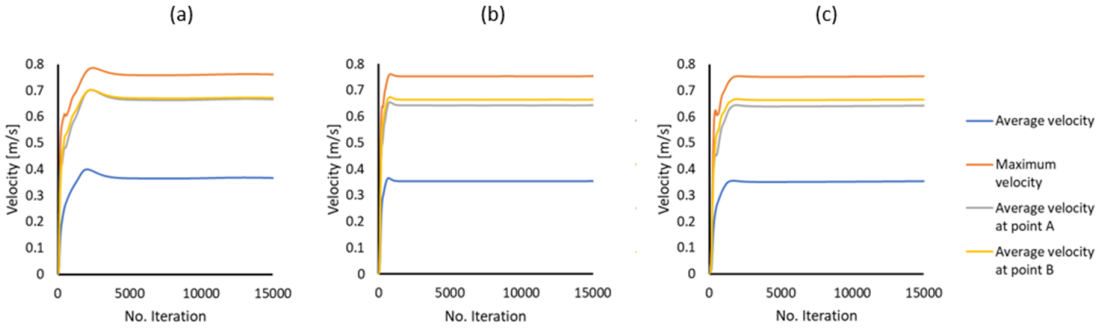


Figure 21. Average and maximum velocity measured inside the fluid domain, and average velocity measured at points [221]A and B for (a) coarse, (b) medium and (c) fine mesh.

The obtained results confirm that the variables do not depend on the mesh used in the simulation because the error measured as a difference of variables between the fine and then selected medium mesh in relation to variables for the medium mesh is not larger than 5%. The error between the medium and coarse mesh is calculated in that same way and is higher, up to 13%. In this case, the medium mesh was used for further research to avoid the longer calculation time typically associated with the fine mesh. Moreover, the results remain very stable throughout the simulation process, confirming that the simulation has converged and the results can be treated as reliable.

Finally, after the mesh sensitivity study and selection of the mesh for further investigations, the main calculation process for steady-state simulation was executed, and then the results were compared between the numerical simulation and experiment. The comparison between the velocity distribution in particular planes described in Figure 17a from the simulation and experiment is presented in Figure 22.

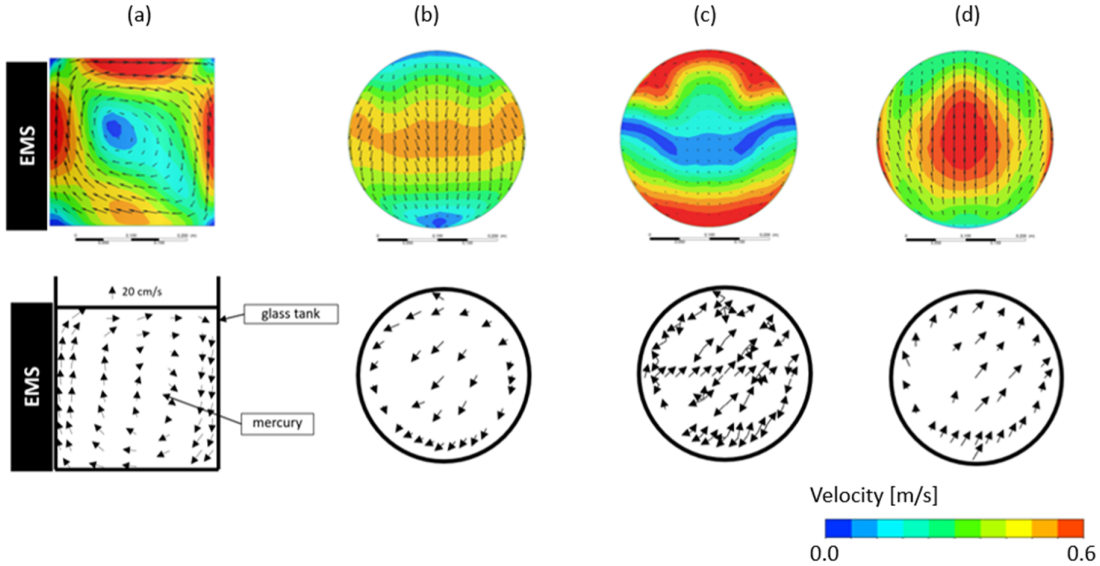


Figure 22. Comparison between steady state numerical simulation (top) and experiment (bottom) for (a) longitudinal, (b) bottom, (c) middle and (d) top cross-section.

The above comparison suggests that the general velocity distribution in different parts of the furnace is compatible, but in the case of the CFD simulation, the rotation of the flow present in the real case is not observed. Therefore, the more advanced approach, transient and multiphase model, was used for further model validation.

5.2.3 Transient approach

The computational domain was extended to include a two-phase fluid domain, where the mercury and air phases are considered. The gravitational acceleration was included to model the hydrostatic pressure properly, but the energy equation was not considered due to the constant room temperature assumption. Again, the boundary conditions were set to project the real conditions of the experiment into a numerical model. The walls are modelled as standard no-slip wall, and the top boundary condition is modelled as a pressure outlet with atmospheric pressure. Moreover, due to the multiphase simulation, the volume fraction of 100% of air is assigned in the case of the backflow. The description of the boundary conditions used in the model is presented in Figure 23.

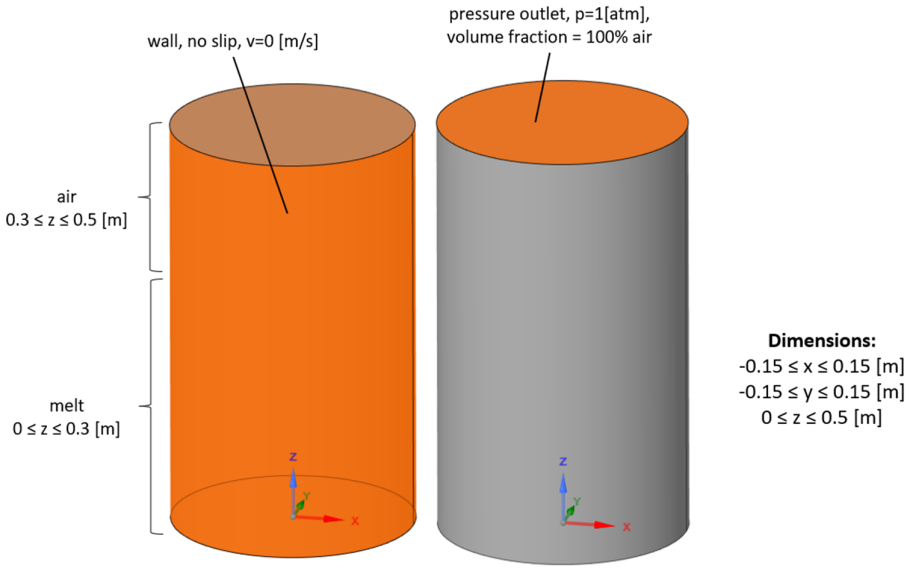


Figure 23. Updated boundary conditions in case of the multiphase, transient simulation.

Similar to the steady-state simulation, the transient approach's mesh sensitivity study was conducted first. The comparison of the meshes used in the mesh sensitivity study is presented in Figure 24 and Table 4.

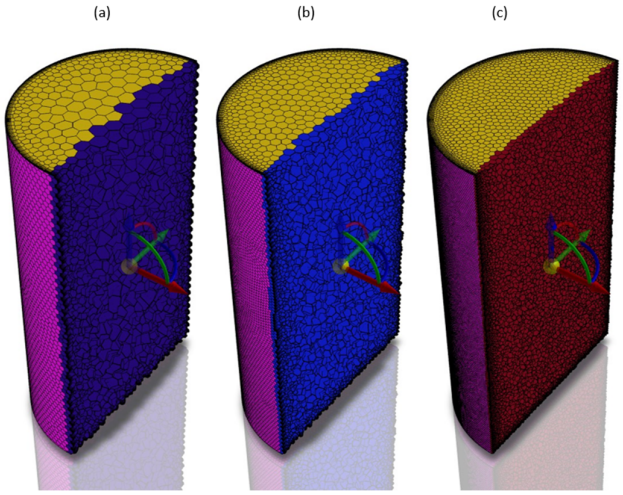


Figure 24. Three different meshes used to mesh sensitivity study for multiphase simulation: (a) coarse, (b) medium and (c) fine.

Table 4. Mesh parameters.

Mesh	Coarse	Medium	Fine
Number of elements	111 041	286 637	1 189 239
Min. Orthogonal quality	0.558	0.562	0.512
Max. Skewness	0.442	0.438	0.488

The maximum speed and turbulent kinetic energy were measured at the same points as in steady state simulation. The graphical interpretation of the comparison between results obtained from different meshes is presented in Figure 25. Again, the exemplary results for velocity measurements, but now in time due to the transient approach, are presented in Figure 26.

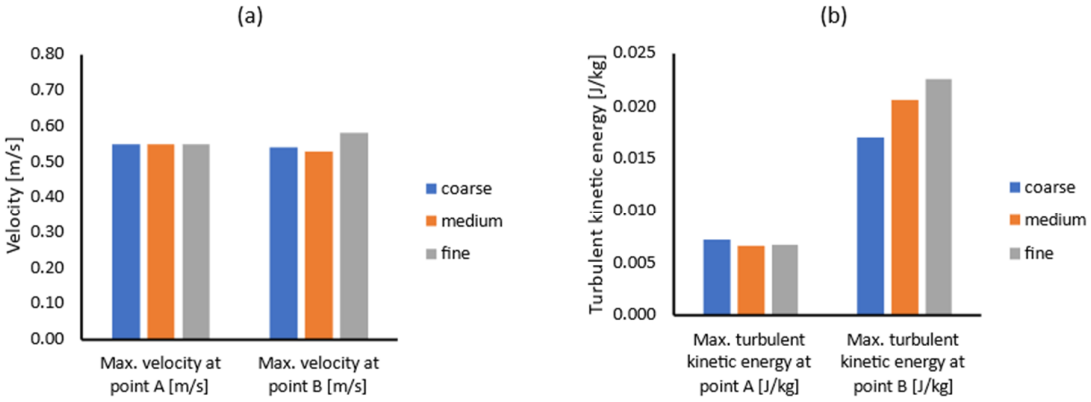


Figure 25. Comparison between maximum velocity (a) and maximum turbulent kinetic energy (b) in selected points for different meshes – transient, multiphase simulation.

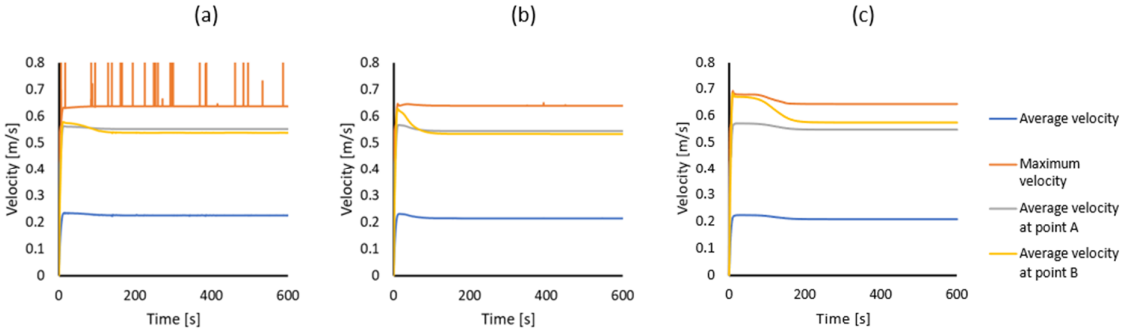


Figure 26. Average and maximum velocity measured inside the fluid domain, and average velocity measured at points A and B with (a) coarse, (b) medium and (c) fine mesh.

The analysis of the results confirms that the relative error between the fine and medium mesh is not higher than 6% for velocity measurements. The error between the medium and coarse mesh is higher, mainly in the case of turbulence kinetic energy measurements. Based on that, the medium mesh is used for further calculations to avoid the long calculation time. Moreover, the model's convergence is confirmed by the observations of velocity evolution over time. One doubt can be related to coarse mesh, where some picks of the maximum velocity are observed, but the time-average value is comparable to the other values.

Finally, as for steady-state simulation, the comparison between the velocity distribution in particular planes, as described in Figure 17a, from simulation and experiment is presented in Figure 27.

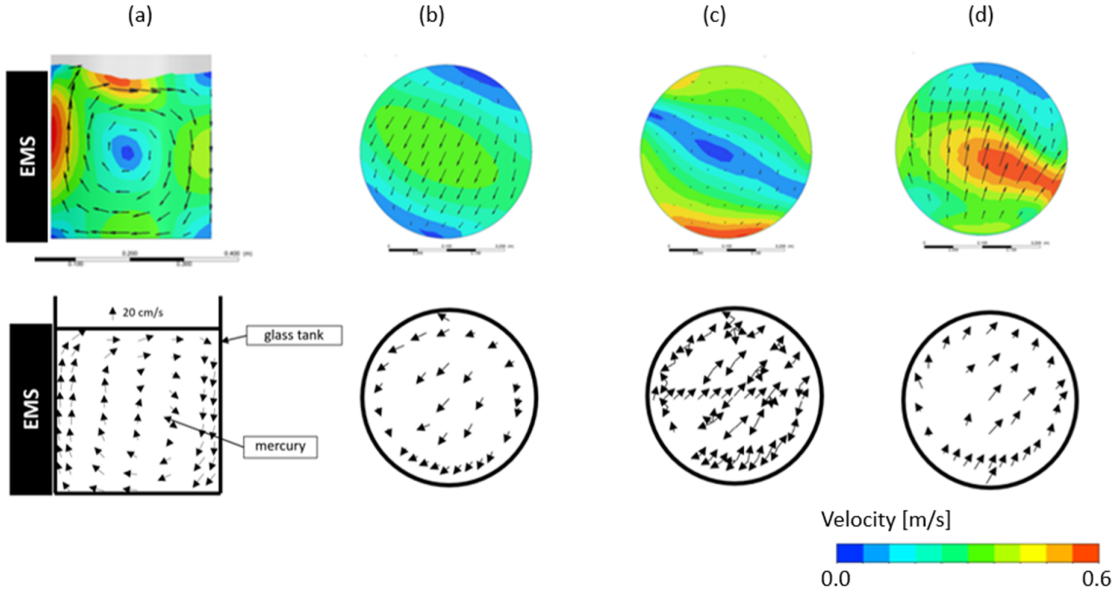


Figure 27. Comparison between transient, multiphase numerical simulation (top) and experiment (bottom) for (a) longitudinal, (b) bottom, (c) middle and (d) top cross-section.

The transient, multiphase simulation, including the VOF approach, enables the obtained simulation results to be compatible with the experimental results. The velocity distribution has

the same character as observed during the test. The additional rotation of the flow distribution is also observed in the numerical approach. The laboratory measurements confirm that the asymmetric flow is observed for full mercury level, where few first mercury circulations seem stable and symmetric. After some time, the distribution turns around 20 degrees[221].

The final comparison between the results from the experiment and CFD simulations for both the steady-state, one-phase approach and the transient, multiphase approach are gathered in Table 5.

Table 5. Comparison between the experiment and two different numerical approaches (steady-state with one-phase and transient with multiphase).

Method	Experiment	Steady-state simulation	Transient simulation
Max. speed at point A [m/s]	0.40	0.64	0.55
Max. speed at point B [m/s]	0.45	0.66	0.53
Max. turbulent kinetic energy at point A [J/kg]	0.0040	0.0119	0.0066
Max. turbulent kinetic energy at point B [J/kg]	0.0170	0.0156	0.0382 (0.0206 – point B)

The analysis confirmed that both, steady-state and transient multiphase approaches replicate experimental results. The major difference between both approaches is an occurrence of the rotation in the velocity field, which has not occurred in the steady state case. The rotation can be directly related to the free surface behavior, which is modelled in a transient, multiphase approach. The rotation of the flow can also be caused by:

- Unstable behavior of turbulences, which are random phenomena.
- Unstable behavior of the free surface in time which significantly influences the behavior of the flow inside the ladle and the distribution of the velocities.
- The real experimental setup is not ideally symmetrical; moreover, the stirring forces are harmonic and transient.

The impact of the free surface, modelled in multiphase simulation, is vast because of its direct influence on the velocity distribution inside the mercury. The shape of the free surface after 100 [s] obtained in the CFD simulation is presented in Figure 28.

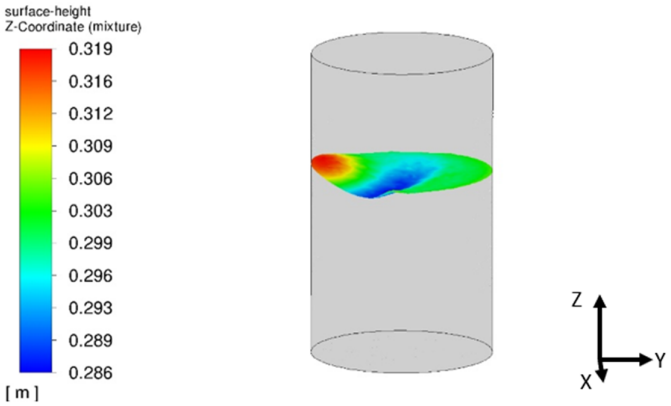


Figure 28. Free surface shape obtained in CFD simulation with the VOF after 100 [s].

Moreover, based on the results presented in Figure 27, it appears that the transient, multiphase simulation provides a more accurate prediction of reality as the results are closer to the experimental data. The most significant difference is observed in the case of the velocity and maximum turbulent energy parameter at point A (along the stirrer). However, it should be pointed out that this point was not precisely specified in the experimental setup. The only available information suggests that the point is along the stirrer diameter, but there is a lack of data about the distance from the wall of the vessel[221]. To address that issue, several additional points were defined in the model where the velocity and maximum turbulent kinetic energy were then measured. Each point was located at a distance of 5 [mm] from the previous one. The definition of the additional points is presented in Figure 29, and the values of maximum turbulent energy at these points are gathered in Table 6.

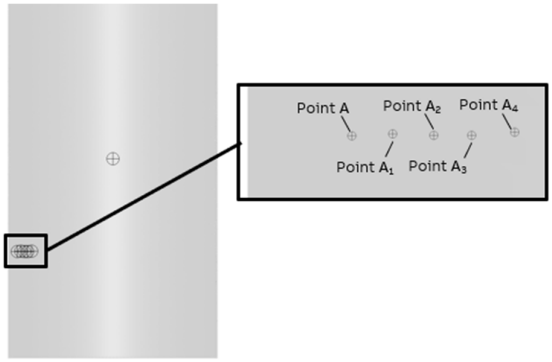


Figure 29. Investigated positions of point A.

Table 6. Velocity and turbulent kinetic energy at subsequent locations of point A.

	Point A	**Point A_1**	**Point A_2**	**Point A_3**	**Point A_4**	**Experiment**
Max. speed [m/s]	0.55	0.50	0.49	0.45	0.42	0.45
Max. turbulent kinetic energy [J/kg]	0.0066	0.0072	0.0074	0.0076	0.0077	0.0040

As presented, the third variant of the location of point A is the closest to experimental measurements.

Therefore, it can be concluded that the model validation procedure confirms that the best approach to numerical simulation includes the transient and multiphase modelling of the phenomena. The approach enables the projection of all the phenomena, which can be unstable, like the influence of the free surface behavior on the velocity distribution or turbulences. The steady-state approach can be used for the initial evaluation of the proposed solution, setup of the stirrer parameters and evaluation of its influence on the velocity distribution. It can also be used to identify conditions where a more advanced multiphase modelling is required.

Both presented methods will be used in this research for further evaluation and the proper selection of the electromagnetic stirrer and designing solutions for particular devices: electric arc furnace (Chapter 6), ladle furnace (Chapter 7) and tundish (Chapter 8).

However, it should also be mentioned that the above-presented approach does not consider the role of non-metallic inclusions. A model for the evolution of non-metallic inclusions needs to be developed and incorporated into the above-presented numerical solution to better reflect the behavior of molten steel under industrial conditions. The details of such a developed model and its implementation aspects are explained in the next subsection.

5.3 Development and implementation of the inclusion model

Due to the high requirements for the quality of the final steel product, additional improvements are necessary to consider non-metallic inclusions in the liquid steel at different manufacturing stages, especially inside the ladle furnace and tundish, where the final structure of the steel is formed.

The approach used within this work is a PBM (population balance model), a more advanced multiphase model, which enables detailed tracking of the concentration of the particles. Details about the theoretical assumptions of this model can be found in Section 3.3.3.

The developed model for inclusion modelling is based on several assumptions:

- Inclusions modelling is only for EMS stirring or without stirring. The additional dependence on argon gas is outside the scope of the PhD research and will be included in the future.
- Two Eulerian phases are included: the molten steel and inclusion phases, where the surface tension between both phases is equal to 1.257 [N/m]. The material properties of both phases are presented in Table 7.
- Sixteen bins with different particle's diameters are considered (Table 8)[222].
- Energy equation with temperature distribution is not taken into consideration due to the assumption of the absence of the high-temperature gradient in the case of the ladle furnace and tundish.
- The numerical approach includes the aggregation and removal of inclusions[222].

Table 7. Material properties of melt and inclusions used in the simulation.

Phase	Density [kg/m^3]	Dynamic viscosity [kg/(m s)]
Molten steel	6900	0.0069
Inclusions	4413	0.0067

Table 8. Diameters of non-metallic particles considered in the molten steel[222].

Bin's number	Particle's diameter [μm]
15	1
14	1.36
13	1.84
12	2.50
11	3.39
10	4.61
9	6.25
8	8.48
7	11.51
6	15.63
5	21.21
4	28.78
3	39.06
2	53.02
1	71.95
0	97.66

The aggregation process between particles of inclusions is modelled based on the assumption of the collisions and growth. In general, the Brownian, Stokes and turbulent collisions are considered and captured by the following equations:

$$\frac{\partial}{\partial t}(\rho_M \cdot C_i) + \frac{\partial}{\partial x_j}\left(\rho_M \cdot \vec{u}_{i,I} \cdot C_i\right) = \frac{\partial}{\partial x_j}\left(\Gamma \frac{\partial C_i}{\partial x_j}\right) + \rho_M \cdot S_\phi, \tag{26}$$

where ρ_M – density of molten steel [kg/m^3], C_i – dimensionless concentration of the i^{th} group inclusions in the molten steel: $C_i = \frac{n_i}{n_0}$, n_i – number density of the i^{th} group inclusions at a time, n_0 – initial number density of inclusions with an initial average size $d_{initial}$, Γ – diffusion coefficient of inclusions [kg/(m s)], $u_{i,I} = \left(u_x, u_y, u_z - U_i\right)$ – flow velocity of inclusions particles [m/s], U_i – floating velocity of the i^{th} group of inclusions [m/s], S_ϕ – source term of collision and growth of inclusion:

$$\begin{aligned} S_\phi = \frac{dC_k}{dt} = {} & \frac{2V_{k-1}}{V_k} \cdot \beta(r_{k-1}, r_{k-1}) \cdot C_{k-1} \cdot C_{k-1} \\ & + \sum_{i=1}^{k-1} \frac{V_i}{V_k} \cdot \beta(r_i, r_k) \cdot C_i \cdot C_k - \sum_{i=k}^{M} (1 + \delta_{ik}) \cdot \beta(r_i, r_k) \cdot C_i \cdot C_k, \end{aligned} \tag{27}$$

The first two terms are the generation of inclusions, and the last term is the sink term of inclusions, where: $\beta(r_i, r_k)$ – the collision frequency of inclusion particles with a radius r_i and r_j, δ_{ik} – Kronecker's delta function (for $i = k$, $\delta_{ik} = 1$, for $i \neq k$, $\delta_{ik} = 0$).

In case where $k = 1$ and $k = M$, the equations are simplified to:

$$\frac{dC_1}{dt} = -\sum_{i=1}^{M}(1+\delta_{i1})\cdot\beta(r_i,r_j)\cdot C_i\cdot C_1, \tag{28}$$

$$\frac{dC_M}{dt} = \frac{2V_{M-1}}{V_M}\cdot\beta(r_{M-1},r_{M-1})\cdot C_{M-1}\cdot C_{M-1} + \sum_{i=1}^{M-1}\frac{V_i}{V_M}\cdot\beta(r_i,r_M)\cdot C_i\cdot C_M, \tag{29}$$

where: M – maximum group of inclusion size using particle size grouping method.

$$\beta(r_i,r_j) = \beta_B(r_i,r_j) + \beta_S(r_i,r_j) + \beta_T(r_i,r_j), \tag{30}$$

where: $\beta_B(r_i,r_j)$ – Brownian collision, $\beta_S(r_i,r_j)$ – Stokes collision, $\beta_T(r_i,r_j)$ – turbulent collision.

The source term of collision and growth of inclusion is responsible for aggregation phenomena included in the population balance model in Ansys Fluent. All of the above-mentioned processes are incorporated into the numerical model using the implemented user-defined procedure.

In the case of aggregation, the coalescence process is realized. The mechanism of the Brownian, Stokes and turbulent collision is as follows:

1. Brownian collision:

$$\beta_B(r_i,r_j) = \frac{2k_BT}{3\mu_M}\cdot\left(\frac{1}{r_i}+\frac{1}{r_j}\right)\cdot(r_i+r_j), \tag{31}$$

where: k_B – Boltzmann's constant [J/K], T – absolute temperature [K], μ_M – molecular viscosity of the molten steel [Pa s], r_i, r_j – radius of the i^{th} and j^{th} group inclusions [m].

2. Stokes collision:

$$\beta_S(r_i,r_j) = \frac{2\pi g(\rho_M-\rho_I)}{9\mu_M}\cdot\left|r_i^2-r_j^2\right|\cdot(r_i+r_j)^2, \tag{32}$$

where: g – gravitational acceleration [m/s^2], ρ_M – density of melt [kg/m^3], ρ_I – density of inclusions [kg/m^3].

3. Turbulent collision:

$$\beta_T(r_i,r_j) = 1.3\alpha\cdot\sqrt{\pi}\cdot(r_i+r_j)^3\cdot\left(\frac{\varepsilon}{\vartheta}\right)^{\frac{1}{2}}, \tag{33}$$

where: ε – turbulent energy dissipation rate [m^2/s^3], ϑ – kinematic viscosity of the molten steel [m^2/s], α – coagulation coefficient:

$$\alpha = 0.738\left(\frac{\mu_M\cdot(\min(r_i,r_j))^3\cdot\left(\frac{\varepsilon}{\vartheta}\right)^{\frac{1}{2}}}{A_{131}}\right)^{-0.242}, \tag{34}$$

where: A_{131} – Hamaker constant.

The final coalescence rate is the sum of Brownian, Stokes and turbulent collision.

The removal process of inclusions in real conditions relates to the different mechanisms, like the rupture of inclusions to the ladle walls/argon bubbles (if included) or to the slag layer.

This work is focused on one mechanism related to the interaction between the inclusions and slag layer. The slag layer is not modelled directly, but the conditions between the inclusions and the top layer of cells mathematically cover the relation between them. All the conditions are realized by mathematical relations and focus on each particle and its relative velocity, rupture and collision time. The relationship between inclusions and the slag layer is again modelled in this work by implemented UDFs. The more detailed description is as follows:

1. Relative velocity between the slag and the inclusion u_R:

$$u_R = U_i + u_z^{'}, \tag{35}$$

where: U_i – floating velocity of the i^{th} group inclusions [m/s] and is described by the equation:

$$U_i = \frac{2g \cdot (\rho_M - \rho_I) \cdot r_i^2}{9\mu_M}, \tag{36}$$

$u_z^{'}$ – random velocity fluctuation in the vertical direction at the top surface [m/s] and is described by the equation:

$$u_z^{'} = \zeta \cdot \sqrt{\frac{2}{3}k}, \tag{37}$$

where: ζ – normally distributed random number generated in each time step (at this moment, a random number in a range between -500 to 500, this number is generated for each particle), k – turbulent kinetic energy [m^2/s^2].

2. Collision time:

$$t_C = \left(\frac{d_I^3 \cdot \rho_I}{12\sigma_{MS}}\right)^{\frac{1}{2}} \cdot \left\{\pi + 2\arcsin\left[1 + \frac{12u_R^2\sigma_{MS}\rho_I}{d_I^3 g^2(\rho_I - \rho_M)^2}\right]^{-\frac{1}{2}}\right\}, \tag{38}$$

where: d_I – diameter of inclusions [m], σ_{MS} – interfacial surface tension between the molten steel and the slag [N/m], g – gravitational acceleration [m/s^2], ρ_I – density of inclusions [kg/m^3] ρ_M – density of melt [kg/m^3].

3. Rupture time:

$$t_F = \frac{3}{64}\mu_M \frac{\phi^2}{m\sigma_{MS}h_{Cr}^2} d_I^3, \tag{39}$$

$$\phi = \arccos\left\{1 - 1.02 \cdot \left(\frac{\pi d_I \rho_I u_R^2}{12\sigma_{MS}}\right)^{\frac{1}{2}}\right\}, \tag{40}$$

where: h_{Cr} – critical thickness of the liquid film for film rupture [m], m – constant equal 1 for inclusion particles, μ_M – molecular viscosity of the molten steel [Pa s].

Removal conditions are the following:

- $u_R \leq 0$ – the condition when the inclusions are not able to reach the slag and then cannot be absorbed them;
- $u_R > 0, t_C < t_F$ – the condition when the film between the molten steel and slag is not able to rupture during a collision between the particle of inclusion and the slag

layer. Therefore, the particle of the inclusion is rebounded from the slag layer and is not able to be removed.

- $u_R > 0, t_C \geq t_F$ – the condition when, finally, the particle of the inclusion is able to rupture the slag layer during the collision. Therefore, the three phases (steel, slag and inclusion) are in contact, and the inclusion is absorbed into the slag layer. This condition is responsible for removing the inclusion.

To sum up, the inclusions are removed when the following conditions are met:

$$Flux = \begin{cases} -\rho_M \cdot u_R \cdot C_i & u_R > 0, t_C \geq t_F \\ 0 & u_R > 0, t_C < t_F \\ 0 & u_R \leq 0 \end{cases}. \quad (41)$$

As mentioned above, the slag layer is not considered in the current simulation cases. The removal process is modelled by the assignation of the above functions and conditions only to the cells located near the top boundary condition of the ladle furnace (Chapter 7) or tundish (Chapter 8), to which this type of simulation will be applied.

The general schematic of analysis of the inclusion behavior inside the melt is presented on the scheme in Figure 30.

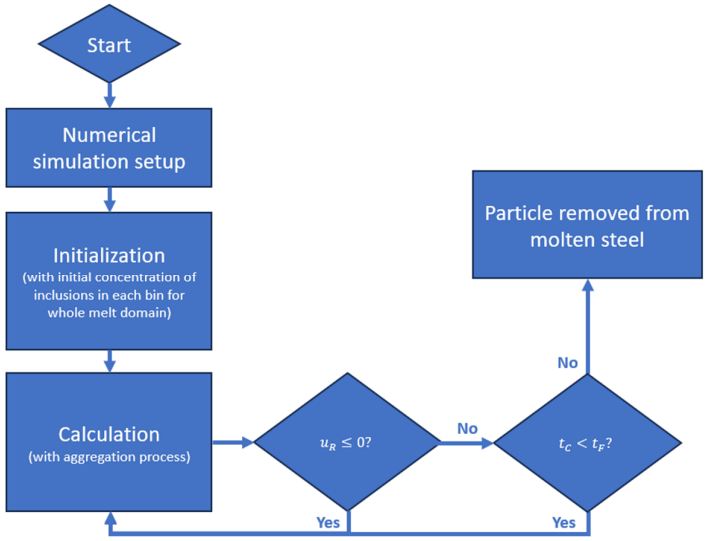


Figure 30. Block diagram of the developed inclusion removal algorithm.

The effectiveness of the inclusion removal process and other phenomena are directly related to the efficiency of the mixing inside the liquid steel. In that case, it is crucial to identify an indicator that assesses the mixing efficiency for different vessels and under various stirring conditions. Unfortunately, standard indicators have limitations when EMS systems are considered. Therefore, the development of a new indicator became an important part of the thesis.

5.4 Development of the indicator for specific stirring energy

As pointed out, the stirring energy parameter is often used to assess the mixing process's effectiveness. Its definition is well-known in standard gas stirring applications. Different authors have also proposed various formulas to describe the stirring energy in the case of some particular applications[223,224]. However, when the melt is stirred by the EMS system, the proposed formulas are not able to reliably predict the value. To fill this gap in the case of the EMS stirring, a new universal formula is proposed in the thesis.

In general, the behavior of the molten steel can be divided into the laminar and turbulent parts of the flow. In high-turbulence flows, the energy generated by viscous forces is low and can be omitted. The turbulence dissipation rate significantly influences the amount of energy consumed in the process. The total energy in the process includes viscous and turbulence parts, which are described as:

$$\Phi = 2\vartheta S_{ij} S_{ij} + 2\vartheta \overline{s_{ij} s_{ij}}, \tag{42}$$

where:

$$u_i = U_i + u_i', \tag{43}$$

$$S_{ij} = \frac{1}{2}\left(\frac{\partial U_i}{\partial x_j} + \frac{\partial U_j}{\partial x_i}\right), \tag{44}$$

$$s_{ij} = \frac{1}{2}\left(\frac{\partial u_i'}{\partial x_j} + \frac{\partial u_j'}{\partial x_i}\right), \tag{45}$$

where: Φ – dissipation rate of mechanical energy per unit mass, S_{ij} – mean rate of strain, s_{ij} – fluctuating rate of strain, $2\vartheta S_{ij} S_{ij}$ – viscous dissipation rate of the mean flow, $2\vartheta \overline{s_{ij} s_{ij}}$ – dissipation rate of turbulent energy ϵ, U_i – velocity in i^{th} direction, u_i' – fluctuating velocity in i^{th} direction.

If the stirring method is based on the EMS solution, the viscous component of the stirring energy can be omitted. This is supported by studies on the standard EAF with the EMS system, where the dissipation of turbulent and viscous energy were compared, as in Table 9.

Table 9. Stirring energy measurements based on the dissipation of turbulence and viscous energy measurements for different EMS factors.

EMS factor [%]	Dissipation of turbulent energy [W/ton]	Dissipation of viscous energy [W/ton]
0	0.251	0.011
50	7.239	0.100
100	25.173	0.218

The above results confirm that the viscous part of the stirring energy can be omitted when EMS stirring is included, but in the case without the EMS device active, the viscous part plays a significant role and must be considered in the calculation of stirring energy.

In EMS-stirred devices, turbulent flow is mainly present. Therefore, the specific stirring energy $\dot{\epsilon}$ [W/ton] used during the investigations in EMS stirred devices includes only the turbulent part of the flow. In this case, it is assumed that the stirring energy is the sum of the turbulence dissipation rate ϵ [m^2/s^3] in the whole volume of the melt Ω [m^3] multiplied by the gravitational acceleration and factors related to unit conversion. The average value is specified in the whole volume of the molten steel in watts per ton and is described by the proposed equation:

$$\dot{\epsilon} = \frac{\int_0^{\Omega} \epsilon d\Omega}{\int_0^{\Omega} d\Omega} \cdot 9.81 \cdot 1000 \left[\frac{W}{ton}\right]. \tag{46}$$

Specific stirring energy from (46) will be applied in this research in Chapters 6-8 to evaluate the stirring intensity in different vessels and with different stirring methods. The obtained results will also be compared with publicly available data in Chapter 9 to prove the correctness of the proposed method.

6. Development of the robust CFD simulation of the electric arc furnace (EAF)

6.1 Motivation for CFD simulations in EAF

In the steelmaking processes, the issue related to the high-temperature gradients between the scrap and arc heating areas, where the temperature difference is up to 150 [℃] in the case of a common 100-ton furnace, is clearly observed[225]. The problem arises due to the high porosity of the scrap area, which results in inefficient heat exchange. Therefore, different stirring methods can be employed to enhance the heat and mass transfer efficiency between the molten steel and scrap areas, thereby homogenizing the temperature distribution and accelerating the scrap melting process.

Different stirring mechanisms can be distinguished in the EAF. The most straightforward is caused by the natural processes present in the EAF, but the range of the average and maximum velocities are rather low, as presented in Table 1. Moreover, these processes are difficult to control.

Nowadays, there are two main methods that can overcome the mentioned limitations and increase the efficiency of the stirring. The first method is BGS (bottom gas stirring), which is a quite popular method in the case of the LF, and the second one, is electromagnetic stirring with additional EMS devices. A detailed description of these methods is presented in Section 2.2.

Despite the fact that the EMS technology is older than BGS and was successfully applied in industry, the measurement and flow control technologies were not well developed in the 50s, so the development of the optimized EMS solutions tailored for specific furnaces was challenging and limited. Moreover, at that time, environmental regulations did not impose strict limitations on the steelmaking industry as they do now, which made it possible to use high-power-consuming devices in the past. Nowadays, the primary goal is to increase production efficiency while decreasing CO2 emissions and reducing power consumption. This is directly related to the process of replacement of the blast furnaces with green technologies such as EAF furnaces, which often have large capacities, sometimes exceeding 400 tons. Intensive research in this topic is required; therefore, the focus is on numerical simulations to assess the efficiency of mixing without the need for difficult and expensive experimental measurements.

The availability of numerical techniques to understand the molten steel flow without difficult and costly measurements in the steel plants and benefits observed during the EAF processes with the EMS system enable further development of that solution to meet the requirements of the green steel technology and increase the efficiency of the production by designing the technologies dedicated for particular furnaces. Based on that, the design of the EMS device to ensure the highest effectiveness for particular furnace is possible. Moreover, the production process in the EAF is divided into stages, which require different stirring intensities, which can be easily controlled by EMS. The present work investigates the stirring efficiency and its dependence on the EMS device setup. Moreover, the lack of a direct comparison between the EMS stirring and BGS motivates to additional studies to confirm the higher efficiency of

the EMS solutions. The EMS method appears to be a significantly better approach than BGS, particularly in the process of replacing blast furnaces, where EAFs with large capacities are considered. Thanks to the investigations, weak points can be identified and improved, thereby enhancing the existing technology and helping to fulfil the requirements related to green steel technology. The separate topic is the decarbonization process, where the goal is to achieve the lowest possible carbon content. The technology requires control of the processes inside the furnace to reduce the carbon footprint, where the EMS system can be beneficial. Understanding the phenomena inside the EAF under EMS stirring, with the development of EMS solutions, is required to achieve improved solutions in the future.

Therefore, the main goal of this chapter is to develop a robust CFD simulation for the EAF with the EMS, based on the model proposed in Chapter 5. Such a CFD model will be used to evaluate the efficiency of the EMS method in comparison to the reference case based on natural convection and the BGS for temperature homogenization and heating processes. Moreover, the characteristics of the mixing process with EMS will be widely discussed to highlight its capabilities and limitations. As a result, the EMS EAF technology guidelines could be designed using a computer-aided approach that has been developed.

6.2 Description of the EMS EAF simulation

6.2.1 Geometry of the model

The 160-ton of total weight (100 tons of tapping) electric arc furnace (EAF) is considered a case study to evaluate the effectiveness of the electromagnetic stirring compared to the case without any stirring and with classical gas stirring. The geometry of the furnace with EMS is presented in Figure 31. The real furnace includes the refractory on the whole shell; moreover, the additional window made from non-magnetic steel is included to enable the penetrating and acting of the EMS forces through the shell. The geometry of the furnace with a window in the shell influences the distribution of electromagnetic forces and is included in the electromagnetic simulations, but then only melt is considered in the CFD part. Furthermore, in the BGS method, the gas stirring is realized by three direct purging plugs located at the bottom of the furnace. Each plug has a diameter of 200 [mm] with dedicated holes, as seen in Figure 32.

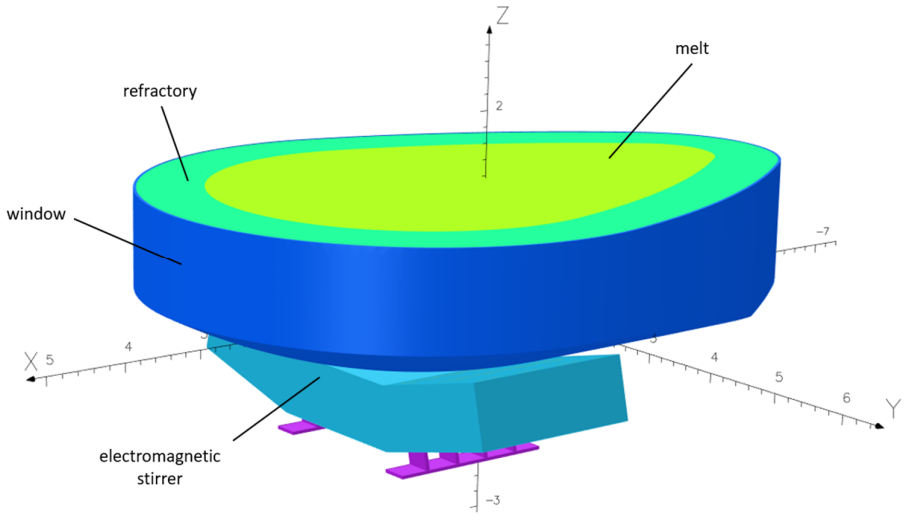


Figure 31. Geometry of the 160-ton industrial EAF with EMS system.

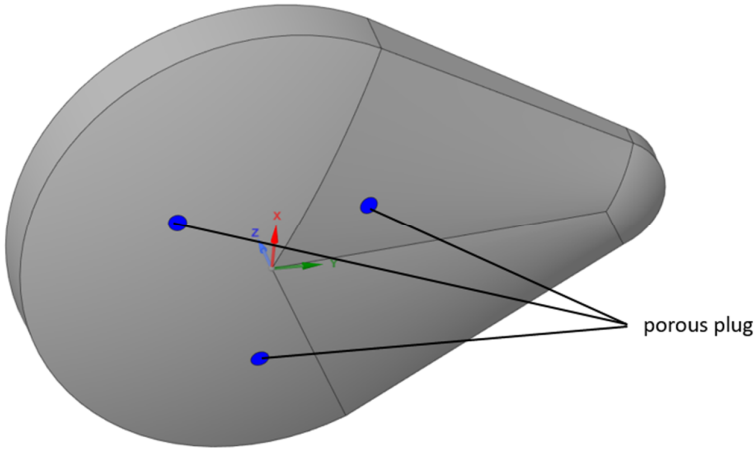


Figure 32. Location of 3 direct purging plugs for industrial 160-ton EAF.

The geometry is divided into subdomains to measure particular regions' velocity and stirring energy distribution. Moreover, due to the fact, that in EAF a high temperature gradient is expected and in the numerical approach the homogenization and heating processes are included, the model is improved about the energy equation consideration and the temperature is also measured in these volumes. The subdomains are located in the bottom and top parts of the melt.

The separate analysis will include the multiphase model, where apart from molten steel, the slag and air phases will be considered. This model will be described in detail in the following sections.

6.2.2 Boundary and initial conditions

The developed CFD model includes the three major processes occurring inside the EAF:

- Homogenization – process which includes the changes of the velocity and temperature in time under electromagnetic stirring to obtain the homogenized temperature in the whole bath. The initial condition required the temperature

gradient assigned to the whole bath, where the initial temperature of the bottom of the furnace is equal to 1560 [℃] and the initial temperature of the top part of the bath is equal to 1620 [℃], as presented in Figure 33. The temperature gradient is assumed based on the results obtained from the industrial measurements. The temperature gradient in the case without stirring is in the range of 50-70 [℃] in the flat bath[226,227]. The efficiency of the process is indicated by the time required to achieve a uniform temperature across the entire bath.

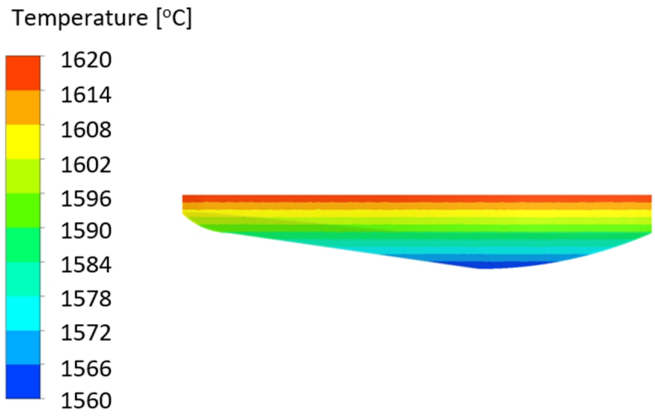


Figure 33. The temperature gradient applied to the EAF in homogenization process investigations.

- Heating – process which includes the additional heating generated by the electrodes at the top of the furnace bath. The velocity and temperature distributions in time under electromagnetic stirring are tracked to assess the heat and mass transfer efficiency in the whole bath. The initial temperature of the whole bath is equal to 1560 [℃] and increases due to the presence of an arc. The maximum temperature of the tap should be 1660 [℃]. The heating rate depends on the power generated by the electrodes.

The total active power generated by the electrodes can be divided into three different components:

- 55% of the power transferred to the melt is due to convection. The power distribution can be described as a function of the distance to the electrode as:

$$P = \int_0^R \frac{K}{(r+1)^2} dr, \tag{47}$$

where: $\frac{K}{(r+1)^2}$ – distribution of the power, K – constant, R – radius of the bath surface, r – distance between the current position and the center of the electrodes.

The graphical interpretation of the above equation is presented in Figure 34.

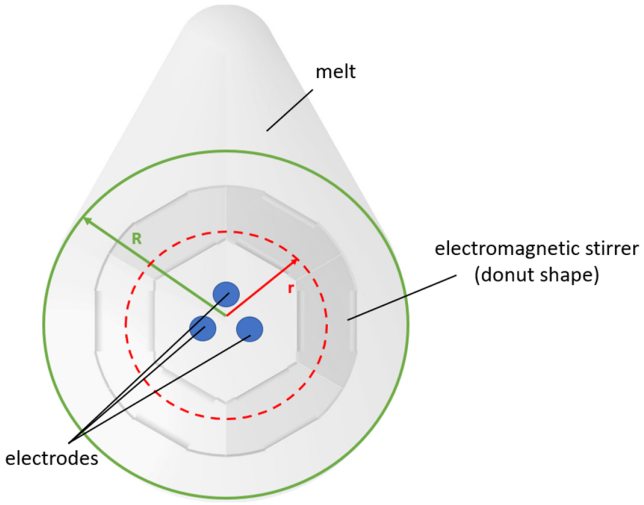


Figure 34. Concept of the arc power input.

- 20% of the power transferred to the melt is due to the radiation. The power distribution can be considered homogeneous throughout the melt.
- 25% of the power is lost to the walls, roof and electrodes.

- Scrap charging – process with additional heating from the electrodes but with an additional scrap area presented in the fluid domain. The scrap area is modelled as the porous zone with a porosity of around 30%, which is in line with industrial observations. The fluid flow is enabled in the scrap area but is related to the additional resistance of the flow in this region, which influences the mass and heat transfer between the molten steel and the scrap area. The process is executed with the assumption of constant scrap temperature equal to 1470 [℃]. The initial temperature of the molten steel is equal to 1560 [℃] and increases during the process thanks to the heat from electrodes. The electromagnetic stirring influences the flow behavior as well as the velocity and temperature distribution, which directly affect the mass and heat transfer between the scrap and melt zone. The heat flux from the melt into the scrap is tracked to assess the efficiency of the EMS solutions. The separated scrap area modelled as a porous zone in EAF is presented in Figure 35. During the process, the same 160-ton furnace is taken into consideration, but the effective capacity for this simulation is only 100 tons, due to the assumption that the furnace is during the operation of the scrap charging and melting.



Figure 35. The fluid and scrap zones for the effective capacity of the furnace for scrap charging simulation equal to 100 tons in operating 160-ton EAF.

On the top of the furnace, the wall with a specified shear equal to 0 [Pa] is defined to correspond to the free surface of the fluid. In the case of the heating and scrap charging simulation, where the energy equation is enabled to calculate the heat transfer, the walls are assumed to be adiabatic, with no heat exchange. The heat source is assigned to the top volume and created thanks to the sectioned geometry. This volume has 50 [mm] of thickness and is placed on the top part of the furnace. The heat source distribution is assigned according to (47). The boundary conditions are summarized in Figure 36. Moreover, the process parameters for the EMS are presented in Table 10.

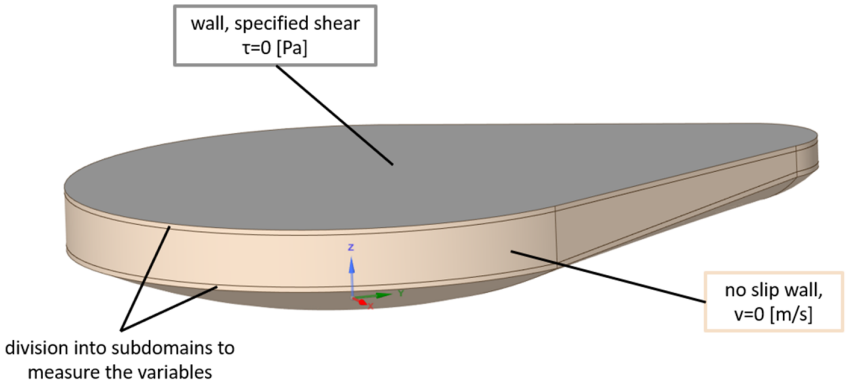


Figure 36. The concept of boundary conditions for the single-phase numerical simulations.

Table 10. Process parameters for linear EMS for EAF.

ORB54U	
Active power [kW]	522.6
Current [A]	1700.0
Frequency [Hz]	0.65
Weight [ton]	28
Distance stirrer – furnace bottom [mm]	50

For comparison purposes, the simulation of the BGS is realized for 30 [Nl/min] of argon flow per plug. Moreover, to increase the accuracy of the model, an additional, separate multiphase simulation was conducted for gas stirring. The boundary conditions of that simulation are slightly different than those of the single-phase simulation presented above. The geometry is extended to include the additional air phase on the top. Also, the boundary conditions of the top surface's are modified to the pressure outlet to reflect the atmosphere (Figure 37). Multiphase simulation includes the VOF approach to model the continuous phases (steel, slag and air) and the DPM approach to simulate the argon bubbles.

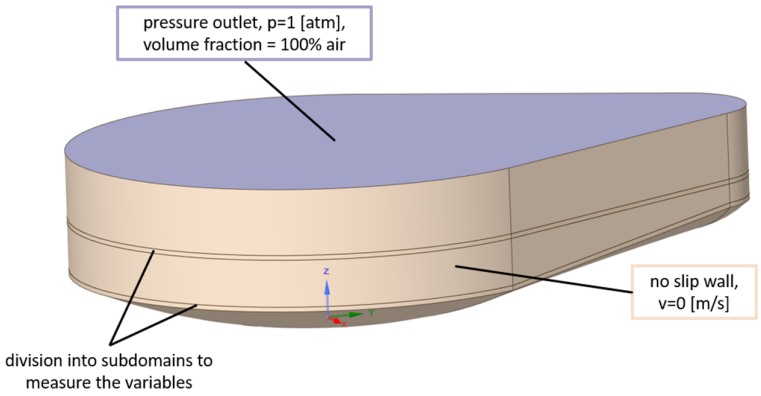


Figure 37. The concept of boundary conditions for the multiphase numerical simulations.

6.2.3 Material properties

In the case of the EMS, forced stirring causes, convection flow inside the furnace to be negligible, as the stirring affects the whole bath. The flow inside the furnace is fully turbulent. The melt is modelled as an incompressible, viscous fluid with temperature-independent properties. For BGS stirring, the high risk of the zones with low values of velocity is present, so to increase the accuracy of the model, the dependence of density on temperature is included. In the case of the reference model, without any stirring, due to the influence of the natural convection flow, the density of the steel is also modeled as temperature dependent. The material properties used in the simulation are presented in Table 11.

Table 11. Material properties of the steel.

Material properties of steel	
Density [kg/m3] for EMS stirring	6900
Density [kg/m3] for BGS stirring and reference model	$\rho = -0.6427 \cdot T[K] + 8151.2$
Kinematic viscosity [m2/s]	1.0x10-6
Thermal conductivity [W/m/K]	35
Specific heat [J/kg/K]	792

The argon in BGS is modelled with the ideal gas assumption to catch the effect of bubble expansion according to the hydrostatic pressure inside the melt. The mass of each bubble is constant, but the density of argon changes with the pressure and temperature. The diameter and volume of each bubble evolve with height in the bath. The argon properties are gathered in Table 12.

Table 12. Material properties of argon.

Material properties of argon under normal conditions	
Density [kg/m3]	1.6288
Dynamic viscosity [kg/(m s)]	2.125x10-5
Specific heat [J/kg/K]	520

Moreover, in the case of the BGS multiphase simulation, the additional slag layer is included to increase model predictive capabilities. The thickness of the slag layer is 200 [mm], and its properties are presented in Table 13.

Table 13. Material properties of slag.

Material properties of slag	
Density [kg/m3]	3000
Dynamic viscosity [kg/(m s)]	0.3
Specific heat [J/kg/K]	1170
Thermal conductivity [W/m/K]	6

Finally, in the case of the multiphase simulation, additional surface tension was considered, as presented in Table 14.

Table 14. Surface tension between phases.

Surface tension between phases	
Steel and slag [N/m] [222]	1.257
Steel and air [N/m] [228,229]	1.75
Slag and air [N/m]	0.45

6.2.4 Mesh sensitivity study

The mesh sensitivity study was conducted for three different polyhedral meshes. Both, steady-state and transient CFD simulations were considered for linear EMS stirring. The middle cross-section of each mesh is presented in Figure 38, while a summary of the number of elements in each mesh is provided in Table 15.

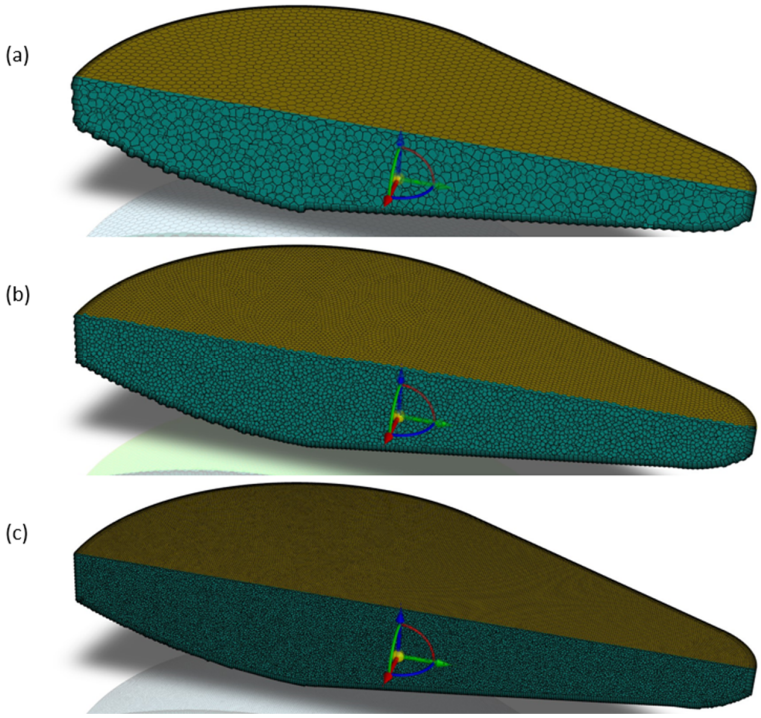


Figure 38. Three different meshes for sensitivity study: (a) coarse, (b) medium, and (c) fine.

Table 15. Number of finite volume elements in each mesh.

Mesh	Number of elements
coarse	75 067
medium	412 130
fine	2 627 618

The velocity and stirring energy were measured and compared during the mesh sensitivity study for both steady-state and transient approaches, respectively. The comparison of the volume average velocity and maximum velocity is presented in Figure 39. The corresponding stirring energy comparison is in Figure 40.

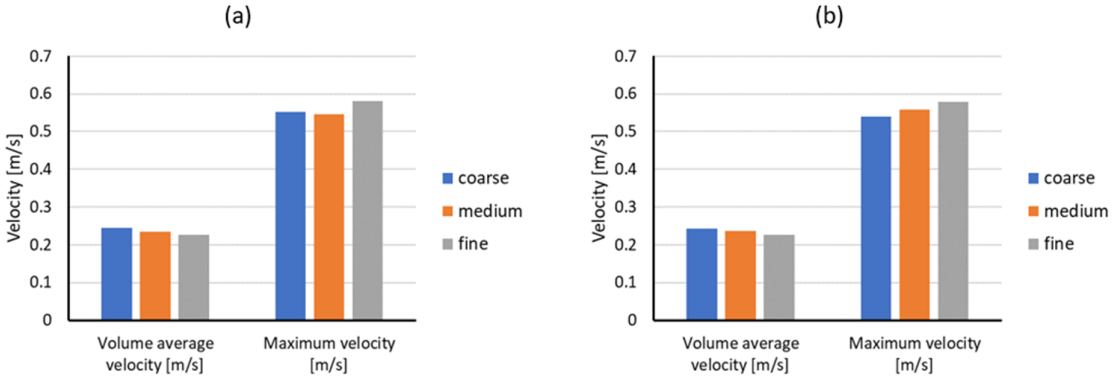


Figure 39. Volume average velocity and maximum velocity for whole EAF volume for (a) steady-state and (b) transient approach.

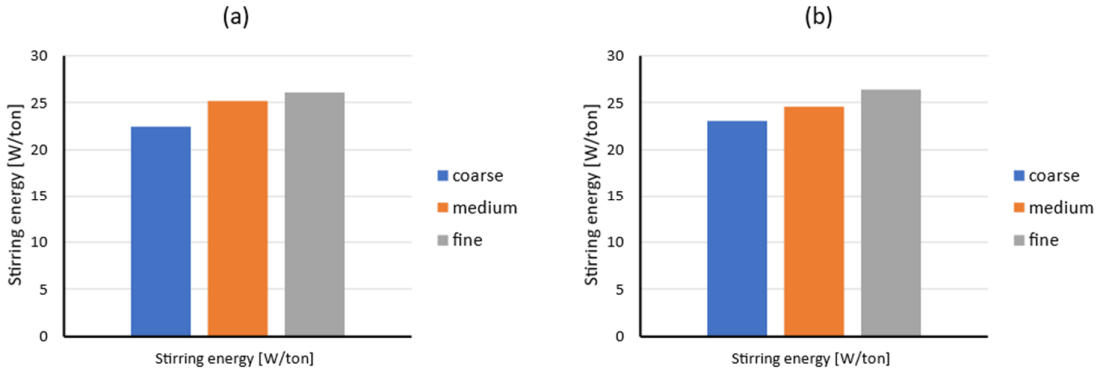


Figure 40. Volume average stirring energy for whole EAF volume for (a) steady-state and (b) transient approach.

It can be concluded that even the largest difference in the number of the finite volume elements among the meshes does not significantly affect the results, as the difference between the values of velocity and stirring energy is lower than 10% in the worst case. To avoid the long calculation time and ensure that the mesh is not too coarse, the medium mesh was selected for further analysis. Moreover, the results suggest that, in the case of the simplified, steady-state approach, the findings are comparable to those of the more advanced, transient approach.

It is worth mentioning that, in general, the same computational mesh is used for both reference and gas stirring models. The one exception is regarding the multiphase simulation, where the model had to be extended to include additional phases; however, the mesh setup was selected according to the above-presented study. For multiphase simulation, a slightly coarser mesh is used to fulfil the requirements regarding the Courant number formulated by the equation:

$$C = \Delta t(\sum_{i=1}^{n} \frac{u_i}{\Delta x_i}) \leq C_{max,} \tag{48}$$

where u – magnitude of velocity [m/s], Δt – time step [s], Δx – length interval (size of the mesh cell in one dimensional case) [m] and C_{max} – dimensionless value dependent on the discretization method.

6.3 Temperature homogenization

The numerical simulation of the temperature homogenization is prepared for four stirring cases: reference case with natural convection, CO stirring simplified to the EMS stirring with 5% of EMS power, the BGS and the 100% EMS method. The simulation of the CO bubbles mixing is very complex and time-consuming, but based on the separate study confirmed by the experimental measurements, the 5% of the EMS power stirring reflects the efficiency of the CO mixing[104,108]. This assumption enables to simulate the effect of the CO bubbles in a simple way with reduced EMS power. In the simulation, the temperature gradient between the top and bottom of the furnace was assumed as the initial conditions, as indicated in Figure 33. The goal

of the simulation was to find the homogenization time until the temperature difference between the maximum and minimum value inside the molten steel is less than 5 [°C]. This limit indicates that a full temperature homogenization is achieved in the furnace. The comparison of the temperature homogenization in selected time steps for three investigated methods is presented in Figure 41.

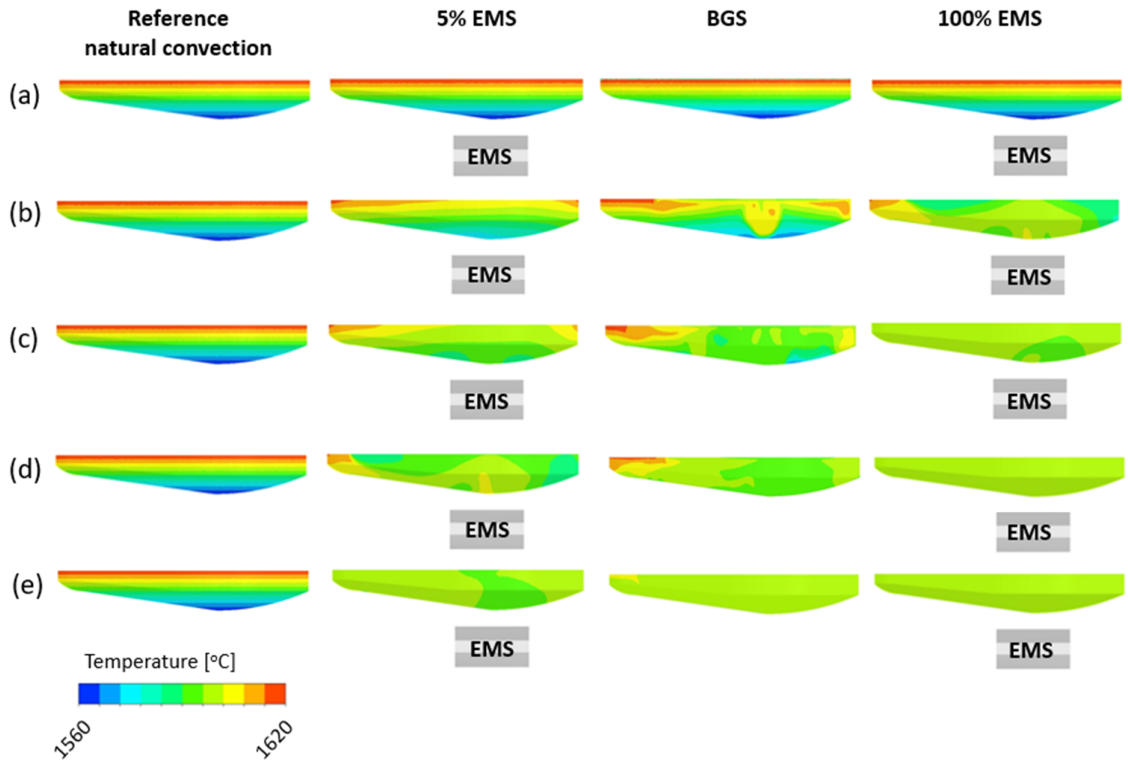


Figure 41. Temperature homogenization at the longitudinal cross-section of 160 tons furnace in (a) 0 [s], (b) 20 [s], (c) 50 [s], (d) 100 [s] and (e) 200 [s] for reference model, case with assumption of CO mixing (5% EMS), BGS and EMS.

Based on the simulation results, it is clearly visible that for the reference model with only natural convection, the homogenization is almost zero, while the CO bubbles mixing is characterized by the low efficiency of the stirring. The BGS has a similar homogenization level, but it is still not as effective as EMS stirring. The temperature homogenization time is directly related to the velocity and stirring energy distribution that occurred inside the melt. The final comparison between the homogenization time and the velocity and stirring energy distribution for particular methods is presented in Figure 42, Figure 43 and Figure 44, respectively. A more detailed view of the stirring energy for the reference model and CO mixing is presented in Figure 45.

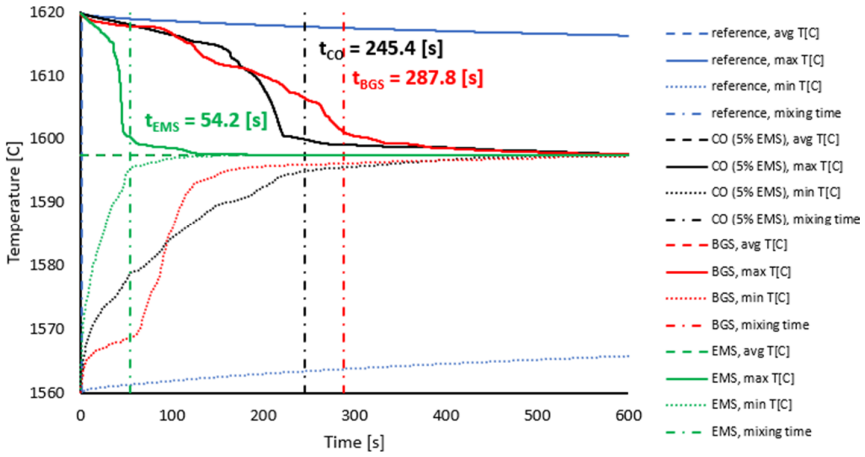


Figure 42. Temperature homogenization evolution.

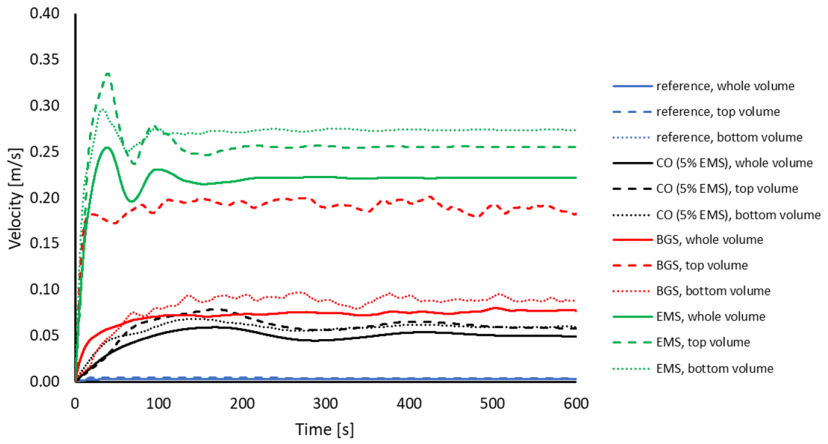


Figure 43. Velocity evolution.

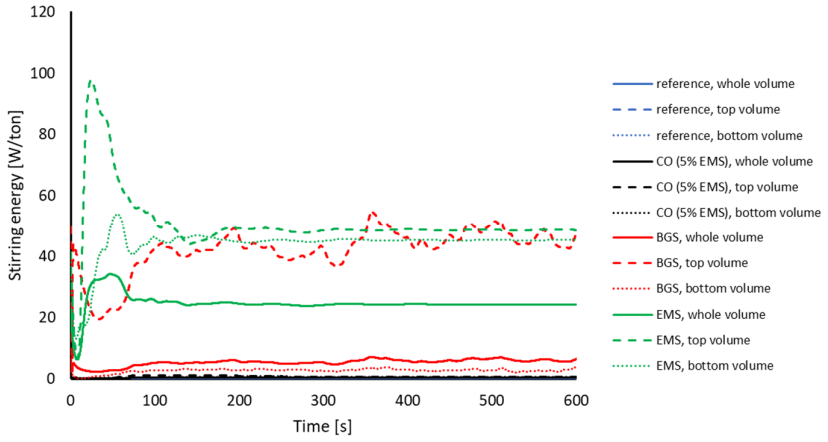


Figure 44. Stirring energy evolution.

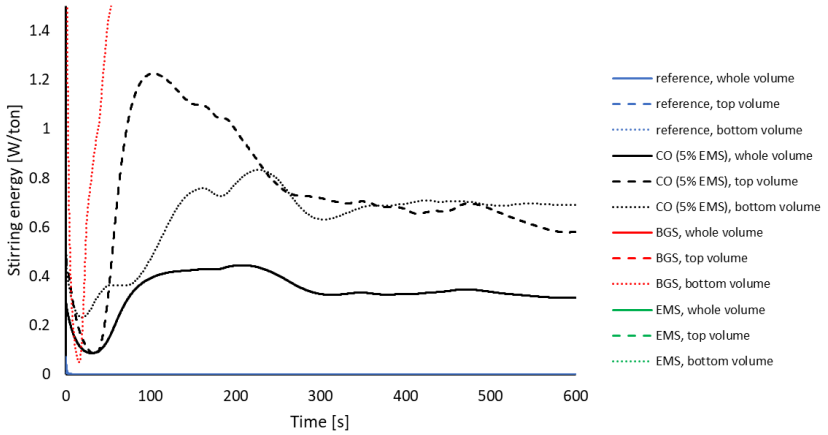


Figure 45. Stirring energy evolution for reference and CO mixing.

The results confirm the effectiveness of the EMS method, which is characterized by the shortest temperature homogenization time. These results can be directly related to the velocity and stirring energy distribution. When comparing velocity and stirring energy across various regions of the furnace, it is evident that the EMS method achieves the highest levels throughout the entire volume Moreover, the values that occurred in the selected regions located at the bottom and top of the furnace are also characterized by similar and high values. In the case of the BGS, this difference is significantly higher than in the case of EMS. For BGS, the highest values of the velocity are observed in the top area of the furnace, similar to the stirring energy, which is quite low in the rest of the furnace. The results show that BGS has a longer homogenization time like for CO bubbling, this is because the EBT top area is a big dead zone with BGS, and the argon bubbles are not able to mix the melt efficiently, so the number of plugs or the flow rate should be verified in the future. The CO mixing modelled by the 5% of EMS is characterized by low efficiency and homogenization time above 4 [min]. The reference case with only natural convection is inefficient, and the temperature homogenization time is longer than 10 [min].

Due to the limitations of one-phase modelling in the case of the BGS method and the need for more detailed simulations, an additional multiphase study focused solely on the evaluation of dead zones was performed and is presented in the next part of this work.

6.4 Dead zones evaluation for BGS – multiphase simulation

As mentioned, the multiphase simulation was additionally prepared to increase the prediction of the BGS model. Two separate analyses were conducted, one simulation without a slag layer and one with a slag layer, to understand its influence on the velocity field.

It is challenging to determine the optimal threshold of velocity that characterizes the occurrence of dead zones. Due to that, three different velocity limits were investigated: 0.02 [m/s], 0.03 [m/s] and 0.05 [m/s]. The graphical comparison of the simulation without slag and with slag is presented in Figure 46. The distribution of the dead zones is presented after 10 [min] when the flow was stabilized.

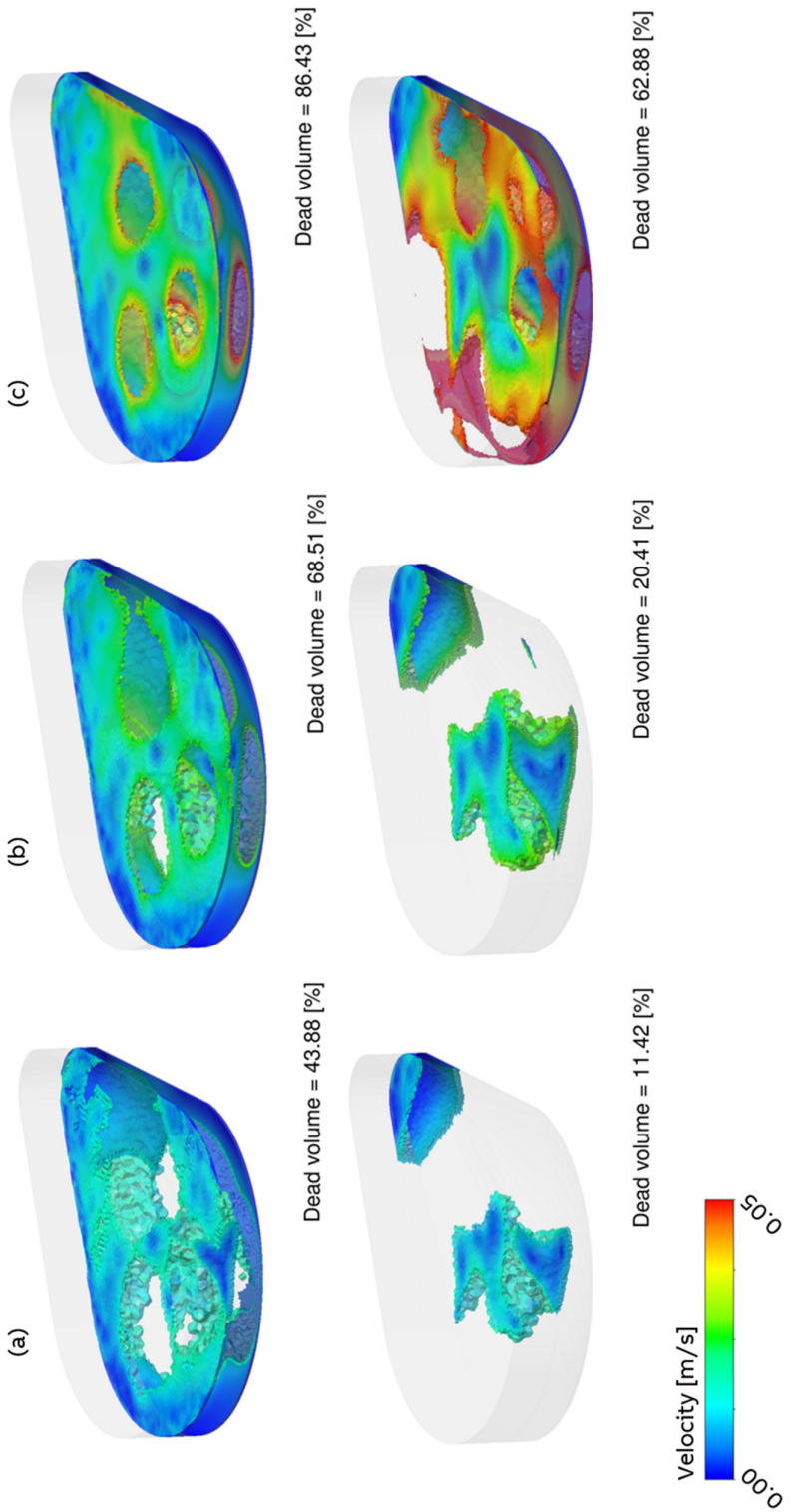


Figure 46. Dead zones for the model without slag layer (top) and with slag layer (bottom) for selected velocity limits: (a) under 0.02 [m/s], (b) under 0.03 [m/s] and (c) under 0.05 [m/s].

The initial evaluation of the dead zones clearly confirmed a significant difference between the simulation with and without the slag layer. To understand that difference, the evaluation of

the velocity distribution in time was also considered. The graphical interpretation is presented in Figure 47 for velocity and Figure 48 for stirring energy. Moreover, the velocity and stirring energy were measured over time, and the results are gathered in Figure 49 and Figure 50, respectively.

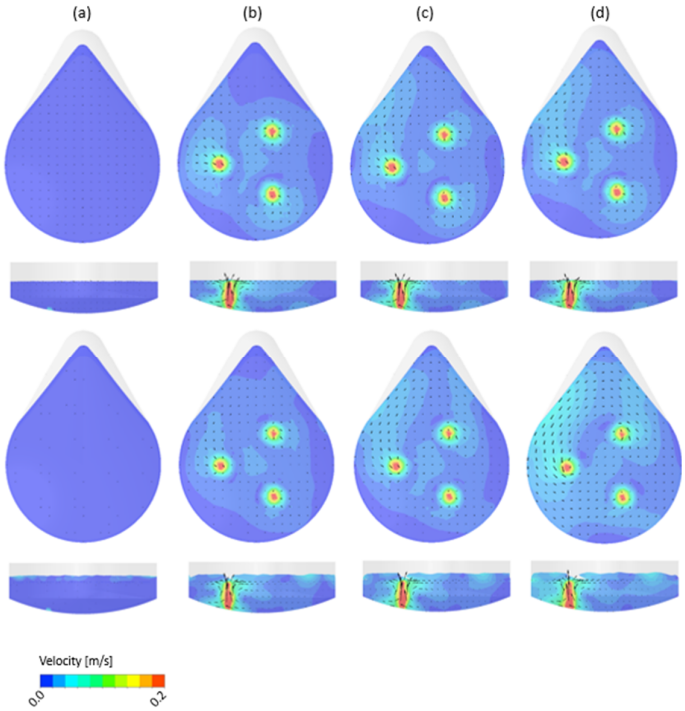


Figure 47. Velocity distribution for simulation without slag (top) and with slag (bottom). The velocity is presented in the middle horizontal and vertical cross-section of the melt in (a) starting point, (b) 50 [s], (c) 100 [s] and (d) 200 [s].

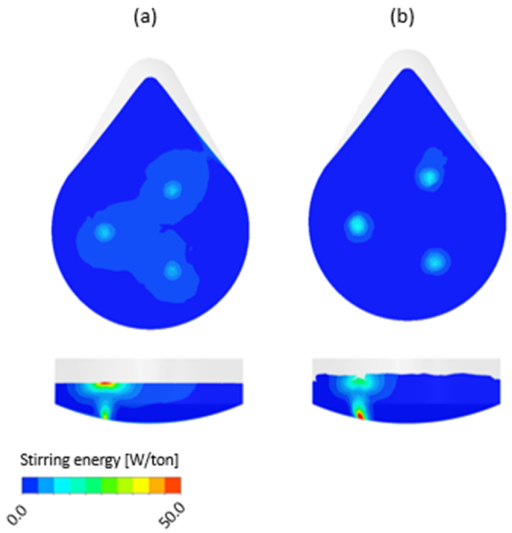


Figure 48. Stirring energy for simulation (a) without slag, (b) with slag after 600 [s].

The numerical investigations confirm the differences between the simulation with and without slag. The slag layer influences the behavior of steel quite significantly. It is well visible that higher velocity in the melt is present when the slag layer is considered. The stirring energy distribution also has a different character. In the simulation without slag, the highest values are observed in the top part of the melt, while in the case of the simulation with slag, the stirring energy in the top part of the melt is reduced.

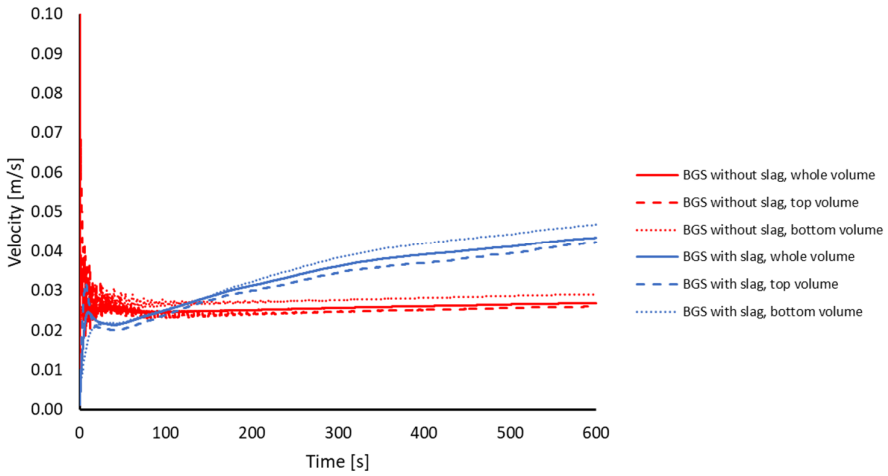


Figure 49. Velocity in time for BGS case without and with slag.

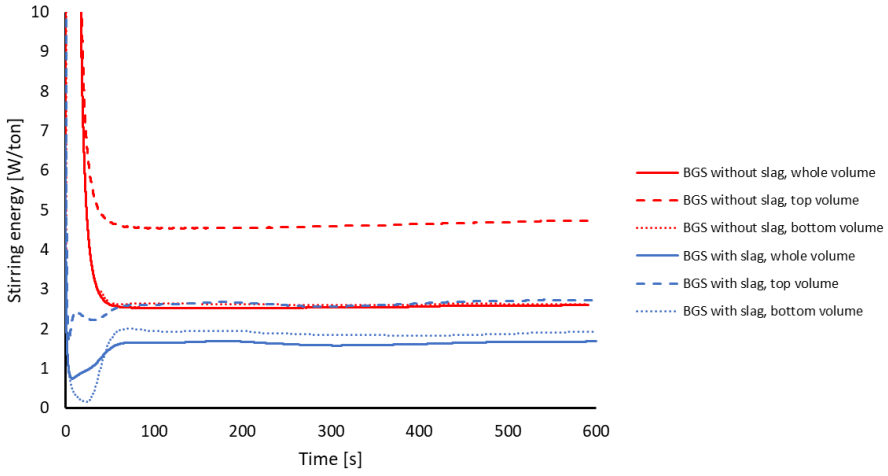


Figure 50. Stirring energy in time for BGS without and with slag.

The direct comparison of the time-averaged values over 100[s] of the process is presented in Figure 51 for velocity and Figure 52 for stirring energy.

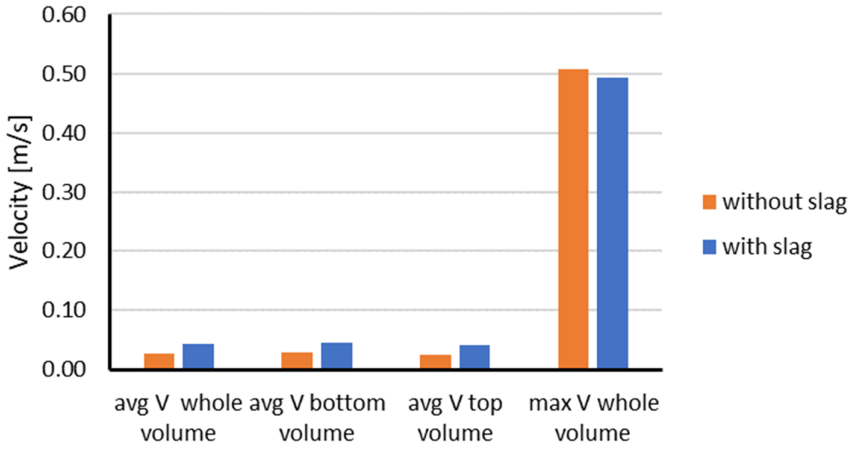


Figure 51. Time-averaged velocity for cases without and with slag.

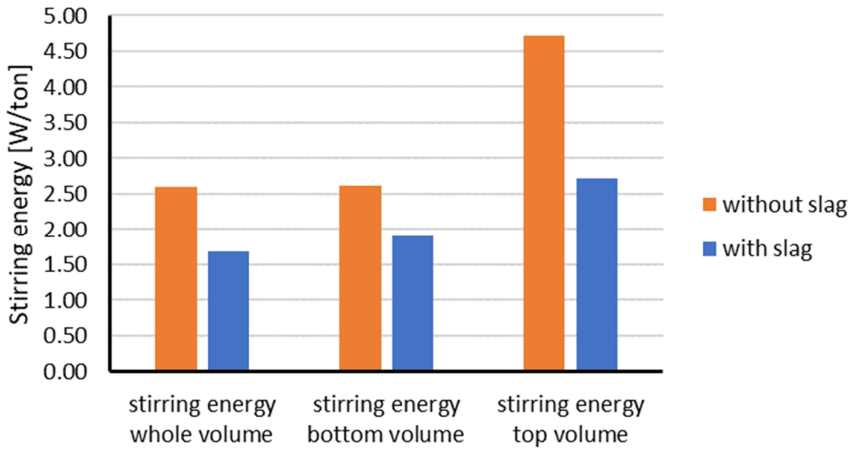


Figure 52. Time-averaged stirring energy for cases without and with slag.

The presented analysis confirms that the difference between the velocity distribution exists, but is not pronounced as much as for stirring energy. The introduction of the slag increases the accuracy of the model, but due to the elongated calculation time, this approach is difficult to implement in the case of industrial cases and still needs to be improved to be able to model the full homogenization, heating and scrap charging processes in reasonable calculation time. It should also be mentioned that this numerical model is under continuous development. The implementation of the multiphase model for homogenization simulation is ongoing, and the validation and comparison of the results are planned as future work.

6.5 Heating

A separate analysis was prepared for the heating process, where the heat from electrodes on the top is considered. During the simulation, the temperature, velocity and stirring energy were evaluated for particular stirring methods: the reference one with natural convection, CO mixing with a simplified approach with the assumption of 5% of EMS power, BGS and 100% EMS. A

detailed description of the boundary conditions used in this case is presented in Section 6.2.2. For all cases, the initial condition is the same to compare the effectiveness of the stirring. The primary objective is to achieve efficient flow and heat transfer from the electrodes to the melt within the furnace. The analysis serves as an initial investigation for a more detailed analysis of the scrap area, which will be considered as the next step. The temperature and velocity distribution are presented in Figure 53 and Figure 54, respectively.

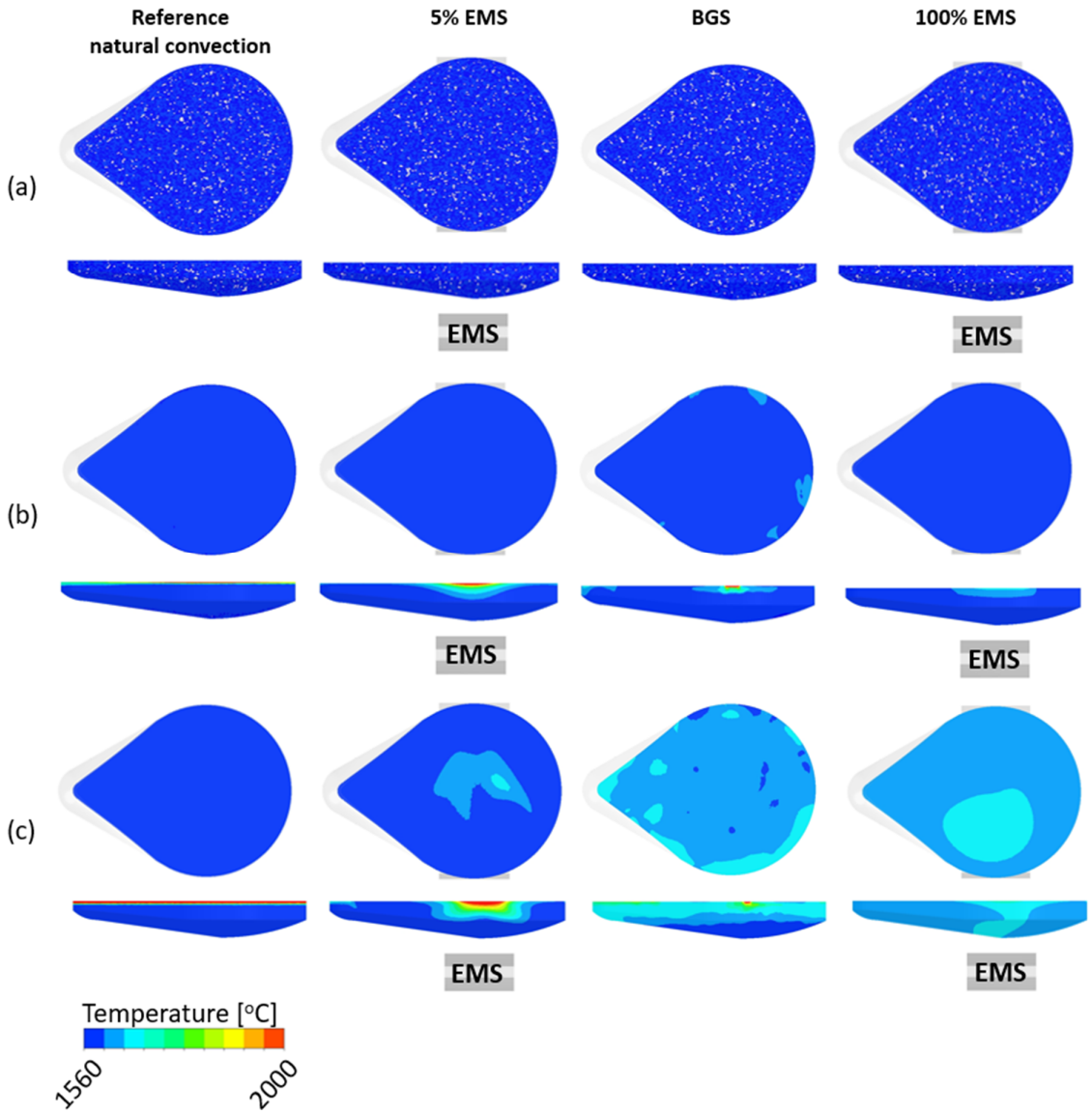


Figure 53. Temperature distribution in the middle cross-section (horizontally and vertically) of 160-ton furnace in (a) 0 [s], (b) 50 [s] and (c) 100 [s] for reference model, case with assumption of CO mixing (5% EMS), BGS and EMS.

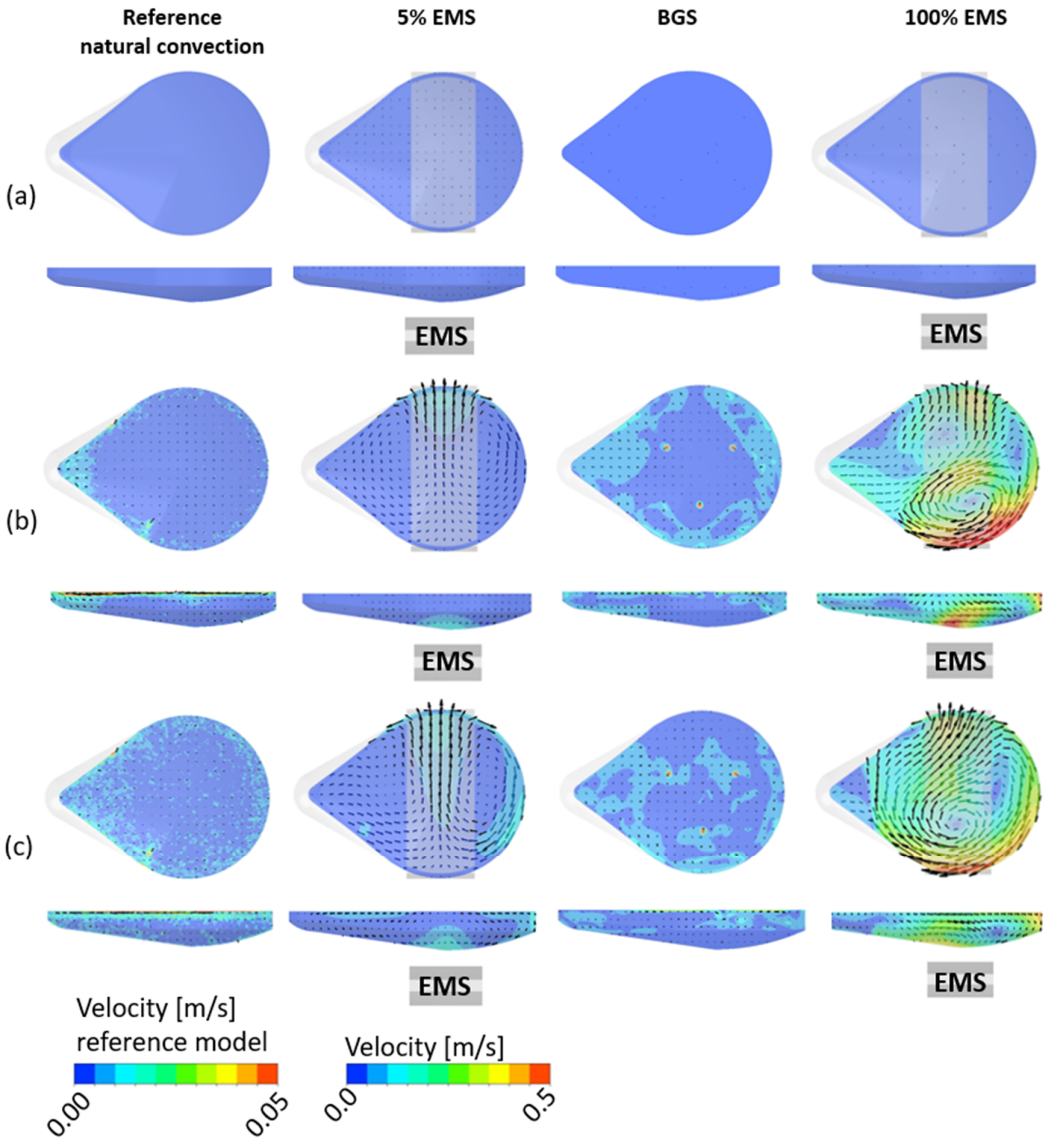


Figure 54. Velocity distribution in the middle cross-section (horizontally and vertically) of 160-ton furnace in (a) 0 [s], (b) 50 [s] and (c) 100 [s] for reference model, case with assumption of CO mixing (5% EMS), BGS and EMS.

As presented, in the case of natural convection, the highest temperature is in the top part of the furnace, and the heat transfer due to the convection is almost zero. Better heat exchange, but still with the highest temperature on the top area of the furnace is observed for CO bubbles stirring, which is reflected by 5% of EMS power. In the case of the gas stirring, the high-temperature areas are also visible close to the arc. Significant heat transfer is present for the case with 100% EMS, where the best mixing process has occurred. However, the temperature gradient is not as high as in the case of the gas stirring. This is directly related to the velocity and stirring energy distribution, with the highest values recorded in the case of EMS. This is clearly confirmed by Figure 55, Figure 56 and Figure 57, respectively. The reduced scale of the stirring energy for reference and CO mixing results is presented in Figure 58.

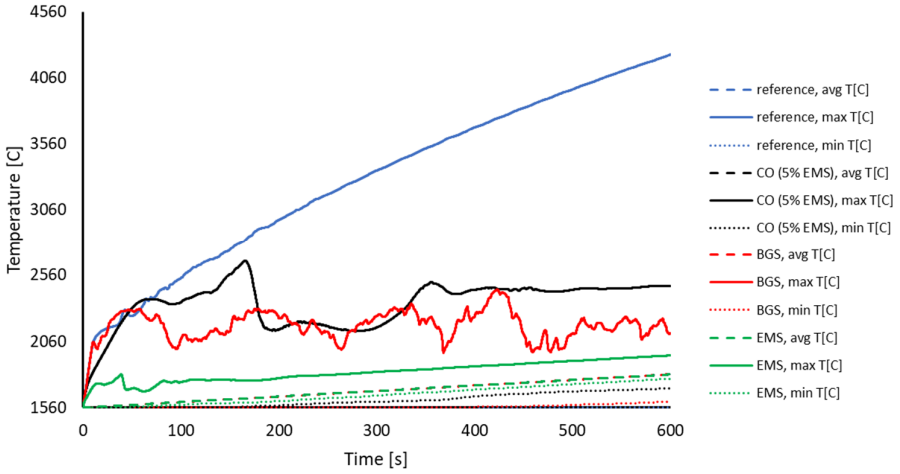


Figure 55. Temperature evolution during various stirring setups.

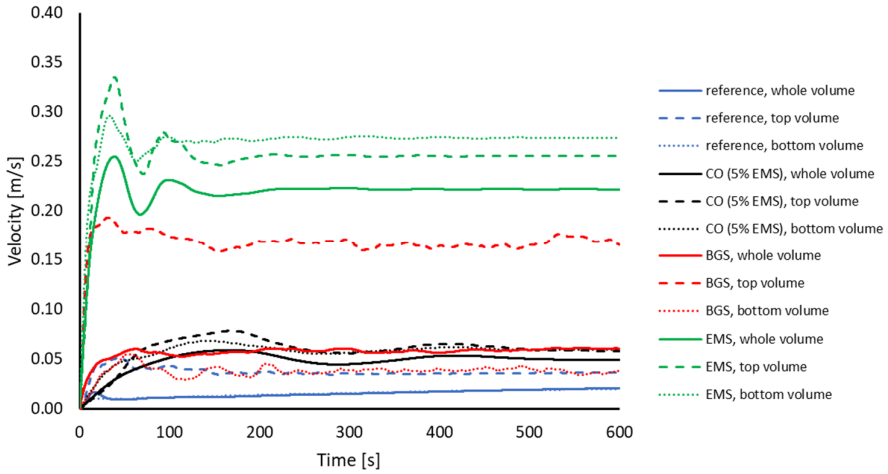


Figure 56. Velocity evolution during various stirring setups.

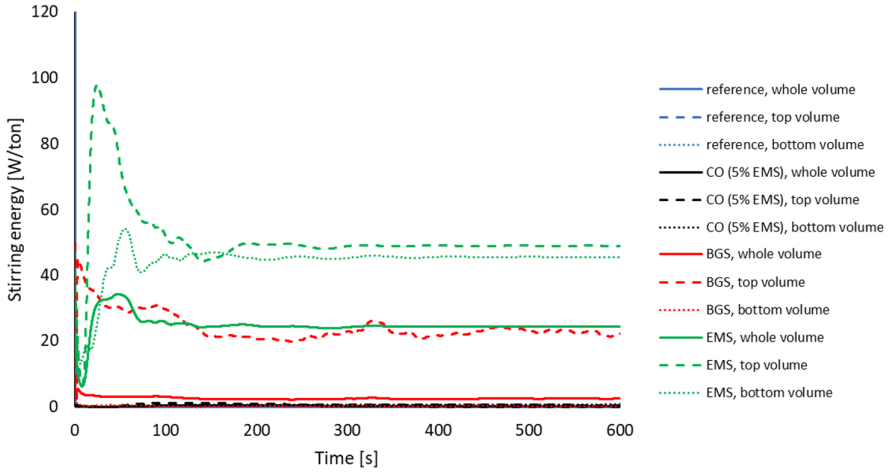


Figure 57. Stirring energy evolution during various stirring setups.

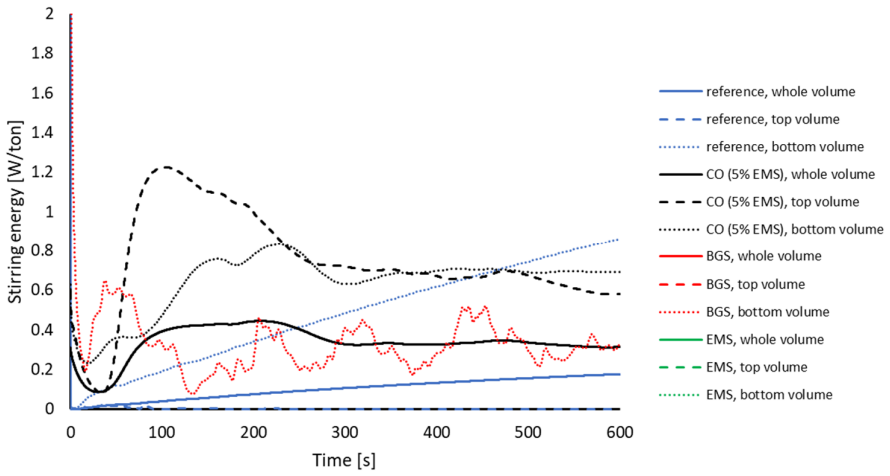


Figure 58. Stirring energy evolution during various stirring setups for reduced scale to be able to observe the reference and CO mixing results.

The temperature difference between the maximum and minimum values in the melt is the lowest for EMS, indicating that this stirring method effectively prevents uncontrolled temperature gradients. This difference is both the smallest and constant over time, ensuring greater control of the process. In the case of gas stirring, the maximum temperature fluctuates significantly, making temperature control difficult.

The biggest difference in the results of homogenization and heating processes in the case of the velocity and stirring energy is observed for the reference and CO mixing case, where the flow of the molten steel strongly depends on the temperature gradient.

A more detailed assessment of the benefits of EMS stirring will be presented during the model validation stage in Section 6.7.

6.6 Scrap charging

The scrap charging analysis was prepared according to the assumptions presented in Section 6.2.2. The analysis is executed only for EMS stirring to present the results for the most efficient solution. The scrap area is modelled as a porous zone, which is characterized by the lower temperature and velocity due to the high flow resistance of the scrap. The exact evaluation of the porosity is difficult to assess, and the assumption of 30% was taken into consideration to reflect the real case. The temperature (Figure 59), velocity (Figure 60) and stirring energy (Figure 61) distributions were investigated.

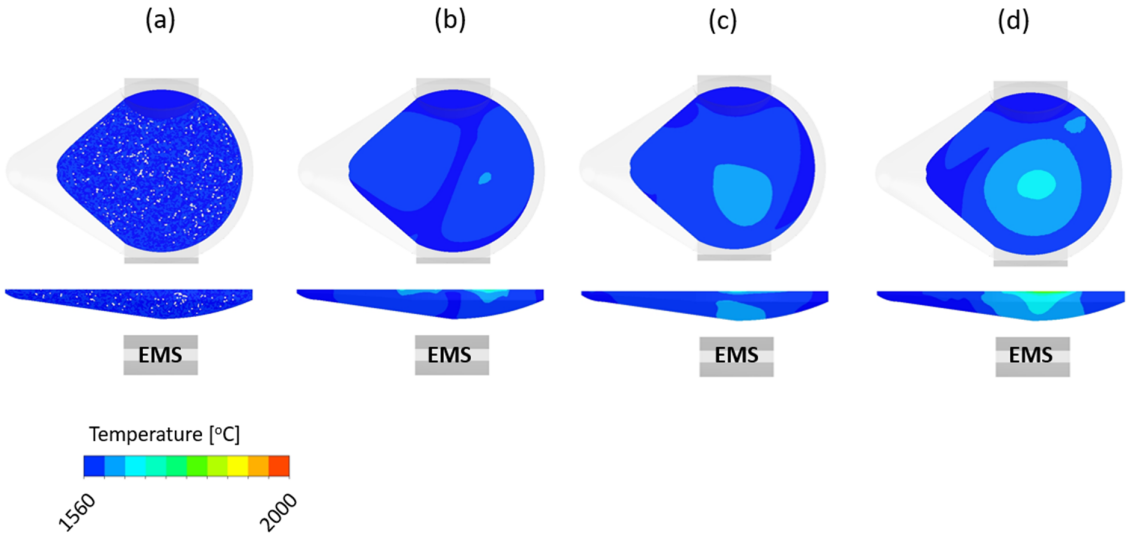


Figure 59. Temperature distribution for scrap charging process for a middle cross-section (top) and longitudinal cross-section (bottom) of 100-ton furnace in (a) 0 [s], (b) 50 [s], (c) 100 [s] and (d) 200 [s].

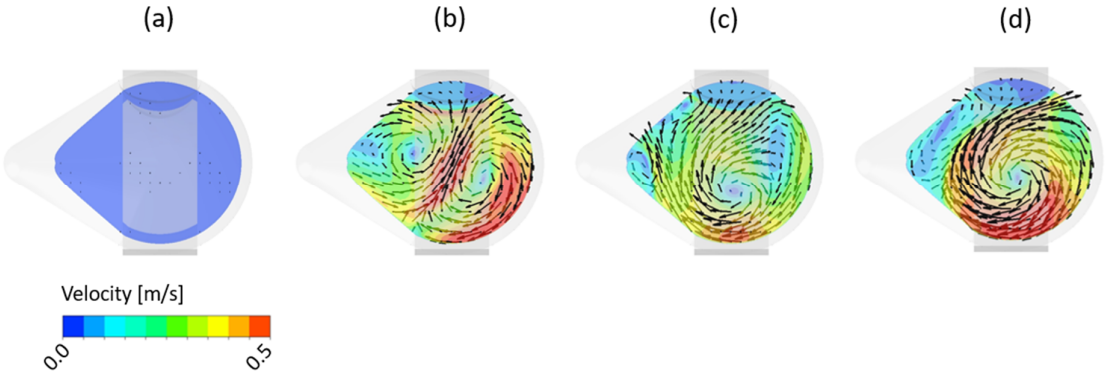


Figure 60. Velocity distribution for scrap charging process for a middle cross-section of 100-ton furnace in (a) 0 [s], (b) 50 [s], (c) 100 [s] and (d) 200 [s].

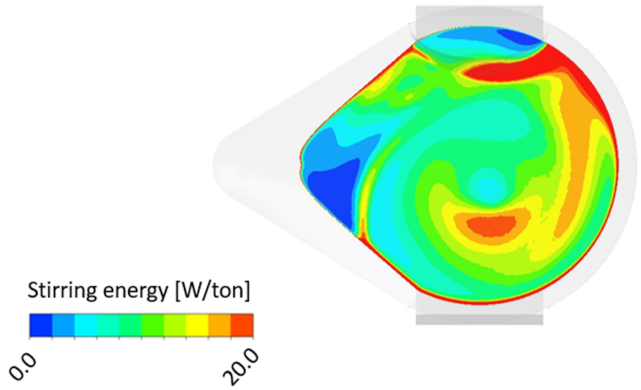


Figure 61. Stirring energy distribution for scrap charging process for a middle cross-section of 100-ton furnace at the time of 200 [s].

The scrap charging simulation enabled to confirm that the temperature is well distributed in the whole volume of the furnace.

The simulation of the scrap charging process is simplified and does not include the melting process itself, but based on the analysis of the results, it is confirmed that the simulation model is working correctly. The scrap area is characterized by lower temperatures during the whole simulation process. Moreover, that region is characterized by lower values of velocity due to its porosity. That region is also characterized by lower stirring energy, but on the border of the scrap, where the high-velocity gradients occur, the stirring energy is the highest.

6.7 Validation of the CFD results with EAF industrial data

EMS systems are more frequently applied to EAFs around the world. However, access to the industrial data is not an easy task. For the purpose of this research, data from a test plan in Italy with a 450-ton furnace were acquired. The simulation methodology was the same as that presented above for the smaller furnace[80].

The real test scenario on EAF includes data from one period with EMS off (3 days and 60 continuous heats) as a reference and one period with the EMS turned on (14 days and up to 300 heats). The data collected during these periods were used for model validation purposes.

The simulation was performed for two different scenarios, first for the full power of EMS (100%) and second for 5% of EMS power to reflect the non-stirred bath, with only natural stirring processes with CO mixing. Both scenarios included initial conditions with a bottom temperature of 1560 [°C] and a surface temperature of 1620 [°C]. The main goal of the simulation was to measure the homogenization time for both cases. The homogenization is the duration of the process until the difference between the maximum and minimum temperature in the bath is less than 5 [°C]. For the case with only 5% of EMS, the homogenization time in the simulation is equal to 477 [s], while for the case with 100% of EMS, the homogenization time in the simulation is equal to 113 [s]. These results confirm the high efficiency of EMS stirring at full power, for which the homogenization time is significantly shorter and requires only 24% of the time needed in the case of natural stirring[99].

The additional explanation requires the assumption of the 5% of EMS to reflect the natural stirring (mainly CO bubbles mixing) effect. This factor was proved based on another experiment, where the copper tracer was introduced into the 90-ton EBT furnace. These tests were conducted at Steel Dynamics, Inc. (SDI), Roanoke, VA, USA, and the main goal was to confirm the efficiency of the EMS stirring[77]. The tests proved, that the mixing time of the copper tracer is equal to 62 [s] with EMS versus 260 [s] without EMS. That result means that the mixing time with EMS power on required only 24% of the mixing time with EMS power off. The results are consistent with the numerical model with 100% versus 5% of EMS power. Based on the prior experience, the assumption that 5% EMS power can effectively replicate the behavior of natural stirring is supported[104,108].

To compare the simulation results with experimental ones, the temperature was measured twice in the same location (before tapping). The first measurement was recorded directly after switching off the arc (T_1), and the second was done 30 [s] later (T_2). The measurements were repeated 30 times to obtain reliable statistical data. The average measured absolute temperature difference as [ABS(T_1-T_2)] was 9 [°C] with EMS power on, while it was 24 [°C] with EMS switched off. It is worth mentioning that temperature measurements at only one point provide limited information, and a higher temperature difference may be expected in the case without EMS stirring if measured in other locations. Unfortunately, the real tests are difficult to conduct, and the measurement results were very limited[99].

A similar comparison was made in the case of the heating process. In the simulation, the initial melt temperature is equal to 1560 [°C] and the temperature distribution on the bath surface and the temperature gradient between the top surface and the bottom of the furnace were observed. It was demonstrated that the increase in EMS power reduced the temperature gradient between the top and bottom parts of the furnace, ensuring better efficiency of the heating process.

During the experimental measurements, the tapping temperature was measured. In the case of the EMS stirring, the tapping temperature was reduced by 18 [°C]. After the tapping process, the temperature decreased from the EAF to the LF, reaching 48 [°C] with EMS and 65 [°C] without EMS, which confirms that the temperature drop is 17 [°C] lower with EMS than without the EMS solution. This is very important because the decrease in temperature leads to a reduction in the final oxygen content and an improvement in the quality of the molten steel[99].

A great benefit is observed in the case of the scrap melting processes due to the fact that the velocity with EMS increases 10 times in comparison to the case with natural processes[230]. The furnace process time is reduced, resulting in a reduction of heat losses during its operation. The real-world tests confirm that the energy reduction for the EMS solution is approximately 3.6%. Due to the reduced energy consumption and reduced superheat of the surface bath, the electrode consumption is lower by about 3.3%[99].

The conducted experimental tests confirmed that all the assumptions from the simulation were achieved in reality.

6.8 Development of the new stirrer (Donut-shaped stirrer)

The continuous development of EAF processes requires the search for new technologies to increase the efficiency of the stirring process. Therefore, based on the developed numerical model, a new type of EMS stirrer for EAF was proposed within the thesis. The new design of the electromagnetic stirrer does not include the classical linear direction of the stirring, but the donut-shaped stirrer, as presented in Figure 62. Such a device can generate an electromagnetic field that forces the rotational flow of the molten steel inside the furnace.

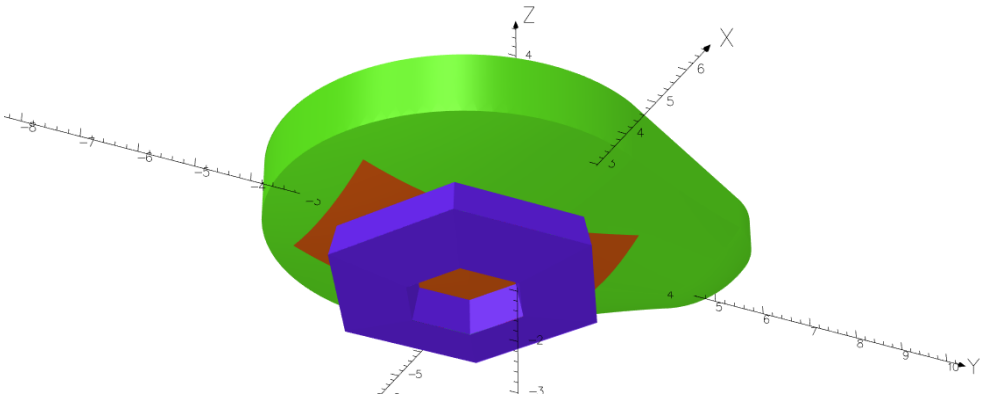


Figure 62. New technology with donut-shaped EMS device.

The process parameters for the new concept of a donut-shaped stirrer are presented in Table 16.

Table 16. Process parameters for EMS donut-shaped stirrer for EAF.

Donut-shaped stirrer	
Active power [kW]	91.6
Current [A]	650.0
Frequency [Hz]	0.6
Weight [ton]	20
Distance stirrer – furnace bottom [mm]	50

The homogenization process is realized for the 160-ton furnace and with the assumption of the initial temperature, as shown earlier in Figure 33. The velocity distribution in molten steel obtained during the active EMS system is presented in Figure 63, and the temperature homogenization over time is shown in Figure 64.

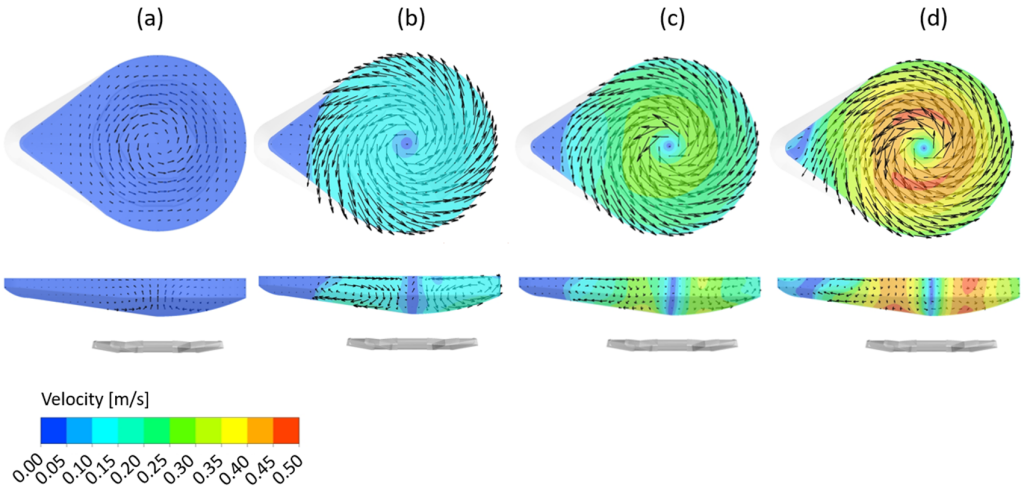


Figure 63. Velocity distribution for middle cross-section (top) and longitudinal cross-section (bottom) of 160-ton furnace in (a) 0 [s], (b) 50 [s], (c) 100 [s] and (d) 200 [s].

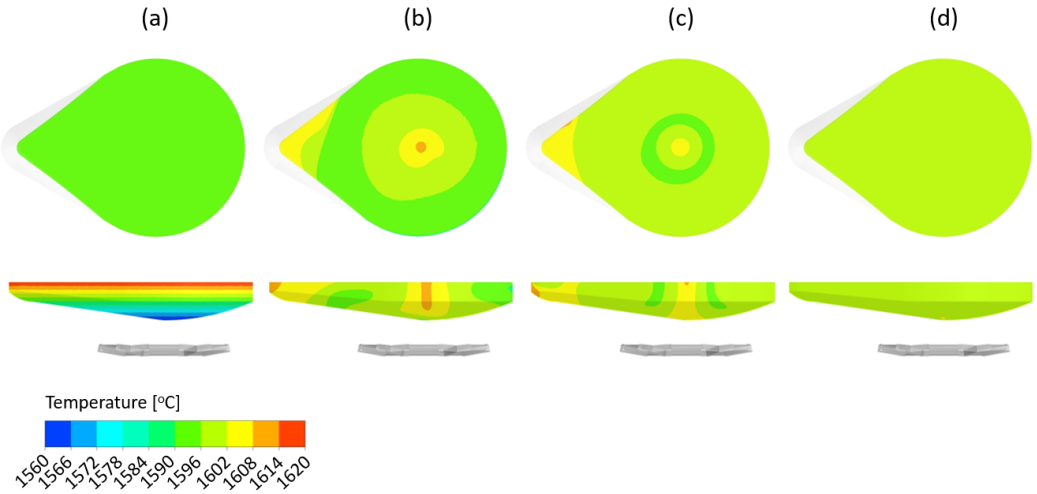


Figure 64. Temperature homogenization for middle cross-section (top) and longitudinal cross-section (bottom) of 160-ton furnace in (a) 0 [s], (b) 50 [s], (c) 100 [s] and (d) 200 [s].

In the second simulation case study, heating was achieved by applying a total active power of 70 [MW], where 38.5 [MW] was applied as convection and 14 [MW] as radiation heat transfer from the electrodes to the melt. The rest of the power is treated as heat losses to the walls and roof of the furnace. The temperature distribution in time during the heating process with an active donut-shaped stirrer is presented in Figure 65.

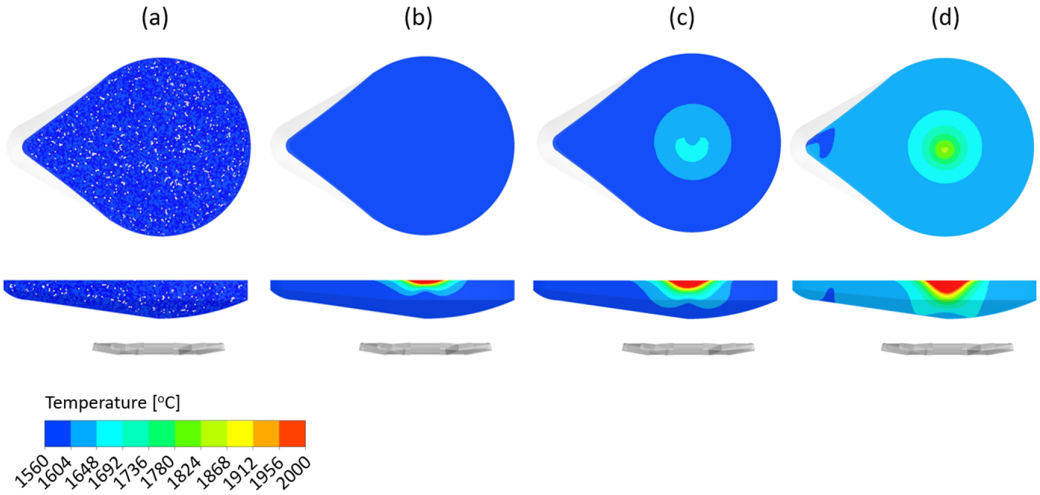


Figure 65. Temperature distribution for heating process for middle cross-section (top) and longitudinal cross-section (bottom) of 160-ton furnace in (a) 0 [s], (b) 50 [s], (c) 100 [s] and (d) 200 [s].

Finally, the scrap charging process simulation included the additional domain of the scrap area realized by the porous domain. This simulation couples scrap charging with additional heating due to active electrodes. The temperature distribution is presented in Figure 66. Moreover, in that case, the velocity and its dependence on the stirring energy can be

investigated, as seen in Figure 67. What is very interesting is the fact that the scrap zone can be clearly visible, and lower values of velocity and stirring energy in that region are observed.

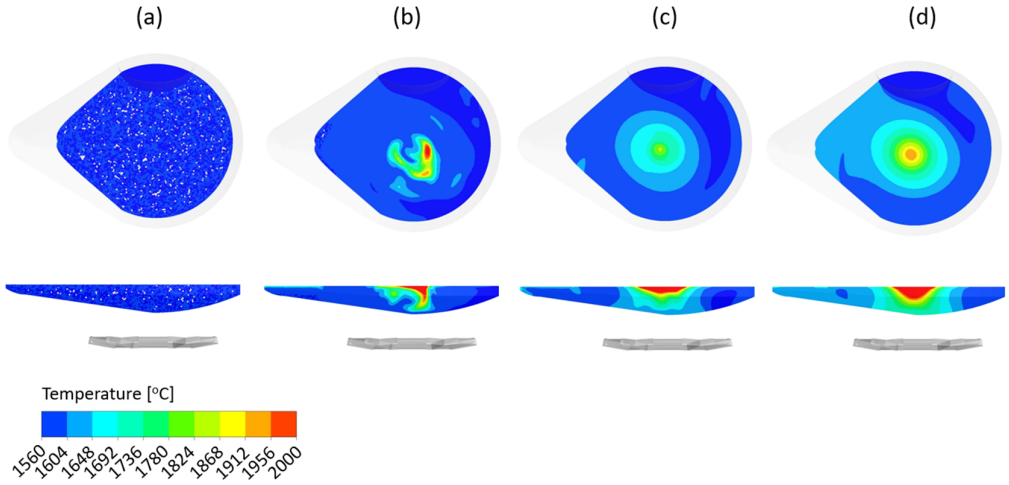


Figure 66. Temperature distribution for scrap charging process for middle cross-section (top) and longitudinal cross-section (bottom) of 100-ton furnace in (a) 0 [s], (b) 50 [s], (c) 100 [s] and (d) 200 [s].

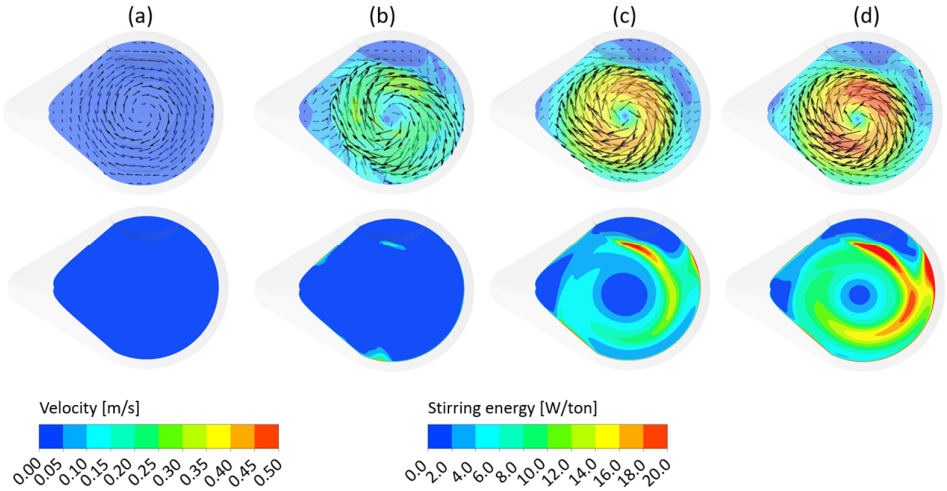


Figure 67. Velocity (top) and stirring energy (bottom) distribution for scrap charging process for middle cross-section of 100-ton furnace in (a) 0 [s], (b) 50 [s], (c) 100 [s] and (d) 200 [s].

The simulation results confirm that the EMS system is more efficient than BGS. The evaluation of the dead zones showed that the BGS is characterized by prominent regions where the velocity is below the threshold. It can directly influence the efficiency of the processes inside the molten steel. The EMS temperature homogenization time is over 5 times shorter than in the case of BGS. Moreover, the heating simulation confirms that the temperature gradients are smaller and that temperature distribution is more uniform in the case of EMS stirring. The simulation of scrap charging demonstrated the beneficial behavior of heated steel, which can easily penetrate the scrap area, thereby increasing the efficiency of melting and accelerating

steel production. Moreover, the BGS is characterized by a quite short lifetime of the porous plugs and often failures due to the direct contact of the plug with the molten steel, which is not an issue in the case of the EMS.

The proposed new type of EMS device is characterized by a totally different character of the flow, where the heated steel penetrates the scrap area but under another angle. Moreover, during the heating process, the heat is concentrated in the center of the furnace, close to the scrap area, which can be beneficial in the case of the melting process. Due to the rotational flow, the temperature homogenization time can be extended, but on the other hand, the flow pattern enables full control of the processes due to its stability. The stable flow pattern with the stagnant velocity in the center of the vortex can be beneficial in the case of increased use of direct reduced iron (DRI) in the EAF processes to control decarbonization, but the process must be investigated more in the future. Moreover, it is worth mentioning that the power of the donut-shaped stirrer is less than the standard linear stirrer with the same ranges of velocity, furthermore, the power of the EMS system can be freely modified during the process and include the stages with or without the EMS power. The flow direction can be easily changed during the process to increase the mixing efficiency. However, due to the high turbulences during this process, the proper balance between the effectiveness of the stirring and power consumption must be calculated.

To summarize, it was demonstrated that the proposed solution with EMS stirring has the potential to successfully replace the blast furnace and introduce additional online control of the processes in the EAF in the future.

7. Development of the robust CFD simulation of the ladle furnace (LF)

7.1 Motivation for CFD simulations in LF

As mentioned in Chapter 2, a technological step involving the ladle furnace is between the electric arc furnace and the tundish. The primary role of the LF is to transport the liquid steel to the continuous casting step. However, LF is also used to improve mixing inside the steel to increase the efficiency of the reduction of non-metallic inclusions. In general, it is assumed that the LF is responsible for the reduction of non-metallic inclusions from the melt [78,231,232]. The high turbulent energy inside the bath enhances and accelerates the inclusion removal process, thanks to additional collisions and subsequent absorption into the slag layer and vessel walls. Moreover, an intense mixing process increases the collision rate between small inclusions, leading to their agglomeration.

Most of the research[111–113,144,145,224,233–244] is focused on gas stirring applications as the most popular method for increasing the mixing phenomena inside the ladle. The researchers focus on the phenomena related to the slag layer formation and the influence of the mass flow rate and the number of gas plugs on the open-eye area formation. From the available literature[111,112,144,224,245] and industrial practice, it is known that the gas stirring, which is realized by the argon, generates high turbulences in the top part of the ladle furnace, between the metal and slag layer interface. This behavior leads to the occurrence of the open eye and increased oxidizing conditions, which can create non-metallic inclusions from atmospheric oxygen and nitrogen. The occurrence of the open eye leads to additional and uncontrolled heat losses, which is a considerable disadvantage. Also, the stagnant velocity close to the bottom of the furnace is typical. In the top part of the ladle furnace, high turbulences are observed, which influence the oscillations of the free surface. The character of the oscillations is random and generates unstable flow behavior. These factors are the driving forces for the development of EMS stirring systems[78].

The EMS systems in the ladle furnace can be used to increase the efficiency of the mixing[78,245–247]. However, the industrial solutions are based on vertical stirring for both upward and downward directions[245]. The goal of such stirring is to increase the efficiency of the homogenization of the temperature and chemical structure and reduce the inclusions by adhesion to the ladle walls or slag layer. As mentioned, the ladle furnace is responsible for the largest reduction of the inclusions from the melt. Often, stirring is also achieved by combining gas and EMS methods, known as the EMGAS approach.

Therefore, mixing in the ladle furnace is realized by gas stirring (GAS), electromagnetic stirring (EMS) or a combination of both approaches (EMGAS). It is confirmed that the EMGAS method, which includes gas and EMS stirring, gives excellent results in the purification of the steel. Moreover, the solutions with the EMS system enable the control of the molten steel velocity thanks to the wide range of electrical current conditions, which can be applied to the EMS device. The velocity distribution inside the ladle furnace generated by the EMS influences

the shape of the gas plume, reactions between the slag and molten steel, the stirring energy in the vessel, and the mixing time. The advantage in the desulphurization rate is around 20-30% for the EMGAS approach in comparison to the gas stirring alone[78]. The selection of stirring methods depends on the characteristics of the production line and the type of vessel, and should be tailored individually.

As mentioned, a recent increase in requirements for environmental safety and high-quality of the final steel products caused the continuous development of proposed solutions to increase the efficiency of production, control the steel composition and save energy to reduce atmospheric pollution such as carbon dioxide emission. This motivates the search for better solutions, also for more effective EMS stirring. Often, the results are not obvious, and only the combination of different stirring methods gives the best results. They should be tested for each device and process parameters to achieve the goals of the steel plants related to green steel technology.

Therefore, to combine the high quality of the steel with environmental safety, the new horizontal electromagnetic stirrer was designed within the thesis with the developed CFD model to obtain better efficiency of the process compared to the known vertical stirring treated as a benchmark case. Moreover, the approach was also used in conjunction with an additional well-known method of gas stirring for a comprehensive comparison of the proposed solution's capabilities.

7.2 Description of the model

7.2.1 Geometry

An industrial scale ladle furnace was selected to investigate the differences in the effectiveness of stirring by the EMS, gas, and a combination of both, the EMGAS. The geometry of the 160-ton industrial ladle furnace with a standard vertical EMS system is presented in Figure 68.

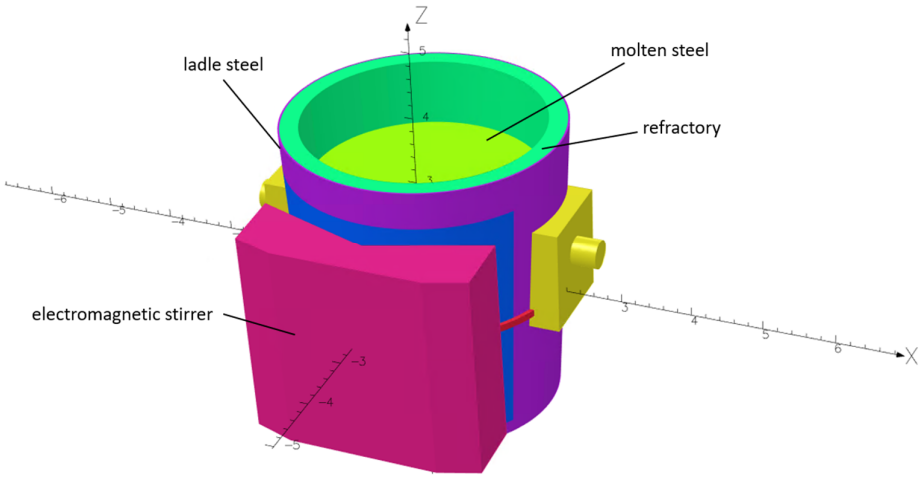


Figure 68. Geometry of 160-ton industrial ladle furnace with EMS system.

As mentioned, gas and EMGAS stirring will also be taken into consideration in this part of the research. The corresponding scheme of the ladle furnace geometry with argon gas plugs is presented in Figure 69.

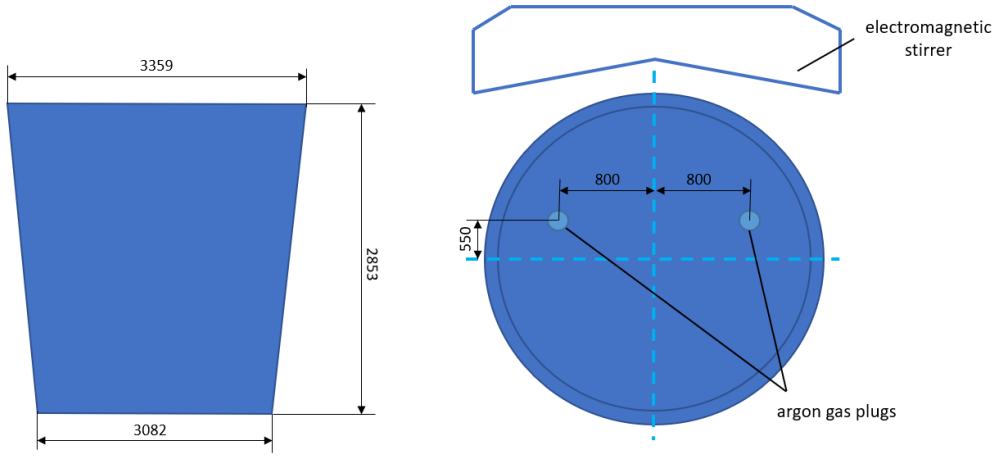


Figure 69. Scheme of the ladle furnace geometry with EMS system and additional argon gas plugs.

For more detailed investigations, the melt domain was divided into subregions in the ladle's bottom, middle, and top parts to measure variables of interest, such as velocity or stirring energy, in different parts of the furnace. Each subregion is 100 [mm] long.

7.2.2 Boundary and initial conditions

In general, the boundary conditions for an industrial ladle furnace with an EMS system are the same as for experimental validation presented in Chapter 5 for both one-phase and multiphase approaches. Therefore, this part focuses on the definition of boundary conditions for gas stirring, where the argon flow rate is applied. The flow rate is presented in normal conditions and must be recalculated to obtain proper values like mass flow rate and velocity for argon properties in working conditions.

In the case of the gas stirring and EMGAS approach, the argon flow rate is considered as 30 [Nl/min] for both active plugs. Other scenarios focused on the influence of different flow rates or positions of plugs were not considered at this stage and will be the goal of future investigations.

The initial condition is related to the definition of the phases in the case of the multiphase approach. Two Eulerian phases are defined in the VOF multiphase mode: molten steel as the primary phase and air as the secondary phase.

The melt height is equal to 2.85 [m], followed by the air phase, as presented in Figure 70. The initial melt velocity is set to 0.

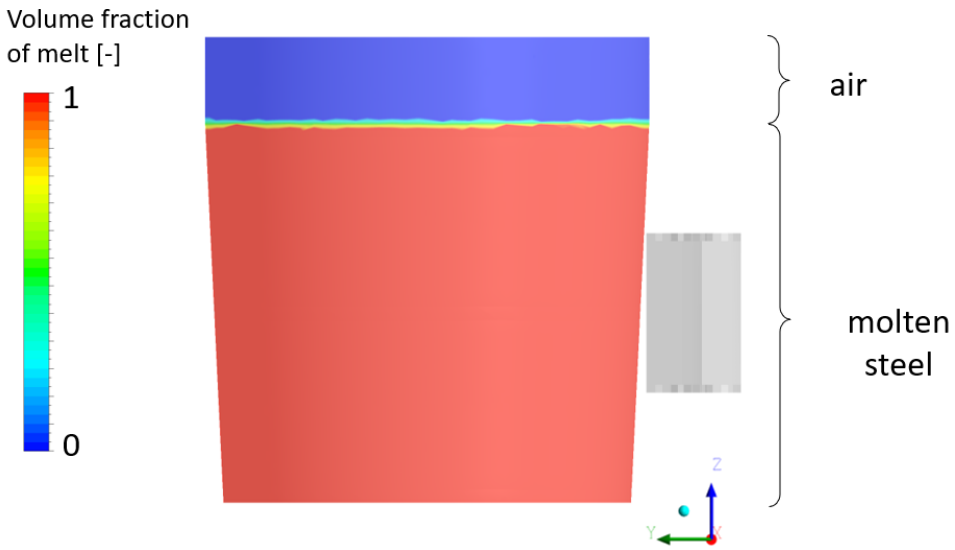


Figure 70. Initial conditions for the developed multiphase model of the ladle furnace.

The research considered two different directions of EMS stirring: vertical and horizontal. The horizontal stirring is a new concept of the device investigated within the thesis, while the vertical commercial solution is used as a benchmark case. The process parameters of each stirrer are presented in Table 17.

Table 17. Process parameters for vertical and horizontal EMS stirrer, respectively.

	ORT1215	**New concept of stirrer**
Active power [kW]	338.7	358.5
Current [A]	1350.0	1200.0
Frequency [Hz]	1.1	1.0
Weight [ton]	18	7.5
Distance stirrer – furnace bottom [mm]	25	60

7.2.3 Material properties

For the industrial case of the ladle furnace, the melt was considered as an incompressible, viscous molten steel. The argon is modeled with the ideal gas assumption with one exception. In the simulation, energy is not considered, and argon density depends on the pressure occurring in the ladle due to gravity and the modeling of hydrostatic pressure. The main materials' properties are gathered in Table 18.

Table 18. Material properties used for CFD simulation of the ladle furnace.

Material properties	
Melt density [kg/m^3]	6900
Melt viscosity [kg/(m s)]	0.0069
Argon density [kg/m^3] (normal temperature)	1.6228
Argon viscosity [kg/(m s)]	2.125 x 10^{-5}
Air density [kg/m^3] (normal temperature)	1.225
Air viscosity [kg/(m s)]	1.7894 x 10^{-5}

7.2.4 Mesh sensitivity study

As the main goal is to investigate the new type of horizontal EMS stirrer, this model was selected as a case study for mesh sensitivity analysis.

The model was again meshed in Ansys Fluent Mesher software with the polyhedral volume finite elements. The first analysis was conducted using a simplified transient approach with a one-phase model. The graphical comparison between the three generated meshes is presented in Figure 71. Moreover, the summary of the number of elements for particular meshes is presented in Table 19.

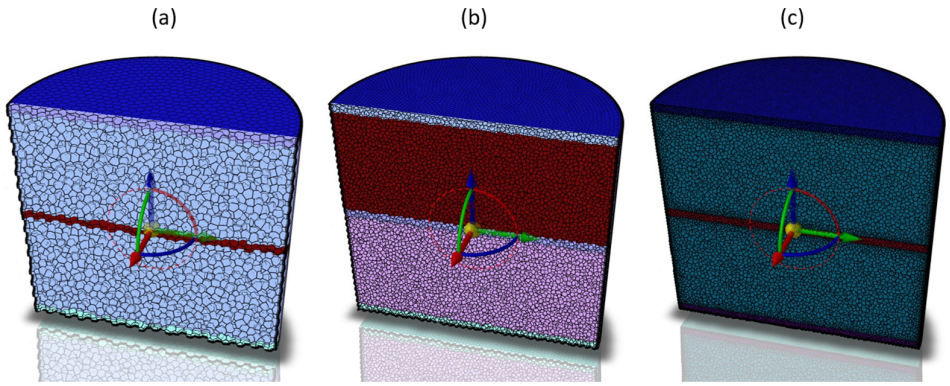


Figure 71. Three different meshes for transient simulation with a one-phase approach for a ladle furnace with horizontal EMS: (a) coarse, (b) medium, (c) fine.

Table 19. Number of finite volume elements for each one-phase model of LF's mesh for mesh sensitivity study.

Mesh	Number of elements
coarse	87 117
medium	441 539
fine	1 252 539

During the mesh sensitivity study, the average value of the velocity and stirring energy were measured in selected regions located in the furnace's bottom, middle, and top parts and in the whole melt domain. The comparison of results is presented in Figure 72 and Figure 73, respectively.

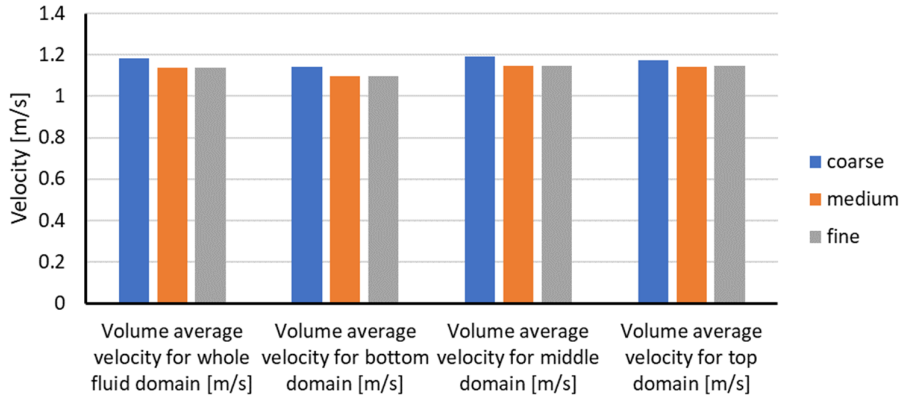


Figure 72. Volume average velocity for the whole melt, bottom, middle and top region of the LF for three different meshes.

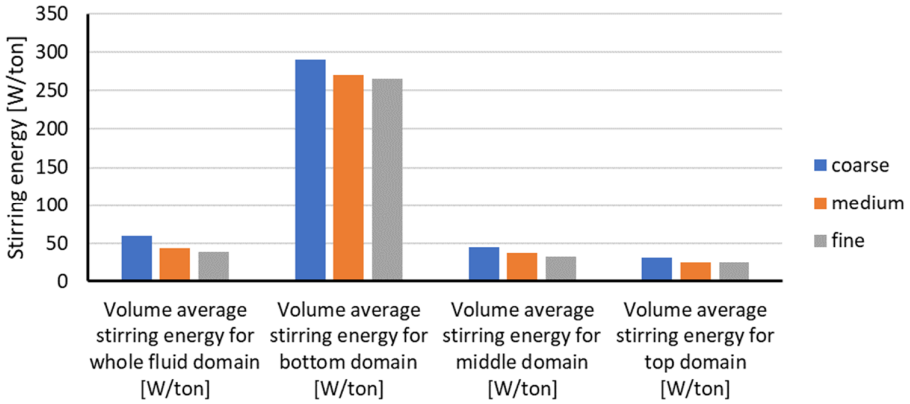


Figure 73. Volume average stirring energy for the whole melt, bottom, middle and top region of the LF for three different meshes.

As presented, the difference between the fine and medium mesh is significantly lower than between the coarse and medium mesh. In the case of the velocity, the maximum relative error between the medium and fine mesh is equal to 0.5%. This relative error is higher but not more than 12% for the stirring energy in the middle region. The difference is related to the influence of the mesh size close to the inflation layer and the relation to the turbulence modelling, but nevertheless, the difference is still on acceptable low level. Therefore, the medium mesh was used for further investigations to avoid the longer calculation time.

To complete the mesh sensitivity study, the more complex transient multiphase model with the EMS was evaluated next. It should be mentioned that the EMS power was reduced in this case to avoid significant average velocity values exceeding 1 [m/s], as observed in Figure 72 and to obtain the average value comparable to the existing solution: vertical stirring treated as a benchmark case. As in the previous research for transient, one-phase simulation, three different polyhedral meshes were generated in Ansys Fluent Mesher software. The graphical comparison is presented in Figure 74, and then the number of elements for particular meshes is gathered in Table 20.

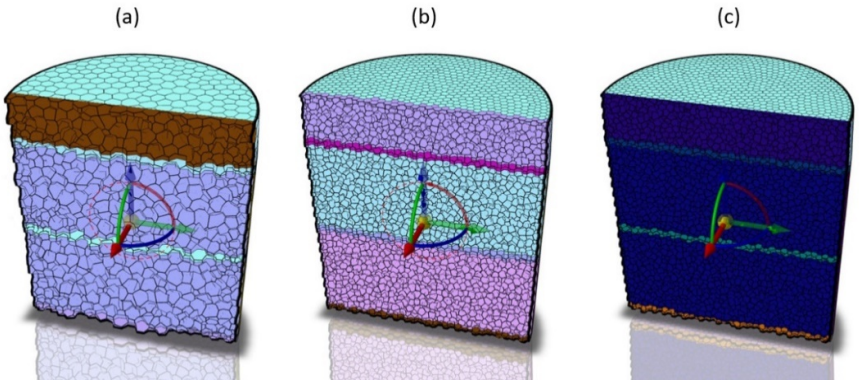


Figure 74. Three different meshes for transient simulation with a multiphase model for a ladle furnace with horizontal EMS: (a) coarse, (b) medium, (c) fine.

Table 20. Number of finite volume elements for each multiphase model of LF's mesh from mesh sensitivity study.

Mesh	Number of elements
coarse	49 847
medium	104 012
fine	117 785

In general, it is worth mentioning that even with the extended geometry of the multiphase model, the number of elements is lower than in the one-phase model. It is directly related to the Courant number for the time-dependent VOF approach. To obtain a stable solution, the characteristic size of a cell should be increased to decrease the Courant number without decreasing the time step[136].

Calculated volume average velocity and stirring energy in selected areas are compared between meshes in Figure 75 and Figure 76, respectively.

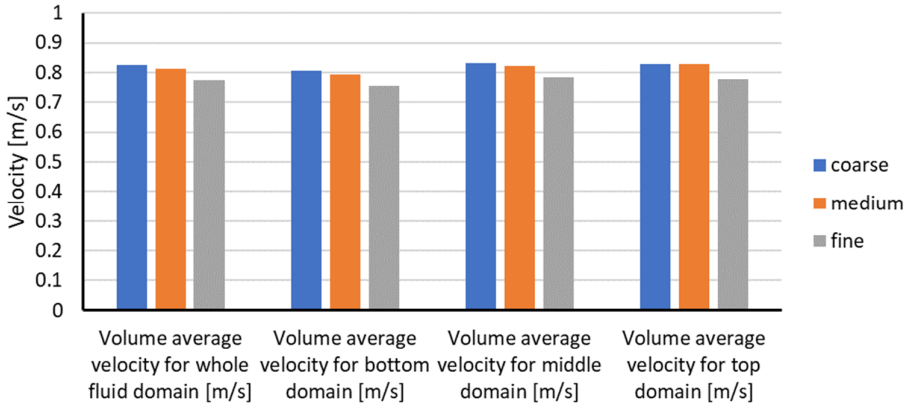


Figure 75. Volume average velocity for the whole melt, bottom, middle and top region of the LF for three different meshes.

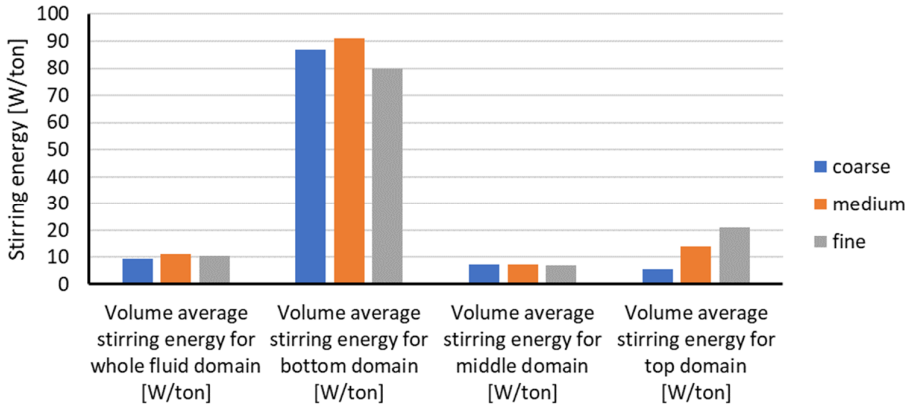


Figure 76. Volume average stirring energy for the whole melt, bottom, middle and top region of the LF for three different meshes.

The analysis confirms that the difference between the coarse, medium and fine mesh is not significant. Regarding the velocity, the maximum error between medium and coarse/fine meshes does not exceed 6%. For the stirring energy, the error is lower than 14%. One exception is related to the stirring energy measured for the top domain of the LF. This error is significant, up to 60%. However, this volume is irrelevant due to the occurrence of the oscillations of the free surface of the melt, which is characteristic of multiphase simulations. Proper measurement of that value is difficult. Finally, based on this investigation, the medium mesh will be used for further simulations.

7.3 Single-phase and multiphase simulations

Since horizontal stirring is a new design of the EMS stirrer, a simplified single-phase simulation of the EMS system was used during initial investigations. The simulation aimed to determine the optimal EMS parameters for effective stirring. The first simulation case included the same EMS parameters as in the vertical system. The comparison between volume average velocity measured in the whole domain of the ladle furnace for different values of EMS power is presented in Figure 77.

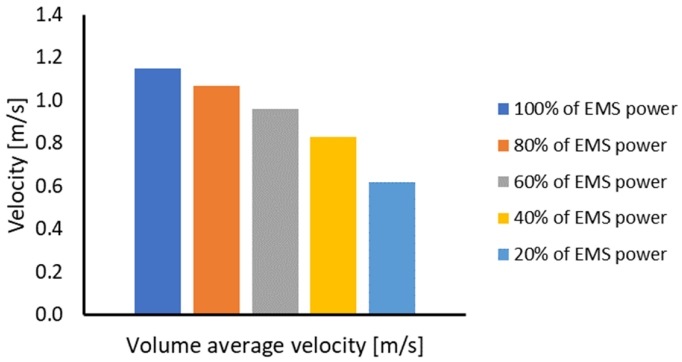


Figure 77. Volume averaged velocity for different power applied to the horizontal electromagnetic stirrer for ladle furnace investigations.

The analysis of the benchmark vertical stirring case for the same capacity of the furnace from[83] suggests that the average velocity measured in the whole volume of the melt is not higher than 0.6 [m/s]. It indicates that the same power applied to EMS, but for horizontal stirring, leads to significantly increased volume average velocity inside the melt, and that is why this power must be reduced. The above results confirm that to obtain a similar range of velocity as in the benchmark test, the horizontal stirring uses less energy by up to 80% in comparison to the classical vertical stirring. Thus, 20% power applied to the horizontal stirring EMS results in the same range of the volume average velocity as in the case of the commonly used EMS solution with vertical stirring in a ladle furnace. That is why such reduced power will be used for horizontal stirring in further investigations and comparisons.

What is important from a metallurgical point of view is that the average velocity of the melt is on similar level in the whole ladle furnace. Such behavior increases the efficiency of the inclusion removal process. In the top part of the furnace, close to the slag/metal interface the non-metallic inclusions collide frequently and their residence time in the steel increases. That leads to improved absorption of inclusions to the slag layer.

As presented, initial results with the simplified approach are very encouraging. However, the simulation of gas stirring and EMGAS stirring requires the use of a more complex multiphase model combining the Euler and Lagrange approaches. Such a setup enables tracking the behavior of the interface between the molten steel and air and the additional influence of the gas bubbles on the flow.

It should be noted that the phase interactions are not included during the current solution but can be involved in the future to make the model even more comprehensive.

The Lagrange approach was used to model the argon gas particles with an additional discrete phase, the DPM module. The standard interaction between the particles and melt is included, which also captures the movement of the bubbles from the molten steel and vice-versa. Additionally, the DPM source is updated in every flow iteration to provide full coupling between the continuous and discrete models.

As the argon particles are simulated only in the melt domain, the additional UDF responsible for the removal process of the particles which reach the top layer of the melt was implemented. The argon particles are modelled as inert particles with mass and have a different density than molten steel. Moreover, they have the momentum associated with the flow rate at the inlet and go up to reach the top layer of the melt. With the changing height, the hydrostatic pressure is also changing. These changes are directly related to the diameter of particles. Diameter distribution is also updated by the implemented UDF independently of the uniform diameter distribution in the Fluent program.

The main goal of the developed UDF is to model the hydrostatic dependences between pressure and the expansion of bubbles according to physical phenomena. The dependences are modelled based on the assumption of the constant mass of the particles[245]. The hydrostatic pressure at the bottom of the ladle, for the inlet of the gas bubbles, is defined as:

$$\Delta P_{tot} = \rho_{melt} g \Delta h_{melt} + \rho_{slag} g \Delta h_{slag}. \quad (49)$$

The local pressure is related to the current position in the ladle and can be calculated based on the equation:

$$\Delta P_{local} = \Delta P_{tot} - \rho_{melt} g \Delta h_{local}. \quad (50)$$

According to the ideal gas assumption, the local bubble diameter can be calculated as:

$$V_{bubble,local} = \frac{\Delta P_{tot} V_{bubble,inlet}}{\Delta P_{local}}. \quad (51)$$

The density of the bubbles changes with the height of the ladle due to the hydrostatic pressure and can be calculated based on the linear interpolation:

$$\rho_{bubble,local} = \rho_{bubble,inlet} + (1 - \frac{\Delta z}{\Delta h_{melt}})(\rho_{bubble,inlet} - \rho_{bubble,atm}). \quad (52)$$

The above equations enable to analytically calculate the diameter and density of the gas bubbles. These values are assigned to the Fluent variables and updated in each time step based on the local position of the particles. The calculations assume the constant mass of the bubbles for each position in the melt[245] according to the equation:

$$m_{bubble,local} = const = \rho_{bubble,inlet} V_{bubble,inlet}. \quad (53)$$

It should also be mentioned that these calculations are realized only for the melt domain and particles above the inlet boundary condition.

An additional conditional statement replicates the removal of the particles. For particles located outside the melt domain, the diameter and mass are equal to zero, and their trajectory calculation is stopped.

7.4 Comparison between horizontal, vertical and gas stirring for multiphase simulations

The main goal of the investigation is to obtain the highest mixing rate with reduced stirring energy close to the free surface and lower energy consumption. Moreover, the mixing process should ensure a stable free surface to avoid unexpected turbulences in the flow distribution inside the ladle. The comparison presented below enables to see the advantages and disadvantages of each stirring approach.

The simulation results include a comparison between gas stirring (as a reference), classical vertical EMS stirring (the benchmark case for initial calculations), EMGAS with a vertical direction of stirring, and then the new concept of EMS with horizontal stirring and EMGAS with horizontal stirring. A set of parameters was evaluated during the research, e.g., velocity and stirring energy distribution, free surface and gas bubbles behavior (for gas and EMGAS approaches) and efficiency of the mixing process. The velocity distribution for five different stirring methods is presented in Figure 78. The stirring energy distribution for EMS (vertical and horizontal), gas and EMGAS (vertical and horizontal) approaches is presented in Figure 79. The surface height as a separate variable to free surface behavior is presented in Figure 80. The gas stirring and both EMGAS approaches include the additional inert gas injection. The

gas used for the stirring process is argon, and its behavior for different stirring methods is presented in Figure 81, where the diameter of the argon gas bubbles is tracked. Moreover, the efficiency of the mixing process is tracked by the DPM particles. In this case, the massless particles are used and coupled with the continuous phase (molten steel). The particles are treated as tracers and follow the steel behavior so their motion can be precisely observed. The colormap of the particles depends on their velocity and is presented in Figure 82.

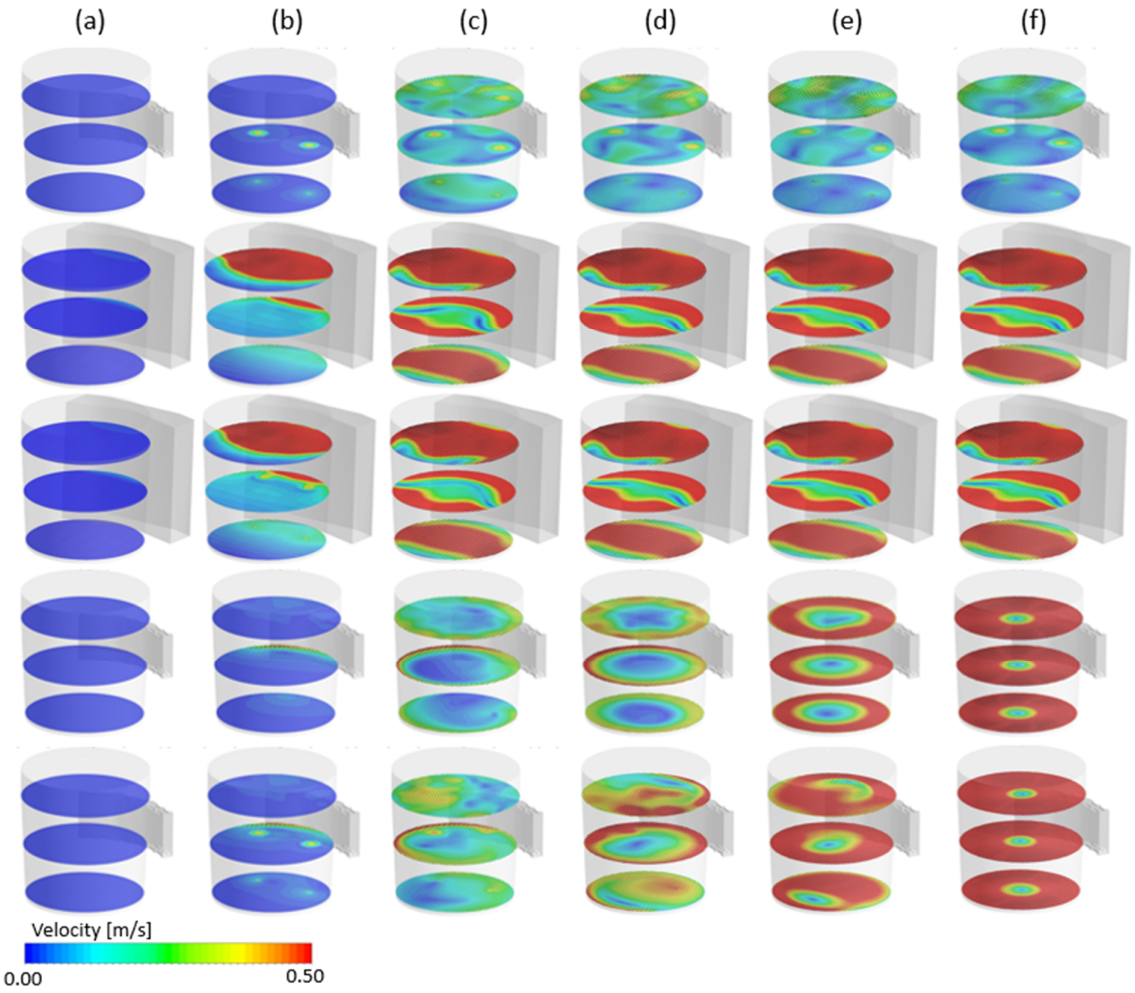


Figure 78. Velocity distribution for different types of stirring like gas stirring (top), EMS vertical stirring (2nd row), EMGAS vertical stirring (3rd row), EMS horizontal stirring (4th row) and EMGAS horizontal stirring (bottom) for (a) 0 [s], (b) 5 [s], (c) 50 [s], (d) 100 [s], (e) 200 [s] and (f) 500 [s].

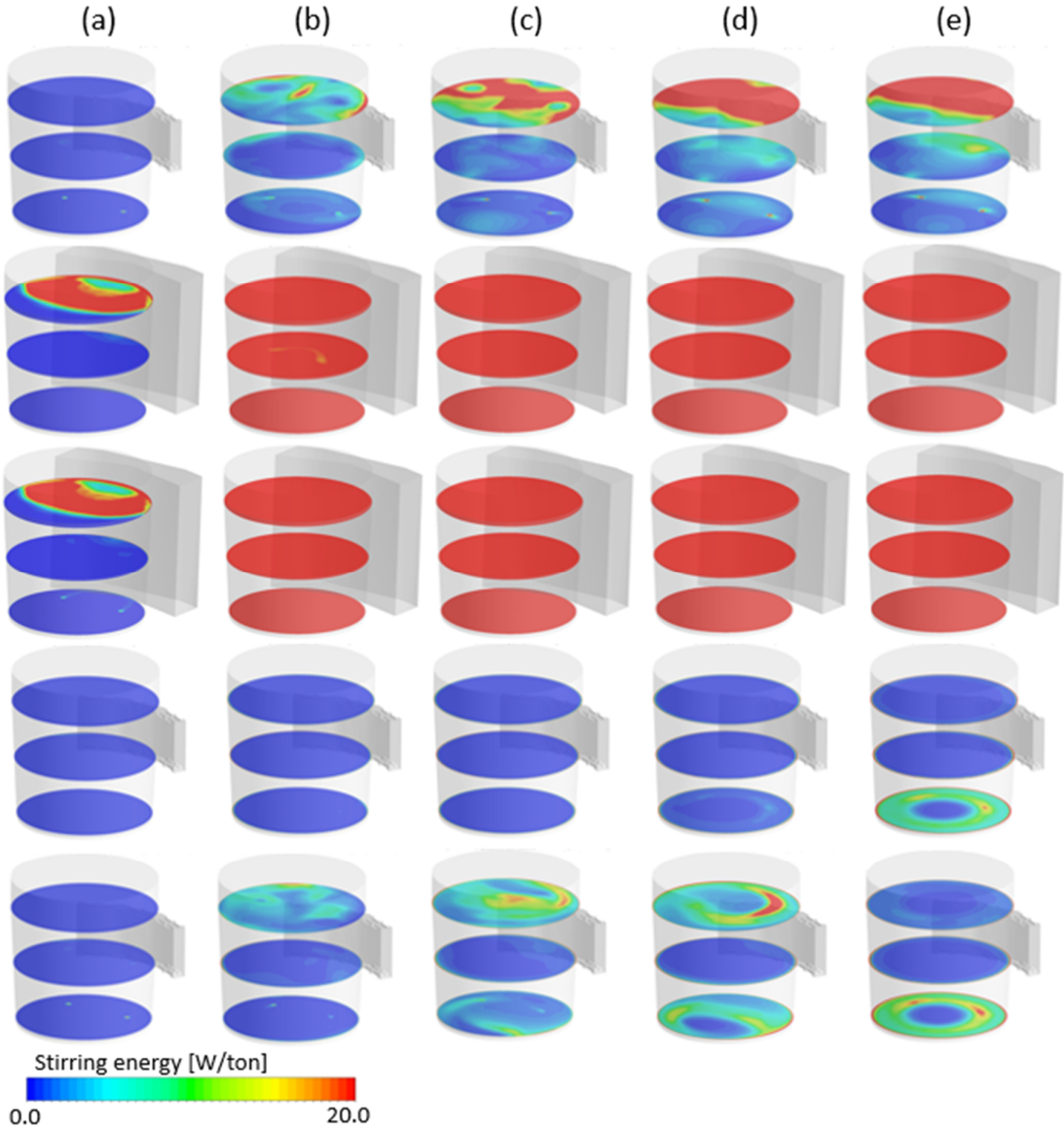


Figure 79. Stirring energy distribution for different types of stirring like gas stirring (top), EMS vertical stirring (2nd row), EMGAS vertical stirring (3rd row), EMS horizontal stirring (4th row) and EMGAS horizontal stirring (bottom) for (a) 5 [s], (b) 50 [s], (c) 100 [s], (d) 200 [s], (e) 500 [s].

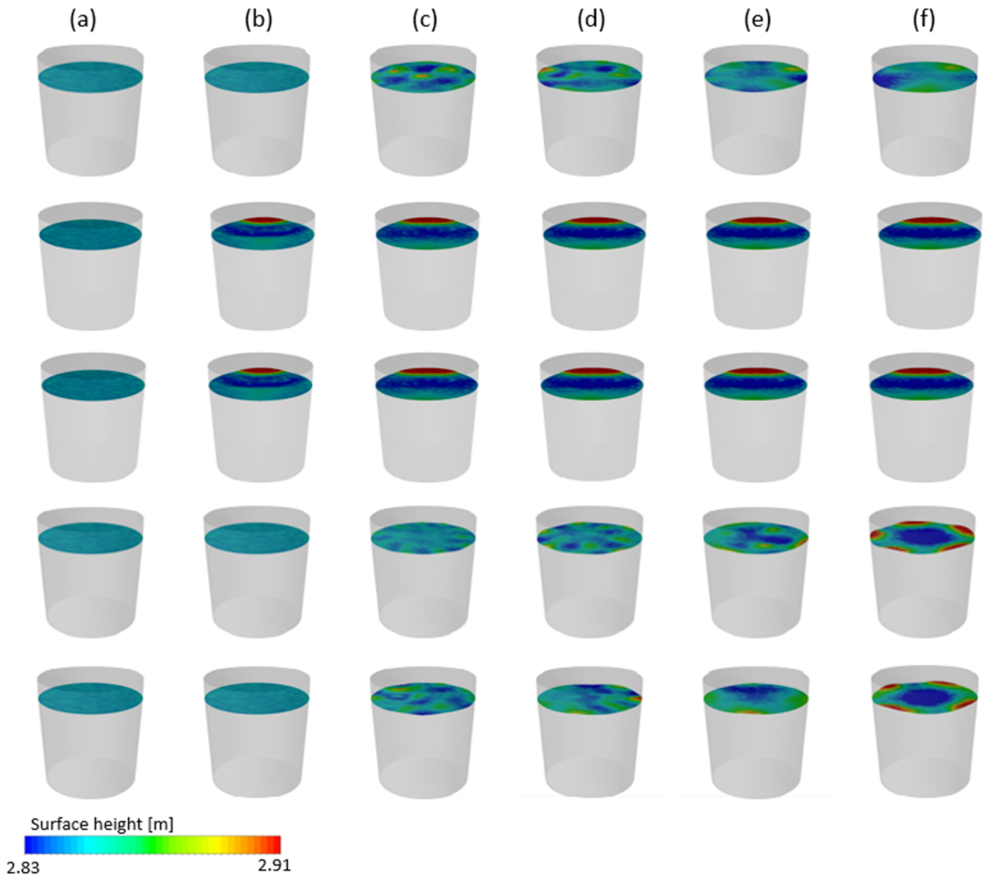


Figure 80. Surface height for different types of stirring like gas stirring (top), EMS vertical stirring (2nd row), EMGAS vertical stirring (3rd row), EMS horizontal stirring (4th row) and EMGAS horizontal stirring (bottom) for (a) 0 [s], (b) 5 [s], (c) 50 [s], (d) 100 [s], (e) 200 [s] and (f) 500 [s].

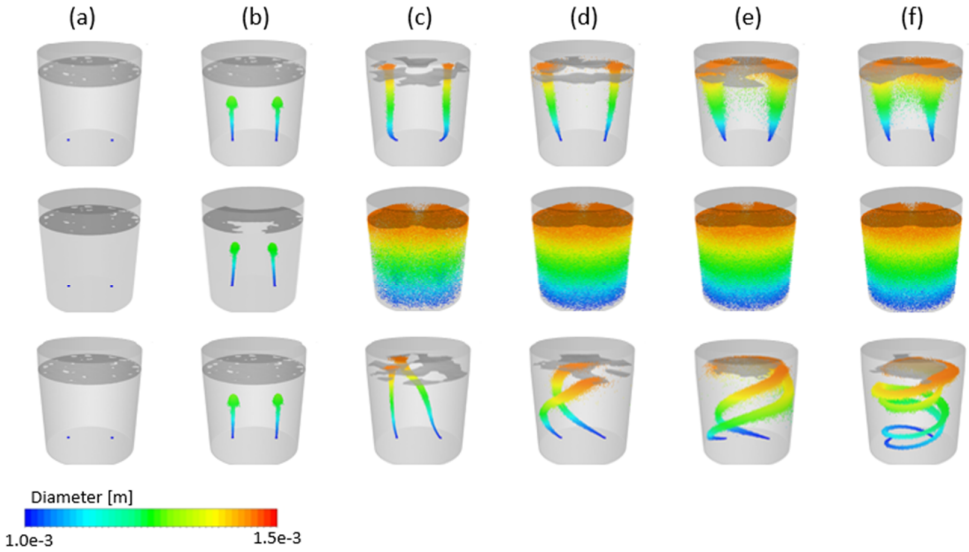


Figure 81. Diameter of the argon gas bubbles for gas stirring (top), EMGAS vertical stirring (middle) and EMGAS horizontal stirring (bottom) for (a) 0 [s], (b) 5 [s], (c) 50 [s], (d) 100 [s], (e) 200 [s] and (f) 500 [s].

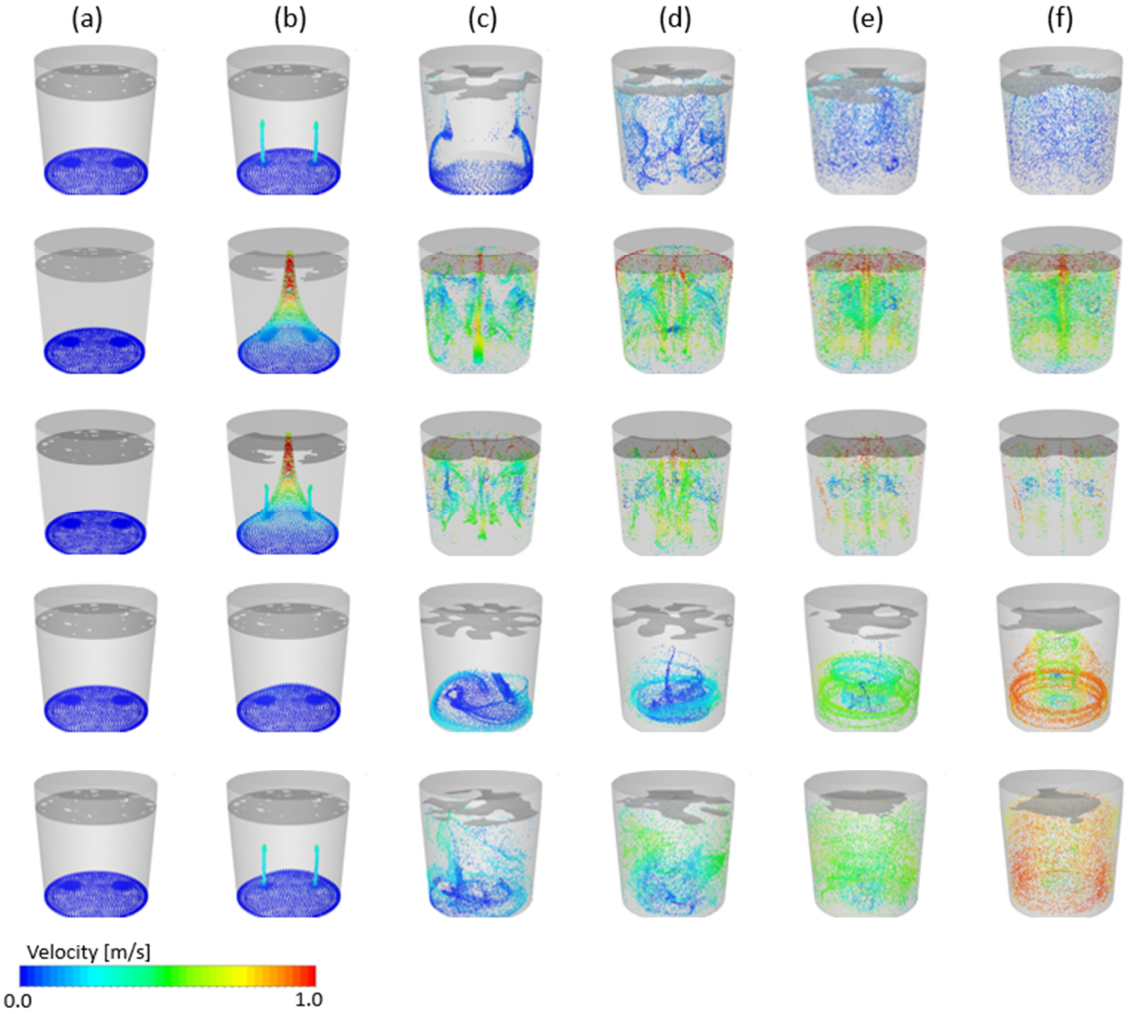


Figure 82. Mixing process for different types of stirring like gas stirring (top), EMS vertical stirring (2nd row), EMGAS vertical stirring (3rd row), EMS horizontal stirring (4th row) and EMGAS horizontal stirring (bottom) for (a) 0 [s], (b) 5 [s], (c) 50 [s], (d) 100 [s], (e) 200 [s] and (f) 500 [s].

The analysis of the results suggests that the commonly used vertical EMS stirring and EMGAS method with the vertical direction of stirring provides very similar results with high mixing performance. However, as they are characterized by high energy consumption, they will be used only for comparison purposes. The horizontal direction of stirring enables a reduction of the power applied to the stirrer at the level of 80%, and this method will be widely commented on in this thesis. Based on the results, the velocity distribution is confirmed to be very uniform for the newly proposed EMS horizontal stirring. For only gas stirring, which is the most popular method, the highest value of the velocity is observed in the top area of the furnace. The EMGAS approach with horizontal stirring ensures uniform velocity in the whole domain of the ladle furnace. The stirring energy distribution is very important in the case of the inclusion removal process. The highest stirring energy distribution in the case of the EMS horizontal stirring is observed in the bottom area of the furnace. In the case of gas stirring, the

highest value of the stirring energy is located in the top area of the furnace, which decreases the efficiency of the inclusion removal process due to adhesion to the top slag layer. The EMGAS approach with horizontal stirring ensures high stirring energy in the bottom part of the furnace and a relatively low value of the stirring energy in the top area of the furnace. The distribution of the stirring energy affects the behavior of the free surface. For gas stirring, the behavior of the free surface is very unstable and random oscillations are observed. Moreover, the situation will worsen if the flow rate of argon increases. High oscillations of the free surface can lead to the interruption of the surface between the molten steel and slag in the real application, which can be dangerous from a steel cleanliness point of view due to the high risk that the part of the slag enters into the melt[234]. The EMGAS horizontal approach ensures more stable behavior of the free surface compared to EMS stirring alone, what can help to further increase the efficiency of the inclusions removal process due to the adhesion to the slag layer. In the case of the gas stirring and EMGAS approach, the argon gas bubbles were injected into the simulation domain. The behavior of the bubbles depends on the behavior of the molten steel, where for both EMGAS approaches, argon bubbles plume is mixed with steel. The mixing process, realized by massless particles, enables the observation of molten steel behavior. The EMS stirring for the horizontal direction of stirring is characterized by great mixing in the bottom of the furnace. The gas stirring is characterized by the intensive stirring in the whole volume, but at the beginning of the process the mixing is limited as both the velocity and efficiency of the stirring are relatively low. The EMGAS stirring for both directions of stirring is characterized by a very good mixing in the whole volume of the ladle furnace. From the metallurgical point of view, the results confirm that the contact area between the bubbles and the steel is increased, while the turbulence between the slag and metal interface is reduced. The residence time of the steel between the slag and metal interface increases, intensifying the inclusions' absorption into the slag layer.

7.5 Comparison between mixing times

Mixing time is one of the most important parameters in secondary steelmaking and in the evaluation of the purity and composition of the final product. The main reason for measuring the mixing time relates to the alloy additions, which are provided to the melt via open-eye for gas stirring. These additions should be homogeneously distributed inside the melt during the process. As a criterion for measurements of the mixing time, 95% of the full homogenization of the addition is specified.

In the presented work, due to the complexity of the phenomena and difficulties with the specification of the boundary conditions for the additional tracer used for measurements of the mixing time in the case of the multiphase simulation, the simplified approach will be used to compare the differences between various stirring methods described in previous chapters for the 160-ton industrial ladle furnace from Figure 68. The simulation is based on the transient, single-phase approach, where the slag layer is not taken into consideration. The area of the

open-eye is estimated based on the measurements of the time-averaged area in the other 150-ton industrial ladle furnace with gas stirring[144], as presented in Figure 83.

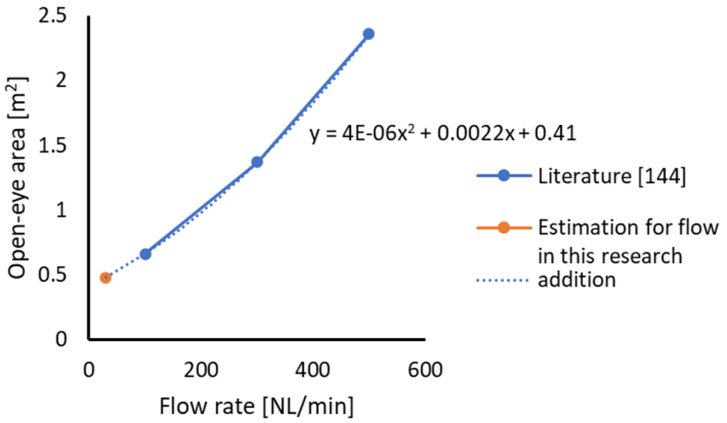


Figure 83. Estimation of the open-eye area generated by the argon gas injection.

The geometry of the melt domain with open-eye areas located directly above the argon plugs with a particular diameter assigned based on the above calculations is presented in Figure 84.

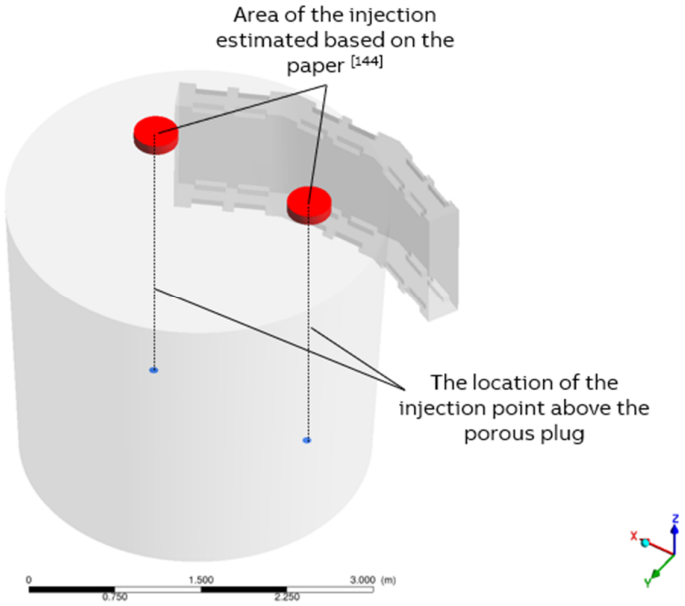


Figure 84. Scheme of the computational domain with open-eye areas.

The alloy addition is realized by the additional tracer specified by UDS (User Defined Scalar), where concentration in time is measured in selected points located in the whole computational domain (Figure 85). The concentration of the UDS is equal to 1 within the first 5 [s] of the simulation and then is mixed and tracked in the whole melt domain for 5000 [s] to avoid the doubts related to the presence of the measurement points in so-called dead zones.

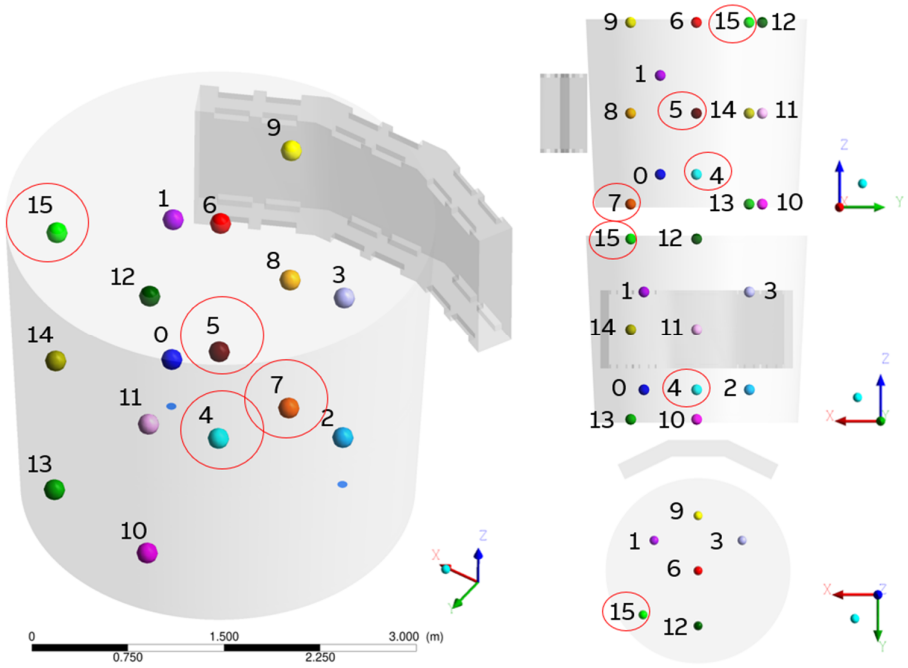


Figure 85. Locations of the points where the concentration of the UDS is measured with a marked position of the sensors for later water model experiment.

The measured dimensionless concentration of UDS in time at different points for gas stirring, vertical EMS stirring, vertical EMGAS approach, horizontal EMS stirring, and finally, horizontal EMGAS approach are presented from Figure 86 to Figure 90. The additional dotted lines are marked as a condition of 95% of the homogenized distribution of the alloy additions. This means the dimensionless concentration is included in the range of 0.95 to 1.05[234,248]. Such a condition serves as a baseline for evaluating the mixing time, which is the time when the concentration at all points reaches the required limit. The mixing time for different stirring methods is indicated in each Figure as the shortest time required for 95% homogenization.

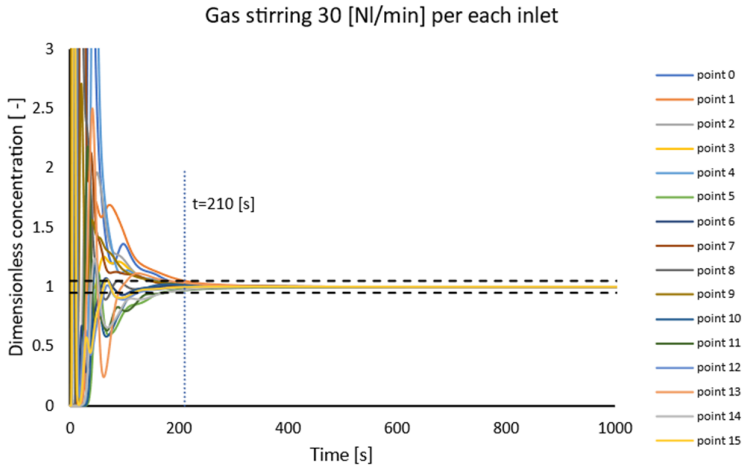


Figure 86. Mixing time for only gas stirring as a reference case for further comparisons.

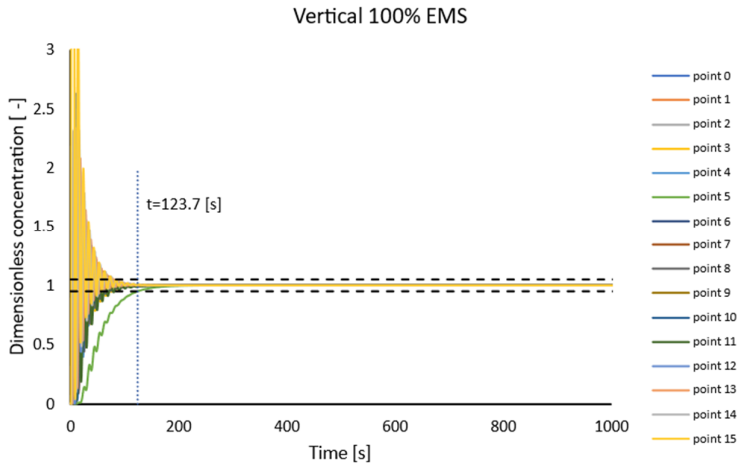


Figure 87. Mixing time for only the EMS stirring with the vertical direction of stirring.

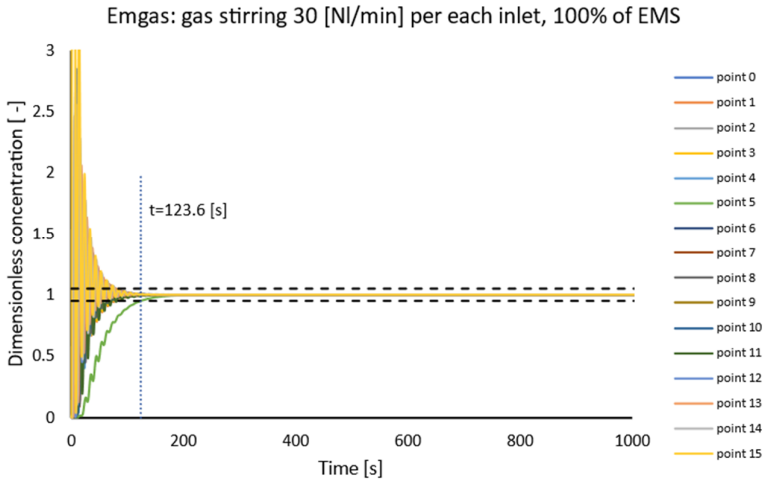


Figure 88. Mixing time for the EMGAS approach with the vertical direction of stirring.

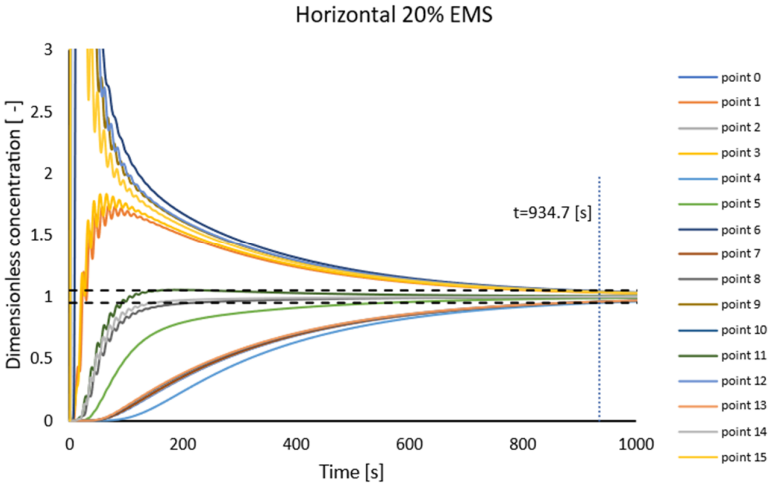


Figure 89. Mixing time for only the EMS stirring with the horizontal direction of stirring.

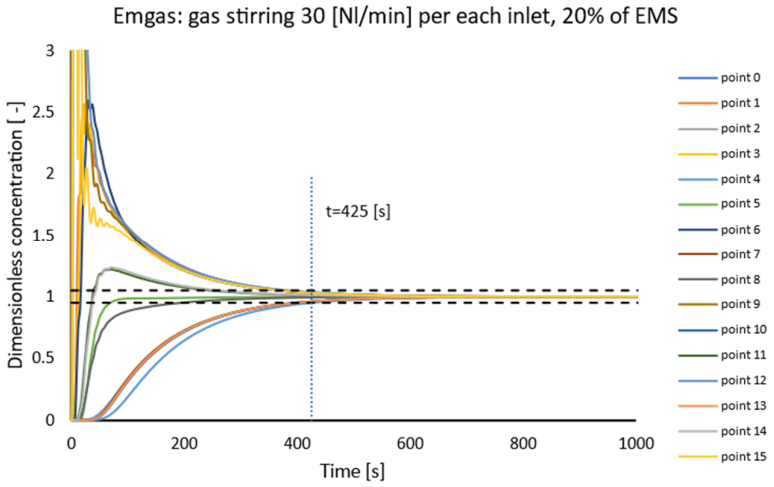


Figure 90. Mixing time for the EMGAS approach with the horizontal direction of stirring.

The presented results suggest that the mixing time for gas stirring with two porous plugs and a flow rate equal to 30 [Nl/min] via each plug is equal to 210 [s], which is a good result. The investigations can be compared to very similar research in [245], where the mixing time for only gas stirring was above 400 [s]. The main difference relates to the boundary conditions of the gas. In [245], one porous plug was active; moreover, the flow rate was lower, equal to 25 [Nl/min]. The results suggest that the dual plug system is beneficial in reducing the mixing time almost twice.

A similar comparison can be made between vertical EMS stirring and the EMGAS approach, particularly in terms of the vertical direction of stirring. The results suggest that vertical stirring is more efficient in reducing the mixing time than gas stirring. The time needed to obtain 95% of the homogeneity of the melt is lower than 130 [s]. Moreover, when comparing the vertical EMS and vertical EMGAS approaches, the influence of the additional gas is almost negligible in the case of mixing time reduction but can affect the inclusion removal process. It can be concluded that vertical stirring increases the distribution of bubbles in the whole melt, which can be beneficial for the reduction of non-metallic inclusions.

The analysis of the EMS stirring with the horizontal direction of stirring and then, the EMGAS approach is a first trial to evaluate the mixing time for this type of the solution. The conducted CFD simulations confirmed that pure EMS stirring enables an increase in the velocity inside the melt with reduced power applied to the stirrer, but significantly increases the mixing time. The alloy additions are unable to reach the center of the vortex in a short time, resulting in an extended time needed to obtain the homogeneous condition. The addition of the gas stirring in the EMGAS approach enables a decrease in the mixing time from over 930 [s] to 425 [s]. That is a significant reduction, which is beneficial also from a steel purity point of view. Additionally, gas stirring enables an increase in the number of non-metallic inclusions, which will be removed from the melt by flotation[224,249].

It is worth mentioning that the mixing time depends on the location of the measurement points and also the location of the alloy addition areas. In the current research, 16 different points were defined throughout the entire melt domain to minimize the influence of point location on the results. Moreover, the time when homogenization reached at least 95% in all points was considered a mixing time. The influence of the position of the alloy addition injection was not taken into consideration.

7.6 Inclusions modelling for horizontal EMS

The application of the inclusions modelling to the LF is realized by the definition of the 16 bins within the inclusions continuous phase with increasing particle diameter. Moreover, these bins are initialized with the proper fraction, as presented in Table 8. The general concentration of the inclusions in the whole melt is equal to 10 [ppm] as an initial step. Then, due to the application of the specified boundary conditions regarding the removal process, the concentration of the inclusions decreases over time. The effectiveness of the removal process is directly dependent on the mixing phenomena in the ladle.

The simulation study in the case of the LF was executed for horizontal EMS stirring only as it was the primary focus of this investigation.

The model parameters were selected based on the literature review[222] to be able to track the behavior of the Al_2O_3. The exemplary results show a changing volume fraction of the inclusions in time (Figure 91). The measurements of the average value of the volume fraction of the inclusions in the whole melt domain are presented in Figure 92. Moreover, the behavior of each bin corresponds to the behavior of each particle size. These size distributions are based on the measurements of the fraction of each bin and are presented in Figure 93.

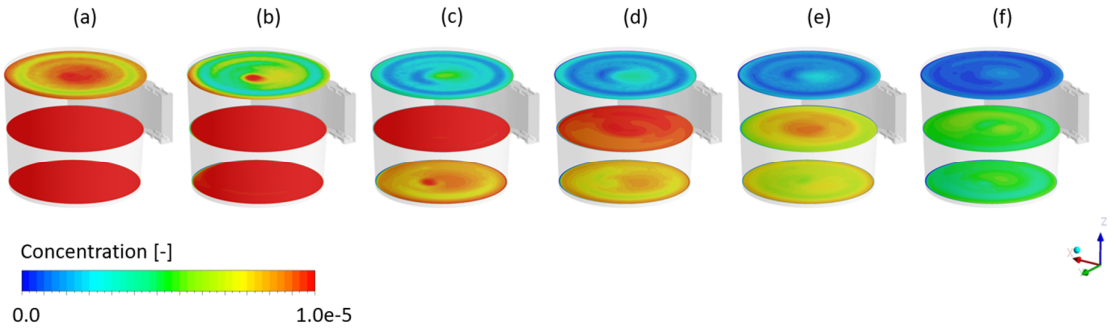


Figure 91. Volume fraction of inclusions in the LF after (a) 1[s], (b) 5[s], (c) 50[s], (d) 100[s], (e) 200[s] and (f) 500[s].

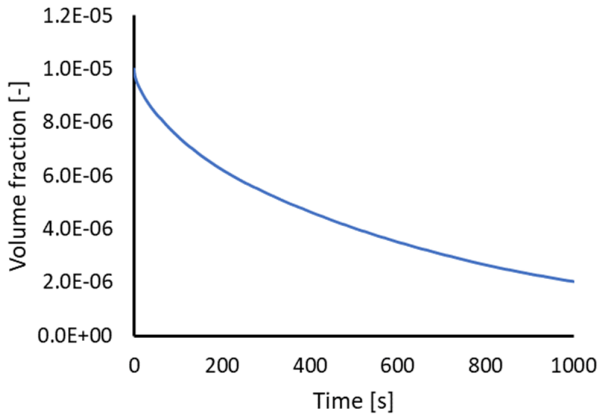


Figure 92. Volume average fraction of inclusions in the whole melt domain in time for horizontal EMS stirring.

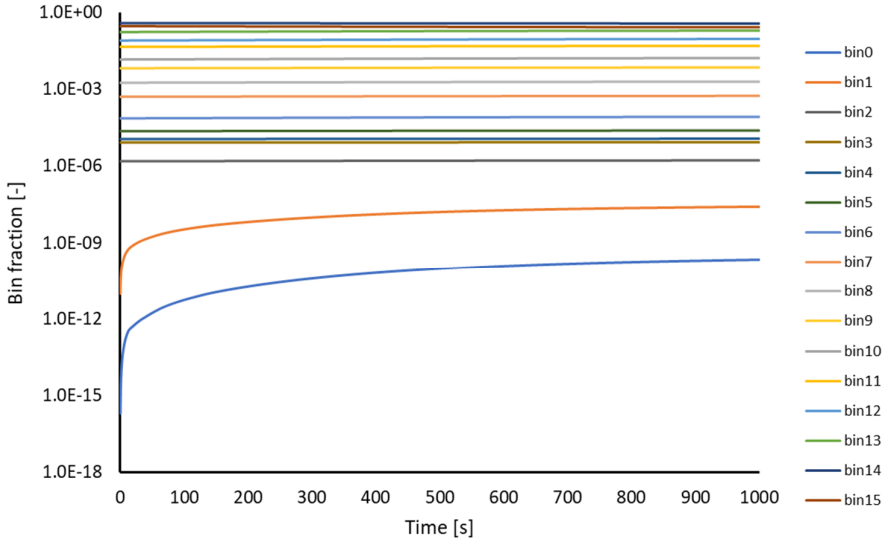


Figure 93. Bin fraction corresponding to the fraction of each inclusion diameter for horizontal EMS stirring.

The analysis confirms that the model predicts a decreasing concentration of the inclusions over time. The highest effectiveness of the inclusion removal process is in the top area of the LF, which is directly related to the condition of the removal process controlled by the UDFs. Moreover, the observation of each bin behavior suggests that the agglomeration and removal processes are included, which is confirmed by the changes of each bin fraction in time.

Finally, it has to be mentioned that the modelling of non-metallic inclusions is a very complex phenomenon. The presented numerical simulation of these particles has a preliminary character with the goal of obtaining a correct prediction of the behavior of Al_2O_3 inclusions. Research on inclusions is based on mathematical assumptions, and an extensive validation process should be conducted to accurately identify the model parameters. Therefore, the

presented approach serves as a starting point for further investigations and the development of the numerical model of spinel inclusions' behavior.

7.7 Comparison of CFD results with water model results

Since the industrial data for LF were not available to confirm the numerical evaluations and better understand the flow inside the ladle furnace, additional qualitative observations were performed based on the lab-scale water model. Water is considered a suitable substitute for molten steel in physical modeling due to the similarity in their kinematic viscosities, water at 20 [℃] and steel at 1600 [℃][250]. The author conducted the experimental part of the work during a research stay in the ABB Metallurgy Lab in Sweden. The LF water model experimental setup that was used within the research includes the cylindrical transparent vessel with a height of 1.5 [m] and an internal diameter of 1 [m]. The maximum water height for this setup is 0.85 [m]. The laboratory setup is presented in Figure 94.

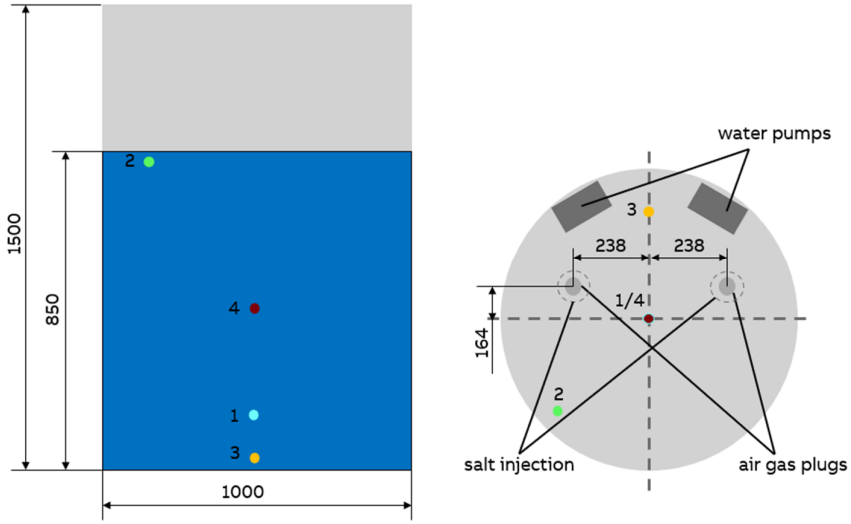


Figure 94. Test setup of water model for ladle furnace with location of the sensors.

At the bottom of the water model, the additional scale was included to properly set up the porous plug. A more detailed view of the scale and porous plug used in the experiment is presented in Figure 95.

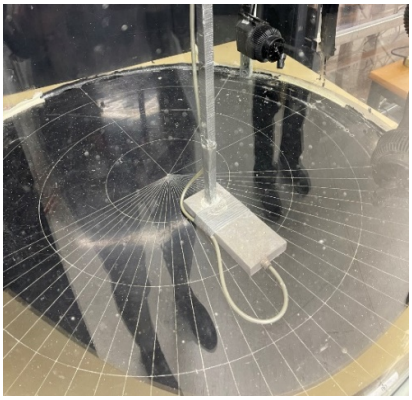


Figure 95. Bottom of the water model of ladle furnace with scale and porous plug.

The ladle furnace model was filled with water at room temperature during the tests. The submerged water pumps realize the electromagnetic stirring. The gas stirring is realized by air[250], which is injected via the porous plug (perforated plate) of 2.5 [cm] diameter with additional injection holes 0.5 [mm] in diameter, located at the bottom of the model. The perforated plate can be moved to change the position of the inlets. In the real scenario and the simulation case, two porous plugs were modelled. Based on that, the water model was also equipped with an additional perforated plate. The tank construction from plexiglass enables in-situ observations of the flow during the mixing in real-time, which is not possible under industrial conditions.

The water model is prepared at a scale; moreover, the material properties of the water and air are different than the steel and argon, respectively. In addition, all of the water experiments are conducted at room temperature. All these aspects imply the preparation of scaling the process parameters to obtain similarity in the flow behavior between the numerical simulation of the real case and the water model. The comparison between the simulation model of the industrial furnace with the scaled water model is presented in Table 21.

Table 21. Comparison between the numerical and water model.

	Numerical simulation	**Water experiment**
Diameter of vessel [m]	3.359	1
Bath height [m]	2.853	0.85
Density [kg/m^3]	6900	1000
Dynamic viscosity [kg/(m s)]	0.0069	0.001
Kinematic viscosity [m^2/s]	1 x 10^{-6}	1 x 10^{-6}
Stirring energy for gas stirring [W/ton]	7.43	8.09

The proper scaling of all of the parameters is impossible, and particular attention must be paid to the most important phenomena. In the case of gas stirring, two of the most important

criteria can be distinguished: the plume dynamic similarity and scaling of the flow rate to obtain similarity for the stirring energy obtained for the ladle. In the case of the EMS stirring, which is realized by the pumps, the criteria related to the stirring energy are difficult to obtain due to the fact that even though the input power of each pump is known, the output to the water is difficult to assess, and other criteria must be taken into consideration. Finally, in the case of the EMS stirring, the similarity of the Froude number is used[250]. Nevertheless, it must be noted that the results from water modelling are of a qualitative nature.

As pointed out, the gas stirring similarity is based on the evaluation of the plume dynamic or stirring energy similarity. In our case, the similarity between the stirring energy is used, due to the fact, that the stirring energy can be a crucial parameter for non-metallic inclusions behavior prediction. In the case of the real application, which is modelled by the CFD approach, Sundberg[223] proposed, that the stirring energy can be calculated by the following formula:

$$\dot{\epsilon} = 371\frac{QT_1}{M_1}\left[\left(1-\frac{T_0}{T_1}\right)+ln\frac{P_1}{P_2}\right], \tag{54}$$

where: $\dot{\epsilon}$ – specific mechanical stirring energy [W/ton], Q – argon gas flow [Nm^3/s], T_1 – steel temperature [K], T_0 – room temperature [K], P_1 – pressure the ladle bottom [Pa], P_2 – pressure above the melt [Pa], M_1 – the melt weight [ton].

The presented formula is well known in the case of real experiments, but in the case of water modelling, the formula presented by Pluschkell[251] must be taken into account:

$$\dot{\epsilon} = 840\frac{QT_1}{M_1}\log\left(\frac{P_1}{P_2}\right). \tag{55}$$

The comparison between the input data and the obtained stirring energy is in Table 22.

Table 22. Comparison between different models for stirring energy calculations.

	Sundberg	**Pluschkell**	**CFD**
Argon gas flow [Nl/min]	2x30	2x3	2x30
Steel temperature [C]	1600	1600	1600
Room temperature [C]	25	-	-
Melt height [m]	2.853	0.85	2.853
Pressure above the melt [Pa]	101325	101325	101325
Pressure the ladle bottom [Pa]	294442	109664	294442
Melt weight [ton]	160	0.67	160
Stirring energy [W/ton]	**8.29**	**8.09**	**7.43**

The above comparison confirms that to obtain the correct similarity of the stirring energy in the gas modelling case, the airflow rate in the water model must be equal to 3 [Nl/min] per plug. The control of flow rate is fully done by the flow meters available in the laboratory (Figure 96). What is worth mentioning is that the CFD model has a good prediction of the stirring energy compared to the theoretical assumptions.



Figure 96. Flow meter for airflow control.

A separate analysis was conducted for the proper scaling of the water pumps to reflect the behavior of the EMS stirrer in the real furnace. As mentioned, the similarity of the stirring energy in that case is difficult to obtain due to the unknown value of the energy applied to the water, generated by each pump. To avoid the misleading and low accuracy of the similarity, the other criterion was used, namely the Froude number[252–255]. This criterion enables to reflect of the flow behavior in the scaled model and can be presented by the following formula:

$$Fr = \frac{u_m}{\sqrt{g D_m}} = \frac{u_s}{\sqrt{g D_s}}, \tag{56}$$

where: Fr – Froude number, u_m – velocity in the water model [m/s], u_s – velocity in the steel [m/s], g – gravitational acceleration [m/s^2], D_m – diameter of the water model [m], D_s – diameter of the real furnace [m].

Thanks to the numerical simulations, it was possible to select a particular area in the furnace and check the velocity of the steel. The same area was investigated in the case of the water models, and the velocity in the interesting regions was measured by the velocity meter presented in Figure 97. Based on that, it was possible to assess the number of water pumps needed to obtain similar conditions as in the case simulated numerically.



Figure 97. Velocity meter Nixon Streamflo 430 used for velocity measurements in the water model.

Finally, 6 pumps were used for vertical stirring, while only 4 pumps were sufficient for horizontal stirring to achieve the proper velocity range.

When the laboratory stand was prepared, the measurements focused on the flow visualization and mixing time evaluation.

The visualization of the flow behavior was conducted for all of the stirring methods: gas and EMS (both vertical and horizontal) and also for the combination of the gas and EMS stirring as EMGAS method (both for vertical and horizontal stirring). The investigations were conducted from a macroscopic point of view to capture the behavior of the flow throughout the entire furnace, as well as from a microscopic point of view to observe the behavior of small particles within the water. A high-speed camera was used to observe the behavior of the particles (Figure 98).

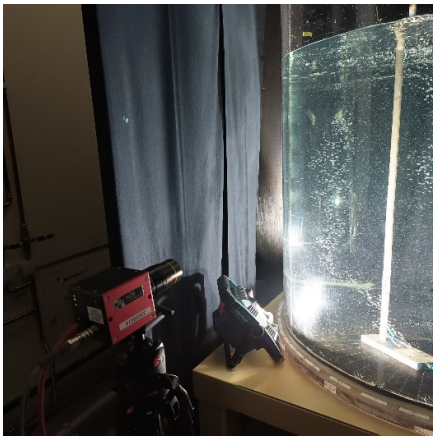


Figure 98. High-speed camera AOS Technologies AG used for recording of particles' behavior.

The videos, recorded from a macro point of view, were taken from side and top views to observe the behavior of the free surface in the water model. The observations are presented for gas stirring (Figure 99), EMS vertical stirring (Figure 100), EMGAS vertical stirring (Figure 101), and finally new proposition of the horizontal stirring (Figure 102) as well as combination with gas as EMGAS horizontal stirring (Figure 103). Particular attention should be paid to the free surface behavior, where the pictures were made for EMGAS vertical and horizontal stirring. This behavior is shown in Figure 104 and Figure 105, respectively.

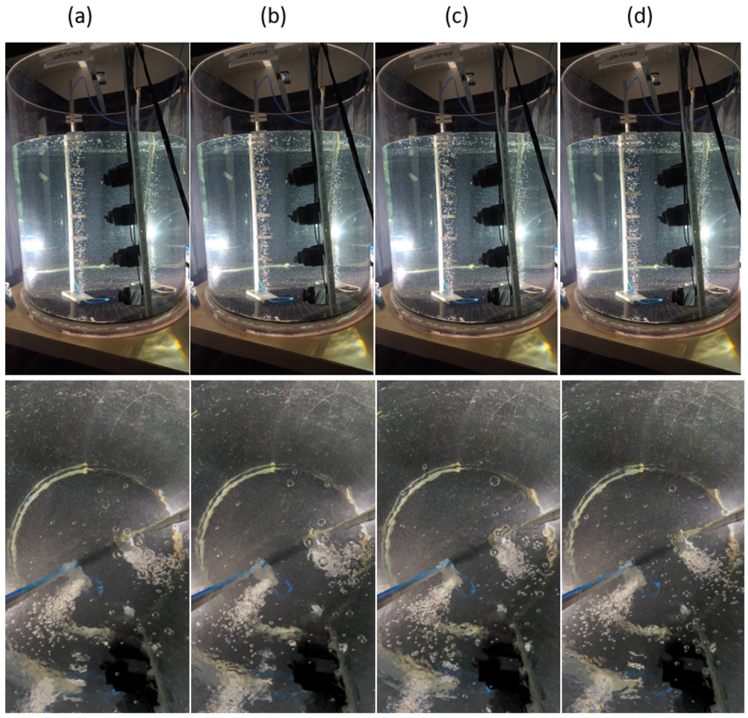


Figure 99. The flow behavior in the water model for gas stirring for side view (top) and top view (bottom) after (a) 1[s], (b) 2[s], (c) 5[s] and (d) 10[s] of observations.

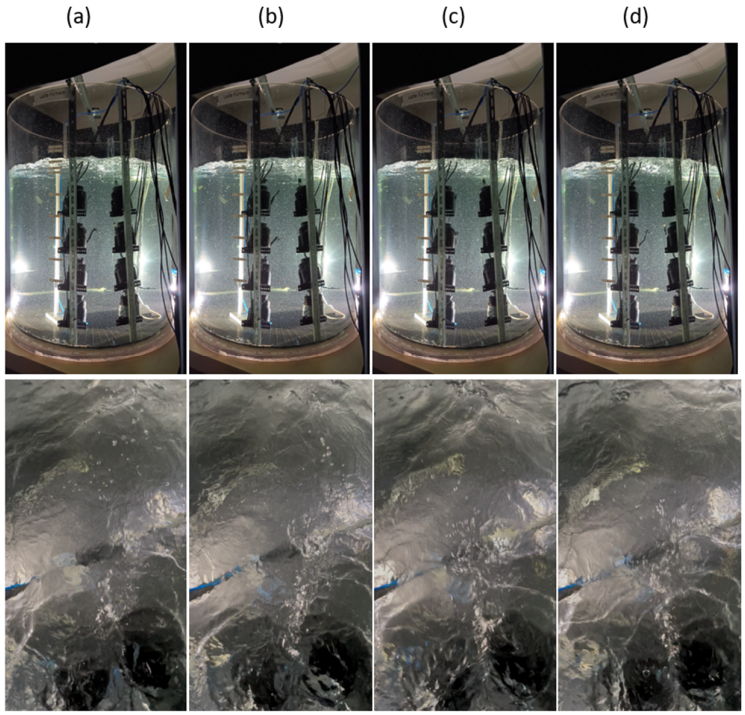


Figure 100. The flow behavior in the water model for vertical EMS stirring for side view (top) and top view (bottom) after (a) 1[s], (b) 2[s], (c) 5[s] and (d) 10[s] of observations.

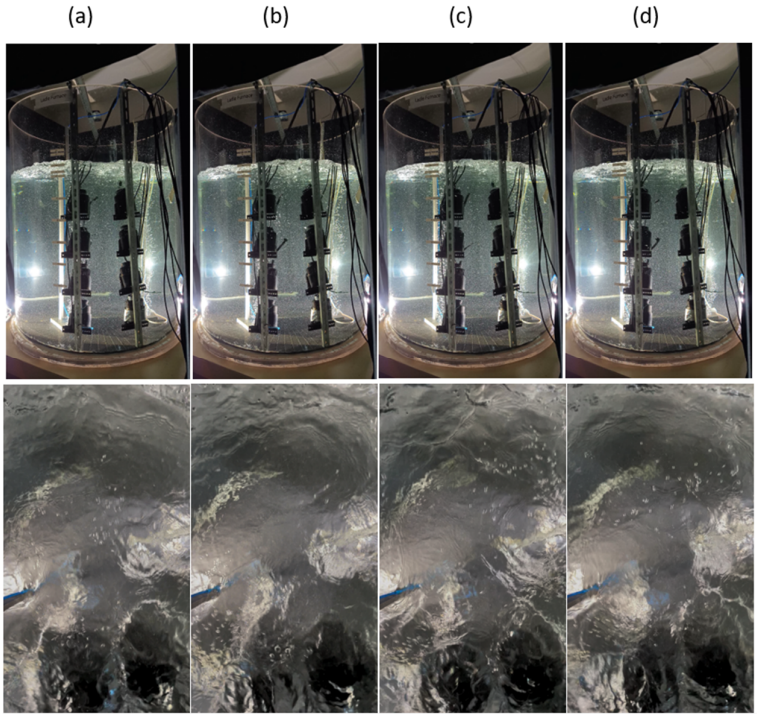


Figure 101. The flow behavior in the water model for vertical EMGAS stirring for side view (top) and top view (bottom) after (a) 1[s], (b) 2[s], (c) 5[s] and (d) 10[s] of observations.

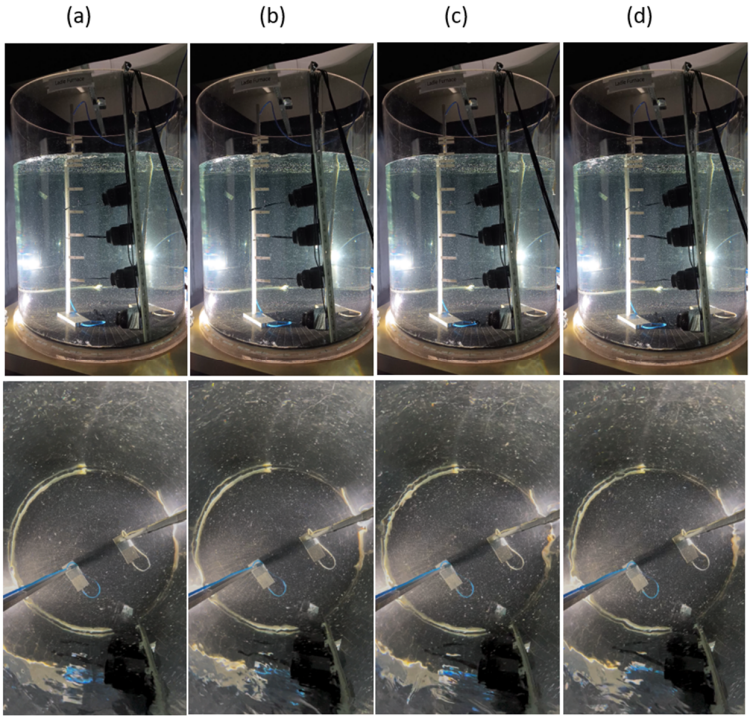


Figure 102. The flow behavior in the water model for horizontal EMS stirring for side view (top) and top view (bottom) after (a) 1[s], (b) 2[s], (c) 5[s] and (d) 10[s] of observations.

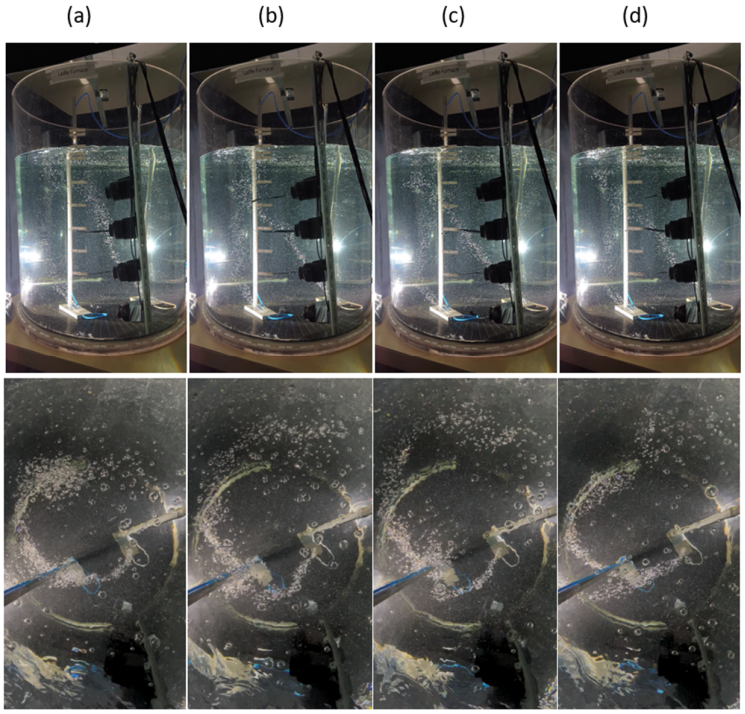


Figure 103. The flow behavior in the water model for horizontal EMGAS stirring for side view (top) and top view (bottom) after (a) 1[s], (b) 2[s], (c) 5[s] and (d) 10[s] of observations.

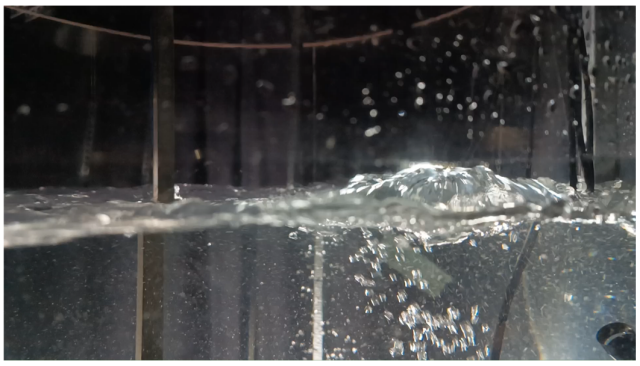


Figure 104. Free surface behavior observed for EMGAS vertical stirring.

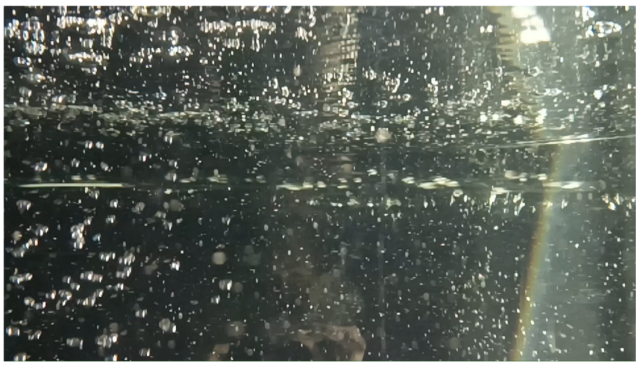


Figure 105. Free surface behavior observed for EMGAS horizontal stirring.

The above described research provides information about the general flow behavior in the ladle furnace under different stirring conditions. The additional measurements conducted using a high-speed camera were done to facilitate a more detailed evaluation. These measurements aimed to investigate the behavior of small particles included in the water to assess the effectiveness of the stirring. These small particles are partially visible in the previous Figures, but are not relevant due to the relatively small dimensions compared to the whole model of the furnace. Due to that, the measurements by the high-speed camera were limited to the small scale and only part of the ladle furnace. Moreover, an additional meter was included to catch the sharpness and be able to further evaluate the speed of particles. The measurements were done again for all of the stirring methods. Results of the investigations are presented in Figure 106 for gas stirring, Figure 107 for vertical EMS stirring, and Figure 108 for vertical EMGAS stirring. Finally, the new proposed horizontal EMS stirring is presented in Figure 109 and the horizontal EMGAS approach is in Figure 110. In each Figure, one particular particle is selected to observe its movement.

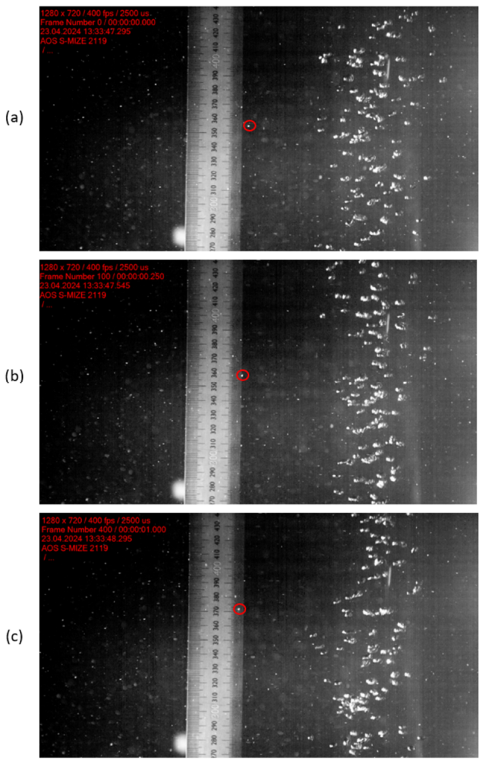


Figure 106. The particle tracking for only gas stirring after (a) 0 [s], (b) 0.25 [s] and (c) 1 [s] of observations.

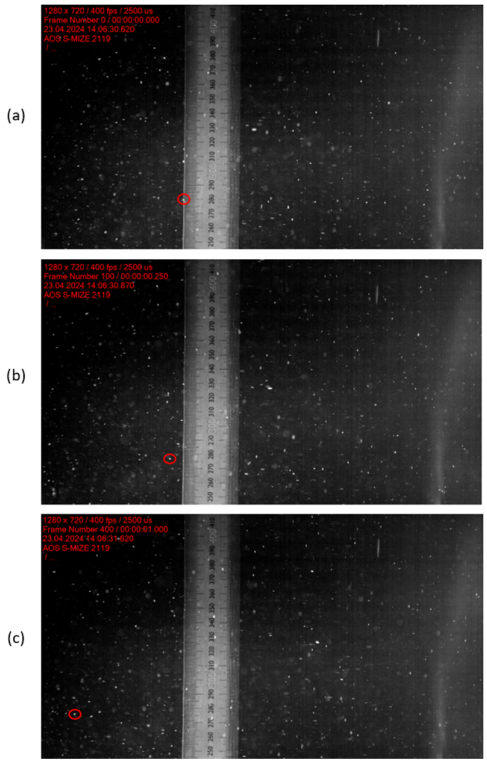


Figure 107. The particle tracking for EMS vertical stirring after (a) 0 [s], (b) 0.25 [s] and (c) 1 [s] of observations.

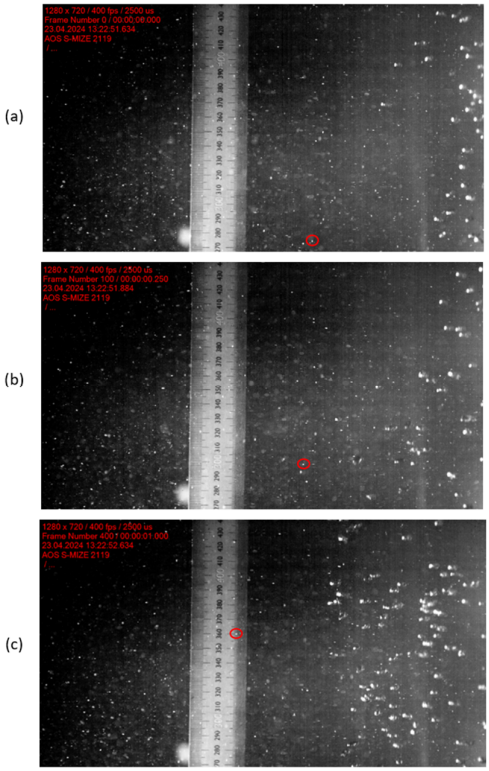


Figure 108. The particle tracking for EMGAS vertical stirring after (a) 0 [s], (b) 0.25 [s] and (c) 1 [s] of observations.

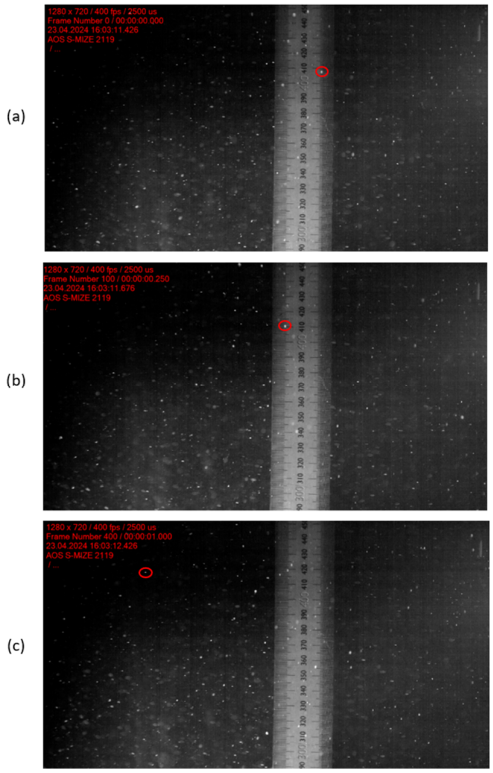


Figure 109. The particle tracking for EMS horizontal stirring after (a) 0 [s], (b) 0.25 [s] and (c) 1 [s] of observations.

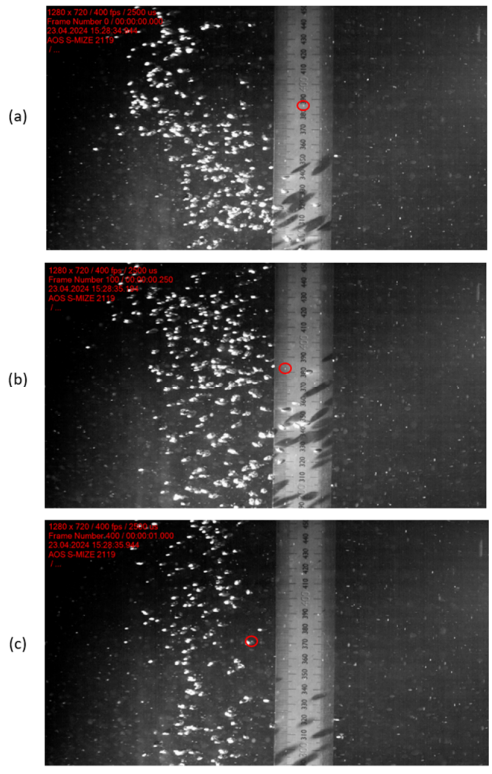


Figure 110. The particle tracking for EMGAS horizontal stirring after (a) 0 [s], (b) 0.25 [s] and (c) 1 [s] of observations.

The observations of the flow confirm that the movement of the particle is slow and almost stagnant. It seems that for this kind of stirring, the dead zones are observed, and the stirring influences only a small part of the furnace's volume. Moreover, the gas can cause uncontrolled oscillations of the free surface. Nevertheless, the gas stirring is soft for the selected flow rate, and this issue is not significant. This is clearly visible in Figure 99. For the rest of the proposed methods, the particle movement is much better pronounced, which suggests that the additional EMS system provides efficient stirring inside the furnace. It is worth mentioning that for the vertical direction of the stirring, the free surface oscillations are significant and can lead to less efficient adhesion of non-metallic inclusions to the slag layer in the real case. Moreover, some pieces of slag can tear off and drop into the molten steel, which also increases the risk of uncontrolled homogeneity of the melt structure. The observations of the water models confirm that the free surface for horizontal stirring is stable, without such prominent oscillations, which ensures the stability of the slag and increases the probability of catching the non-metallic inclusions to the slag layer and better stability and control of the structure of the melt.

To fully confirm the efficiency of the proposed EMS solution, an additional study of the mixing time for water models was conducted, building on the initial numerical study. The test setup was prepared to measure the salt concentration. The model was equipped with four conductivity sensors placed in the selected regions from CFD simulations. The sensors were calibrated before the measurements by submerging them in the KCl solution treated as a calibration standard.

All the measurement points defined in the numerical research are presented in Figure 85. From these sixteen points, only four were selected for the water model. Their location in the experimental setup is presented in Figure 94. In the real test setup, the sensor 1 corresponds to point 4 in the CFD, sensor 2 corresponds to point 15 in the CFD, sensor 3 corresponds to point 7 in the CFD and sensor 4 corresponds to point 5 in the CFD.

The sensors were connected to the multi-parameter portable meters WTW Multi 3620 IDS (Figure 111). Each meter had the possibility of gathering data from two cells. The data were directly imported to the MultiLab software and stored as an Excel sheet. The conductivity of the salt was measured directly by the sensor and then recalculated to obtain the dimensionless concentration of the salt over time. The measurements were conducted at room temperature for all stirring methods. The salt injection was realized by serving 30 [ml] of the 20% NaCl on the water surface, directly above the location of porous plugs' locations to obtain similar boundary conditions as in the numerical simulations. Based on that, a direct comparison between the curves could be prepared.

The analyses that were conducted enabled the preparation of the mixing time curves to compare different stirring methods, their efficiency in mixing, and the character of the flow behavior based on the curves' characteristics. The position of the mixing time curves between the CFD model and the experiment is presented in Figure 112.



Figure 111. Multi-parameter meter to measure the conductivity of the salt in the water during the water experiment.

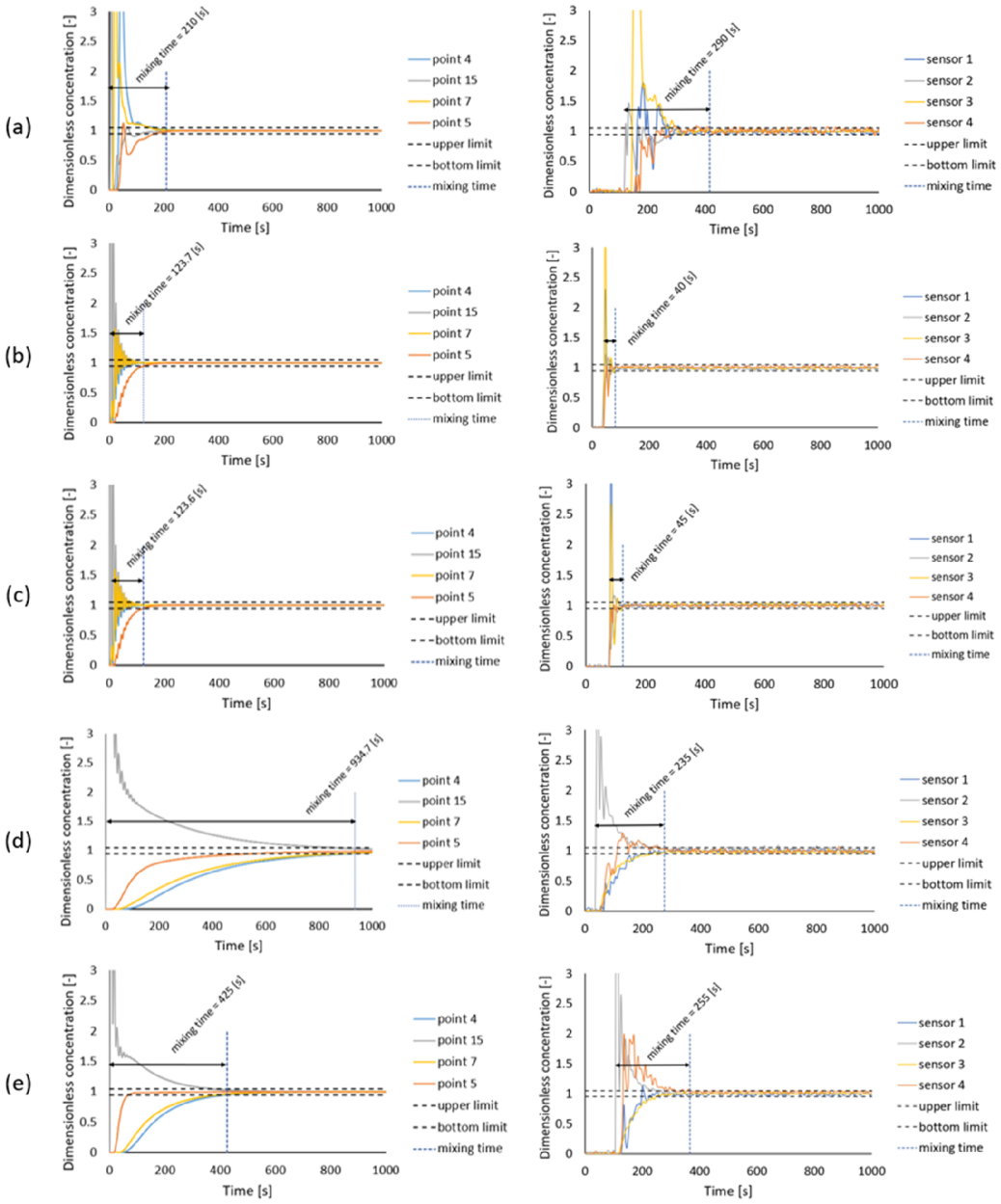


Figure 112. Mixing curves comparison for CFD simulations (left) and for water models (right) for (a) gas stirring, (b) vertical EMS, (c) vertical EMGAS, (d) horizontal EMS and (e) horizontal EMGAS.

The analysis of the mixing curves confirms that the shortest mixing time is for vertical EMS stirring. Moreover, the addition of the gas does not influence much the reduction of the mixing time. In the case of the horizontal stirring, a big difference is observed between the simulation and test results. This difference is caused by the additional equipment in the laboratory model, which has influenced the distribution of the velocity and turbulences and increased the effectiveness of the stirring. The impact is very high, due to the fact, that the character of the flow for horizontal stirring is very stable and sensitive to disturbances. In the case of the numerical simulations, the ideal conditions are taken into account, which increases the mixing time due to the difficulties with homogenization of the flow in the center of the vortex. What is worth mentioning is that the character of the curves is comparable between the simulation and test results, what indicates that the simulation model was correctly developed. The discrepancy between the results is caused by the different scaling criteria for gas and EMS stirring in water experiments, which can be improved in future work. The results obtained in the water experiment confirm that the additional soft stirring by gas in the EMGAS approach has no negative impact on the mixing time results. It can be beneficial in the case of horizontal EMGAS in industrial applications, as the additional gas has a positive influence in the case of the inclusions removal process.

All the presented results enable to prepare the final conclusions. From a metallurgical perspective, a separate discussion can be held regarding the benefits of the EMGAS approach. The observations confirm that the EMS system ensures much better flow control[78]. Moreover, the EMGAS vertical stirring ensures increased contact between gas bubbles and steel and effective control of the turbulences at the interface between slag and metal. This type of stirring ensures a shorter residence time of steel in the top area of the furnace (slag and metal interface). On the other hand, the EMGAS horizontal stirring is responsible for increased contact area between gas bubbles and steel, while also reducing turbulences at the interface between slag and metal. At the same time, an increased residence time of the steel in the top area of the furnace, near the interface between the slag and metal, which increases the absorption of inclusions into the slag, is evident.

In the case of the inclusions, the more homogenous distribution of the velocity prevents the occurrence of the dead zones and increases the generation of the larger inclusions, which can be transported to the slag layer.

As presented, the advantages of EMS solutions encourage the improvement of the technology to achieve even more homogeneous flow with high stirring energy and a more stable behavior of the free surface. Such research can additionally increase the cleanliness of the steel.

8. Development of the robust CFD simulations of tundish

8.1 Motivation for CFD simulations in tundish

Similar to other metallurgical equipment described above, a significant amount of research has also been conducted to improve the efficiency of the mixing process inside the tundish. In this case, homogenization of the velocity and temperature distribution is required to increase the efficiency of the inclusion removal process and prevent the clogging of strands caused by improper solidification and sedimentation processes.

As described in Chapter 2, the tundish is the vessel responsible for distributing the molten steel into the casting strands to the casting machine, and its geometry depends on the number of strands. In this case, the velocity and temperature distribution are very important due to the presence of so-called dead zones, which can lead to quality issues and clogging of the strand's outlets, which can be dangerous and force production faults.

The additional, very important function of the tundish is again the inclusion removal process, which can be improved by proper modelling of the flow control devices.

Operations like the non-metallic inclusion removal process can be improved by proper selection of the dams/weirs or baffle walls in the tundish to increase the mixing and increase the residence time of steel.

The efficiency of the inclusion removal process is based on the improved flotation of the inclusions by increasing the ratio of plug flow volume to dead zone volume. However, the mentioned, commonly used solutions do not ensure homogenized and efficient flow among multiple strands. Moreover, it is observed that the inclusions smaller than 50 [μm] are difficult to remove.

The new approach with the EMS solution, which is a novel method to increase the mixing inside the tundish, could prevent the dead zones. Gentle EMS stirring is expected to increase the active volume of liquid steel and decrease the dead zone area, homogenize the temperature among the different strands and improve the cleanliness of the steel by the increased residence time. The latter can lead to an increase in the probability of additional collisions of inclusions and their better adhesion to the slag layer. Moreover, the direction and strength of the stirring can be freely modified by the EMS. As a result, baffle walls, dams, and weirs can be eliminated, which simplifies the tundish design. The EMS system is used outside the tundish and does not come into contact with hot, liquid steel, which is important from a maintenance point of view.

8.2 Description of the model

8.2.1 Geometry

The overview of the investigated industrial 40-ton multi-strand billet caster tundish geometry with the location of the EMS system is presented in Figure 113.

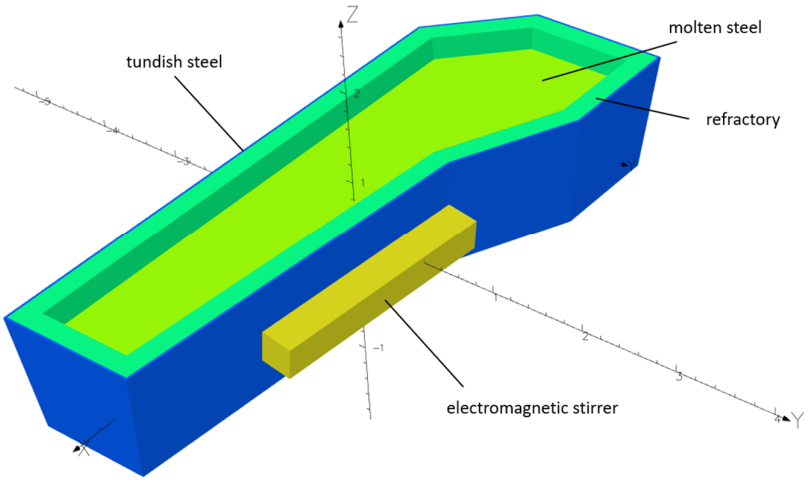


Figure 113. The geometry of the investigated industrial 40-ton tundish with EMS system.

The CFD results for the case with the EMS system were compared to the results for the standard tundish geometry with baffle walls. The parametric study was also prepared for different dimensions of the dam and weir in the case of the EMS solution to investigate their influence on the results. As a result, the best configuration to increase the homogeneity and prevent the clogging phenomena was proposed.

The developed fluid domains of the CFD models for the EMS and baffle wall cases of tundish are presented in Figure 114.

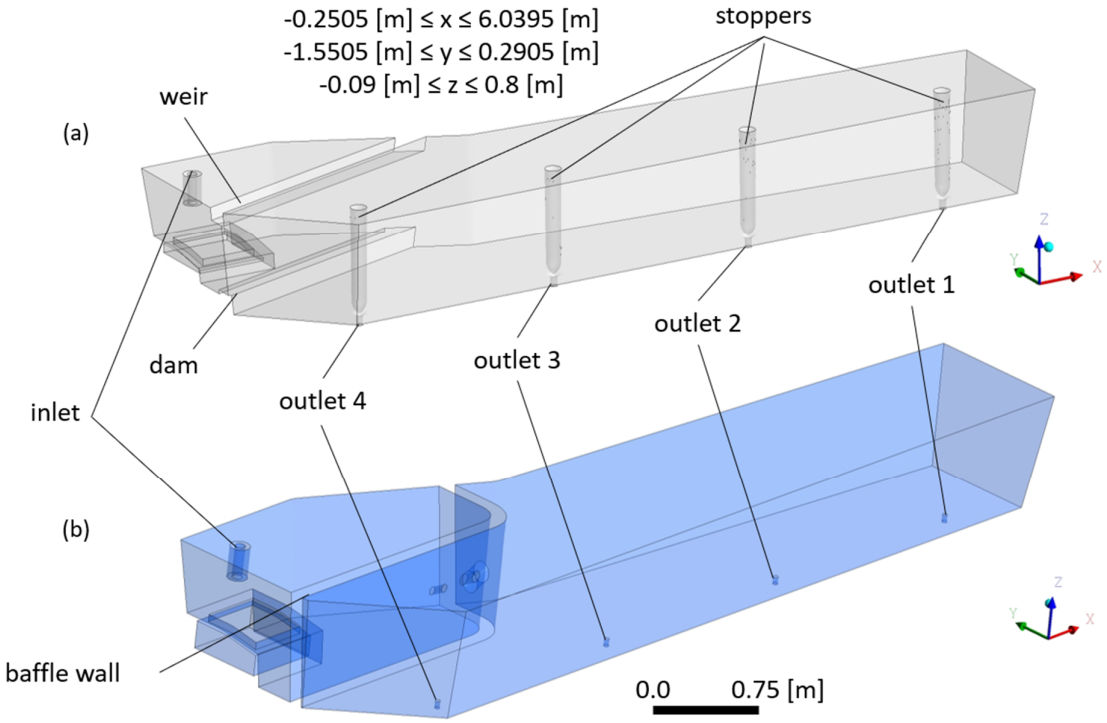


Figure 114. The geometries of the tundish used in the CFD simulations (a) with EMS and (b) with baffle wall.

The EMS tundish model also contains additional stoppers, which are used to control the mass flow rate via each outlet and are a safety system in case of any failure in the production line.

The investigations of the tundish with the EMS include the comparison between different stirring powers and the flow direction. The tundish without additional improvements and a typical baffle wall case were simulated to compare the efficiency of the EMS approach. The summary of the investigated case studies is presented in Table 23.

Table 23. Summary of the tundish parametric studies.

Case no.	Description
1	without EMS, without baffle wall, without stoppers
2	with 100% of EMS, without baffle wall, without stoppers
3	with 100% of EMS, reversed direction of stirring, without baffle wall, without stoppers
4	without EMS, with baffle wall
5	with 100% of EMS, without baffle wall, with stoppers
6	with 84% of EMS, without baffle wall, with stoppers
7	with 69% of EMS, without baffle wall, with stoppers
8	with 60% of EMS, without baffle wall, with stoppers
9	with 31% of EMS, without baffle wall, with stoppers

Moreover, a separate parametric study of the influence of dams' and weirs' dimensions, in relation to the EMS power influence on the steel flow, was conducted. The main goal was to understand the clogging phenomena and find the solution (proper dimensions of dams', weirs' and free opening and EMS power) to prevent such an issue. The summary of the evaluated cases is presented in Table 24.

Table 24. Summary of the parametric study for tundish with EMS system.

Case No.	**Current [Amp]**	**Force factor**	**Dam height [mm]**	**Weir depth [mm]**	**Free opening [mm]**	**Mass flow at inlet [ton/min]**	**Bath depth [mm]**
11	360	1.00	150	100	550	1.3	800
12	330	0.84	150	100	550	1.3	800
13	300	0.69	150	100	550	1.3	800
14	280	0.60	150	100	550	1.3	800
15	200	0.31	150	100	550	1.3	800
21	360	1.00	250	200	350	1.3	800
22	330	0.84	250	200	350	1.3	800
23	300	0.69	250	200	350	1.3	800

24	280	0.60	250	200	350	1.3	800
25	200	0.31	250	200	350	1.3	800
31	360	1.00	350	200	250	1.3	800
32	330	0.84	350	200	250	1.3	800
33	300	0.69	350	200	250	1.3	800
34	280	0.60	350	200	250	1.3	800
35	200	0.31	350	200	250	1.3	800
41	360	1.00	150	200	450	1.3	800
42	330	0.84	150	200	450	1.3	800
43	300	0.69	150	200	450	1.3	800
44	280	0.60	150	200	450	1.3	800
45	200	0.31	150	200	450	1.3	800
51	360	1.00	250	100	450	1.3	800
52	330	0.84	250	100	450	1.3	800
53	300	0.69	250	100	450	1.3	800
54	280	0.60	250	100	450	1.3	800
55	200	0.31	250	100	450	1.3	800
61	360	1.00	350	100	350	1.3	800
62	330	0.84	350	100	350	1.3	800
63	300	0.69	350	100	350	1.3	800
64	280	0.60	350	100	350	1.3	800
65	200	0.31	350	100	350	1.3	800

8.2.2 Boundary and initial conditions

All the cases include the standard wall boundary conditions without slip except the top wall, which is modelled without shear stress. This type of boundary condition maps the free surface conditions. Moreover, four active outlets are modelled as pressure outlet boundary conditions without any additional bulk pressure to enable free flow via each outlet. The mass flow rate of the molten steel via the inlet is equal to 1.3 [ton/min] for each case.

The investigations focus on the evaluation of velocity and stirring energy distribution without considering the energy equation. One exception is related to the simulation with temperature homogenization, where the temperature distribution is evaluated. The setup of that case requires the energy equation and the definition of proper boundary conditions related to the heat exchange at specific walls. The temperature of the injected molten steel is also needed to properly evaluate the temperature distribution inside the tundish. The description of the temperature boundary conditions is based on qualitative considerations and is presented in Figure 115.

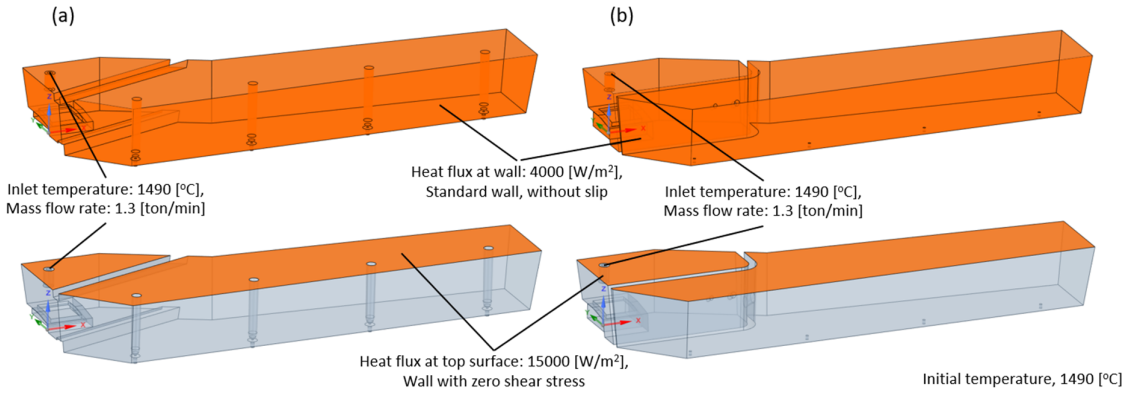


Figure 115. Temperature boundary conditions in the case of tundish geometry (a) with stoppers and (b) with baffle wall.

8.2.3 Material properties

The molten steel is modelled as incompressible, viscous fluid due to the turbulent character of the flow inside the tundish. In the case of the simulation, in which the energy equation is enabled to measure the temperature distribution and homogenization inside the cavity, the additional properties, such as specific heat and thermal conductivity, need to be specified. The summary of the steel properties used in the numerical simulation is presented in Table 25.

Table 25. Material properties used for CFD simulation of the tundish.

Material properties	
Melt density [kg/m^3]	7200
Melt viscosity [kg/(m s)]	0.0072
Specific heat [J/(kg K)]	692
Thermal conductivity [W/(m K)]	35

8.2.4 Mesh sensitivity study

As in the previous cases, the mesh sensitivity study was performed first to ensure the quality of the developed model. The analysis was done with the steady-state simulations for geometry presented in Figure 114a. The comparison was conducted for four different meshes: mesh 1 – very coarse, mesh 2 – coarse, mesh 3 – medium, mesh 4 – fine. The corresponding cross-section along outlets positions is presented in Figure 116. The number of cells in each mesh is summarized in Table 26.

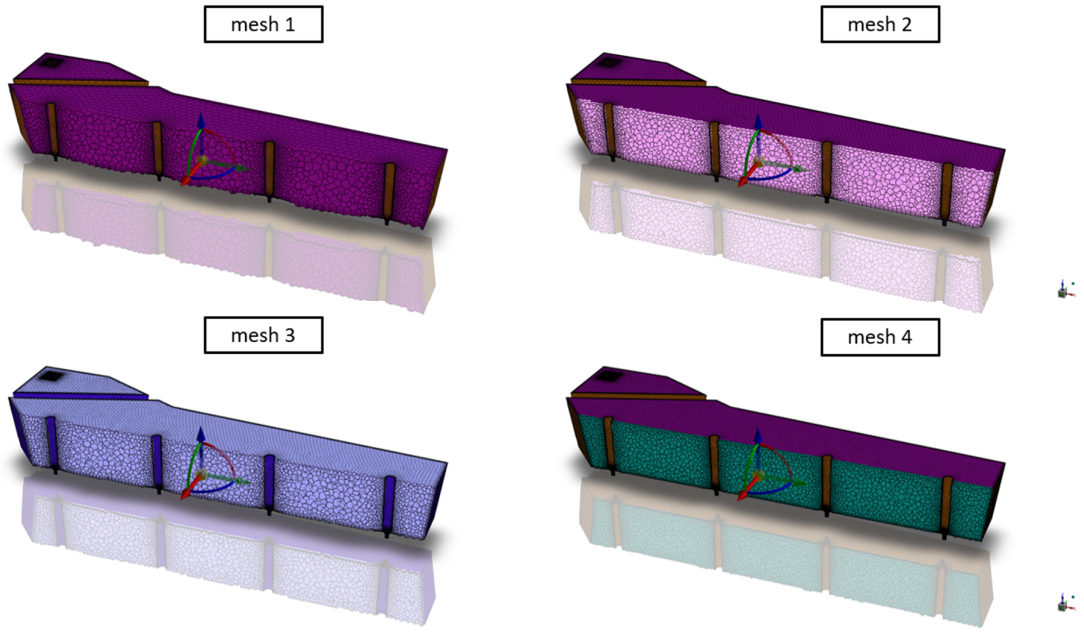


Figure 116. Different meshes in the mesh sensitivity study of tundish.

Table 26. A number of finite volume elements for each mesh in the mesh sensitivity study.

Mesh no.	Number of elements
mesh 1	149 248
mesh 2	176 298
mesh 3	264 270
mesh 4	592 041

The results evaluation confirmed that mesh number 3 is the best selection for further investigations. The mesh number 1 is too coarse as the error between results (average value of the turbulent kinetic energy in the tundish domain) is up to 17%. Between the rest of the results, the error is around 3%. Mesh 4, which is the finest mesh, is not used due to the extended simulation time. The comparison between the obtained results is presented in Figure 117 (average value of velocity) and in Figure 118 (average value of turbulent kinetic energy).

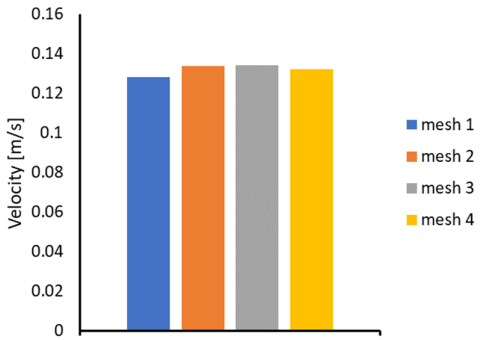


Figure 117. The average value of the velocity in the whole tundish domain obtained during the mesh sensitivity study.

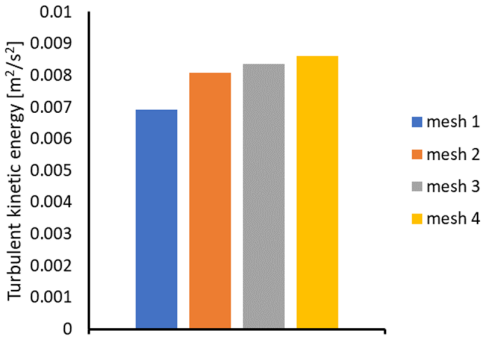


Figure 118. The average value of the turbulent kinetic energy in the whole tundish domain obtained during the mesh sensitivity study.

The graphical comparison between the obtained results for the different investigated meshes is presented in Figure 119 and Figure 120.

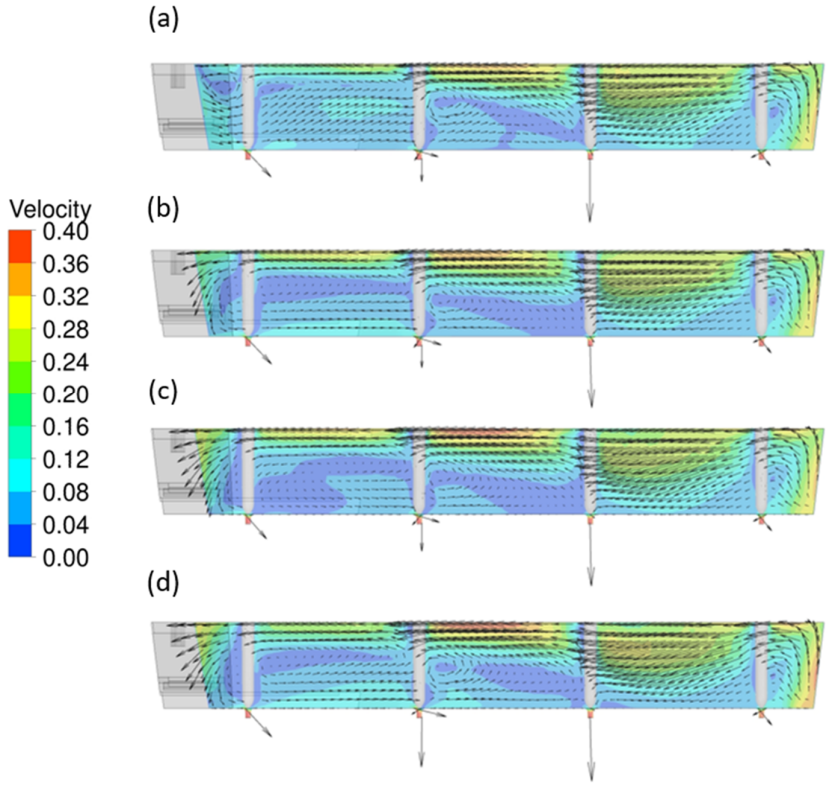


Figure 119. Velocity distribution in the cross-section via middle of the outlets for (a) mesh 1, (b) mesh 2, (c) mesh 3, (d) mesh 4.

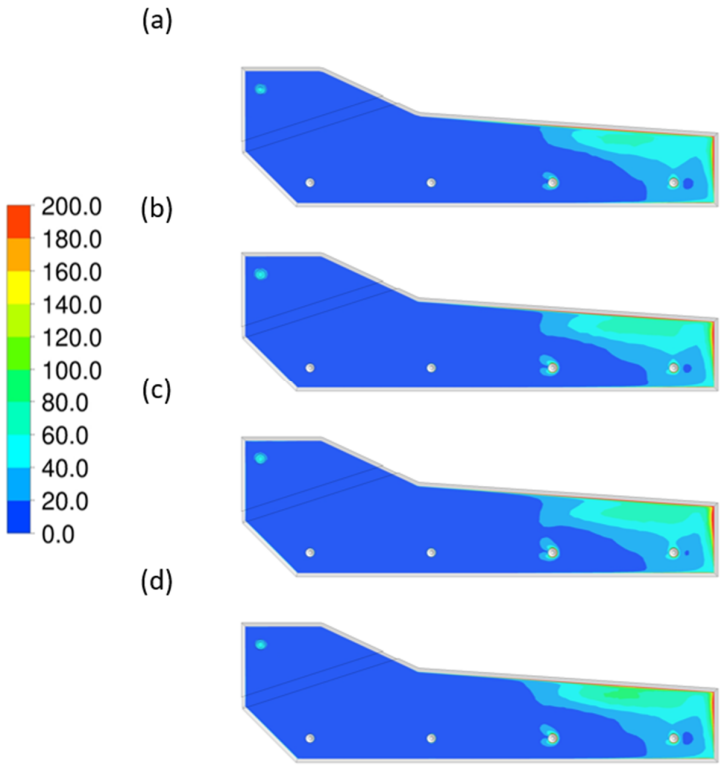


Figure 120. Stirring energy distribution in the cross-section via middle of the height of the tundish for (a) mesh 1, (b) mesh 2, (c) mesh 3, (d) mesh 4.

The graphical interpretation of the results confirms that there is no significant difference between the velocity and stirring energy distribution on selected planes for different mesh sizes. Therefore, as mentioned, mesh number 3 was used for further investigations. In the case of the geometry with a baffle wall, the same method and size distribution as for case number 3 were used.

After the mesh sensitivity study and selection of the discretization scheme, which did not affect the results, the main numerical studies were conducted focusing on the mixing, dead zones evaluation, and clogging of outlets.

8.3 Comparison between cases without EMS, with baffle wall and with EMS

8.3.1 Mixing

CFD simulations help to understand the flow inside the tundish under the additional electromagnetic forces. Based on the evaluated turbulent dissipation rate that occurs in the molten steel, the stirring energy can be calculated. The first comparison between the velocity and stirring energy distribution for 100% , 84%, 69%, 60% and 31% of EMS stirring force and for the case with stoppers is presented in Figure 121. It should also be pointed out that inside the tundish, the clogging of outlets is a rather common phenomenon and depends on the solidification of the molten steel, mainly in the areas of the dead zones and areas affected by

sedimentation, where different remains detach from the walls and tend to obstruct the outlets. This issue is frequently observed inside the tundish because of the relatively low stirring energy compared to the ladle furnace, where the mixing process is the most intensive. This topic will be described in detail in Section 8.3.3. In general, the analysis of the stirring energy close to the outlets can improve the design process and optimization of the operation of the device. The exemplary comparison between the stirring energy distribution in the area of each outlet for cases with stoppers for 100% and 31% of EMS is presented in Figure 122.

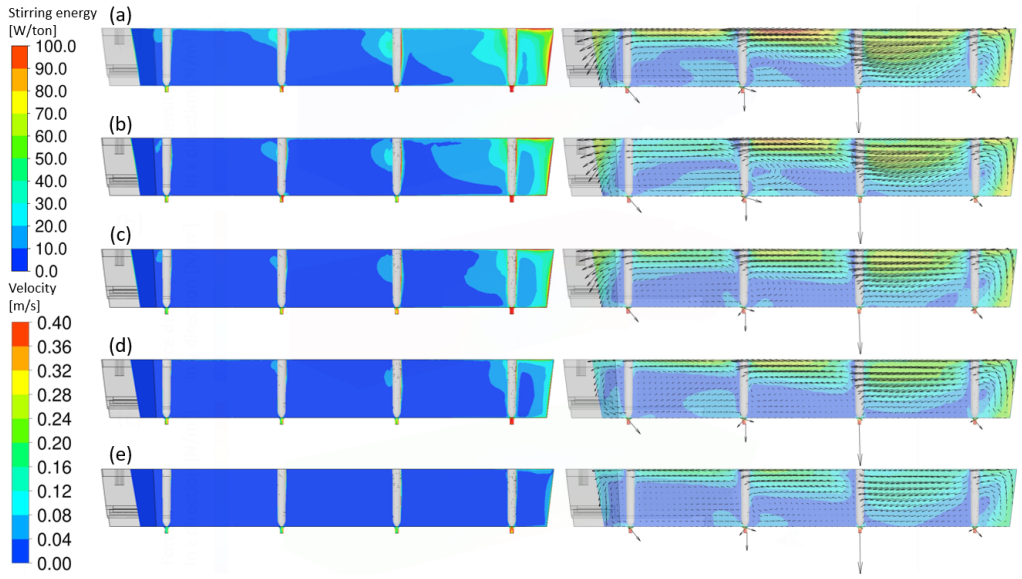


Figure 121. Stirring energy (left) and velocity (right) distribution for different EMS force factors (a) 100% - case no. 5, (b) 84% - case no. 6, (c) 69% - case no. 7, (d) 60% - case no. 8, (f) 31% - case no. 9.

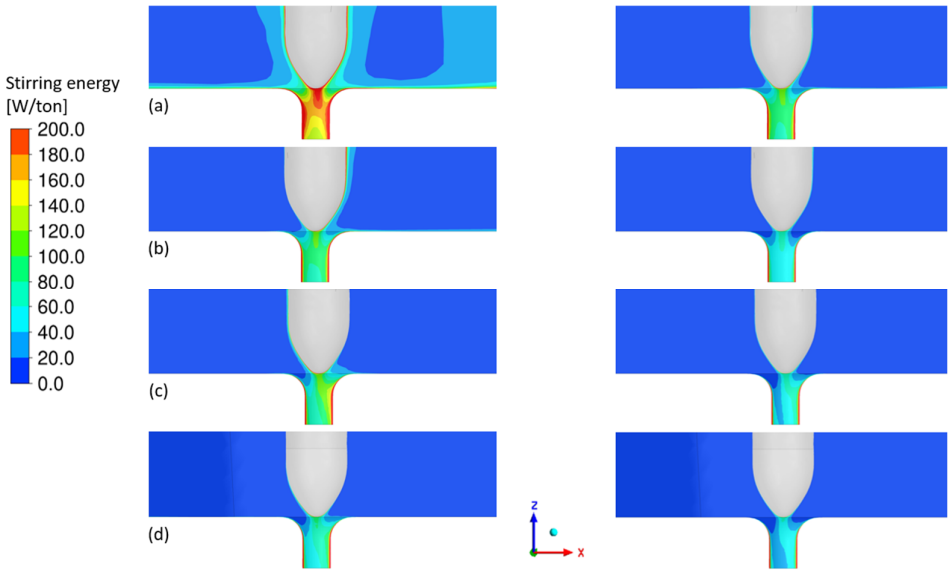


Figure 122. Stirring energy distribution for case no. 5, 100% of EMS (left) and case no. 9, 31% of EMS (right) for different outlets: (a) outlet 1, (b) outlet 2, (c) outlet 3, (d) outlet 4.

Based on Figure 122, stirring energy distribution close to outlet 3 has the most asymmetric character, and the gradients of the values are the highest. The results confirm that the proper selection of the EMS system is crucial for correct flow behavior in the tundish. As mentioned, a more detailed analysis of the areas close to the tundish outlets from the point of view of clogging will be presented in the further part of the work.

All the above investigations are directly related to the mixing process, which occurs thanks to the EMS system. Visualization of the mixing operation in the molten steel is realized by additional discrete phase particles available in the discrete phase model, which interact with the continuous phase. To understand the flow behavior, the massless particles were injected into the domain in accordance with the boundary conditions of the stream. Such tracers travel with the continuous phase and enable observation of the movement of liquid steel. The observation of the tracers in the numerical model can be compared to the analysis of the dye injected into the water during the water model tests, like it will be presented in Section 8.4 related to the water model experiments, especially in Figure 147. The flow of particles inside the device is presented in Figure 123 and Figure 124, where four different cases were compared. The simulation model without any additional control devices is presented as a reference case. Then, the results for the case with 100% of EMS are shown.

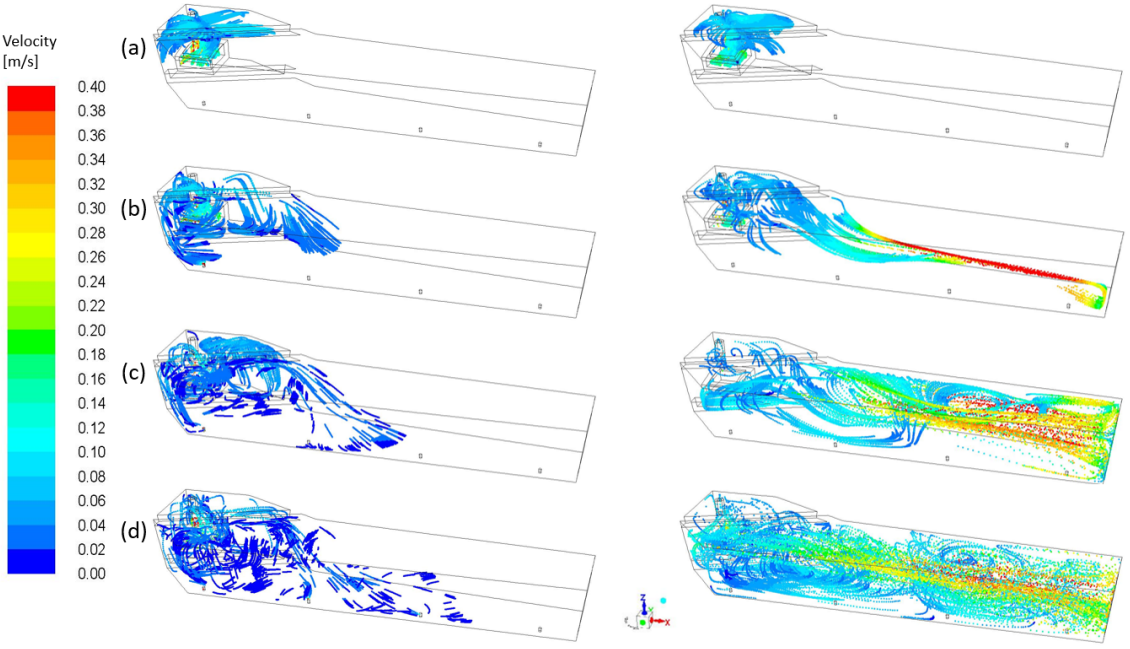


Figure 123. Massless DPM tracers to visualize the mixing process for case no. 1 without EMS, without baffle wall (left) and for case no. 2 with 100% of EMS, the normal direction of stirring at (a) 20 [s], (b) 50 [s], (c) 100 [s], (d) 200 [s].

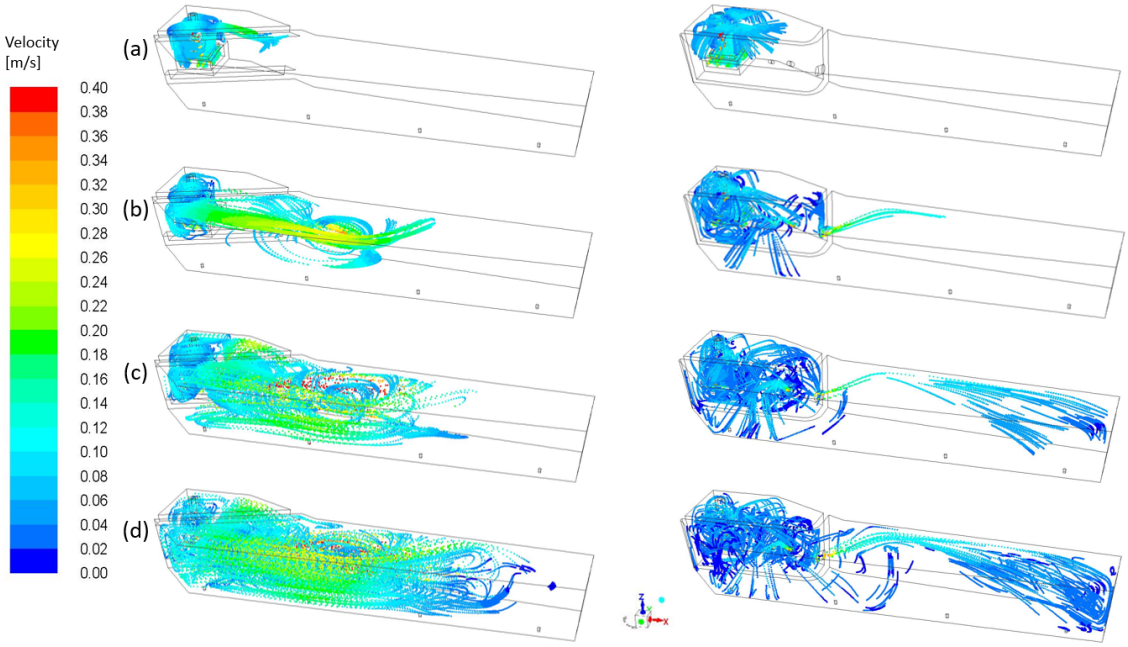


Figure 124. Massless DPM tracers to visualize the mixing process for case no. 3 with 100% of EMS, reversed direction of stirring (left), and for case no. 4 without EMS, with baffle wall at (a) 20 [s], (b) 50 [s], (c) 100 [s], (d) 200 [s].

The investigation also included the reversed direction of the stirring to compare the behavior of particles and the results with a common control device like a baffle wall with openings used to improve the liquid steel mixing process. The comparison confirms that the best mixing is presented in the case with 100% EMS stirring. The results are significantly better than those for the case with the baffle wall, indicating the high efficiency of homogenizing velocities and temperatures. The obtained results also indicate an improvement in the inclusion removal process, which is important for enhancing steel quality.

Visualization of mixing suggests that the EMS system is a great solution to increase the mixing efficiency without the presence of dead areas. Moreover, the reduction of the dead zones in the flow domain positively influences the clogging of the outlets, as it lowers the risk of obstruction. A more detailed description of the problem will be presented in Section 8.3.3.

As mentioned, the numerical calculations were performed for both the normal and reversed directions of the stirring. The results suggest that the normal direction of stirring is more efficient than in the reverse direction. Based on these results, only the normal direction of stirring will be taken into account in further investigations.

8.3.2 RTD curves and dead zone calculations

The flow control theory in tundish includes investigations of three main flow zones: the plug, well-mixed, and dead zones, to classify regions where the flow improvement is required. The investigations are based on the combined or mixed models[37] that assume three different regimes of the flow regions mentioned above. For further analysis, the models will be used to judge the mixing efficiency inside the vessel. The investigations are based on the Residence

Time Distribution (RTD) curves, where two types of the curves are distinguished: C-curve and F-curve. The C-curve represents the response of the pulse-injected tracer, which is a commonly used method to model the steady conditions of the continuous casting, while the F-curve tracks the response of the continuously injected tracer. The F-curve method is used to model the transient conditions in continuous casting, such as changes in the steel grade or ladle during the process. For both methods, the concentration of the tracer at each outlet is measured to provide the RTD curve. The CFD simulation was prepared for a multi-strand billet caster tundish, and calculations of active (plug and well-mixed volumes) and dead volumes were performed for the model with four outlets. The main goal of the analysis was to assess the effectiveness of the new mixing method based on the EMS system used for tundish. Due to a significant number of obtained results only selected ones will be presented within this work.

The flow control theory is considered in the whole volume of the tundish (V). The first region, named the active region, includes both the plug and well-mixed regions of the flow. For the ideal case, the plug volume (V_p) corresponds to the tracer's minimum residence time and maximum dimensionless concentration (C). Well-mixed volume (V_m), for the ideal case, is characterized by the initial concentration of the tracer equal to 1, which then decreases exponentially over dimensionless time (θ). The graphical interpretation of the active volume is presented in Figure 125. It is worth mentioning that there are two different schemes of creation of the active volume, where the order of the plug and well-mixed region could be reversed, but both give the same result of the tracer response.

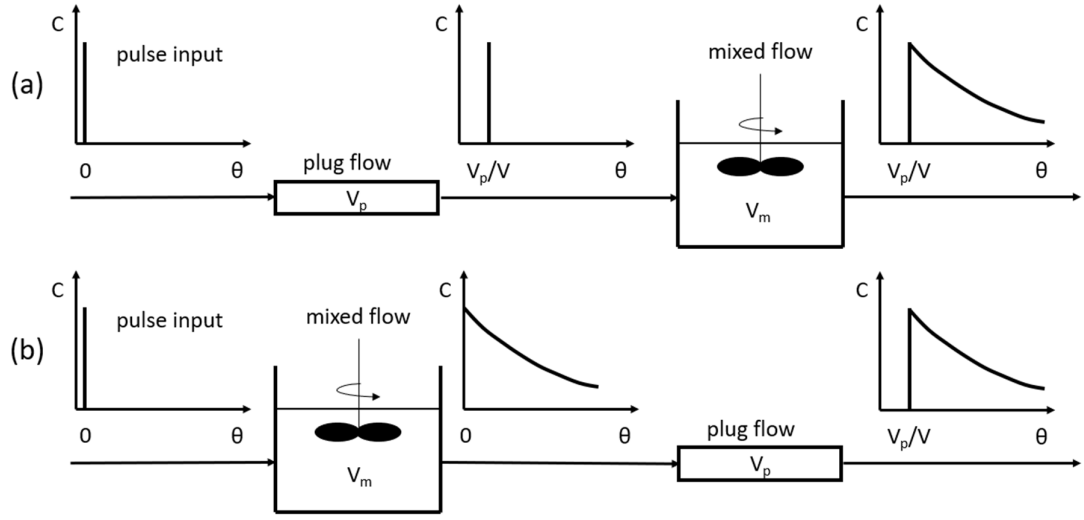


Figure 125. The combined model of the active volume (plug and well-mixed volumes) for two different scenarios (a) scheme 1 and (b) scheme 2.

The active volume can be described by the ideal mixing curve presented in Figure 126. Representation of the ideal mixing curve is related to the vessel without the presence of any dead regions.

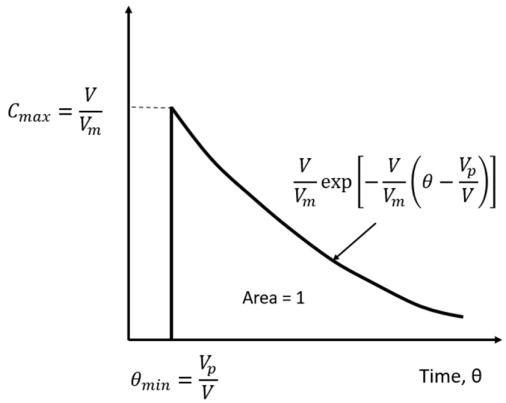


Figure 126. Representation of the ideal mixing curve (C-curve).

The second region, named the dead region, is another volume identified in the tundish flow analyses. The flow region is divided into the active volume (V_a), which includes both the plug and well-mixed volumes, and the dead volume (V_d). The total volume flow rate (Q) occurring in the system is also divided into the active (Q_a) flow rate through the active volume and into the dead (Q_d) flow rate through the dead volume.

For the combined model, the graphical interpretation of the aforementioned regions, along with their corresponding volume flow rates, is presented in Figure 127.

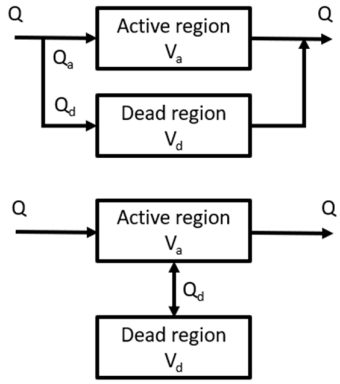


Figure 127. Graphical illustration of the volume flow rate via the active and dead regions in a combined model.

Two different types of dead volume regions are distinguished. The first is characterized by a stagnant velocity distribution, leading to no flow exchange between the active and dead volumes. The second one is characterized by the very slow motion of the fluid in that region, which means that some part of the fluid remain much longer in the device. Levenspiel[256] created the definition, which describes this dead region as the portion of fluid which remains in the vessel for a period over two times longer than the theoretical mean residence time for this device. The dead volume for the exemplary C-curve is presented in Figure 128.

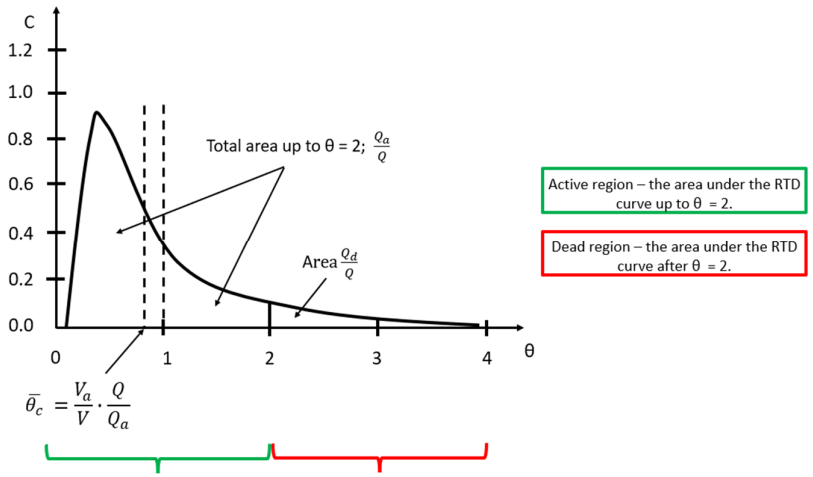


Figure 128. Active and dead volumes based on the C-curve.

The investigations included preparations of the simulation model to obtain such RTD curves. The analysis was done for the case without baffle wall, stoppers and EMS system as a reference (case number 1), for the model with baffle wall presented in Figure 114b, without EMS stirring (case number 4) and for EMS with 100% of its power and geometry with stoppers presented in Figure 114a (case number 5). The concentration of the tracer at each outlet was measured during the whole simulation time. The obtained C-curve results for three main cases are presented in Figure 129. The character of the shape of the curves for the case without any flow control device and the case with EMS stirring will be compared to the results obtained during the water model tests in the next part of the work. Moreover, the additional comparison between different EMS power includes cases 5, 6, 7, 8 and 9, where the EMS power is reduced gradually from 100 to 31%. The comparison of the C-curve shape for this analysis is presented in Figure 130. The results indicate the high efficiency of the EMS system even with its reduced power. Moreover, an additional parameter study was prepared to observe the flow behavior of different dimensions of the dam and weir under different stirring strengths. The analysis was based on both types of RTD curves, for C-curve and F-curve, but only selected, most interesting results characterized by a high risk of clogging will be presented is Section 8.3.3 of this work.

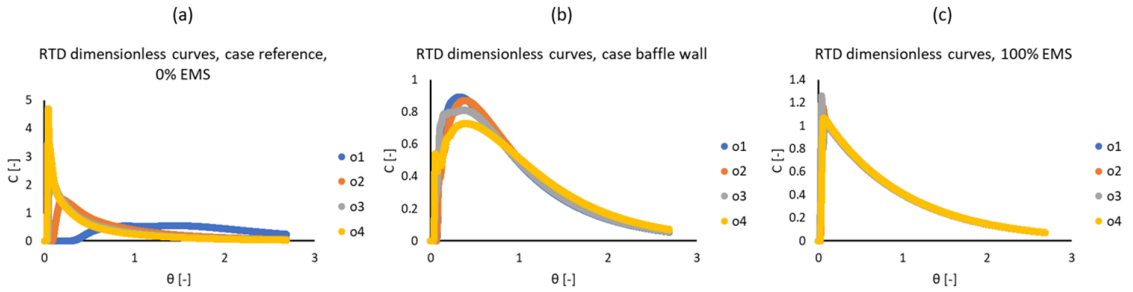


Figure 129. C-curves for (a) reference case without EMS, without baffle wall, (b) case with baffle wall and (c) case with 100% of EMS and without baffle wall, with stoppers.

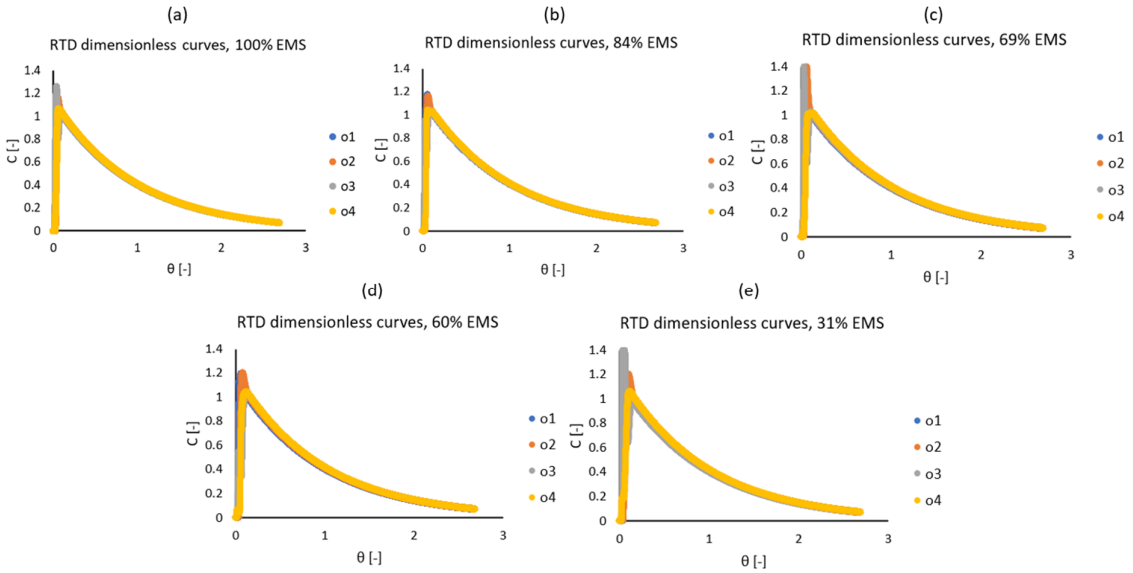


Figure 130. C-curves for (a) case with 100% of EMS and without baffle wall, with stoppers, (b) case with 84% of EMS and without baffle wall, with stoppers, (c) case with 69% of EMS and without baffle wall, with stoppers, (d) case with 60% of EMS and without baffle wall, with stoppers and (e) case with 31% of EMS and without baffle wall, with stoppers.

The C-curves obtained with different EMS power have a similar shape to the ideal mixing curve shape for each strand, which suggests that the efficiency of the EMS stirring is high, and even small input power greatly increases the homogeneity.

The dead, plug and well-mixed volumes were calculated according to the combined model[36,106] for multi-strand billet caster tundish. The results are presented in Table 27. It is confirmed that the dead volume is the highest for the case without a flow control device, in which the high plug volume is also observed. The biggest well-mixed volume and the smallest plug volume are observed in the case with EMS stirring. Moreover, the character of the curves is very similar to the ideal mixing curves. Based on the analysis of these curves, the combined method does not appear to be a good fit for EMS systems, as the curves are similar to the ideal mixing curve, yet still have a considerable value for the dead zone volume. Based on the combined model, it seems that the case with the existing baffle wall should provide the best mixing, which is not true due to observations of the dead zones in the geometry of the tundish.

To visualize the behavior of the tracer in the numerical model and qualitatively compare the simulation and test results, the concentration of the tracer was measured in the whole domain of the tundish during the calculation process. The visualization of the tracer includes the domain above the selected threshold of the concentration to observe its behavior. The results for cases without flow control device and with EMS are presented in Figure 131. These results can be compared to the pictures from water model tests presented in Figure 147 in the next section of the work.

Table 27. Dead, plug and well-mixed volume for analyzed cases.

Case	Dead volume [%]	Plug volume [%]	Well-mixed volume [%]
without EMS, without baffle wall	36.6	14.1	49.3
without EMS, with baffle wall	26.4	13.2	60.5
with 100% of EMS, without baffle wall, with stoppers	34.6	2.2	63.3
with 84% of EMS, without baffle wall, with stoppers	34.2	2.7	63.0
with 69% of EMS, without baffle wall, with stoppers	34.3	3.1	62.5
with 60% of EMS, without baffle wall, with stoppers	33.7	3.7	62.6
with 31% of EMS, without baffle wall, with stoppers	33.7	3.7	62.6

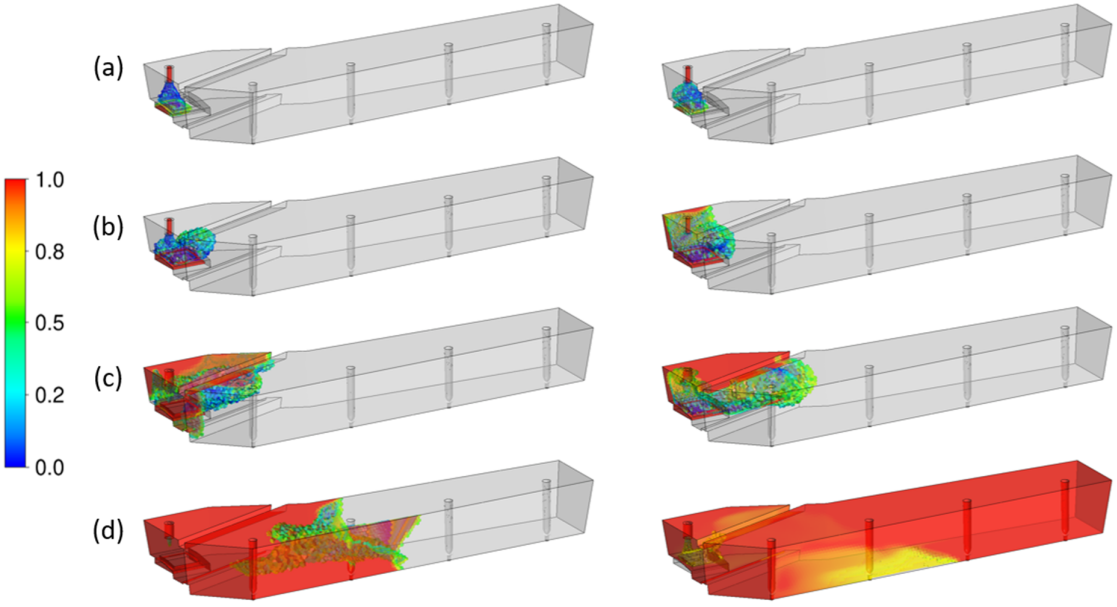


Figure 131. Dimensionless concentration of a tracer obtained from CFD simulation for the case without flow control device (left) and for the case with EMS system (right) for (a) tracer start injection time, (b) observations after 5 [s], (c) observations after 20 [s] and (d) observations after 120 [s].

To visualize the effect of the existing baffle wall, the dimensionless concentration of the tracer for case number 4 is presented in Figure 132.

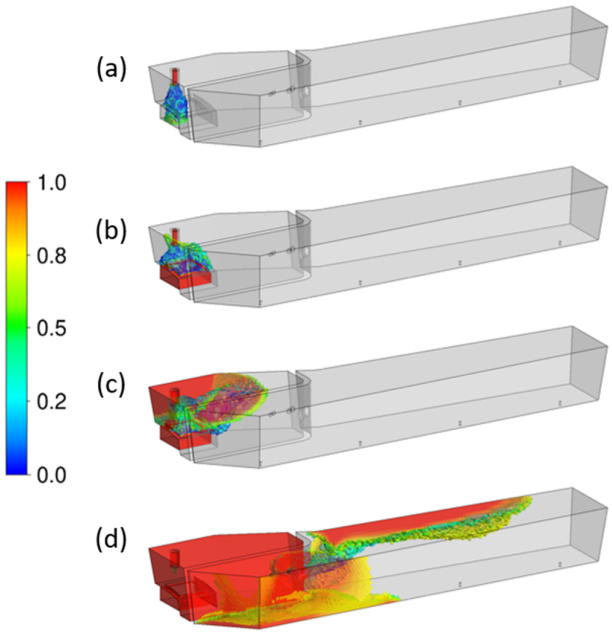


Figure 132. Dimensionless concentration of a tracer obtained from CFD simulation for the case with standard, existing baffle wall for (a) tracer start injection time, (b) observations after 5 [s], (c) observations after 20 [s] and (d) observations after 120 [s].

The above-obtained data confirm the significantly greater effectiveness of mixing in the case with the new EMS system. The mixing time with the new stirring method is shorter, the plug volume is reduced, the RTD curves are similar to the ideal mixing curve, and the character of the curves is similar for each strand, which suggests high homogeneity of the steel.

The additional analysis included the numerical calculations of the F-curve. The model's boundary conditions include the constant injection of the tracer into the tundish via the inlet. The analysis was prepared similarly as it was for the C-curves, for three representative cases and for the EMS power study. Only results for the case without the flow control device (case number 1), for the case with the EMS system (case number 5) and the case with the baffle wall (case number 4) are presented in Figure 133. The study of EMS power (cases number 5-9) is presented in Figure 134.

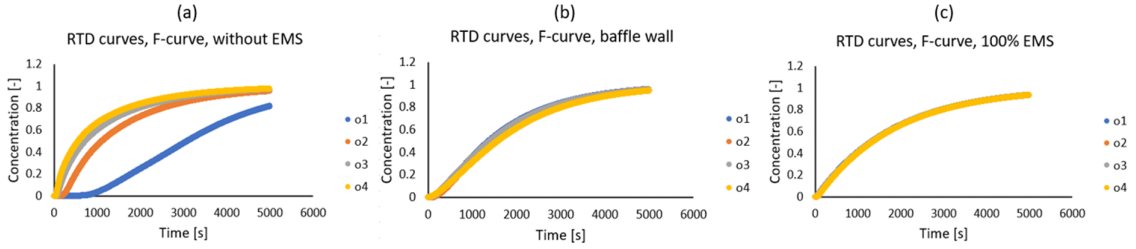


Figure 133. F-curves for (a) reference case without EMS, without baffle wall, (b) case with baffle wall and (c) case with 100% of EMS and without baffle wall, with stoppers.

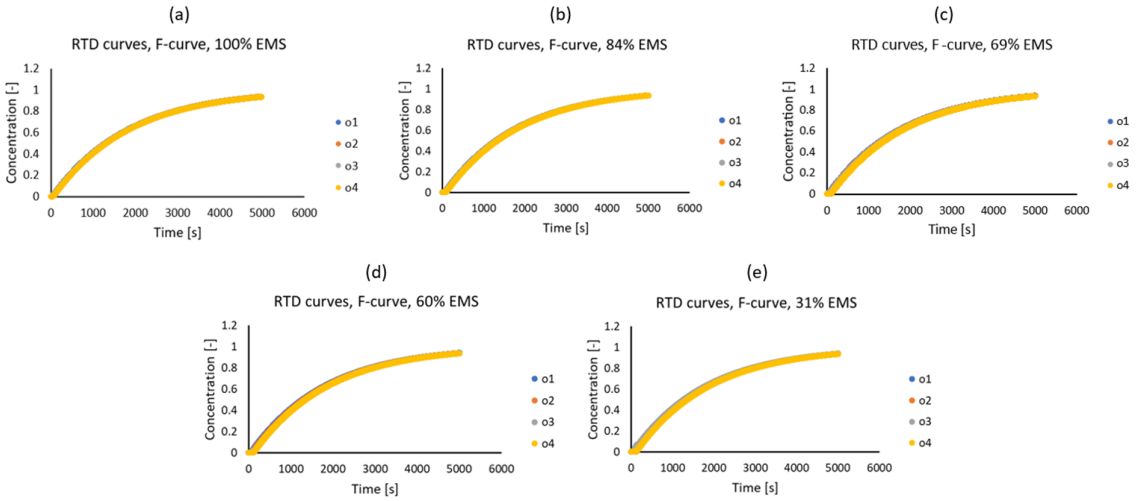


Figure 134. F-curves for (a) case with 100% of EMS and without baffle wall, with stoppers, (b) case with 84% of EMS and without baffle wall, with stoppers, (c) case with 69% of EMS and without baffle wall, with stoppers, (d) case with 60% of EMS and without baffle wall, with stoppers and (e) case with 31% of EMS and without baffle wall, with stoppers.

The obtained results confirm a high level of similarity between different strands for EMS stirring and for different EMS power, which means that the homogenization of the steel in the whole volume of the tundish is effective. This behavior ensures a smooth transition between the steel grades after ladle changes. Moreover, the additional parametric study revealed that even applying low power levels to the EMS is enough to obtain a very good distribution of curves and homogenized structure in the whole bath. It enables a reduction of the power consumption needed for the stirring process.

To extend this investigation, an additional analysis of temperature homogenization was performed to observe and measure the temperature distribution and reduce the risk of earlier solidification. The latter can lead to the clogging of the tundish outlets. The numerical simulations were prepared for three representative models: without any flow control device, for the case with a standard baffle wall and with an EMS system. The full EMS power study was not presented due to the similarity of the RTD curves in all of the calculated cases, which suggests a similar effectiveness of homogenization in the case of EMS stirring. The boundary conditions applied in these simulations are described in Section 8.2.2 and presented in detail in Figure 115.

To simplify and speed up the analysis, only a steady-state CFD simulation was performed for each case to obtain stable conditions in the tundish. Moreover, the real process is difficult to realize in CFD simulation due to the difficulties with recognition of the real boundary conditions resulting from the very expensive and difficult measurement methods. The heat transfer analysis has a qualitative character, where the same boundary conditions were applied to each model to compare the temperature distribution and measure the temperature at each outlet, as well as throughout the entire domain of the molten steel. The comparison between the

temperature distribution in representative cases: case 1 – without EMS, without baffle wall, case 4 – without EMS with baffle wall and case 5 – with 100% of EMS, without baffle wall and with stoppers is presented in Figure 135. It can be clearly observed that the most homogenized temperature field is in the case with EMS.

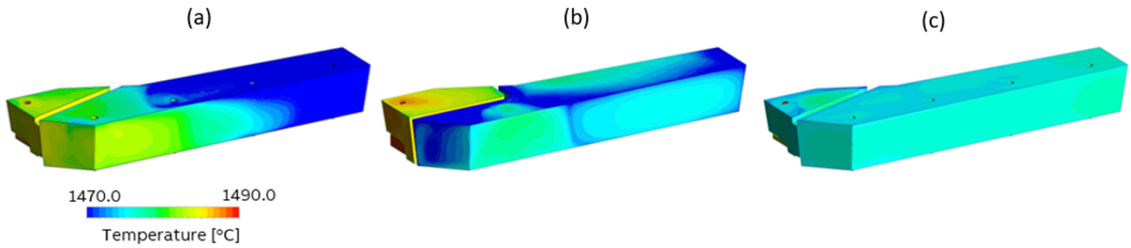


Figure 135. Temperature distribution for (a) case 1 (b) case 4, and (c) case 5.

The homogenization process can also be monitored through the measurements of the average temperature at each outlet of the tundish. An even temperature profile indicates consistent steel behavior across all strands. Comparison of temperature profiles obtained for various cases: with EMS system and three different electrical current levels (200 [A] (31% of EMS power), 300 [A] (69% of EMS power) and 360 [A] (100% of EMS power)), without EMS but with baffle wall, and without EMS and baffle wall is presented in Figure 136. It is evident that the worst temperature distribution occurs in the case without any flow control, where the maximum difference at the outlets exceeds 15 [°C]. The introduction of a baffle wall significantly improves the situation, but the best results are achieved with the use of EMS, where nearly identical results were observed for all tested current levels.

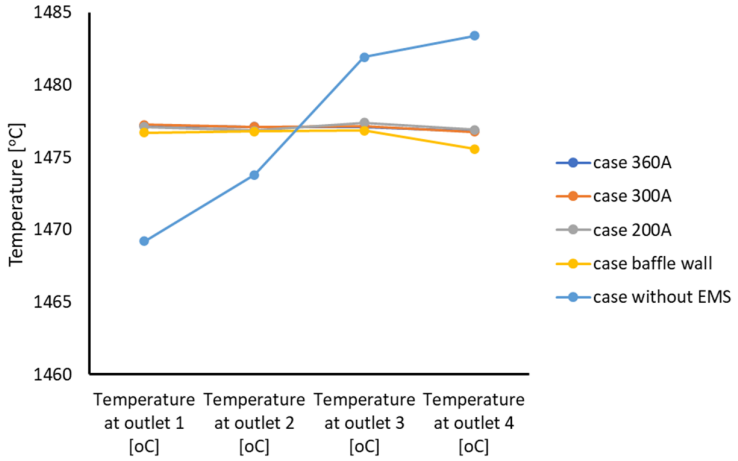


Figure 136. Temperature measured at each outlet.

Moreover, a comparison between the volume-average and minimum temperatures is prepared to better understand the temperature differences inside the tundish, as shown in Figure 137.

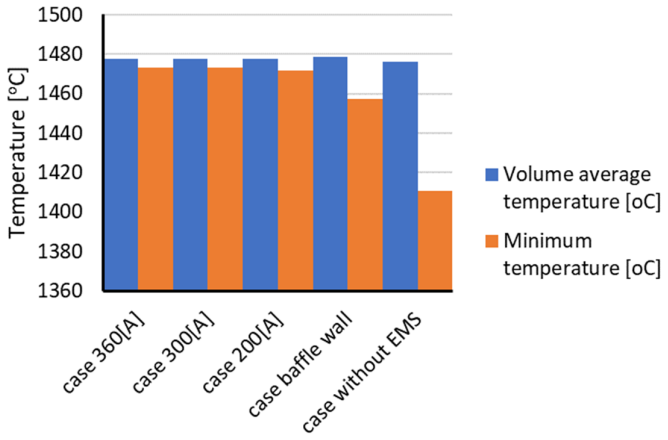


Figure 137. A volume average and minimum temperatures measured in the whole bath of tundish.

The above comparison is very important from a metallurgical point of view. The difference between the volume average and minimum temperatures inside the melt domain suggests that the solidification phenomenon may occur earlier, which increases the risk of clogging and inhomogeneous properties of the steel. Moreover, this situation can lead to sedimentation processes, resulting in further imperfections in the final product. This issue is observed in the case without any control device. The big difference is also observed for the standard baffle wall. This example confirms that the existing solution can be improved significantly by the application of EMS.

Finally, it should also be mentioned that the observation of the RTD curves during the parametric study enabled the design of the new kind of baffle wall, which, with proper selection of the EMS power, enables the prevention of the clogging phenomena caused by improper sedimentation and solidification in the dead zones. The clogging can be caused by biased flow through the strands resulting from the inhomogeneity of the structure and turbulence in the bath. To understand the issue, the observations of the areas close to the outlets will be presented in the next section.

8.3.3 Clogging of outlets

The inhomogeneity of the temperature and velocity distribution in the dead zones can lead to problems with the local solidification and then sedimentation. The small solid particles can clog the strands and block the flow. In such situations, the shutdown of the production line is often necessary, which is very expensive due to downtime and poses a danger to employees. The proper interpretation of the C-curves can be very helpful in understanding the phenomena of clogging. It seems that in the case of the shortcut of the curves and the presence of the double picks in the shape, the risk of clogging is the highest. The comprehensive parametric study of various cases with the EMS system, along with the new proposal of the baffle wall with dam

and weir, enables a comparison of the RTD curves and an analysis of the velocity and stirring energy distribution near the outlets.

The CFD simulation of the RTD curves, especially C-curves, enables to select of two different cases – one in which the clogging of outlets does not occur and the second one, where the risk of clogging is high. The cases, which will be analyzed, are following: case number 11 and case number 21, both have the same EMS power but different dimensions of the flow control device (dam and weir). The comparison between the RTD curves for both cases is presented in Figure 138. On the right side of that figure, a zoomed-in view of the selected results is presented.

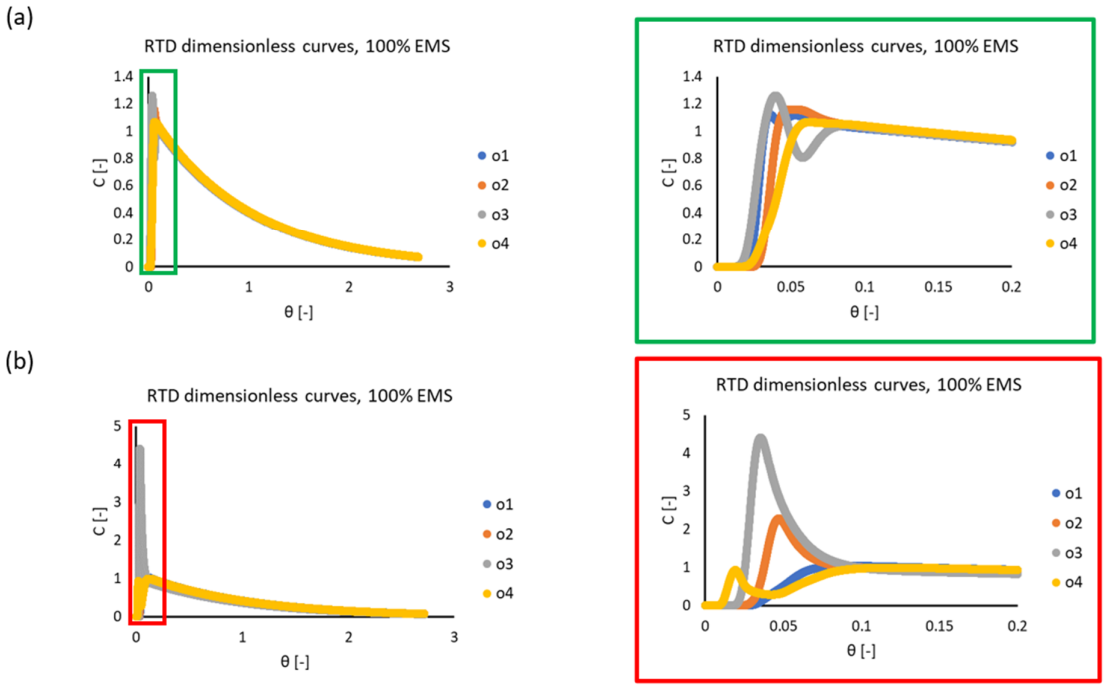


Figure 138. The C-curves for CFD simulation of the case (a) number 11, where the risk of clogging is low and (b) number 21, where the risk of clogging is high.

The velocity and stirring energy distribution close to the strands were investigated to better understand the issue. The velocity distribution for both cases is presented in Figure 139, and the stirring energy distribution for both cases is presented in Figure 140.

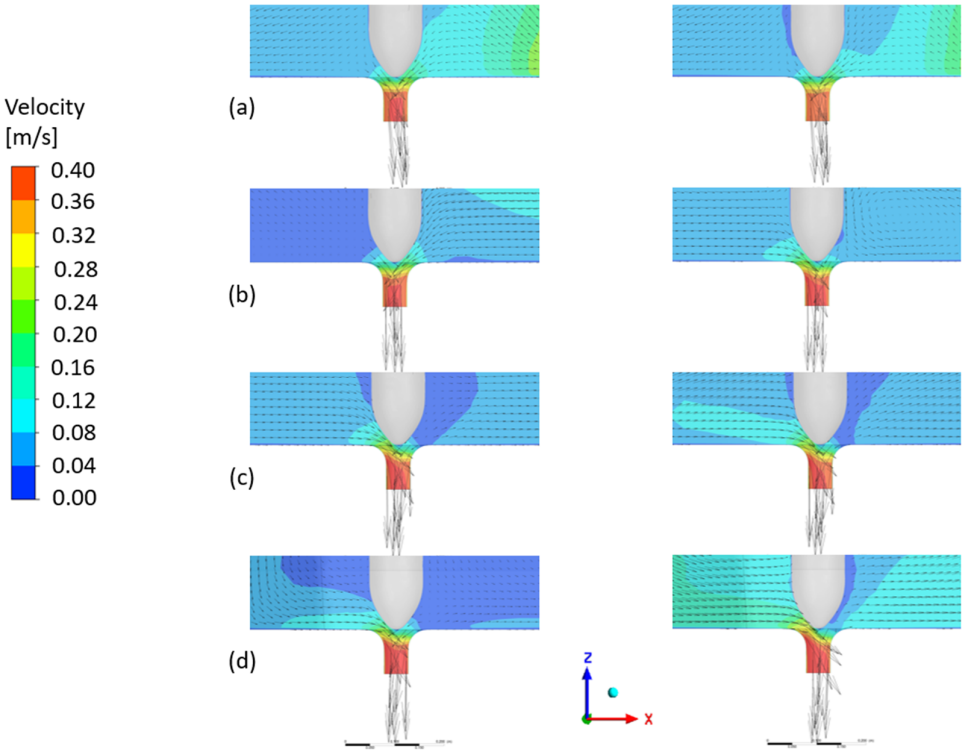


Figure 139. Velocity distribution for the case 11 where clogging is not occurring (left) and for case 21 where the risk of clogging is high (right) for different outlets: (a) outlet 1, (b) outlet 2, (c) outlet 3, (d) outlet 4 for tundish, results after steady-state simulation.

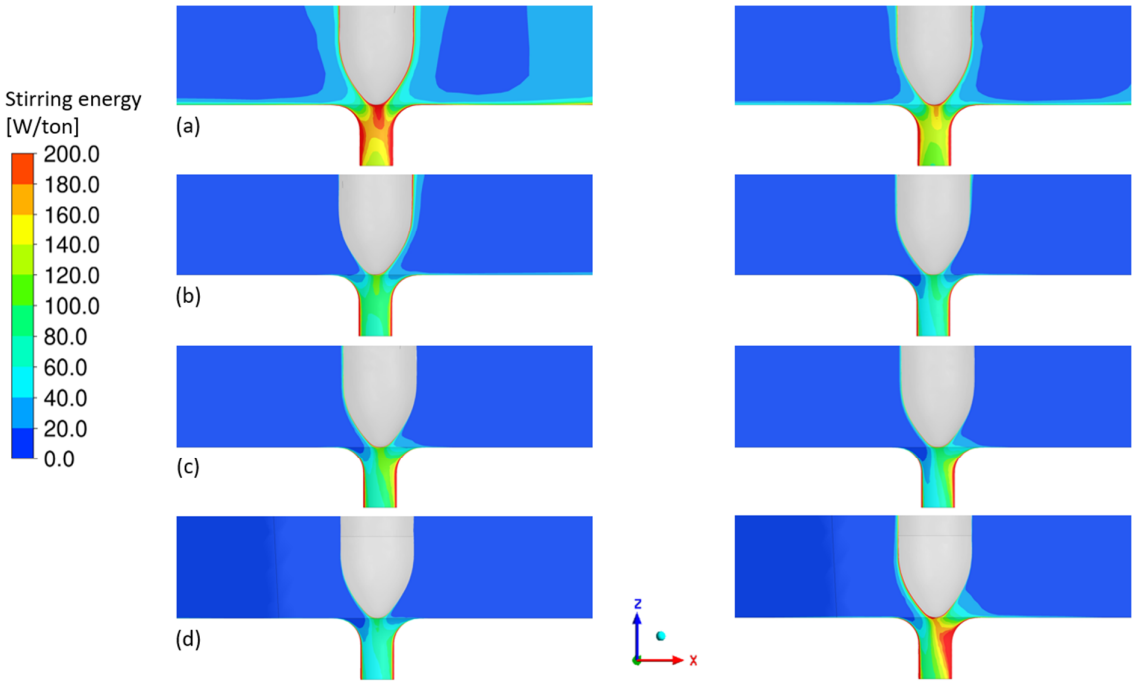


Figure 140. Stirring energy distribution for the case 11 where clogging is not occurring (left) and for case 21 where the risk of clogging is high (right) for different outlets: (a) outlet 1, (b) outlet 2, (c) outlet 3, (d) outlet 4 for tundish, results after steady state simulation.

In the case in which the clogging does not occur, the velocity distribution at the entrance to the strand is more symmetric than in the case with clogging phenomena. The stirring energy distribution is also more uniform and symmetrical for each outlet. It means that the flow close to the outlets is stable and homogenized. The molten steel can flow smoothly via each outlet. In the simulation of the case with a high risk of clogging, the distribution of stirring energy, mainly at outlet number four, is characterized by higher values and asymmetric behavior. The relatively high turbulence dissipation rate that occurs close to the outlet area is responsible for the unstable behavior of the flow. If this kind of phenomenon is combined with additional partially sedimented portions of steel, the risk of clogging is very high. The comparison of the RTD curves, velocity and stirring energy distribution in the outlet area confirms that the highest risk of clogging is for outlet number four.

The above analysis confirmed that clogging can be tracked by measuring the RTD curves and observing the distribution of velocity and stirring energy in the outlet areas. The uniform distribution of flow and prevention of high turbulences close to the outlets should reduce the risk of clogging and faults inside the tundish.

8.3.4 Inclusions modelling

The numerical approach to modelling the non-metallic inclusions for the tundish is the same as for the ladle furnace, with one exception. Due to the fact that the tundish has the inlet/outlets boundary conditions, the proper boundary conditions related to the concentration of inclusions must be applied. The outlets are automatically calculated by the software, and no additional parameters need to be defined. However, the inlet is responsible for providing the fresh melt to the tundish with a specific concentration of the inclusions. The initial concentration of the inclusions in the whole tundish geometry is specified as 10 [ppm], and the same condition was used as a concentration of the inclusions at the inlet. Moreover, the fraction of each bin at the inlet is the same as the initial concentration in the whole fluid domain, which was presented in Table 8. The non-metallic inclusions are removed when touching the mesh cells' top layer under the special conditions described in Section 5.3.

The tundish with the EMS system is an innovative solution, and additional comparison was conducted to compare the inclusions behavior in the case of scenario without stirring (case number 1), with EMS stirring, but reduced EMS power up to 75% (due to the fact, that the homogenization is similar in a wide range of EMS power, what was proved in Section 8.3.2) and with existing baffle wall (case number 4). The concentration of the inclusions in time across selected vertical cross-sections in the area of the outlets is presented in Figure 141. The concentration of the inclusions in the whole melt area in time for all three cases is presented in Figure 142. Moreover, the average value of the number density of each bin was measured at the outlets area and presented in Figure 143.

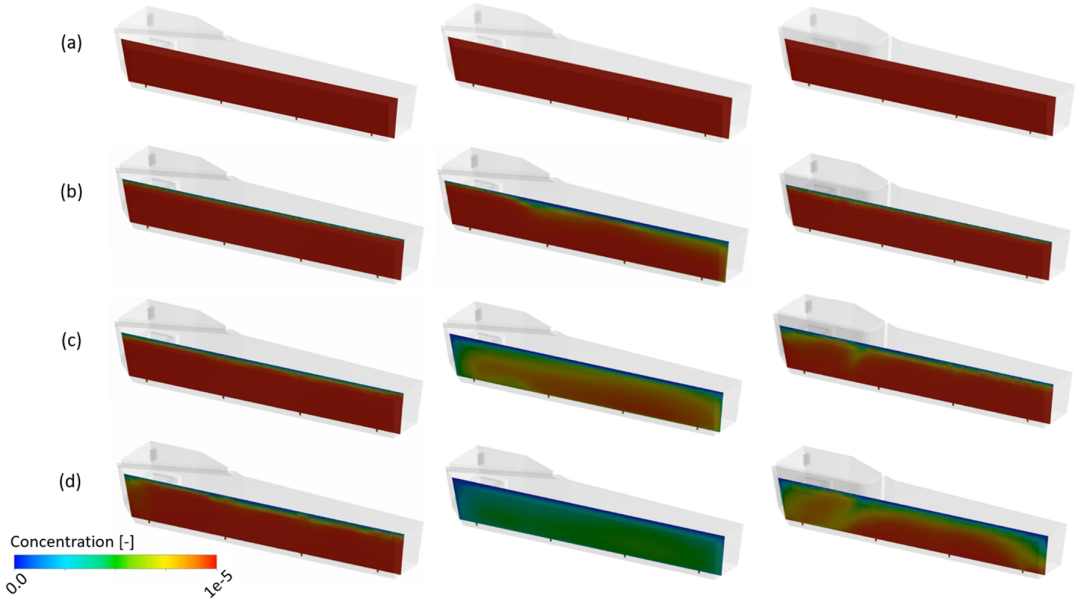


Figure 141. The dimensionless concentration of the inclusions inside the tundish without any flow control device – case no. 1 (left), for the case with 75% of EMS (middle) and for the case with baffle wall – case no. 4 (right) for a) starting point, and after b) 20, c) 100, d) 250 [s].

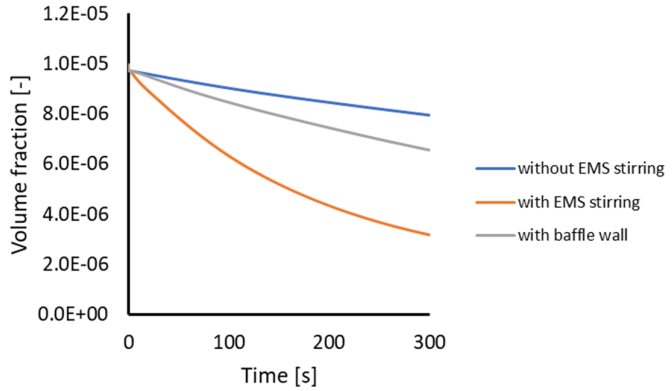


Figure 142. Volume average fraction of inclusions in the whole melt domain in time for different stirring scenarios.

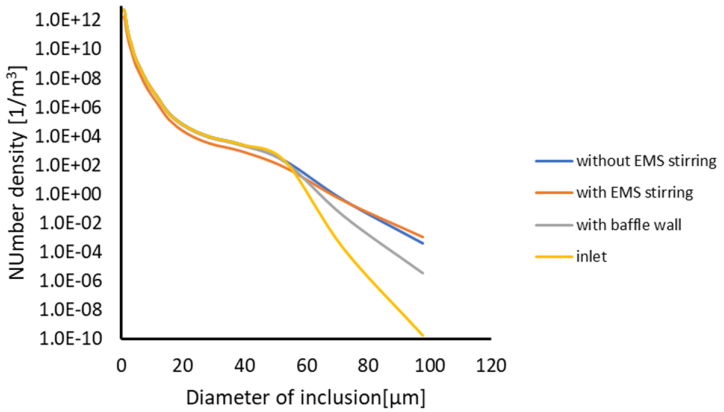


Figure 143. The number density of the inclusions depending on their diameter for different stirring scenarios and at the inlet.

The obtained results clearly show that the best efficiency in the case of the inclusions removal process is achieved with the EMS stirring, where the final concentration of the inclusions after 300 [s] is almost 2 times lower than in the case of the baffle wall solution. On the vertical cross-section, where the concentration of the inclusions in Figure 141 is shown, the effect of the UDF control scripts is visible, where the concentration of the inclusions close to the top layer is equal to 0 during the whole simulation time. Moreover, an additional analysis was conducted to measure the number density of inclusions of different sizes at the end of the simulation and compare it with the number density of inclusions at the inlet, which was the same for all cases. The interpretation of the results confirms that the inclusions agglomerate to each other and for all of the methods, the smallest sizes of the inclusions have the highest number density. The EMS stirring is characterized by the lowest number density of the inclusions up to 60 [μm] compared to the other methods and the highest number density of the biggest inclusions. The study was conducted for Al_2O_3 inclusions, and the results have a preliminary character and must be verified in the future to be able to predict the sizes of the different types of non-metallic inclusions in the correct way and control their behavior by proper selection of the stirring conditions. However, the presented results confirm the power of the CFD simulations in designing and understanding the metallurgy process.

In general, the EMS system applied to the tundish greatly increases the mixing efficiency, enabling good homogenization of the steel in the whole bath and reduction of the plug and dead zones, as well as the presence of the non-metallic inclusions. Moreover, the EMS configuration setup can be easily adapted to the shape of the tundish and fully controlled. The research shows that even the low power of the EMS enables an increase in the effectiveness of stirring. The selection of the EMS system should be prepared based on the geometry and requirements of the customer and should be designed individually to ensure the best results. An additional advantage of this solution is that the maintenance of the EMS stirrer is accessible as it operates without direct contact with the hot, molten steel.

These results were validated using the water models, similar to the approach applied in the case of a ladle furnace. Once again, the results can be treated as qualitative, not as quantitative, as the CFD simulation results correspond to the real operating conditions of the tundish while the laboratory model is presented in scale, and the selection of the operating parameters is based on the scaling according to the Froude and Reynolds number similarity, as it was in the ladle furnace case.

8.4 Comparison of CFD results with water model results

The setup of the laboratory configuration of tundish is described in Figure 144, and a more detailed view of the water pumps is shown in Figure 145. Outlets with an additional system that enables measuring the salt tracer's concentration for RTD curves analysis are shown in Figure 146.



Figure 144. Laboratory setup of tundish for water modelling.

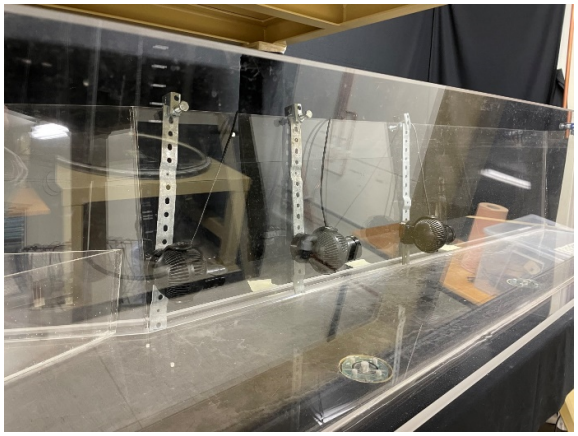


Figure 145. Water pumps to model EMS stirring.

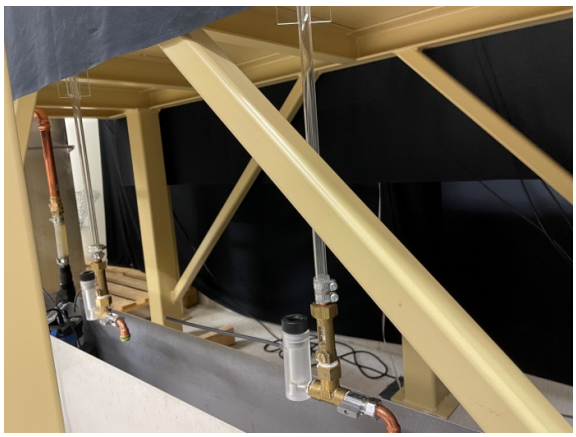


Figure 146. Outlets area with a system to measure the salt concentration in case of RTD curves evaluation.

The first test was conducted for the tundish without any additional control system, while the second one, with EMS, was replicated by properly selecting the pump setting to ensure the model's scaling. The comparison between both solutions is presented in Figure 147. The yellow

dye was injected into the vessel to observe the mixing process. The manner of the measurements is comparable to the simulation results presented in Figure 131.

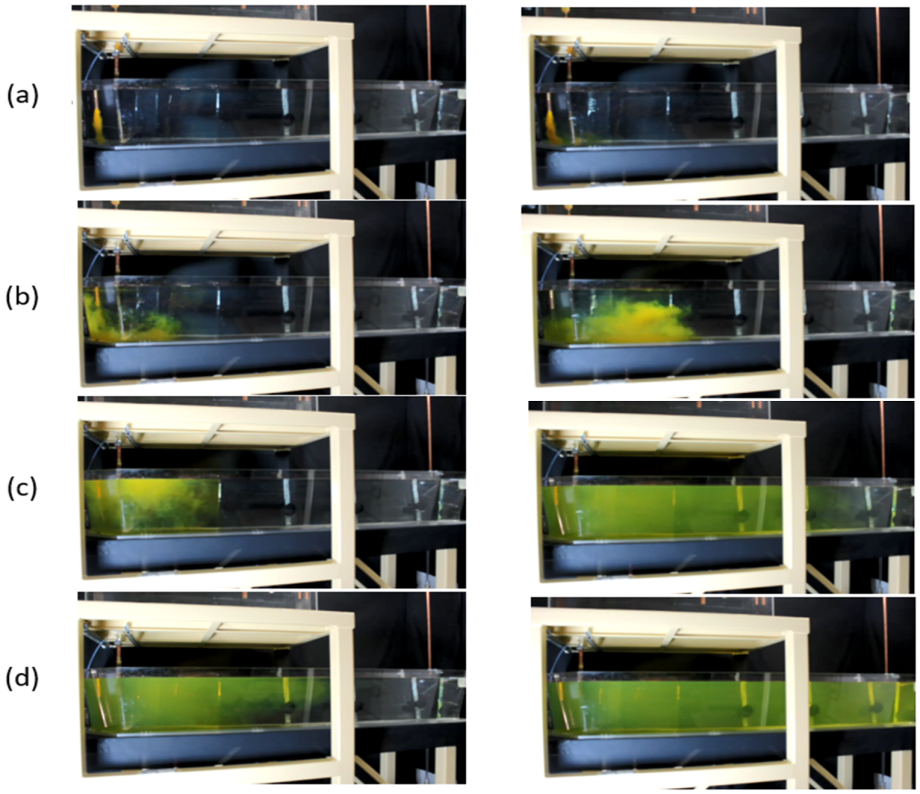


Figure 147. The water test results for tundish without flow control devices (left) and for EMS system (right) for (a) dye start injection time, and observations after (b) 5 [s], (c) 20 [s], (d) 120 [s].

The observations demonstrated that the extended dead zone is observed in the case of the tundish without any flow control device. The homogenization time is very long, reaching up to 567 [s]. These results suggest that there are little to no inclusion collisions. On the other hand, the dead zone is almost removed in the case of the EMS system, and the homogenization time is around 29 [s]. The results suggest that the inclusion collisions level should be enough to ensure the high cleanliness of the steel.

The first observations were made during the water modelling in the laboratory for models presented in Figure 147. The C-curves obtained for different strands are presented in Figure 148. The results of the case without any flow control device are unsymmetric for particular curves; moreover, the shortcut flow for strands number 2, 3 and 4 is observed, which suggests that the clogging phenomena can occur in this area due to issues with smooth flow via these outlets. RTD curves present the extensive area of the plug and dead zones, mainly for strand number 1. What is important is that the EMS system enables the shape of RTD curves to approach the ideal mixing curve, where the plug zone and dead zone are minimized.

The RTD curves were measured similarly to mixing curves in the ladle furnace, and the injection parameters were the same as for numerical simulation to compare the character of the curves and to obtain the qualitative validation of the model. The concentration of the additional tracer in the CFD (salt in the water model) was measured at the particular outlets. The comparison of results obtained from simulation and water experiments for cases without flow control devices and with the EMS system is presented in Figure 148.

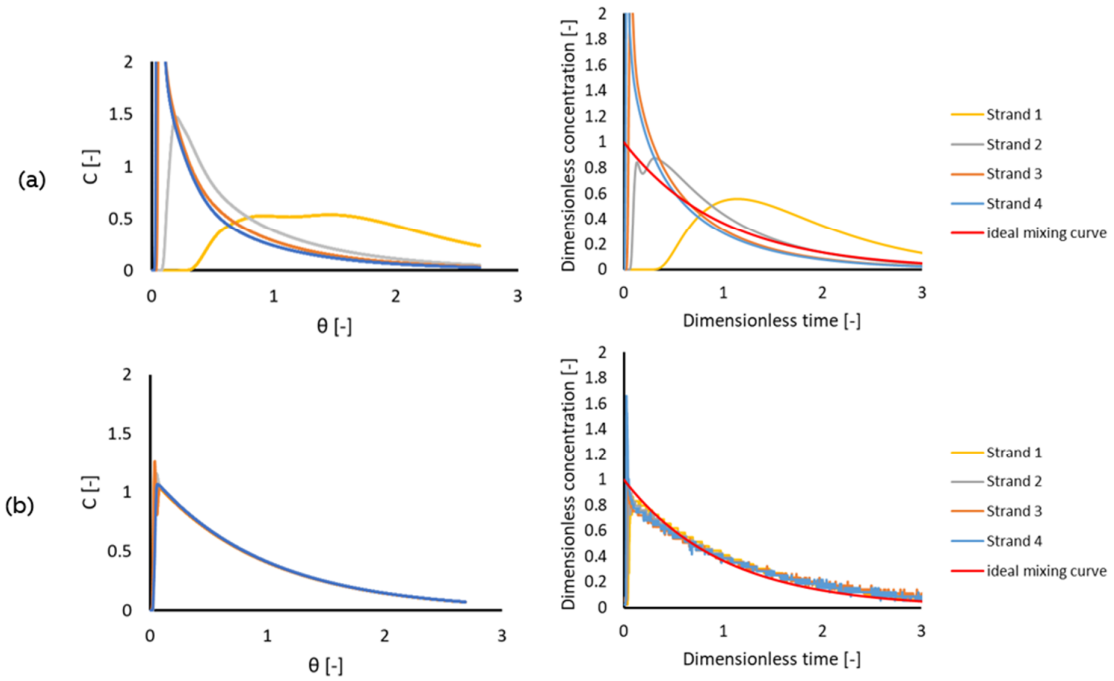


Figure 148. RTD curves for CFD simulation (left) and water experiment (right) for cases (a) without flow control devices and (b) with EMS system.

The character of the curves in the CFD simulation is the same as in the water experiment, which confirms the correctness of the presented model. Moreover, the shape of each curve for the EMS solution is similar, suggesting that the flow is homogenized in the whole area of the tundish.

8.5 Transfer to industrial application and comparison between the numerical simulations and real test results

The presented CFD study and water modelling results confirmed many benefits related to the EMS stirring compared to the standard baffle wall solution, which is commonly used in such kinds of devices. Certainly, the EMS stirring enables gentle stirring of the liquid steel throughout the entire volume of the tundish, preventing the formation of dead zones. This increases the homogeneity of velocity and temperature, and improves steel cleanliness by increasing inclusion collisions and removal due to the increased stirring energy. Moreover, gently stirring should calm the slag layer and prevent the slag from entrapment in the liquid

steel. All the benefits led to the development of the real EMS device and its implementation in a real case study of a steel plant in China.

The designed stirrer is responsible for linear flow movement, and it was installed in the same position as in the CFD simulations, as presented in Figure 149.

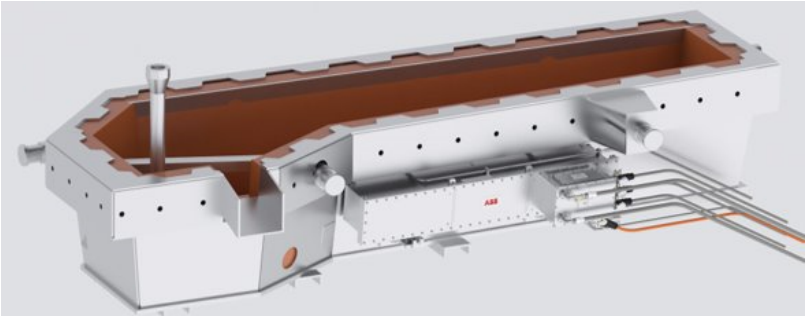


Figure 149. Real tundish installation with EMS system located in the same position as in the CFD simulations.

The pilot project for that stirrer includes two tundishes for one ladle with a bath depth equal to 800 [mm]. The tundish capacity is around 40 [ton]. Moreover, each tundish has four strands. Due to the symmetry conditions, the CFD simulations and water model covered only half of the whole installation (one tundish).

The real test setup includes two active tundishes. One of them was stirred by EMS solution, and the second one was stirred by existing baffle wall solution. The measurements were prepared for both of them for the same test conditions like steel grade: GCr15 (bearing steel), billet cross-section 220 [mm] × 260 [mm], casting speed 0.76 [m/min], which means, that the throughput of each tundish is 1.25 [ton/min]. Moreover, the casting sequence consisted of 6 heats, as presented in Figure 150. The real EMS device mounted on one of the tundishes is presented in Figure 151.

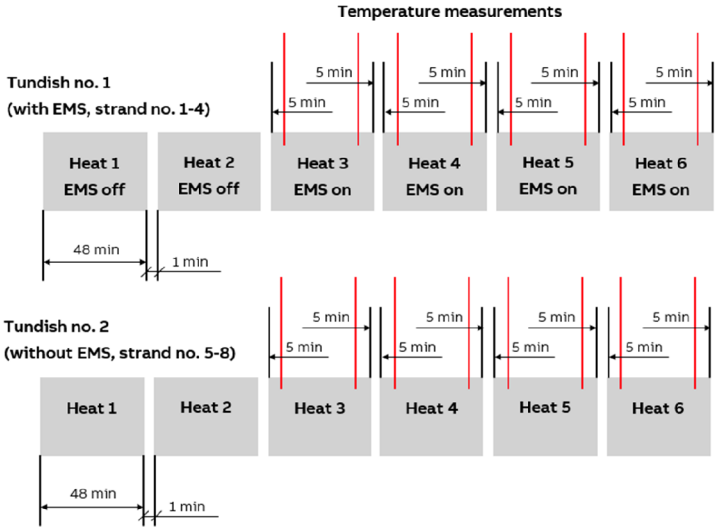


Figure 150. Heating sequence conditions.



Figure 151. Site picture of the installed tundish EMS.

During the test, the temperature measurements were conducted. The measurement points were located between strands 1-2 and 3-4 for tundish with EMS system and between strands 5-6 and 7-8 for tundish with baffle wall. The temperature was measured 300[mm] below the free surface. The results from the real experiment of the temperature homogeneity between strands and temperature stability are presented in Figure 152 and Figure 153, respectively.

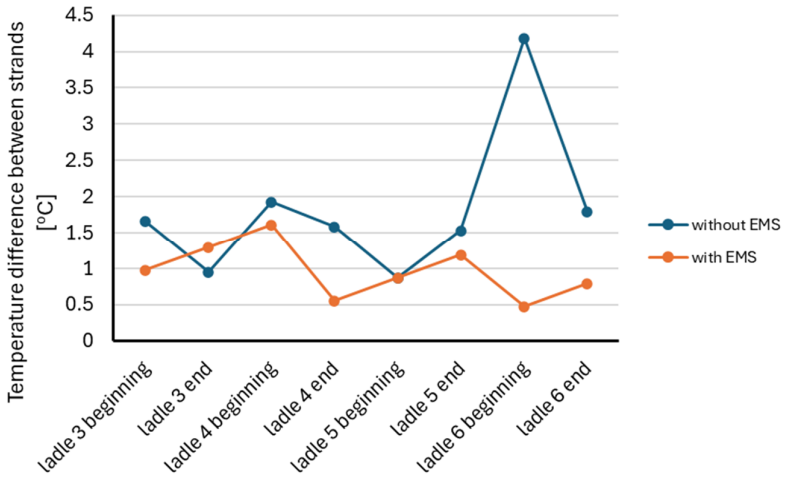


Figure 152. Temperature homogeneity between strands.

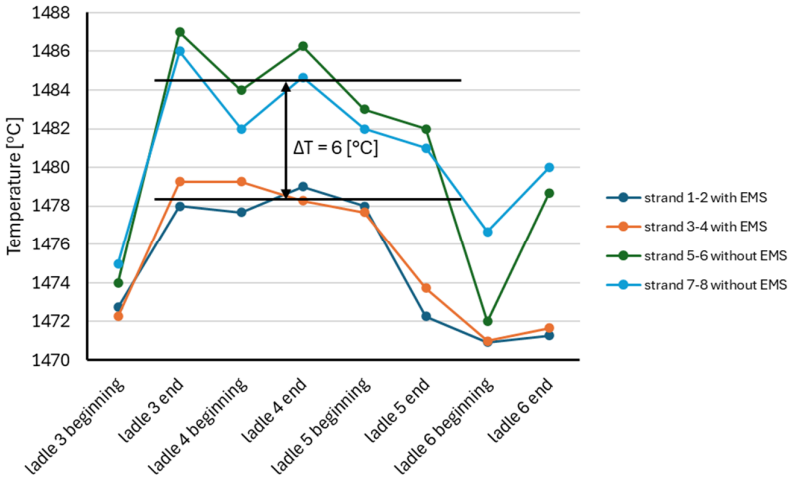


Figure 153. Temperature stability between strands.

The results clearly show that the temperature difference between strands without EMS is up to 2.5 [°C] and with EMS up to 1.1 [°C]. Moreover, the temperature for tundish with EMS is around 6 [°C] lower than in the case of the tundish without EMS. The average temperature variation without EMS is up to 4.9 [°C], while with EMS is up to 2.1 [°C]. The results suggest that significantly better homogenization of temperature is achieved in the proposed EMS solution.

During the real experiment, the behavior of the inclusions was also investigated. This kind of result is really difficult to obtain, and these results can be treated as a reference for further investigation of the non-metallic inclusions behavior and tuning of the CFD model. In such kinds of tests, two types of inclusions were investigated: $CaO\text{-}Al_2O_3$ system (B-type, D-type, cluster or globular) and Al_2O_3-MgO named spinel. The behavior of both systems is different and presents some intriguing characteristics.

In the case of the $CaO\text{-}Al_2O_3$ system, EMS stirring reduces the number of inclusions very well. This is clearly observed in Figure 154, where the quantity of the inclusions decreases a lot in the solution with EMS compared to the solution without EMS. The reduction of the inclusions is presented in Figure 155. Moreover, the inclusion size is reduced for the case with EMS, which is presented in Figure 156.

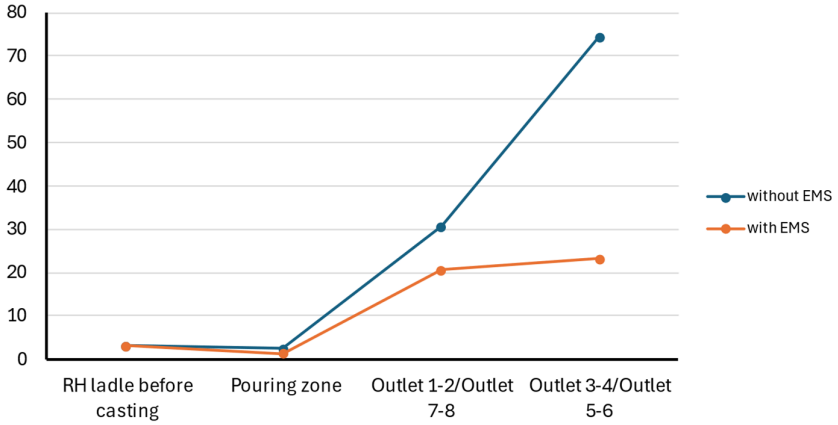


Figure 154. Inclusions evolution for the number of inclusions.

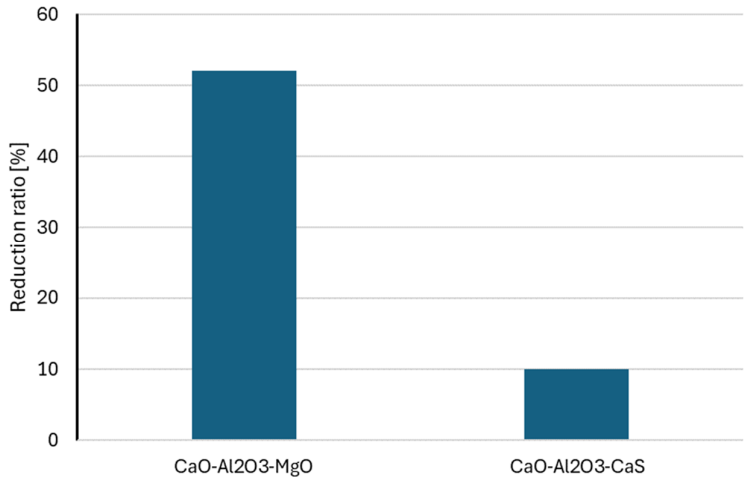


Figure 155. Reduction ratio of $CaO\text{-}Al_2O_3$ system.

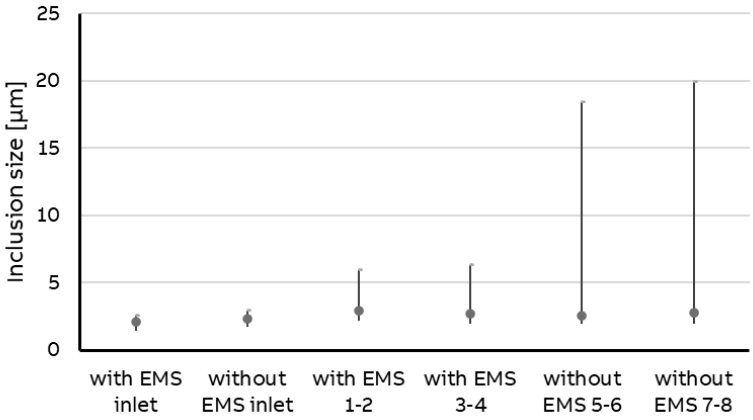


Figure 156. Inclusion size for solutions with and without EMS.

The above results clearly show that the EMS system is working very well and is able to reduce the inclusions of the $CaO\text{-}Al_2O_3$ system, which is for sure beneficial. On the other hand, the Al_2O_3-MgO was also tested, where the number density of the inclusions was measured to

try to understand the behavior of the spinel. Unfortunately, the results are not as good as expected, and the reduction of the inclusions is not observed, as shown in Figure 157. It is caused by the very small size of the inclusions between 2-6 [µm] and no coagulation between these particles. Certainly, the spinel is not crucial to the quality of the final product, but there is still room for further improvement.

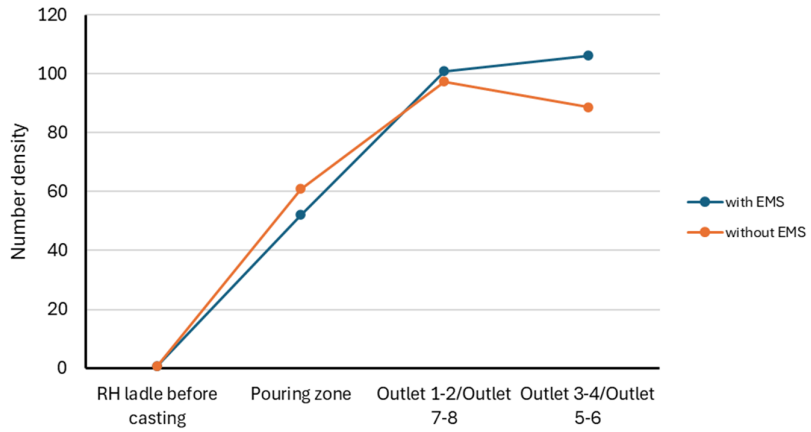


Figure 157. Spinel's number density for cases with/without the EMS system.

The presented results suggest that the leading parameter is the coagulation coefficient[222]. The proper selection of that coefficient enables the correct modelling of each type of inclusions. Further study of this phenomena is planned in the future to be able to model the wide range of the different non-metallic inclusions types and continue developing proposed solutions with EMS devices. The main focus of the research will be modelling of the spinel to improve the reduction of inclusions for EMS solutions. The example of the coagulated non-metallic inclusion is presented in Figure 158.



Figure 158. Example of coagulated non-metallic inclusion.

9. Comparison of stirring speed and stirring energy in investigated metallurgical vessels

As presented during the research, stirring energy influences the flow behavior and depends on the investigated device. Therefore, insightful research is important to understand the processes inside the metal flow and to accurately assess the efficiency of the stirring process.

A lot of work is focused on gas stirring[113,223,224,236], and only several, focuses on induction stirring[33]. The lack of measurements of the stirring energy for electromagnetic stirrer devices motivated to compare the values across different investigated metallurgical equipment. The goal of this study was to define typical stirring energy ranges and better understand the nature of steel flow at different stages of the production route. After collecting the obtained results and literature data, and then comparing them with the results obtained by other authors, a summary was prepared and is shown in Figure 159. The range of average stirring energy values for each investigated metallurgical equipment is presented in that Figure; furthermore, the values were collected for different stirring types to understand how the stirring method affects the stirring energy. The local values strictly depend on the geometry of the device and the boundary conditions of the stirring, that is why the measurements present the averaged stirring energy to assess the behavior of the flow.

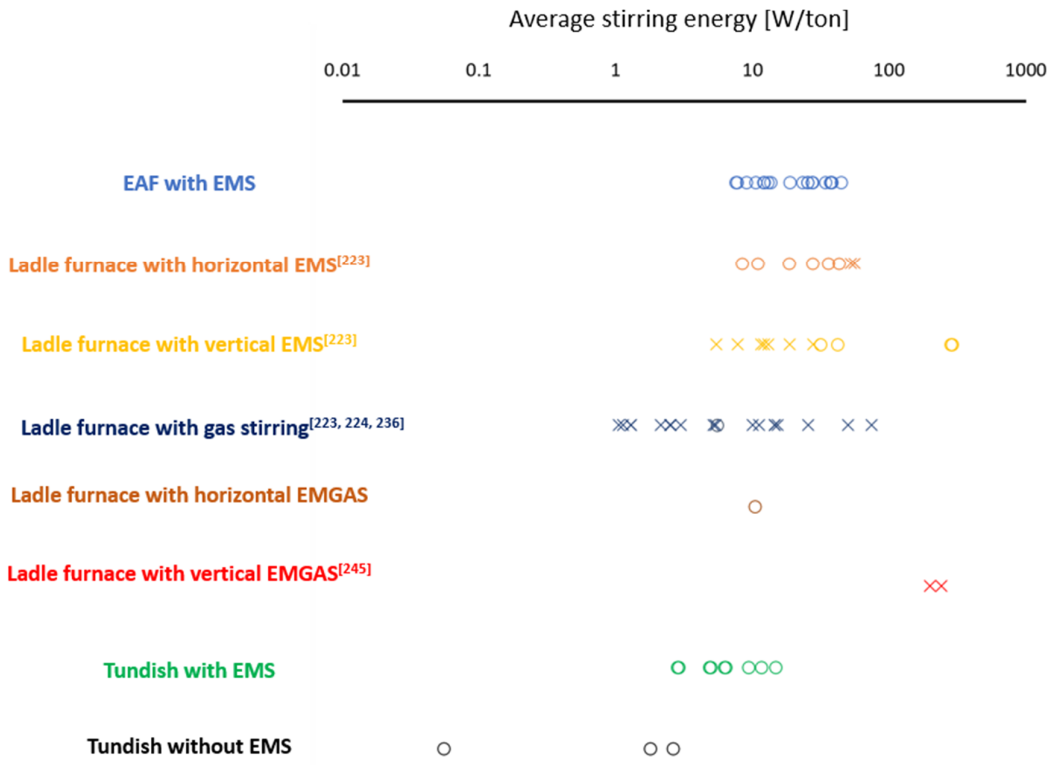


Figure 159. The range of average stirring energy values calculated for various metallurgical equipment. Authors' results are marked as circles, while literature data are represented as crosses.

Figure 159 clearly shows that the arc furnace, as a first step of the process, is characterized by relatively high values of stirring energy due to the initial homogenization of the properties after the melting process. Then, the ladle furnace, as a second step, is also characterized by high stirring energy values. In this case, high mixing is crucial to clean up the steel and reduce the size and number of non-metallic inclusions in the molten steel and eventually improve the quality of the final product. The stirring energy during this process is highly dependent on the stirring method. The stirring energy during the mixing processes in the ladle can be set up in a wide range of values to increase inclusions removal by controlling the stirring energy in the selected parts of the furnace and generally in the whole volume of the molten steel. The proper selection of stirring energy depends on the type of stirring method and the applied electrical current in the case of an electromagnetic stirrer. Tundish, as the last step before slab casting, is characterized by quite a low value of stirring energy to improve the adhesion of the non-metallic inclusions to the top slag layer, but enough to enable good mixing and prevent dead zones from forming inside.

A presented summary of the stirring energy evaluations in different vessels was also compared to the comprehensive work on that topic by Taniguchi et al.[257], (Figure 160).

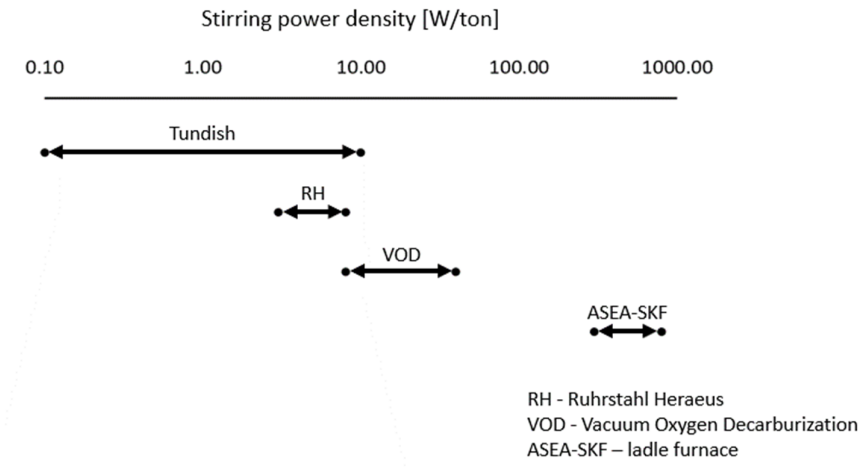


Figure 160. Estimated values of stirring power density based on the investigations from[257].

The presented results are commonly treated as a literature reference for this kind of investigation. As presented, values of the stirring energy correspond well to the obtained results, with one exception. A noticeable difference is observed in the stirring energy for the ASEA-SKF ladle furnace, which should be comparable to the ladle furnace with a vertical stirring direction. In this case, the results obtained by the authors seem to be overestimated. The main difference can be attributed to the measurement techniques used in the past, which did not yield accurate results. At the same time, all the results were commonly validated only for gas stirring applications. Moreover, the measurements were not focused on the estimation of the turbulence dissipation rate in the ladle furnace under induction stirring because of difficulties with the

mensuration of this value. As a result, the research focused mainly on the dependence between the speed and stirring force[257]. Nowadays, based on advanced numerical methods, the correctness of the stirring energy prediction is high, and the values obtained within this work are binding.

10. Conclusions

Extensive numerical research on various metallurgical equipment was undertaken within this dissertation. The new numerical models have been developed and validated, and can now be successfully implemented in industrial applications. Their use can accelerate the development, optimization, and implementation of advanced solutions in steel plants, and at the same time, also support a better understanding of metallurgical processes that are difficult to measure online. Moreover, a new proposal for assessing the stirring efficiency in equipment with an EMS system was proposed, and new stirring devices for various steps of the molten steel route were developed.

The first step presented in Chapter 5 was focused on the development and validation of the proposed numerical approach. The analysis was prepared based on the scaled model of the LF, which was tested at Cambridge University in the early 80s. Two numerical approaches were tested: a simplified one-phase steady-state approach and a more advanced multiphase and transient approach. Based on this study, the following conclusions can be formulated:

- The proposed numerical approach is working correctly; moreover, the effect of the EMS system is included, and the comparison with the experimental data confirms the accuracy of the electromagnetic Lorentz forces implementation, even in the case of simplified one-way coupling with the addition of stirring forces compensation term;
- The steady-state, single-phase approach can be used for a quick evaluation of the correctness of the EMS system selection. The obtained results are correct, but some specific phenomena, like the impact of the free surface oscillations, are omitted due to the level of the simplifications applied;
- The multiphase, transient approach fully captures the results obtained in the real experiment; moreover, the interesting behavior of the velocity field and its rotation in the real experiment was also captured in the numerical simulation. The rotation of the flow can be caused by the unstable behavior of the free surface, unstable behavior of the turbulences and harmonic and unsymmetric behavior of the EMS forces;
- The proposed model is prepared in a general manner and can be easily adapted for numerical calculations of various metallurgical equipment, such as EAF, LF, and tundish, as well as for industrial-scale applications.

The next step involved a detailed analysis of other types of furnaces using the proposed numerical model, which was applied to calculate various processes in the steel production chain. The first device that was calculated was the EAF, where the proposition of the EMS system was compared to the more common BGS method. Such a comparison enables the filling of a gap in the literature, where a direct comparison of these two methods has not been available. The analysis was conducted for three different EAF processes: temperature homogenization,

heating and scrap charging. Moreover, based on this analysis, a new type of EMS system was proposed and calculated using the proposed numerical approach. Additionally, the correctness of the conducted analysis was confirmed based on industrial measurements for this type of furnace. The whole investigations are included in Chapter 6 and can be concluded as follows:

- The development of the proposed model enables the possibility of calculating the additional processes like temperature homogenization with applied temperature gradient, heating generated by the electrodes and scrap charging with assumptions of the porosity of the scrap area. Moreover, the developed solution includes the capability to simulate the argon gas injection in the BGS method;
- To increase the accuracy of the model, a more advanced multiphase approach was introduced, and an additional slag layer was included to assess the influence of this layer on the occurrence of dead zones. At the current stage, the model includes only mixing phenomena, the addition of the temperature homogenization and heating processes will be a subject of further development;
- The comparison between the BGS and EMS methods enables to confirm a much better efficiency of the EMS solution, which is characterized by 5 times shorter homogenization time, almost 3 times higher average steel velocity and almost 4 times higher stirring energy than the BGS;
- The analysis of the dead zones confirms, that in the BGS method, the big area of the furnace is characterized by low velocity, which can suggest the occurrence of the dead zones, while in EMS, the dead zone almost does not occur;
- The influence of the slag layer is noticeable and should be included in the more detailed simulations;
- The validation of the approach conducted for the real furnace confirmed that the EMS system enables better efficiency of heat and mass exchange, speeds up the melting process, improves homogenization of temperature in the melt bath, and prevents superheating. Additionally, it achieves a better decarburization rate and a reduced tapping temperature. Moreover, productivity is increased, and the safety of the operations is higher due to the use of contactless devices like EMS. Moreover, during the validation, the assumption of the 5% of EMS power to model the natural mixing in a simplified way was confirmed;
- The EMS system in the EAF is a very effective solution, which can be used for big EAF with a capacity of 450-ton, which can be beneficial in the case of the process of replacement of BF;
- The new proposed solution of the donut-shaped stirrer is characterized by improved flow distribution inside the furnace. The solution can be beneficial for melting processes due to the concentration of the heat in the center of the furnace. This solution is characterized by a longer homogenization time. Still, the velocity field

remains very stable, enabling full control of the process, which can be beneficial for DRI processes. This approach should be investigated more in the future. Definitely, the results confirm that the EMS device can be freely modified to obtain the best results for a particular furnace;

- In the future, further development of this solution with a full multiphase model is planned. Additionally, the higher flow rate of argon in the case of the BGS method will be analyzed to compare that solution with the EMS.

An extensive additional analysis was then conducted for the industrial model of the LF, where the new approach to the electromagnetic stirring was proposed, calculated numerically and validated in the water modelling laboratory. The whole investigation is covered by Chapter 7 and can be concluded as follows:

- The most popular methods used in the industry, together with a new proposed EMS stirring approach, were investigated and compared in terms of the mixing time, velocity, and stirring energy distribution;
- The newly proposed horizontal EMS system is characterized by an 80% reduction of the power input while maintaining average velocity of the melt on comparable level as in the classical, vertical EMS stirring. Moreover, the new horizontal stirring is characterized by the reduced stirring energy in the top part of the furnace and a more calm behavior of the free surface, which is beneficial for removal process of a non-metallic inclusions due to increased adhesion to the slag layer. The strength of the EMS can be easily controlled, allowing full control of these processes;
- The shortest mixing time is possible with classical vertical EMS stirring and vertical EMGAS stirring. The proposed horizontal EMS solution is characterized by the longest mixing time, but it can be beneficial from a perspective of removal of non-metallic inclusions, due to the longer residence time and better coagulation. Moreover, in the case of the horizontal EMGAS method, the inclusion removal process can be further improved by the presence of argon gas, though this effect must be further investigated in the future;
- The experiments conducted on the water model confirmed the accuracy of the results obtained from the numerical model. The experimental results can be treated qualitatively due to the scaling parameters, but the curves related to the mixing time can be used for a quantitative comparison with numerical results. The character of the curves and behavior of the mixing time are comparable, which confirms the effectiveness of each solution;
- The results related to the inclusion modelling are preliminary. At this moment, the potential of the numerical model is confirmed by the reduction of non-metallic inclusions over time, as they are caught by the slag layer. The model will be further developed to increase its accuracy. The author considers including an in-depth study

of the Hamaker constant to predict different kinds of inclusions and additional interactions with argon gas bubbles.

A similar study was conducted for the first step of the continuous casting process, the tundish, where the EMS system is an innovative solution in the industry. The ABB company is a pioneer in implementing this solution in real plants, so an extensive study was required before implementation to improve the processes inside the tundish and apply the proper solution to the real device. The whole research was presented in Chapter 8, and the conclusions can be summarized as follows:

- The conducted research confirms that the best mixing in the tundish can be achieved with the use of the proposed solution with an EMS system, where the plug volume is reduced, and the mixing curve is similar to the ideal mixing curve;
- The RTD curves of all the strands have the same trend, which suggests that the homogenization of the velocity, temperature and stirring energy is stable in the whole tundish bath;
- Even a small amount of power applied to the EMS system significantly improves the shape of the curves and suggests much improved mixing inside the tundish;
- The analysis of temperature distribution confirms that the homogenization of temperature is much better in the case of the EMS system than in the case of the baffle wall, which is a standard existing solution. The additional measurements in the outlets and in the whole melt domain confirm the benefits of the EMS system. That aspect is very important from a metallurgical point of view, due to the reduced risk of occurrence of clogging of the outlets;
- Additional study related to the presence of the additional pikes on the RTD curves, which can suggest the occurrence of clogging, reveals the alignment of the curve shape with the distribution of stirring energy near the outlets. If the distribution is uniform, the risk of clogging is low, in the case of the high values and non-symmetrical behavior of the stirring energy, the risk of clogging increases;
- The model of the non-metallic inclusion prediction confirms that the best reduction effectiveness is in the case of the EMS system, which is characterized by almost 2 times lower volume fraction of inclusions after 300 [s] compared to the case of baffle wall as an existing solution. The approach of the calculation of the non-metallic inclusions will be investigated more in the near future to be able to predict the behavior of the spinel;
- The water modelling conducted for tundish confirms the high effectiveness of the EMS solution. Moreover, the mixing curves obtained from the numerical simulation and water modelling have a similar character and confirm the correctness of the presented model;

- The proposed solution was implemented in the tundish furnace in steel plants and tested to compare it to the existing baffle wall solution. The obtained results confirm better temperature homogenization for EMS solution. Moreover, during the tests, the behavior of the inclusions was measured. Two different types of non-metallic inclusions were investigated: $CaO\text{-}Al_2O_3$ and Al_2O_3-MgO (spinel). The conducted analyses confirm that the EMS reduces the amount of $CaO\text{-}Al_2O_3$ inclusions. However, in the case of the spinel, the behavior must be improved due to the very small particles, which do not coagulate with each other and cannot be removed – a point that will be further investigated in the future.

During the study, a new concept of stirring energy measurements was proposed to address the lack of methodologies for EMS applications in the literature. This research was presented in Chapter 9 and can be concluded as follows:

- The value of stirring energy strictly depends on the investigated device and stirring method:
  - in EAF with EMS stirring, it may range from 6 to 45 [W/ton],
  - in LF with EMS, from 8 to 300 [W/ton],
  - in LF with gas stirring, from 1 to 75 [W/ton],
  - in LF with EMGAS stirring, from 10 to 240 [W/ton],
  - in tundish with EMS stirring, from 5 to 22 [W/ton],
  - in tundish without stirring, from 1 to 3 [W/ton];
- The proposed method for calculation of the stirring energy for applications with EMS system, based on the turbulent kinetic energy assumption and comparison of that methodology to the other results and stirring methods presented by other authors to be correct in the prediction of that value;
- The values of stirring energy presented in the literature for the LF seem to be overestimated; moreover, presented in the literature relationship between the average speed and stirring force seems to be incorrect;
- The selection of the EMS method and device should be done carefully to take into account the dependence of the stirring energy value on the shape and geometry of the furnace. The solution should be designed individually for each particular metallurgical device, and the developed numerical approach will be very beneficial in that process.

Based on the gathered experience, the plans for future research can also be defined. Some of these issues are already being addressed to improve the accuracy and predictability of phenomena within various devices. The most important development includes:

- Multiphase simulations with an additional slag layer and with an improved approach to the argon gas modelling to achieve more realistic behavior of the bubbles with additional coalescence and breakup phenomena;

- Improvements of the non-metallic inclusion model, which require more studies to achieve better accuracy of the results and to enable detailed investigation of the spinel. Additionally, the interaction between the inclusions and argon bubbles should be included as an additional mechanism for the inclusions removal process.

Moreover, ongoing projects require the continuous development of the proposed solutions, creating a strong demand for further improvement, therefore, the work is planned to be continued.

11. References

1. Kim, J., Sovacool, B. K., Bazilian, M., Griffiths, S., Lee, J., Yang, M. & Lee, J. Decarbonizing the iron and steel industry: A systematic review of sociotechnical systems, technological innovations, and policy options. *Energy Research & Social Science* 89, 102565 (2022).
2. Sovacool, B. K., Kim, J. & Yang, M. The hidden costs of energy and mobility: A global meta-analysis and research synthesis of electricity and transport externalities. *Energy Research & Social Science* 72, 101885 (2021).
3. Vogl, V., Olsson, O. & Nykvist, B. Phasing out the blast furnace to meet global climate targets. *Joule* 5, 2646–2662 (2021).
4. European Commission. *Emissions Database for Global Atmospheric Research (EDGAR).* (2020).
5. IEA. *Iron and Steel Roadmap (International Energy Agency).* (2020).
6. Archer, D. & Brovkin, V. The millennial atmospheric lifetime of anthropogenic CO2. *Climatic Change* 90, 283–297 (2008).
7. Nilsson, L. J., Bauer, F., Ahman, M., Andersson, F. N. G., Bataille, C., de la Rue du Can, S., Ericsson, K., Hansen, T., Johansson, B., Lechtenböhmer, S., van Sluisveld, M. & Vogl, V. An industrial policy framework for transforming energy and emissions intensive industries towards zero emissions. *Climate Policy* 21, 1053–1065 (2021).
8. Rogelj, J., Huppmann, D., Krey, V., Riahi, K., Clarke, L., Gidden, M., Nicholls, Z. & Meinshausen, M. A new scenario logic for the Paris agreement long-term temperature goal. *Nature* 573, 357–363 (2019).
9. Rogelj, J., Luderer, G., Pietzcker, R. C., Kriegler, E., Schaeffer, M., Krey, V. & Riahi, K. Energy system transformations for limiting end-of-century warming to below 1.5 °C. *Nature Climate Change* 5, 519–527 (2015).
10. Somers, J. *Technologies to decarbonise the EU steel industry*. (2021).
11. Griffin, P. W. & Hammond, G. P. The prospects for 'green steel' making in a net-zero economy: A UK perspective. *Global Transitions* 3, 72–86 (2021).
12. Fischedick, M., Marzinkowski, J., Winzer, P. & Weigel, M. Techno-economic evaluation of innovative steel production technologies. *Journal of Cleaner Production* 84, 563–580 (2014).
13. Kirschen, M., Dieguez, U., Gruber, M., Schmidt, V. & Lückhoff, J. Energy savings of inert gas stirring to EAF steelmaking – with a focus on green steel transformation. in *6th European Steel Application Days (ESTAD)* (Düsseldorf, 2023).
14. Wang, P., Ryberg, M., Yang, Y., Feng, K., Kara, S., Hauschild, M. & Chen, W. Q. Efficiency stagnation in global steel production urges joint supply- and demand-side mitigation efforts. *Nature Communications* 12, 2066 (2021).
15. Meier, T. Modellierung und simulation des elektrolichtbogenofens. (RWTH Aachen University, 2016).
16. Cicutt, C. E., Valdez, M., Pérez, T., Donayo, R. & Petroni, J. Analysis of slag foaming during the operation of an industrial converter. *Latin American Applied Research - An international journal* 32, 237–240 (2002).
17. Lee, B. & Sohn, I. Effect of hot metal on decarburization in the EAF and dissolved sulfur, phosphorous, and nitrogen content in the steel. *ISIJ International* 55, 491–499 (2015).
18. Conejo, A. N. & Yan, Z. Electric arc furnace stirring: A review. *Steel Research International* 94, (2023).
19. https://worldsteel.org/data/world-steel-in-figures-2024/. (2025).

20. Koolen, D. & Vidovic, D. *Greenhouse gas intensities of the EU steel industry and its trading partners*. (2022).
21. https://zpe.gov.pl/a/proces-wielkopiecowy/D1CYP0be7. (2025).
22. https://worldsteel.org/about-steel/steelmaking-process/. (2025).
23. European Commission. *SWD(2021) 353 Final*. (2021).
24. Material Economics. *Pathways to net-zero emission from the EU heavy industry*. (2019).
25. Lis, T. *Współczesne metody otrzymywania stali*. (Wydawnictwo Politechniki Śląskiej, Gliwice, 2000).
26. Holtzer, M. *Procesy metalurgiczne i odlewnicze stopów żelaza. Podstawy fizykochemiczne*. (Wydawnictwo Naukowe PWN, 2013).
27. Nutting, J., Wondris, E. F. & Wente, E. F. Steel, https://www.britannica.com/technology/steel. *Encyclopedia Britannica* (2024).
28. Pater, Z. *Podstawy metalurgii i odlewnictwa*. (Politechnika Lubelska, Lublin, 2014).
29. Reis, B. H., Bielefeldt, W. V. & Vilela, A. C. F. Efficiency of inclusion absorption by slags during secondary refining of steel. *ISIJ International* 54, 1584–1591 (2014).
30. Chang, S., Cao, X., Zou, Z., Isac, M. & Guthrie, R. I. L. Micro-bubble formation under non-wetting conditions in a full-scale water model of a ladle shroud/tundish system. *ISIJ International* 58, 60–67 (2018).
31. Yang, H., Vanka, S. P. & Thomas, B. G. Mathematical modeling of multiphase flow in steel continuous casting. *ISIJ International* 59, 956–972 (2019).
32. Souza, G. M. de, Mendonça, A. de F. G. de & Tavares, R. P. Physical and mathematical modeling of inclusion behavior in a tundish with gas curtain. *REM - International Engineering Journal* 73, 531–538 (2020).
33. Lei, H., Yang, B., Bi, Q., Xiao, Y., Chen, S. & Ding, C. Numerical simulation of collision-coalescence and removal of inclusion in tundish with channel type induction heating. *ISIJ International* 59, 1811–1819 (2019).
34. Zhang, L., Taniguchi, S. & Cai, K. Fluid flow and inclusion removal in continuous casting tundish. *Metallurgical and Materials Transactions B* 31, 253–266 (2000).
35. Li, B., Lu, H., Zhong, Y., Ren, Z. & Lei, Z. Numerical simulation for the influence of EMS position on fluid flow and inclusion removal in a slab continuous casting mold. *ISIJ International* 60, 1204–1212 (2020).
36. Sahai, Y. & Emi, T. Melt flow characterization in continuous casting tundishes. *ISIJ International* 36, 667–672 (1996).
37. Sahai, Y. & Emi, T. *Tundish technology for clean steel production*. (World Scientific, 2007). doi:10.1142/6426.
38. Robertson, T. & Perkins, A. Physical and mathematical modelling of liquid steel temperature in continuous casting. *Ironmaking and Steelmaking* 13, 302 (1986).
39. Irving, W. R. *Continuous casting of steel*. (The Institute of Materials, 1993).
40. Caley, W. F. On the cause and prevention of tundish nozzle clogging. *High Temperature Materials and Processes* 25, 157–166 (2006).
41. Brian, G. T. & Hua, B. Tundish nozzle clogging - application of computational models. in *18th Process Technology Division Conference Proceedings* 895–912 (Iron and Steel Society, 2001).
42. Yang, W., Zhang, L., Ren, Y., Chen, W. & Liu, F. Formation and prevention of nozzle clogging during the continuous casting of steels: A review. *ISIJ International* 64, ISIJINT-2023-376 (2024).

43. Yuan, F., Wang, X., Zhang, J. & Zhang, L. Online forecasting model of tundish nozzle clogging. *Journal of University of Science and Technology Beijing, Mineral, Metallurgy, Material* 13, 21–24 (2006).
44. Musmeci, M., Rendtorff, N. M., Musante, L., Martorello, L., Galliano, P. & Aglietti, E. F. Characterization of MgO-based tundish working lining materials, microstructure and properties. *Ceramics International* 40, 14091–14098 (2014).
45. Wang, Q., Tan, C., Huang, A., Yan, W., Gu, H., He, Z. & Li, G. Numerical simulation on refractory wear and inclusion formation in continuous casting tundish. *Metallurgical and Materials Transactions B* 52, 1344–1356 (2021).
46. Deng, Z. & Zhu, M. Deoxidation mechanism of Al-killed steel during industrial refining process. *ISIJ International* 54, 1498–1506 (2014).
47. Conejo, A. N. & Hernández, D. E. Optimization of aluminum deoxidation practice in the ladle furnace. *Materials and Manufacturing Processes* 21, 796–803 (2006).
48. Pawełek, A. & Czechowski, J. Methods of eliminating the phenomenon of ladle nozzle clogging. *Archives of Metallurgy and Materials* 57, (2012).
49. Wang, Z., Yang, Z., Wang, X., Yue, Q., Xia, Z. & Xiao, H. Residence time distribution (RTD) applications in continuous casting tundish: A review and new perspectives. *Metals (Basel)* 12, 1366 (2022).
50. Merder, T. & Warzecha, M. Optimization of a six-strand continuous casting tundish: industrial measurements and numerical investigation of the tundish modifications. *Metallurgical and Materials Transactions B* 43, 856–868 (2012).
51. Nájera-Bastida, A., Garcia-Demedices, L., Ramírez-López, P., Torres-Alonso, E. & Morales, R. D. Dissipation of turbulent kinetic energy in a tundish by inhibitors with different designs. *Steel Research International* 78, 318–326 (2007).
52. Sheng, D. Y. & Yue, Q. Modeling of fluid flow and residence-time distribution in a five-strand tundish. *Metals (Basel)* 10, 1084 (2020).
53. Cathcart, C., Chattopadhyay, K., Guerra, F. & Li, D. Mathematical modeling of residence time distribution in a twin-strand slab caster tundish. in *AISTech 2021 Proceedings of the Iron and Steel Technology Conference* 1850–1860 (AIST, 2021). doi:10.33313/382/189.
54. Wang, G., Yun, M., Zhang, C. & Xiao, G. Flow mechanism of molten steel in a single-strand slab caster tundish based on the residence time distribution curve and data. *ISIJ International* 55, 984–992 (2015).
55. Cwudziński, A. Mathematical simulation and water modelling of liquid steel interaction with an argon bubble curtain in a one-strand continuous casting tundish. *Journal of the Southern African Institute of Mining and Metallurgy* 118, (2018).
56. Odenthal, H. J., Bölling, R., Pfeifer, H., Holzhauser, J. F. & Wahlers, F. J. Optimization of the fluid flow in a continuous casting tundish by physical and numerical modelling. in *4th European Continuous Casting Conference* (Birmingham , 2002).
57. Warzecha, P., Hutny, A. M., Warzecha, M. & Merder, T. Optimization of steel flow in the tundish by modifying its working area. *Archives of Metallurgy and Materials* 61, 2071–2078 (2016).
58. Liu, J., Zhou, P., Zuo, X., Wu, D. & Wu, D. Optimization of the liquid steel flow behavior in the tundish through water model experiment, numerical simulation and industrial trial. *Metals (Basel)* 12, 1480 (2022).

59. Gonzalez, O. J. P., Guzman, Y. I. C., Ramirez-Argaez, M. A. & Conejo, A. N. Melting behavior of simulated DRI in liquid steel. *Archives of Metallurgy and Materials* 53, 359–365 (2008).
60. Fornander, S. & Nilsson, F. Inductive stirring in arc furnaces. *Journal of Metals* 2, 256–260 (1950).
61. Arzpeyma, N. Modeling of electric arc furnaces (EAF) with electromagnetic stirring. (Royal Institute of Technology, Stockholm, 2011).
62. Elkoumy, M. M., El-Anwar, M., Fathy, A. M., Megahed, G. M., El-Mahallawi, I. & Ahmed, H. Simulation of EAF refining stage. *Ain Shams Engineering Journal* 9, 2781–2793 (2018).
63. Elkoumy, M. M., El-Anwar, M., Fathy, A. M., Megahed, G. M., El-Mahallawi, I. & Ahmed, H. Computational simulation model for metallurgical effects during EAF refining stage: waiting and arcing time. *ISIJ International* 58, 1669–1678 (2018).
64. Guo, G. A., Gu, D. & Irons, L. *in 58th Electric Furnace Conference and 17th Process Technology Conference proceedings* Preprint at (2000).
65. Wang, G., Zhu, R. & He, C. Two-phase mathematical model of oxygen jet impinging on molten steel bath surface in EAF. *The Chinese Journal of Process Engineering* 625–631 (2010).
66. Han, J., Chen, Y. & Li, S. *Industrial Heating* 39, 30 (2010).
67. He, C., Zhu, R., Liu, C. & Li, J. Analysis on decarburization rate based on numerical simulation in EAF steelmaking. *Steelmaking* 27, 41–44 (2011).
68. Zhu, R. & Wei, G. *in 19th National Steelmaking Academic Conference* Preprint at (2016).
69. Wang, F., Jin, Z. & Zhu, Z. Fluid flow modeling of arc plasma and bath circulation in DC electric arc furnace. *Journal of Iron and Steel Research International* 13, 7–13 (2006).
70. Yang, J. & Wu, Z. *Iron Steel* 30, 20 (1995).
71. Kazak, O. & Semko, O. Modelling magnetohydrodynamic processes in DC arc steelmaking furnace with bottom electrodes. *Ironmaking & Steelmaking* 38, 353–358 (2011).
72. Ramírez, M., Alexis, J., Trapaga, G., Jönsson, P. & Mckelliget, J. Mathematical modeling of iron and steel making processes. Modeling of a DC electric arc furnace. Mixing in the bath. *ISIJ International* 41, 1146–1155 (2001).
73. Bowman, B. & Kruger, K. *Arc furnace physics*. (Verlag Stahleisen, Dusseldorf, 2009).
74. Chen, Y., Silaen, A. K. & Zhou, C. Q. 3D integrated modeling of supersonic coherent jet penetration and decarburization in EAF refining process. *Processes* 8, 700 (2020).
75. Dong, K., Zhu, R. & Liu, W. J. Bottom-blown stirring technology application in Consteel EAF. *Advanced Materials Research* 361–363, 639–643 (2011).
76. Conejo, A. N. Stirring in the EAF. in *Electric arc furnace: methods to decrease energy consumption* 513–553 (Springer Nature Singapore, Singapore, 2024). doi:10.1007/978-981-97-4053-6_9.
77. Teng, L. Yield improvement with electromagnetic stirring in electric arc furnace. in *Proceedings of the 7th International Congress on Science and Technology of Steelmaking (ICS 2018)* (2018).
78. Teng, L. Effect of EMS on inclusion removal in ladle furnace for specialty steel production. in *AISTech Proceedings* 1395–1402 (2017).
79. Teng, L., Meador, M. & Ljungqvist, P. Application of new generation electromagnetic stirring in electric arc furnace. *Steel Research International* 88, (2017).

80. Teng, L., Jaworczak, K., Zielinska, M. & Yang, H. Numerical simulation and industrial results for electromagnetic stirring technology in electric arc furnace. in *5th ESTAD 2021* (2021).
81. Teng, L., Jones, A., Hackl, H. & Meador, M. ArcSave®, Innovative solution for higher productivity and lower cost in the EAF. in *Iron & Steel Technology* 1965–1973 (2015).
82. Teng, L., Hackl, H. & Rezende, L. M. de. The effect of ArcSave on the EAF process with eccentric bottom tapping. in *Anais do Seminário de Aciaria, Fundição e Metalurgia de Não-Ferrosos* 244–251 (Editora Blucher, São Paulo, 2017). doi:10.5151/1982-9345-26378.
83. Zielinska, M., Yang, H., Madej, L. & Malinowski, L. Development and validation of computational fluid dynamics model of ladle furnace with electromagnetic stirring system. *Materials* 17, 960 (2024).
84. Zielinska, M., Yang, H., Madej, Ł. & Malinowski, Ł. Influence of electromagnetic field on stirring energy in selected metallurgical equipment. *Steel Research International* (2023) doi:10.1002/srin.202300534.
85. Lazcano, A., Vargas, G. & Maroto, C. Process to improve the refining of liquid metals by natural gas injection. (1988).
86. Lazcano, A. & Vargas, G. Startup and preliminary results of bottom blowing natural gas into an EBT [eccentric bottom tapping] arc furnace at Deacero, S.A. *Iron & Steelmaker* 17, 58–62 (1990).
87. Ishihara, E. *Introduction to the technology of gas purging plug refractories for steelmaking EAF*. (2023).
88. Ogata, K. & Kago, T. *Development of porous brick for porous plug*. (2019).
89. Ma, G., Zhu, R., Dong, K., Li, Z., Liu, R., Yang, L. & Wei, G. Development and application of electric arc furnace combined blowing technology. *Ironmaking & Steelmaking* 43, 594–599 (2016).
90. Kirschen, M., Hanna, A. & Zettl, K. M. Improvement of EAF process and refractory consumption by advanced slag modeling. in *in AISTech - Iron and Steel Technology Conf. Proc.* (2016).
91. Mimura, N. & Ususaka, M. *GB2254682A*. (1992).
92. Badr, J., Kirschen, K. & Cappel, M. Chemical energy and bottom stirring system - cost effective solutions for a better performing EAF. in *in METEC 2011* (Dusseldorf, Germany, 2011).
93. He, P., Zhang, D. M., Deng, K. W. & Zhang, R. S. Stirring technology of bottom blowing gas in electric arc furnace. *Iron Steel* 27, 65–70 (1992).
94. Sundberg, Y. Principles of the induction stirrer. *ASEA Journal* 44, 71–80 (1971).
95. Fdhila, R. B., Sand, U., Eriksson, J. E. & Yang, H. A stirring history. *ABB review* 45–48 (2016).
96. Widlund, O., Sand, U., Hjortstam, O. & Zhang, X. Modeling of electric arc furnaces (EAF) with electromagnetic stirring. *Engineering, Materials Science* (2011).
97. Arzpeyma, N., Widlund, O. & Ersson, M. Mathematical modeling of scrap melting in an EAF using electromagnetic stirring. *ISIJ International* 53, 48–55 (2013).
98. Walther, H. F. Induction stirring provides better control of operating techniques. *JOM* 6, 21–23 (1954).
99. Aiolfi, A., Arvedi, G., Bianchi, A., Daniele, C., Grasselli, A., Heaslip, L., Lehman, A., Mehraban, Z., Reali, S. & Teng, L. Simulation and performance results for electromagnetic stirring technology on Arvedi 450-ton Consteel® Furnace. in *8th*

International Congress on the Science and Technology of Steelmaking 280–286 (AIST, 2022). doi:10.33313/531/038.
100. Teng, L., Meador, M. & Ljungqvist, P. Application of new generation electromagnetic stirring in electric arc furnace. *Steel Research International* 88, 1600202 (2017).
101. Teng, L., Hackl, H. & Rezende, L. M. de. The effect of ArcSave on the EAF process with eccentric bottom tapping. in *Anais do Seminário de Aciaria, Fundição e Metalurgia de Não-Ferrosos* 244–251 (Editora Blucher, São Paulo, 2017). doi:10.5151/1982-9345-26378.
102. Teng, L., Jones, A., Hackl, H. & Meador, M. ArcSave®–Innovative solution for higher productivity and lower cost in the EAF. in *AISTech 2015 proceedings by AIST* (2015).
103. Teng, L., Ljungqvist, P., Hackl, H. & Andersson, J. Process improvement with EMS. *Steel Times International* (2016).
104. Lee, E. S., Teng, L., Kim, K., Andersson, J., Yang, H., Kim, H. & Jung, E. Problems with and solutions to skull formation in EBT furnace for tooling and stainless steel production. *Iron & Steel Technology* 56–63 (2021).
105. Andersson, J., Teng, A., Memoli, A., Grasselli, F. & Lehman, L. Performance of the electromagnetic stirring system applied to the flat bath Consteel® operation. in *AISTech2019 Proceedings of the Iron and Steel Technology Conference* 775–780 (AIST, 2019). doi:10.33313/377/081.
106. Cendekia, B. B. The effect of electromagnetic stirring and flow control devices on flow characteristics in eight-strand tundish. (Royal Institute of Technology, Stockholm, 2018).
107. De Santis, M., Marx, K., Pierre, R., Kleimt, B., De Miranda, U., Schrader, T., Garcia, J. & Eriksson, J.E. *RFCS Project, Final Report No. EUR 30444-EN*. (2015).
108. Teng, L. Yield improvement with electromagnetic stirring in electric arc furnace. in *Proceedings of the 7th International Congress on Science and Technology of Steelmaking (ICS 2018)* (Venice, Italy, 2018).
109. Rappaz, M., Bellet, M. & Deville, M. *Numerical modeling in materials science and engineering*. vol. 32 (Springer Berlin Heidelberg, Berlin, Heidelberg, 2003).
110. Cwudziński, A. & Jowsa, J. Influence of selected alloy additions on time mixing for pulse-step method of liquid steel alloying in the tundish. *La Metallurgia Italiana* 111, 20–27 (2019).
111. Lou, W. & Zhu, M. Numerical simulation of desulfurization behavior in gas-stirred systems based on computation fluid dynamics–simultaneous reaction model (CFD–SRM) coupled model. *Metallurgical and Materials Transactions B* 45, 1706–1722 (2014).
112. Cheng, R., Zhang, L., Yin, Y. & Zhang, J. Effect of side blowing on fluid flow and mixing phenomenon in gas-stirred ladle. *Metals (Basel)* 11, 369 (2021).
113. Bhansali, A., Godinez, J., Guo, X., Oltmann, H., Pretorius, E., Silaen, A., Thapliyal, V., Walla, N. & Zhou, C. Computational studies and optimization of inclusion removal in a steel ladle. in *AISTech 2021 Proceedings of the Iron and Steel Technology Conference* 874–889 (AIST, 2021). doi:10.33313/382/086.
114. Guthrie, R. I. L. Fluid flows in metallurgy—friend or foe? *Metallurgical and Materials Transactions B* 35, 417–437 (2004).
115. Skrzypczak, T. & Węgrzyn-Skrzypczak, E. Mathematical and numerical model of solidification process of pure metals. *International Journal of Heat and Mass Transfer* 55, 4276–4284 (2012).

116. Mochnacki, B. Numerical modeling of solidification process. in *Computational Simulations and Applications* 513–542 (2011).
117. Skrzypczak, T., Sowa, L. & Węgrzyn-Skrzypczak, E. Numerical model of solidification including formation of multiple shrinkage cavities. *Archives of Foundry Engineering* 37–42 (2019) doi:10.24425/afe.2020.131280.
118. White, D. A. & Verdone, N. Numerical modelling of sedimentation processes. *Chemical Engineering Science* 55, 2213–2222 (2000).
119. Furmanski, P. & Banaszek, J. Modelling of the mushy zone permeability for solidification of binary alloys. *Materials Science Forum* 508, 411–418 (2006).
120. Ni, J. & Beckermann, C. A volume-averaged two-phase model for transport phenomena during solidification. *Metallurgical Transactions B* 22, 349–361 (1991).
121. Stefani, F., Gundrum, T. & Gerbeth, G. Contactless inductive flow tomography. *Physical Review E* 70, 056306 (2004).
122. Ludwig, A., Wu, M. & Kharicha, A. Simulation in metallurgical processing: recent developments and future perspectives. *JOM* 68, 2191–2197 (2016).
123. Kharicha, A., Ludwig, A. & Wu, M. Spatio-temporal variation of the electromagnetic field during the electroslag remelting process. in *8th International Pamir Conference Fund. Appl. MHD* 695–699 (Borgo, France, 2011).
124. Goldstine, H. H. *A History of Numerical Analysis from the 16th through the 19th Century*. vol. 2 (1977).
125. Lin, C., Segel, L. A. & Handelman, G. H. *Mathematics applied to deterministic problems in the natural sciences*. (SIAM: Society for Industrial and Applied Mathematics, 1988).
126. Duff, I. S. & Watson, G. A. *The state of the art in numerical analysis*. (Oxford University Press, 1997).
127. Anderson, E., Bai, Z., Bischof, C., Blackford, S., Demmel, J., Dongarra, J., Croz, J., Greenbaum, A., Hammarling, S., McKenney, A. & Sorensen, D. *LAPACK Users' Guide*. (Society for Industrial and Applied Mathematics, 1992).
128. Golub, G. & Van Loan, C. *Matrix Computations*. (The Johns Hopkins University Press, 1996).
129. Kelley, C. *Iterative methods for linear and nonlinear equations*. (Society for Industrial and Applied Mathematics, 1995).
130. Nocedal, J. & Wright, S. *Numerical optimization*. (Springer-Verlag, 1999).
131. Brenner, S. & Scott, R. *The mathematical theory of finite element methods*. (Springer-Verlag, 1994).
132. Ascher, U. & Petzold, L. *Computer methods for ordinary differential equations and differential-algebraic equations*. (SIAM: Society for Industrial and Applied Mathematics, 1998).
133. Brenan, K., Campbell, S. & Petzold, L. *Numerical solution of initial-value problems in differential-algebraic equations*. (SIAM: Society for Industrial and Applied Mathematics, 1996).
134. Iserles, A. *A first course in the numerical analysis of differential equations*. (Cambridge University Press , 1996).
135. Sobieski, W. & Šarler, B. Numerical methods in fluid mechanics – an overview. *Technical Sciences* 26, (2023).
136. Ansys® Fluent Release 2022 R2. Help System, Ansys Fluent Theory Guide. *ANSYS, Inc*.

137. Courant, R., Friedrichs, K. & Lewy, H. On the partial difference equations of mathematical physics. *IBM Journal of Research and Development* 11, 215–234 (1967).
138. Causon, D. M. & Mingham, C. G. *Introductory finite difference methods for PDEs*. (Ventus Publishing ApS, 2010).
139. Langtangen, H. P. & Linge, S. *Finite difference computing with PDEs – a modern software approach*. (Springer Open).
140. McDonald, P. W. The computation of transonic flow through two-dimensional gas turbine cascades. in *Proceedings of the ASME 1971 International Gas Turbine Conference and Products Show* (Houston, Texas, USA, 1971).
141. Maccormack, R. & Paullay, A. Computational efficiency achieved by time splitting of finite difference operators. in *10th Aerospace Sciences Meeting* (American Institute of Aeronautics and Astronautics, Reston, Virigina, 1972). doi:10.2514/6.1972-154.
142. Moukalled, F., Mangani, L. & Darwish, M. *The finite volume method in computational fluid dynamics*. vol. 113 (Springer International Publishing, Cham, 2016).
143. Niedźwiedzka, A., Schnerr, G. H. & Sobieski, W. Review of numerical models of cavitating flows with the use of the homogeneous approach. *Archives of Thermodynamics* 37, 71–88 (2016).
144. Ramasetti, E. K., Visuri, V. V., Sulasalmi, P., Fabritius, T., Saatio, T., Li, M. & Shao, L. Numerical modeling of open-eye formation and mixing time in argon stirred industrial ladle. *Metals (Basel)* 9, 829 (2019).
145. Li, M. & Zhang, L. Influence of the gas bubble size distribution on the ladle stirring process. *Processes* 8, 1663 (2020).
146. Sobieski, W. Switch function and sphericity coefficient in the Gidaspow drag model for modeling solid-fluid systems. *Drying Technology* 27, 267–280 (2009).
147. Hughes, T. J. R. & Zienkiewicz, O. C. *Finite elements in fluid mechanics: an introduction to the Galerkin method*. (Pergamon Press, 1979).
148. E, W. & Liu, J.-G. Gauge finite element method for incompressible flows. *International journal for numerical methods in fluids* 34, 701–710 (2000).
149. Zienkiewicz, O. C., Taylor, R. L. & Zhu, J. Z. *The finite element method: its basis and fundamentals*. (Elsevier Butterworth-Heinemann, 2005).
150. Hughes, T. J. R. & Brooks, A. N. A multi-dimensional upwind scheme with no crosswind diffusion. in *Finite element methods for convection dominated flows* vol. 34 (Amer Society of Mechanical Engineers, 1979).
151. Brooks, A. N. & Hughes, T. J. R. Streamline upwind/Petrov-Galerkin formulations for convection dominated flows with particular emphasis on the incompressible Navier-Stokes equations. *Computer Methods in Applied Mechanics and Engineering* 32, 199–259 (1982).
152. Tezduyar, T. E. & Hughes, T. J. R. *Development of time-accurate finite element techniques for first-order hyperbolic systems with particular emphasis on the compressible Euler equations*. (1982).
153. Tezduyar, T. & Hughes, T. Finite element formulations for convection dominated flows with particular emphasis on the compressible Euler equations. in *21st Aerospace Sciences Meeting* (American Institute of Aeronautics and Astronautics, Reston, Virigina, 1983). doi:10.2514/6.1983-125.
154. Tezduyar, T. E. Stabilized finite element formulations for incompressible flow computations. in 1–44 (1991). doi:10.1016/S0065-2156(08)70153-4.

155. Krüger, T., Kusumaatmaja, H., Kuzmin, A., Shardt, O., Silva, G. & Viggen, E. M. *The lattice Boltzmann method*. (Springer International Publishing, Cham, 2017). doi:10.1007/978-3-319-44649-3.
156. Sukop, M. C. & Thorne, D. T. *Lattice Boltzmann modeling – an introduction for geoscientists and engineers*. (Springer, 2006).
157. Wagner, A. J. *A Practical introduction to the lattice Boltzmann method*. (North Dakota State University, 2008).
158. Krause, M. J. Fluid flow simulation and optimization with lattice Boltzmann methods on high performance computers – application to the human respiratory system. (Karlsruhe Institute of Technology, 2010).
159. Abas, A., Mokhtar, N. H., Ishak, M. H. H., Abdullah, M. Z. & Ho Tian, A. Lattice Boltzmann model of 3D multiphase flow in artery bifurcation aneurysm problem. *Computational and Mathematical Methods in Medicine* 2016, 1–17 (2016).
160. Xie, Y., Liu, Y., Li, L., Xu, C. & Li, B. Simulation of different gas–solid flow regimes using a drag law derived from lattice Boltzmann simulations. *The Journal of Computational Multiphase Flows* 10, 202–214 (2018).
161. Schubiger, A., Barber, S. & Nordborg, H. Evaluation of the lattice Boltzmann method for wind modelling in complex terrain. *Wind Energy Science* 5, 1507–1519 (2020).
162. Chung, P. S., Jhon, M. S. & Biegler, L. T. The holistic strategy in multi-scale modeling. in 59–118 (2011). doi:10.1016/B978-0-12-380985-8.00002-6.
163. Samanta, R., Chattopadhyay, H. & Guha, C. A review on the application of lattice Boltzmann method for melting and solidification problems. *Computational Materials Science* 206, 111288 (2022).
164. Korn, C. & Herlitzius, T. Coupled CFD-DEM simulation of separation process in combine harvester cleaning devices. *Landtechnik* 72, 247–261 (2017).
165. Cundall, P. A. & Strack, O. D. L. A discrete numerical model for granular assemblies. *Géotechnique* 29, 47–65 (1979).
166. Fulchini, F., Ghadiri, M., Borissova, A., Amblard, B., Bertholin, S., Cloupet, A. & Yazdanpanah, M. Development of a methodology for predicting particle attrition in a cyclone by CFD-DEM. *Powder Technology* 357, 21–32 (2019).
167. Liu, Z., Ma, H. & Zhao, Y. CFD-DEM simulation of fluidization of polyhedral particles in a fluidized bed. *Energies (Basel)* 14, 4939 (2021).
168. Chu, K. CFD-DEM simulation of complex particle-fluid flows. (The University of New South Wales, 2010).
169. Zou, Y., Chen, C. & Zhang, L. Simulating progression of internal erosion in gap-graded sandy gravels using coupled CFD-DEM. *International Journal of Geomechanics* 20, (2020).
170. Sobieski, W., Matyka, M., Gołembiewski, J. & Lipiński, S. The path tracking method as an alternative for tortuosity determination in granular beds. *Granular Matter* 20, 72 (2018).
171. Platzer, F. & Fimbinger, E. Modelling pasty material behaviour using the discrete element method. *Multiscale Science and Engineering* 3, 119–128 (2021).
172. Gao, Y., Cheng, Y. & Chen, J. Experimental study and 3-D meso-scale discrete element modeling on the compressive behavior of foamed concrete. *Buildings* 13, 674 (2023).
173. Khan, S. A. & Koç, M. Numerical modelling and simulation for extrusion-based 3D concrete printing: The underlying physics, potential, and challenges. *Results in Materials* 16, 100337 (2022).

174. Liu, G. R. & Liu, M. B. *Smoothed particle hydrodynamics*. (World Scientific, 2003). doi:10.1142/5340.
175. Li, S. & Liu, W. K. *Meshfree particle methods*. (Springer Berlin Heidelberg, Berlin, Heidelberg, 2004). doi:10.1007/978-3-540-71471-2.
176. Lind, S. J., Rogers, B. D. & Stansby, P. K. Review of smoothed particle hydrodynamics: towards converged Lagrangian flow modelling. *Proceedings of the Royal Society A: Mathematical, Physical and Engineering Sciences* 476, (2020).
177. Douillet-Grellier, T., Jones, B. D., Pramanik, R., Pan, K., Albaiz, A. & Williams, J. R. Mixed-mode fracture modeling with smoothed particle hydrodynamics. *Computers and Geotechnics* 79, 73–85 (2016).
178. Nguyen, T. T. T. & Hojny, M. Application of smoothed particle hydrodynamics method in metal processing: An overview. *Archives of Foundry Engineering* 67–80 (2022) doi:10.24425/afe.2022.140238.
179. Koukouvinis, P., Kyriazis, N. & Gavaises, M. Smoothed particle hydrodynamics simulation of a laser pulse impact onto a liquid metal droplet. *PLoS One* 13, (2018).
180. Abu-Zidan, Y., Mendis, P. & Gunawardena, T. Impact of atmospheric boundary layer inhomogeneity in CFD simulations of tall buildings. *Heliyon* 6, (2020).
181. Bergantz, G. W. & Ni, J. A numerical study of sedimentation by dripping instabilities in viscous fluids. *International Journal of Multiphase Flow* 25, 307–320 (1999).
182. Hanumanth, G. S., Irons, G. A. & Lafreniere, S. Particle sedimentation during processing of liquid metal-matrix composites. *Metallurgical Transactions B* 23, 753–763 (1992).
183. Rosner, F., Papadias, D., Brooks, K., Yoro, K., Ahluwalia, R., Autrey, T. & Breunig, H., Green steel: design and cost analysis of hydrogen-based direct iron reduction. *Energy & Environmental Science* 16, 4121–4134 (2023).
184. Liang, M., Cho, S. M., Ruan, X. & Thomas, B. G. Modeling of multiphase flow, superheat dissipation, particle transport, and capture in a vertical and bending continuous caster. *Processes* 10, 1429 (2022).
185. Chen, W., Zhang, L., Ren, Q., Ren, Y. & Yang, W. Large eddy simulation on four-phase flow and slag entrainment in the slab continuous casting mold. *Metallurgical and Materials Transactions B* 53, 1446–1461 (2022).
186. Liu, P. & Lin, P. *A numerical model for breaking waves: the volume of fluid method*. (1997).
187. Barral Jr., A. A., Minussi, R. B. & Canhoto Alves, M. V. Comparison of interface description methods available in commercial CFD software. *Journal of Applied Fluid Mechanics* 12, 1801–1812 (2019).
188. Lv, X., Zou, Q., Zhao, Y. & Reeve, D. A novel coupled level set and volume of fluid method for sharp interface capturing on 3D tetrahedral grids. *Journal of Computational Physics* 229, 2573–2604 (2010).
189. Enagi, I. I., Al-attab, K. A. & Zainal, Z. A. Liquid fuels spray and combustion characteristics in a new micro gas turbine combustion chamber design. *International Journal of Energy Research* 43, 3365–3380 (2019).
190. Poozesh, S., Karam, M., Akafuah, N. & Wang, Y. Integrating a model predictive control into a spray dryer simulator for a closed-loop control strategy. *International Journal of Heat and Mass Transfer* 170, 121010 (2021).
191. Jung, M., Park, H. B., Seo, K. & Kim, S. H. A Study on the residence time calculation method of a decay tank in a research reactor. *Transactions of the Korean Nuclear Society Spring Meeting* (2019).

192. Jimeno, G., Lee, Y. C. & Ni, X. The effect of particle size on flow in a continuous oscillatory baffled reactor using CFD. *The Canadian Journal of Chemical Engineering* 100, (2022).
193. Liu, Z., Qi, F., Li, B. & Jiang, M. Vortex flow pattern in a slab continuous casting mold with argon gas injection. *Journal of Iron and Steel Research International* 21, 1081–1089 (2014).
194. Lou, W. & Zhu, M. Numerical simulations of inclusion behavior in gas-stirred ladles. *Metallurgical and Materials Transactions B* 44, 762–782 (2013).
195. Miki, Y. & Thomas, B. G. Modeling of inclusion removal in a tundish. *Metallurgical and Materials Transactions B* 30, 639–654 (1999).
196. Raghavendra, K., Sarkar, S., Ajmani, S. K., Denys, M. B. & Singh, M. K. Mathematical modelling of single and multi-strand tundish for inclusion analysis. *Applied Mathematical Modelling* 37, 6284–6300 (2013).
197. Javurek, M., Gittler, P., Rössler, R., Kaufmann, B. & Preßlinger, H. Simulation of nonmetallic inclusions in a continuous casting strand. *Steel Research International* 76, 64–70 (2005).
198. Joo, S. & Guthrie, R. I. L. Inclusion behavior and heat-transfer phenomena in steelmaking tundish operations: Part I. Aqueous modeling. *Metallurgical Transactions B* 24, 755–765 (1993).
199. Shirabe, K. & Szekely, J. A mathematical model of fluid flow and inclusion coalescence in the R-H vacuum degassing system. *ISIJ International* 23, 465–474 (1983).
200. Sinha, A. K. & Sahai, Y. Mathematical modeling of inclusion transport and removal in continuous casting tundishes. *ISIJ International* 33, 556–566 (1993).
201. Wang, L. T., Peng, S. H., Zhang, Q. Y. & Li, Z. B. Mathematical model for growth and removal of inclusions in molten steel under gas-stirring conditions. *Steel Research International* 77, 25–31 (2006).
202. Ling, H., Zhang, L. & Li, H. Mathematical modeling on the growth and removal of non-metallic inclusions in the molten steel in a two-strand continuous casting tundish. *Metallurgical and Materials Transactions B* 47, 2991–3012 (2016).
203. Yin, Y. & Zhang, J. Mathematical modeling on transient multiphase flow and slag entrainment in continuously casting mold with double-ruler EMBR through LES+VOF+DPM Method. *ISIJ International* 61, 853–864 (2021).
204. Cwudziński, A. & Jowsa, J. Mathematical modeling of behavior a liquid steel flow and a non-metallic inclusions in the one strand wedge type tundish with a subflux turbulence controller and a low dam. *Materials Science Forum* 706–709, 1379–1384 (2012).
205. Zhang, L., Wang, Y. & Zuo, X. Flow transport and inclusion motion in steel continuous-casting mold under submerged entry nozzle clogging condition. *Metallurgical and Materials Transactions B* 39, 534–550 (2008).
206. Zhang, L., Yang, S., Cai, K., Li, J., Wan, X., Thomas, B. G. Investigation of fluid flow and steel cleanliness in the continuous casting strand. *Metallurgical and Materials Transactions B* 38, 63–83 (2007).
207. Takahashi, K., Ando, M. & Ishii, T. Numerical investigation of unsteady molten steel flow and inclusion behavior in the tundish in the ladle change period. *ISIJ International* 54, 304–310 (2014).
208. Lo, S. *Application of population balance to CFD modeling of bubbly flow via the MUSIG model*. (AEA Technology, 1996).

209. Yeoh, G. H. & Tu, J. Y. Population balance modelling for bubbly flows with heat and mass transfer. *Chemical Engineering Science* 59, 3125–3139 (2004).
210. Lo, S. & Zhang, D. Modelling of break-up and coalescence in bubbly two-phase flows. *The Journal of Computational Multiphase Flows* 1, 23–38 (2009).
211. Meisler, K. T. Multi-dimensional population balance models of crystallization processes. (Technical University of Denmark, 2014).
212. Hu, G., Ma, Y., Zhang, H. & Liu, Q. A mini-review on population balance model for gas-liquid subcooled boiling flow in nuclear industry. *Annals of Nuclear Energy* 157, 108174 (2021).
213. Buchholz, M., Haus, J., Pietsch-Braune, S., Kleine Jäger, F. & Heinrich, S. CFD-aided population balance modeling of a spray drying process. *Advanced Powder Technology* 33, 103636 (2022).
214. Das, A. & Kumar, J. Population balance modeling of volume and time dependent spray fluidized bed aggregation kernel using Monte Carlo simulation results. *Applied Mathematical Modelling* 92, 748–769 (2021).
215. Hussain, M., Kumar, J. & Tsotsas, E. A new framework for population balance modeling of spray fluidized bed agglomeration. *Particuology* 19, 141–154 (2015).
216. Gemello, L., Plais, C., Augier, F. & Marchisio, D. L. Population balance modelling of bubble columns under the heterogeneous flow regime. *Chemical Engineering Journal* 372, 590–604 (2019).
217. Besagni, G. & Inzoli, F. Prediction of bubble size distributions in large-scale bubble columns using a population balance model. *Computation* 7, 17 (2019).
218. Sundberg, Y. *Electric furnaces and induction stirrers*. (1979).
219. Li, J. & Eidem, M. *Ladle furnace stirring force calculation including U×B term*.
220. Christiansen, B. B. & Thiellesen, J. Finite element electromagnetic simulator. (Aalborg University, 2021).
221. Borgstrom, L., Kullinger, K. & Bergman, K. *ASEA Technical Report*. (1983).
222. Ling, H., Zhang, L. & Li, H. Mathematical modeling on the growth and removal of non-metallic inclusions in the molten steel in a two-strand continuous casting tundish. *Metallurgical and Materials Transactions B* 47, 2991–3012 (2016).
223. Sundberg, Y. Mechanical stirring power in molten metal in ladles obtained by induction of stirring and gas blowing. *Scandinavian Journal of Metallurgy* 7, 81–87 (1978).
224. Mazumdar, D. & Guthrie, R. I. L. The physical and mathematical modelling of gas stirred ladle systems. *ISIJ International* 35, 1–20 (1995).
225. Grasselli, A., Reali, S., Andersson, J., Lehman, A. & Teng, L. Consteerrer technology: getting the most out of the electric steelmaking process. in *The 4th European Conference on Clean Technologies in the Steel Industry* (Bergamo, Italy, 2018).
226. McIntyre, E. H. & Landry, E. R. AF steelmaking – process and practice update. *Iron & Steelmaker* 17, 61–66 (1993).
227. Fornander, S. & Nilsson, F. Inductive stirring in arc furnace. *Journal of Metals* 188, 33 (1950).
228. Leitner, T., Klemmer, O. & Pottlacher, G. Bestimmung der temperaturabhängigen oberflächenspannung des eisen-nickel-systems mittels elektromagnetischer levitation. *tm - Technisches Messen* 84, 787–796 (2017).
229. Volpp, J. Surface tension of steel at high temperatures. *SN Applied Sciences* 5, 237 (2023).

230. Widlund, O., Sand, U., Hjortstam, O. & Zhang, X. in *Proceedings of 4th International Conference on Modelling and Simulation of Metallurgical Processes in Steelmaking (SteelSim)* (Düsseldorf, 2011).
231. Cao, J., Li, Y., Lin, W., Che, J., Zhou, F., Tan, Y., Li, D., Dang, J. & Chen, C. Assessment of inclusion removal ability in refining slags containing Ce2O3. *Crystals (Basel)* 13, 202 (2023).
232. Warzecha, M. Non-metallic inclusions controlling at the ladle furnace (LF) station. *Metalurgija* 59, 503–506 (2020).
233. Liu, W. Study of inclusion removal in a gas-stirred ladle. (Purdue University, Hammond, 2018).
234. Warzecha, M., Hutny, A., Warzecha, P., Kutyła, Z. & Merder, T. Investigations of dual plug argon blowing for efficient mixing at ladle furnace station. *Archives of Metallurgy and Materials* 561–572 (2020) doi:10.24425/amm.2021.135893.
235. Villela-Aguilar, J. de J., Ramos-Banderas, J. Á., Hernández-Bocanegra, C. A., Urióstegui-Hernández, A. & Solorio-Díaz, G. Optimization of the mixing time using asymmetrical arrays in both gas flow and injection positions in a dual-plug ladle. *ISIJ International* 60, 1172–1178 (2020).
236. Alam, Z. & Mazumdar, D. Fluid flow and mixing phenomena in mechanically agitated and gas stirred ladle systems and their comparisons. *ISIJ International* 62, 112–123 (2022).
237. Zhu, M. Y., Inomoto, T., Sawada, I. & Hsiao, T. C. Fluid flow and mixing phenomena in the ladle stirred by argon through multi-tuyere. *ISIJ International* 35, 472–479 (1995).
238. Aoki, J., Thomas, B. G., Peter, J. & Peaslee, K. D. Experimental and theoretical investigation of mixing in a bottom gas-stirred ladle. in *AISTech Proceedings of the Iron & Steel Technology Conference* 1045–1056 (2004).
239. Tse-Chiang, H., Lehner, T. & Kjellberg, B. Fluid flow in ladles - experimental results. *Scandinavian Journal of Metallurgy* 9, 105–110 (1980).
240. Xin, Z., Sun, J., Zhang, J., He, B., Zhang, J. & Liu, Q. Multiobjective collaborative optimization of argon bottom blowing in a ladle furnace using response surface methodology. *Mathematics* 10, 2610 (2022).
241. Jardón-Pérez, L. E., González-Morales, D. R., Trápaga, G., González-Rivera, C. & Ramírez-Argáez, M. A. Effect of differentiated injection ratio, gas flow rate, and slag thickness on mixing time and open eye area in gas-stirred ladle assisted by physical modeling. *Metals (Basel)* 9, 555 (2019).
242. Terrazas, M. S. C. & Conejo, A. N. Effect of nozzle diameter on mixing time during bottom-gas injection in metallurgical ladles. *Metallurgical and Materials Transactions B* 46, 711–718 (2015).
243. Lou, W. & Zhu, M. Numerical simulation of slag-metal reactions and desulfurization efficiency in gas-stirred ladles with different thermodynamics and kinetics. *ISIJ International* 55, 961–969 (2015).
244. Jardón-Pérez, L. E., González-Rivera, C., Ramirez-Argaez, M. A. & Dutta, A. Numerical modeling of equal and differentiated gas injection in ladles: Effect on mixing time and slag eye. *Processes* 8, 917 (2020).
245. Sand, U., Yang, H., Eriksson, J. E. & Fdhila, R. B. Control of gas bubbles and slag layer in a ladle furnace by electromagnetic stirring. in *Proceedings Iron & Steel Technology* 49–59 (2009).

246. Alexis, J., Jönsson, P. & Jonsson, L. Heating and electromagnetic stirring in a ladle furnace. A simulation model. *ISIJ International* 40, 1098–1104 (2000).
247. Li, Y., Deng, A., Li, H., Yang, B. & Wang, E. Numerical study on flow, temperature, and concentration distribution features of combined gas and bottom-electromagnetic stirring in a ladle. *Metals (Basel)* 8, 76 (2018).
248. Warzecha, M., Hutny, A. & Merder, T. Determining the power of mixing of a metal bath during processing in a ladle furnace. in *Proceedings 27th International Conference on Metallurgy and Materials* 209–214 (2018).
249. Zhang, L. & Thomas, B. G. Inclusions in continuous casting of steel. *presented at XXIV National Steelmaking Symposium* Preprint at (2003).
250. Mazumdar, D. & Evans, J. W. Macroscopic models for gas stirred ladles. *ISIJ International* 44, 447–461 (2004).
251. Oeters, F., Pluschkell, W., Steinmetz, E. & Wilhelmi, H. Fluid flow and mixing in secondary metallurgy. *Steel Research* 59, 192–201 (1988).
252. Sheng, D. Y., Kim, C. S., Yoon, J. K. & Hsiao, T. C. Water model study on convection pattern of molten steel flow in continuous casting tundish. *ISIJ International* 38, 843–851 (1998).
253. Fukushi, K., Nogi, K. & Iguchi, M. Downward air-water two-phase flow near the outlet of a model immersion nozzle. *ISIJ International* 46, 620–622 (2006).
254. Kasai, N. & Iguchi, M. Water-model experiment on melting powder trapping by vortex in the continuous casting mold. *ISIJ International* 47, 982–987 (2007).
255. Wuppermann, C., Giesselmann, N., Ruckert, A., Pfeifer, H., Odenthal, H. J. & Hovestadt, E. A Novel approach to determine the mixing time in a water model of an AOD converter. *ISIJ International* 52, 1817–1823 (2012).
256. Levenspiel, O. *Chemical reaction engineering*. (Wiley, New York, 1972).
257. Taniguchi, S., Kikuchi, A., Ise, T. & Shoji, N. Model experiment on the coagulation of inclusion particles in liquid steel. *ISIJ International* 36, S117–S120 (1996).